

# MECHANICAL PROPERTIES OF MESOSCOPIC OBJECTS

THÈSE N° 2876 (2003)

PRÉSENTÉE À LA FACULTÉ SCIENCES DE BASE

Institut de physique de la matière complexe

SECTION DE PHYSIQUE

ÉCOLE POLYTECHNIQUE FÉDÉRALE DE LAUSANNE

POUR L'OBTENTION DU GRADE DE DOCTEUR ÈS SCIENCES

PAR

**András KIS**

Ingénieur physicien, Université de Zagreb, Croatie  
et de nationalité hongroise

acceptée sur proposition du jury:

Prof. L. Forró, directeur de thèse

Prof. U. Aebi, rapporteur

Dr. J.-P. Aimé, rapporteur

Prof. H. Brune, rapporteur

Lausanne, EPFL

2003



# *Abstract*

This thesis describes measurements of the mechanical properties on the nanoscale. Three different mesoscopic tubular objects were studied: MoS<sub>2</sub> nanotubes, carbon nanotubes and microtubules. The main goal was to investigate the interplay between the fine structure of these objects and their mechanical properties. Measurements were performed by elastically deforming tubes deposited on porous substrates with the tip of an atomic force microscope.

The first experimental part describes the mechanical characterization of MoS<sub>2</sub> nanotube bundles. Elastic deformation of MoS<sub>2</sub> nanotube bundles can be modelled, in analogy with carbon nanotube bundles, using two elastic moduli: the Young's modulus and the shear modulus describing the weak intertube coupling. The measured Young's modulus of 120 GPa has later been confirmed by theoretical modelling. It is in the range of commonly used engineering materials. The shear modulus corresponding to intertube sliding is an order of magnitude lower than in the case of carbon nanotube bundles. MoS<sub>2</sub> nanotubes could therefore prove an interesting model for studying 1D and weakly coupled systems. They could also be interesting as AFM tips, especially for biological applications thanks to their sulphur-based chemistry.

In the case of carbon nanotubes, the weak intertube coupling is a serious problem that has to be solved before they could be used as reinforcing fibers or building blocks of macroscopic objects. This problem was addressed in the second part of this thesis. Stable crosslinks were introduced into carbon nanotube bundles by irradiating them with electrons inside a TEM. AFM measurements performed in parallel with TEM observations show that the irradiation process is composed of two competing mechanisms: crosslinking, which is dominant at low exposures, and degradation of the crystalline structure followed by amorphization in the later stages of irradiation. Theoretical modelling shows that the crosslinks are most probably formed by interstitial carbon atoms.

The third part of this thesis describes measurements of the mechanical properties of microtubules performed in the liquid environment. The bending modulus shows a pronounced temperature dependence, in good agreement with previously published data on the dynamic instability of microtubules. The shear and the Young's moduli were simultaneously measured, on two different temperatures, using a substrate prepared by electron beam lithography. These measurements have demonstrated that microtubules behave as strongly anisotropic cylinders. This is due to their structure, with large gaps separating neighboring protofilaments. The observed stiffening of microtubules on low temperatures (<15°C) is due to increasing interaction between the protofilaments. This manifests itself as a decrease of disassembly velocity, showing that the dynamic behavior of microtubules is reflected in their mechanical properties.



## *Version abrégée*

Ce travail de thèse décrit les mesures de propriétés mécaniques à l'échelle nanométrique. Trois différents objets tubulaires de taille mésoscopiques ont été étudiés : des nanotubes de MoS<sub>2</sub>, nanotubes de carbone et microtubules biologiques. L'objectif principal a été l'étude de la relation entre la structure fine de ces objets et leurs propriétés mécaniques. Les mesures ont été effectuées par déformation élastique des tubes sur une surface poreuse à l'aide d'une pointe de Microscope à Force Atomique (AFM).

La première partie expérimentale traite de la caractérisation mécanique des fagots de nanotubes de MoS<sub>2</sub>. La déformation élastique de ces derniers peut être modélisée, par analogie avec les fagots de nanotubes de carbone en utilisant deux modules élastiques : le module de Young et le celui de cisaillement, décrivant le faible couplage intertube. Le module de Young mesuré expérimentalement a été confirmé par la suite par un modèle théorique. Cette valeur se situe dans les ordres de grandeurs des matériaux communément utilisés en ingénierie. Le module de cisaillement qui correspond au glissement des tubes les uns par rapport aux autres au sein du fagot, est d'un ordre de grandeur inférieur à celui observé pour les fagots de nanotubes de carbone. Les nanotubes de MoS<sub>2</sub>, se pose donc en modèle intéressant pour l'étude de systèmes unidimensionnels et faiblement couplés. Ils pourraient être également appropriés pour une utilisation en tant que pointes AFM, et cela spécialement pour les applications biologiques, du fait du soufre qui les composent.

Dans le cas des nanotubes de carbone, le faible couplage intertube reste un sérieux obstacle qui doit être franchi avant leur utilisation en tant que fibre de renfort mécanique ou toute élaboration d'objets macroscopique. L'étude de ce facteur fait l'objet de la deuxième partie de cette thèse. Une réticulation stable des fagots par irradiation in situ dans un microscope électronique à transmission (TEM) a été réalisée. Des mesures AFM en parallèle avec une observation en TEM indiquent que lors du processus d'irradiation deux mécanismes entrent en compétition. La réticulation qui est dominante à faible exposition et la dégradation de la structure cristalline suivie par une amorphisation des tubes à des degrés d'irradiation plus conséquents. Un modèle théorique indique que la réticulation est le plus probablement induite par les atomes interstitiels de carbone.

La troisième partie de ce travail de thèse décrit l'étude en milieu liquide des propriétés mécaniques des microtubules. En accord avec de précédentes données de la littérature concernant l'instabilité dynamique des microtubules, le module de courbure apparaît comme étant fortement dépendant de la température. Les modules de Young et de cisaillement ont été mesurés simultanément, à deux températures différentes, en utilisant un substrat préparé par lithographie électronique. Ces mesures ont permis de démontrer un comportement des microtubules analogues à celui de cylindres fortement anisotropiques. Ceci est dû à leur structure, avec de larges espaces séparant deux protofilaments adjacents. Le raidissement de ces derniers, observé à basse température (<15°C) provient de l'augmentation de l'interaction entre ces protofilaments. Cela correspond à une diminution de la vitesse de désassemblage, corroborant le fait que le comportement dynamique des microtubules se reflète dans leurs propriétés mécaniques.



# Contents

<b>1. Introduction</b> . . . . .	5
<b>2. Instrumentation</b> . . . . .	7
2.1. Introduction . . . . .	7
2.2. Scanning tunneling microscope . . . . .	7
2.3. Atomic force microscope . . . . .	9
<i>Detection systems</i> . . . . .	9
<i>Basic modes of operation</i> . . . . .	10
<i>Contact mode</i> . . . . .	11
<i>Non-contact mode</i> . . . . .	12
<i>Intermittent contact (tapping) mode</i> . . . . .	13
<i>Other modes</i> . . . . .	13
<i>AFM probes</i> . . . . .	13
<i>The scanner</i> . . . . .	16
2.4. Transmission electron microscope . . . . .	16
<b>3. Physical properties of carbon nanotubes</b> . . . . .	19
3.1. Introduction . . . . .	19
3.2. Basic morphologies and the synthesis . . . . .	20
<i>Arc-discharge growth</i> . . . . .	21
<i>Laser-ablation method</i> . . . . .	22
<i>CVD growth</i> . . . . .	22
<i>Chemical purification</i> . . . . .	23
<i>Mechanical purification</i> . . . . .	24
3.3. Nanotube chirality . . . . .	25
3.4. Electronic properties . . . . .	27
3.5. Mechanical properties . . . . .	29
<b>4. Mechanical measurements on individual nanotubes</b> . . . . .	33
4.1. Introduction . . . . .	33
4.2. Theoretical considerations . . . . .	34
<i>Linear theory of elasticity</i> . . . . .	34
4.3. Continuum models and nanotubes . . . . .	36
4.4. Overview of experimental results on nanotubes . . . . .	37
<i>Mechanical resonance excitation inside a TEM</i> . . . . .	37
<i>Lateral deformation by AFM</i> . . . . .	40
<i>Normal deformation by AFM</i> . . . . .	42
<i>Radial deformation by AFM</i> . . . . .	45
<i>Tensile loading inside a SEM</i> . . . . .	47

<b>5. Molybdenum disulphide (MoS<sub>2</sub>) nanotubes</b>	49
5.1. Introduction	49
5.2. Physical properties of MoS <sub>2</sub> nanostructures	50
<i>Structure of MoS<sub>2</sub> nanotubes</i>	50
<i>Basic electronic properties of MoS<sub>2</sub> nanotubes</i>	51
<i>Tribological properties of MoS<sub>2</sub> nanoparticles</i>	51
5.3. Synthesis of subnanometer-diameter MoS <sub>2</sub> nanotubes	53
5.4. Results: AFM and TEM observations	55
5.5. Results: shear and Young's moduli	57
5.6. Conclusions	61
<b>6. Irradiation-induced crosslinking of SWNT bundles</b>	63
6.1. Introduction	63
6.2. Irradiation effects on solids	64
<i>Excitations</i>	64
<i>Knock-on displacements</i>	65
<i>Displacement cross-section and displacement rate</i>	67
6.3. Irradiation effects on carbon nanostructures	69
<i>Graphite</i>	69
<i>Formation of carbon onions under irradiation</i>	71
<i>Transformation from onions to diamond under irradiation</i>	72
<i>Irradiation effects on carbon nanotubes</i>	73
6.4. Results: connecting carbon nanotubes in ropes	80
<i>Motivation</i>	80
<i>Experimental setup used in this thesis</i>	82
<i>Irradiation with 200keV electrons</i>	83
<i>Irradiation with 80keV electrons</i>	86
6.5. Conclusions	89
<b>7. Shear and Young's moduli of microtubules</b>	91
7.1. Introduction	91
7.2. Microtubule structure	93
<i>High-resolution structure of tubulin and microtubules</i>	96
7.3. Review of previously published results	98
<i>Thermal fluctuations</i>	98
<i>Hydrodynamic flow</i>	100
<i>Optical tweezers</i>	101
<i>Atomic force microscope</i>	103
<i>Summary</i>	104
7.4. Results: elastic deformation by AFM	106
<i>Surface functionalization</i>	106
<i>Microtubule preparation</i>	107
<i>Measurement setup</i>	110
<i>Bending modulus</i>	111
<i>Temperature dependence</i>	113
<i>Shear modulus</i>	117
<i>Finite element analysis</i>	122



7.5. Conclusions . . . . .	125
<b>8. General conclusions . . . . .</b>	<b>127</b>
<b>Appendix: mechanical deformation of beams . . . . .</b>	<b>129</b>
<i>Stretching of beams . . . . .</i>	129
<i>Differential equations for beam bending . . . . .</i>	130
<i>Cantilevered beam under a concentrated load . . . . .</i>	135
<i>Simply supported beam under a concentrated load . . . . .</i>	137
<i>Clamped beam under a concentrated load . . . . .</i>	138
<i>Shear deflections of beams . . . . .</i>	139
<b>Bibliography . . . . .</b>	<b>143</b>
<b>Curriculum Vitae . . . . .</b>	<b>153</b>
<b>Publications . . . . .</b>	<b>155</b>
<b>Acknowledgements . . . . .</b>	<b>157</b>



# 1

## *Introduction*

The accelerating development of nanoscience demands new methods for studying physical properties on the nanometer scale. Measuring and understanding the mechanical properties of nanoscale objects can give valuable insight into their structure, provide sufficient incentive for their practical application and also, as is the case of biological nanostructures, deepen our knowledge on the functioning of living matter.

This thesis is built on the pioneering work of Jean-Paul Salvetat and coworkers at the EPFL, in which a relatively “simple” experiment provided new and valuable insight into the physics of carbon nanotubes. These measurements are based on a classical experiment in which the mechanical properties of suspended bars are probed by flexing them in the middle. However, in order to do the same with carbon nanotubes, one has to shrink the experiment by a factor of several millions. Two mechanical quantities have been measured in this way: the Young’s modulus, corresponding to the “stretchiness” of nanotubes and another quantity, describing sliding between the tubes, which is called the shear modulus because it plays the same role in the bending of nanotube bundles as the shear modulus in the bending of macroscopic tubes. Measuring these two quantities demonstrated that the fine structure of nanotubes can be probed in this way, inspiring a series of experiments which are the subject of this thesis. Measurements were performed on various kinds of nanotubes: inorganic, like carbon and MoS<sub>2</sub> and organic, the microtubules. These various tubular objects are what we mean under the term “mesoscopic objects”.

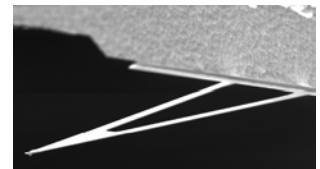
This introduction is followed by a short section describing the basic principles of two scientific instruments playing complementary roles during this work: atomic force and transmission electron microscopes. An overview of the physical properties of carbon nanotubes follows. The fourth chapter gives an introduction to continuum mechanics, providing the theoretical basis for the experiments, with the analytical aspects of beam deformation covered in the appendix; together with an overview of the previously published work on the mechanical properties of nanotubes. The subsequent three chapters present the main experimental results of

this thesis obtained using a variation of the same method, on three different mesoscopic objects, with different goals. MoS<sub>2</sub> nanotubes is an emerging material, possibly an alternative to carbon nanotubes in certain applications. Knowing their mechanical properties is an important first step in their future applications, and in this case also shows that they might have some unique and interesting physical properties. Mechanical measurements on carbon nanotubes, performed in parallel with observations in an electron microscope, proved that they can crosslink under electron beam irradiation. This could open a way to making macroscopic structures, built of interconnected carbon nanotubes. The example of microtubules shows how this kind of measurements can provide additional insight into the biological function of these fascinating biological “nanotubes”.

*Note: This manuscript can be downloaded as a pdf file from  
<http://library.epfl.ch/theses/>*

# 2

## *Instrumentation*



### 2.1. Introduction

The invention of the first scanning tunneling microscope (STM) in 1981 by Gerd Binnig and Heinrich Rohrer [1], enabled for the first time to image surfaces in real-space with atomic resolution. Five years later, this invention would win Binnig and Rohrer (together with Ruska for the development of a transmission electron microscope) the Nobel prize in physics [2].

This also marked the starting point in the development of a whole family of related techniques, commonly known as scanning probe microscopes (SPMs), one of which is the atomic force microscope (AFM). Scanning probe microscopes can not only image, but also measure physical properties such as surface conductivity, static charge distribution, local friction, magnetic fields and mechanical properties, and also manipulate individual atoms and small objects, resulting in diverse applications beyond the boundaries of physics.

### 2.2. Scanning tunneling microscope

STMs use a sharp, conducting tip with a bias voltage on the order of 1 V applied between the tip and the sample. When the tip is scanned close to the surface, within less than  $10\text{\AA}$ , the electron wave functions of the tip and the sample start to overlap, so that electrons can tunnel between the tip and the sample with the direction determined by the sign of the bias voltage (fig. 2.1). The wave function overlap and also the resulting tunneling current  $I_t$  depend exponentially on the tip-sample separation: when the separation changes by  $1\text{\AA}$ , the tunneling current changes by an order of magnitude, giving a mean to control the tip-sample distance with sub-angstrom precision. Most common STM tips are in the form of sharp tungsten needles.

Thanks to the exponential dependence of the tunneling current on the tip-sample separation, it is sufficient that only one atom protrudes from the tip in order to have good resolution.

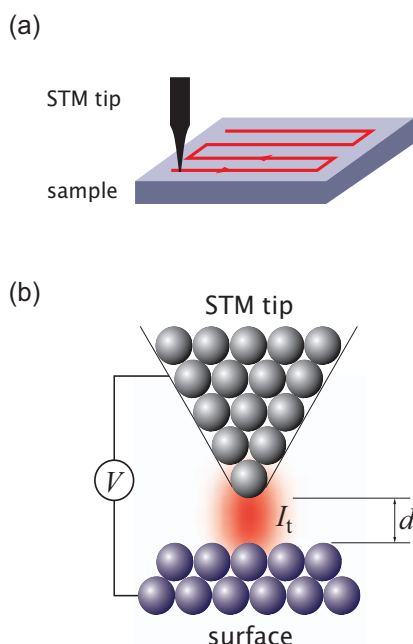


**Fig. 2.1.** (a) An STM tip is raster-scanned in the vicinity of the surface. (b) Schematic drawing of the tip-sample interaction in STM.

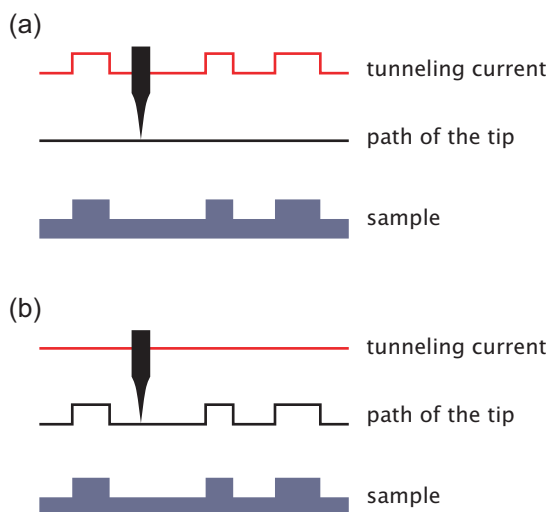


**Fig. 2.2.** (a) Constant height and (b) constant current mode of STM operation.

The tip is raster-scanned in the vicinity of the sample using a piezo-scanner (fig. 2.1) in one of the two basic modes of operation: constant height or constant current mode (fig. 2.2).

In the *constant height mode*, the tip scans in a horizontal plane above the sample, and the tunneling current varies depending on the local topography and electronic properties of the sample. The STM image is constituted from the local tunneling current, effectively mapping the tunneling probability across the surface.

In the *constant-current mode*, a negative feedback loop is used to maintain the tunneling current constant by adjusting the height of the piezo-scanner at each measurement point. The image is constructed from the voltage applied to the piezo-scanner which is converted into the vertical movement of the scanner. The image in this case corresponds to a map of constant tunneling probability.

Both acquisition modes are sensitive to local changes in the electronic structure and give topographic images only in the first approximation. This can be a tremendous advantage as it can yield information on local electronic properties with atomic resolution, implying that the STM can not only be used as an imaging but also as a spectroscopic tool. The systematic study of local electronic properties using an STM, the scanning tunneling spectroscopy (STS), encompasses many methods like taking constant-

current images using different voltages and comparing them, taking constant-height images at different heights and ramping the bias voltage while maintaining the tip position over a feature of interest and recording the tunneling current.

## 2.3. Atomic force microscope

STM relies on electron tunneling for its operation and therefore suffers from serious difficulties when working with insulating surfaces. The surface of an insulator can rapidly charge to the same potential as the tip, stopping the tunneling.

With the aim of overcoming this drawback while achieving a comparable resolution on insulating surfaces, an atomic force microscope (AFM) was developed in 1986 by Binnig, Quate and Gerber [3]. AFM probes the interactions between a sharp tip and a surface. The tip is located at the free end of a cantilever, typically 100 $\mu\text{m}$  long. Forces between the tip and the sample cause the cantilever to bend. The cantilever is raster-scanned across the sample and a detection system used to measure the cantilever deflection. The first AFM cantilever consisted of a small diamond hand-glued to a strip of gold foil.

As no tunneling is involved, AFM can in principle work equally well on insulating and conductive surfaces, as long as they are reasonably flat. Moreover, it can operate in diverse physical conditions like high or cryogenic temperature, ultrahigh vacuum, controlled atmosphere or even under liquid [4]. Although the AFM is a very flexible technique, atomic resolution is still difficult (but not impossible) to achieve [5] because of much larger tip and sample areas participating in the interaction than in the case of an STM where most of the tunneling occurs between a single protruding atom on the tip and 1–2 atoms on the surface.

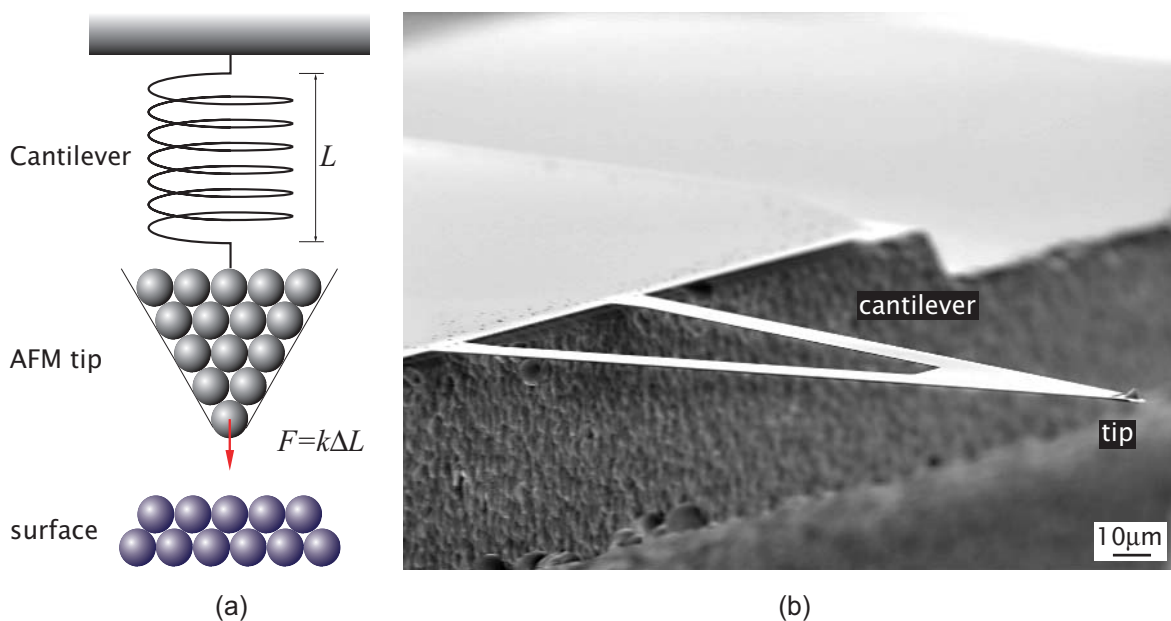


**Fig. 2.3.** (a) Principle of the atomic force microscope (b) Scanning electron microscope (SEM) image of an AFM probe.

### Detection systems

AFM relies on probing the interaction between a sharp tip located at the end of a cantilever and the sample. The tip-sample interaction is detected by monitoring the deflection of the cantilever (fig. 2.4). The first AFM used electron tunneling for detecting cantilever deflection [3]. An STM tip was placed above the cantilever, and changes in the cantilever-STM tip distance were detected by measuring the tunneling current (fig. 2.4a). This method offers high sensitivity

(on the order of  $0.01 \text{ \AA}$ ). It is however very sensitive to cantilever surface contamination and the tunneling itself can change the cantilever's effective spring constant.

A detection scheme offering comparable sensitivity uses laser interferometry [6]. In this technique, a laser beam focused on the backside of a cantilever interferes with a reference beam producing an interference pattern (fig. 2.4b). Cantilever deflection is measured by observing the variation in the intensity of interfering beams.

The simplest detection method to implement is the laser beam deflection method. It is based on focusing a laser beam on the end of a cantilever whose deflections are measured by following the motion of the laser spot on a split-photodiode [7] (fig. 2.4c and fig. 2.6). This method is widely used in commercial AFM systems and is much less sensitive to surface roughness and contamination but requires cantilevers with relatively high reflectivity.

Optical detection methods, both based on interferometry and the laser beam deflection method, require precise aligning of the laser on the cantilever and are relatively spacious. For applications where this might be an issue, piezoresistive cantilevers have been successfully employed [8]. In this case, the deflection sensor in the form of a piezoresistor is embedded into the arms of the cantilever (fig. 2.4d). The deflection changes are detected as resistance changes of this piezoresistive layer using a Wheatstone bridge.

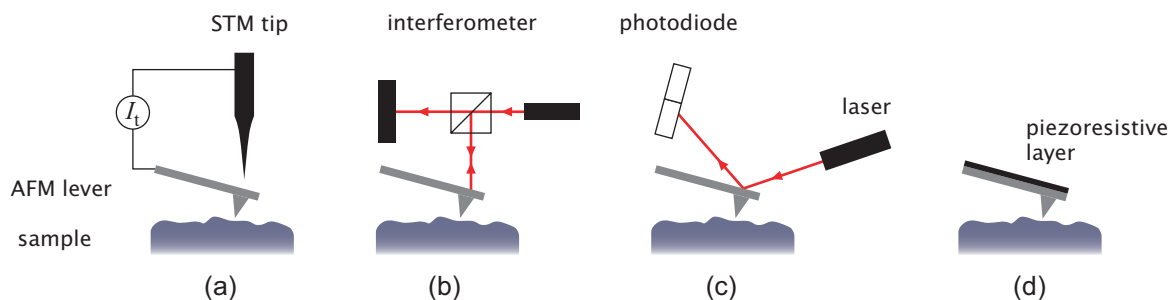


**Fig. 2.4.** Cantilever deflection schemes (a) employing an STM tip, where the tunneling current between the tip and the cantilever is used to detect cantilever deflection (b) based on an interferometer (c) laser beam deflection method (d) piezoresistive method.

### **Basic modes of operation**

Several forces contribute to the cantilever's deflection, most common of which is the van der Waals force, shown on fig. 2.5. Two force and distance regimes are characteristic for AFM operation. In the contact regime, the cantilever is held less than a few angstroms from the sample surface and the interaction between tip and the sample is repulsive. In the non-contact regime, the cantilever is kept further away from the surface and the forces are attractive.

In addition to the van der Waals interaction, other forces can play a significant role during AFM operation like the capillary force exerted by a thin water layer covering the sample under ambient conditions and electrostatic forces due to charged insulating surfaces.



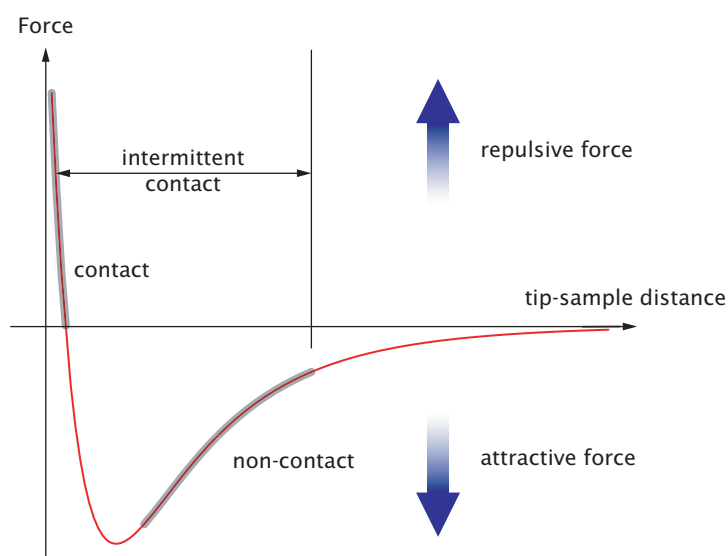


**Fig. 2.5.** Dependence of interatomic force on distance and the regimes of AFM operation.

The most common setup used for AFM imaging is schematically depicted on fig. 2.6. Cantilever deflection is monitored using a laser beam deflection method, by measuring the voltage difference between the upper and lower halves of the split position-sensitive photodiode.

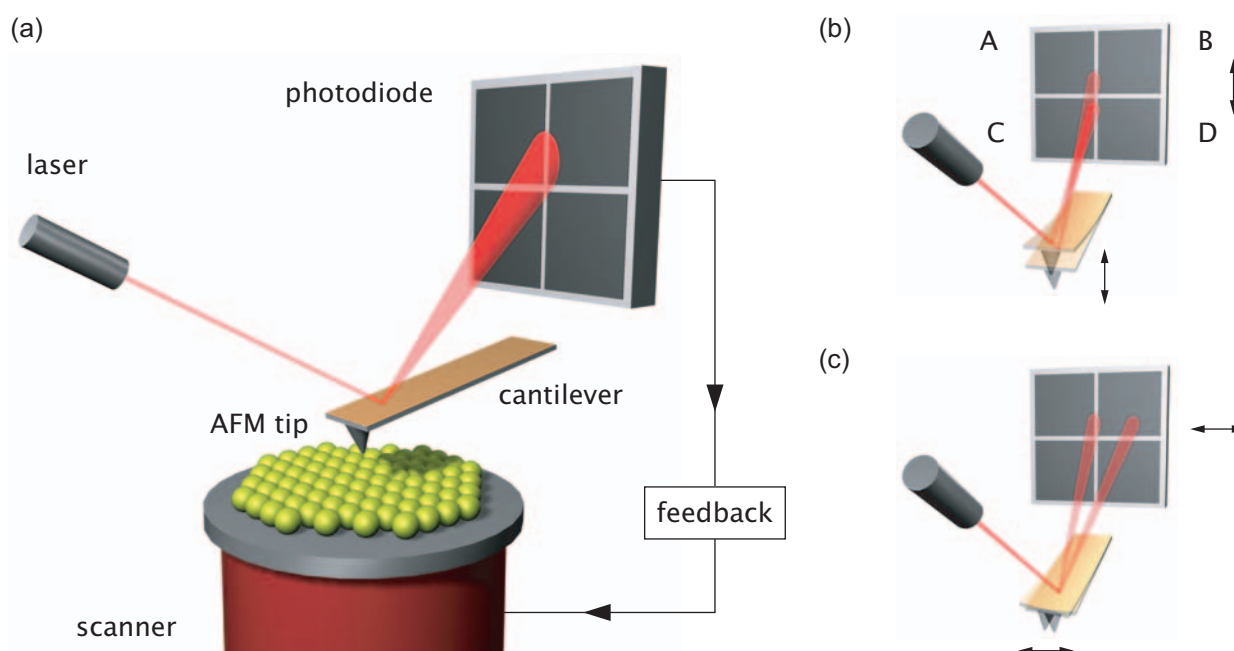


**Fig. 2.6.** (a) AFM setup based on the laser beam deflection method for detecting (b) normal deformation and (c) lateral deformation of the AFM cantilever.

### Contact mode

In contact mode, AFM can generate images by operating in two ways: constant-height or constant-force (fig. 2.7) modes that are analogous to the constant-height and constant-current modes of STM (fig. 2.2 on p. 8). In constant-height mode, the spatial variation of the cantilever's deflection is used to directly construct a topographical image of the surface. This mode is often

used for acquiring atomic-scale images of flat surfaces. On rough surfaces, it can easily damage the AFM probe. The scanning speed is mostly limited by the cantilever's resonant frequency.

In constant-force mode, the cantilever's deflection is used as input to a feedback circuit that moves the scanner up and down in the direction of the z-axis, responding to topographical changes by keeping the cantilever deflection, and therefore also the tip-sample interaction force constant. Typical forces range from 10pN–10nN. Topography is indirectly recorded, by converting the voltage needed to contract or elongate the piezo-scanner into topography. The scanning speed is limited by the response of the feedback-loop.

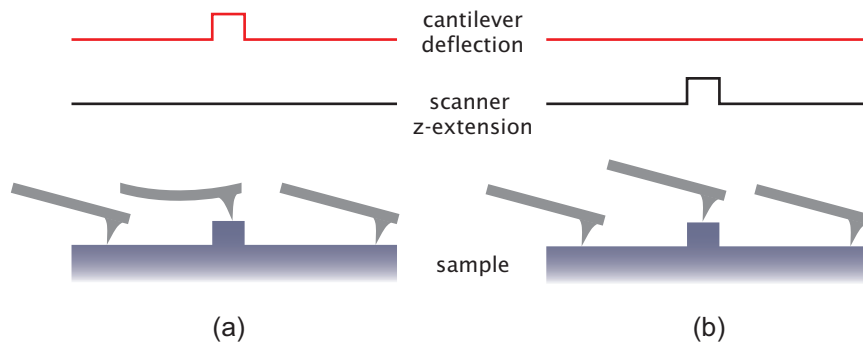


Fig. 2.7. (a) Constant-height (deflection) mode and (b) constant-force mode.

Apart from deflecting in the normal direction, the cantilever can also deflect laterally. There are two sources for lateral deflection: changes in surface friction or changes in local slope. In the first case, the cantilever twists when it encounters an area with a different friction coefficient. In the second, it's a steep slope that may cause the cantilever to twist under the influence of tangential force [9]. The lateral force is the signal used for measurements and imaging in the lateral force microscopy (LFM).

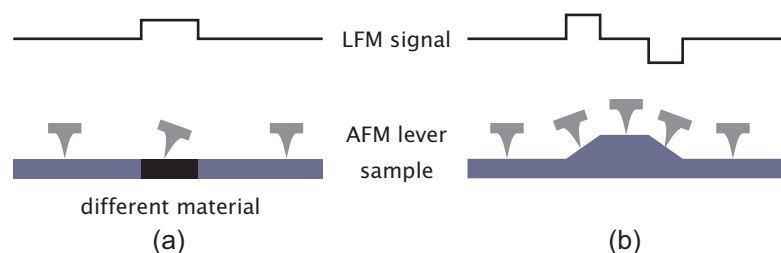


Fig. 2.8. Lateral deflection of a cantilever from changes in (a) local friction (b) slope

### ***Non-contact mode***

Non-contact AFM (NC-AFM) is a group of related techniques in which the cantilever is oscillated near the surface, usually close to or at one of its resonance modes. The tip is scanned very slowly across the surface so that each pixel in the image represents an average of several hundred oscillations. Long-range interactions between the tip and the sample, more precisely their gradient, contribute to the effective spring constant of the cantilever, changing its resonant frequency. Changes in the oscillating amplitude, frequency and phase are tracked and used to control the tip-sample distance [10]. A feedback loop is used to maintain either the resonant frequency or the oscillating amplitude constant by moving the scanner in the vertical direction. The forces involved are generally much lower than in contact-mode, on the order of 10pN,

requiring very sensitive AC detection schemes. Cantilevers are also stiffer than in contact mode in order to avoid snap-in – pulling of the AFM tip into contact with the sample due to surface adhesion.

### ***Intermittent contact (tapping) mode***

This is also a dynamic mode in which the cantilever is oscillated, but in contrast to NC-AFM, the tip is periodically hitting the surface. As in the case of NC-AFM, the image is reconstructed by monitoring changes in cantilever's oscillation amplitude.

Intermittent contact AFM (IC-AFM) is sometimes more appropriate for sample imaging, because it eliminates lateral forces (friction and drag) between the tip and the sample. Even though the lateral forces are absent, normal forces can be comparable to those in contact mode, leading to significant deformation of soft samples. This mode has been successfully adapted for working in liquid [11] and has become very popular among biologists.

### ***Other modes***

Several other imaging/measurement modes of AFM are in use today. Together with topographical images, they can map physical properties like local mechanical properties, magnetic field, electrical conductance, thermal conductance or capacity.

*Force modulation microscopy* is a dynamic mode in which the AFM tip is scanned in contact with the sample and a periodic signal is applied either to the tip or the sample [12]. The amplitude of cantilever modulation that results from this applied signal varies according to the elastic properties of the sample. Quantitative measurements using this technique are difficult.

*Electrostatic force microscopy* applies a voltage between the tip and the sample while the cantilever is held above the surface. Static charges cause cantilever deflection, enabling locally charged domains to be imaged. This technique is a valuable tool for testing microprocessor chips at the sub-micron scale.

*Magnetic force microscopy* uses AFM tips coated with a thin ferromagnetic layer. The system operates in non-contact mode, detecting changes in the cantilever's resonant frequency induced by the local magnetic field.

*Scanning thermal microscopy* can be used to measure local thermal conductivity of the sample. A resistive thermal element is incorporated at the end of a cantilever. The system generates an image of the sample's thermal conductivity from changes in heat dissipated from the integrated heater [13] while the cantilever's deflection is used for tracking the sample surface.

AFMs can also be used to deliberately modify surfaces by nanolithography, by applying high forces or electric current.

### ***AFM probes***

The crucial component of each AFM is its probe. It determines the kind of experiment that can be performed, the force applied on the sample and the imaging resolution. Commercial silicon or silicon-nitride cantilevers microfabricated using photolithographic techniques are in widespread use today.

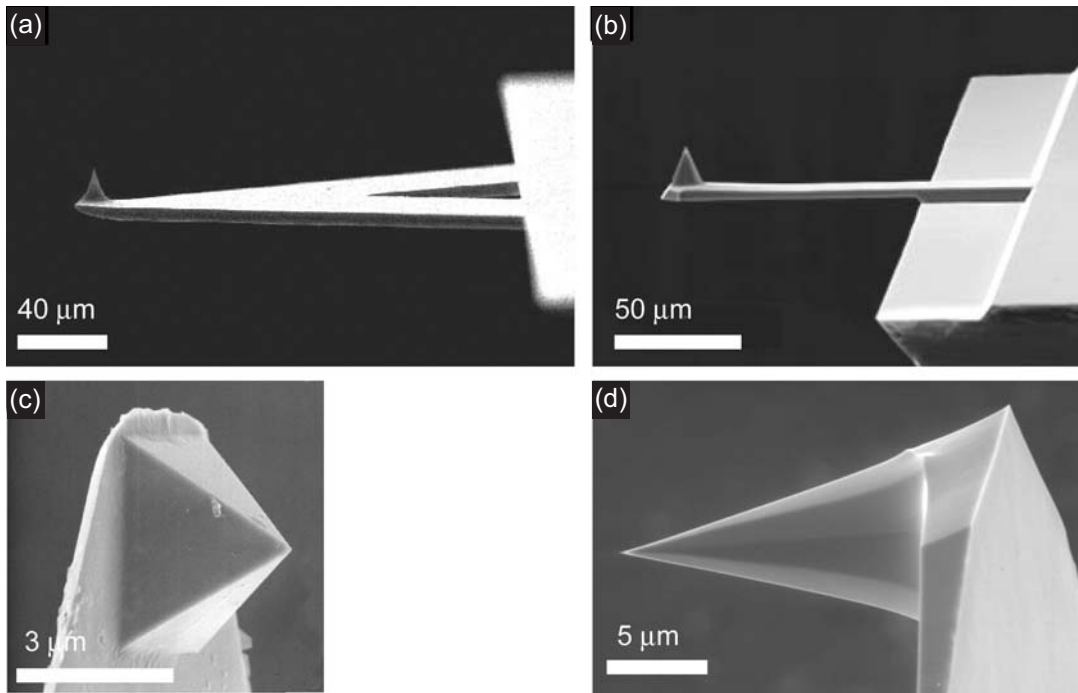


**Fig. 2.9.** Scanning electron microscope (SEM) images of typical AFM probes (a) triangular (b) rectangular (c) Pyramidal  $\text{Si}_3\text{N}_4$  tip (d) etched silicon tip.

According to the shape, there are two main types of cantilevers: triangular (fig. 2.9a) and rectangular (fig. 2.9b). The triangular, V-shaped cantilevers, have low mechanical resistance to vertical deflection and high mechanical resistance to lateral torsion. They are therefore more suited for imaging in contact mode, except for imaging based on frictional contrast where the rectangular cantilevers are more appropriate. Cantilevers typically range from 100 to 200  $\mu\text{m}$  in length, 10 to 40  $\mu\text{m}$  in width and 0.3 to 2  $\mu\text{m}$  in thickness.

Each point in an AFM image represents a spatial convolution of the tip shape with the imaged feature – a phenomenon known as tip convolution (fig. 2.10). This effect is most pronounced on samples with sharp edges and on measurements in the lateral direction. Heights and depths are in general accurately reproduced. Tip convolution can be minimized by using sharp tips with small apex angles. Ideal tip shapes can be achieved using electron-beam induced deposition of material on AFM tips [14] or by attaching or growing carbon nanotubes [15].

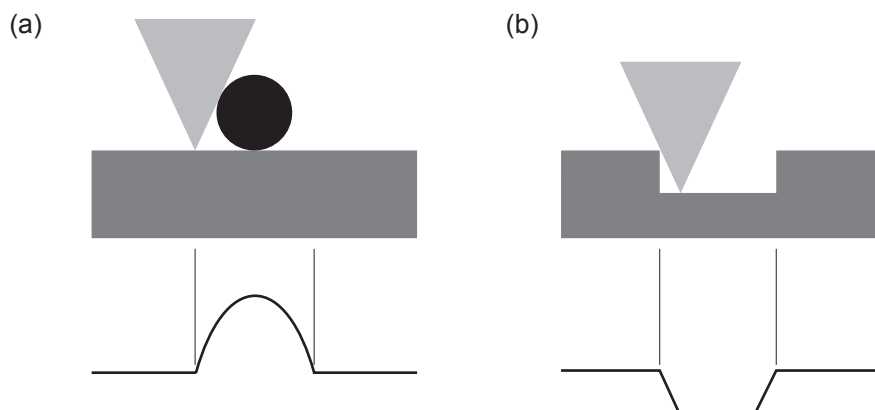


**Fig. 2.10.** Tip convolution of the AFM tip with a (a) circular object (b) rectangular trench.

Apart from having sharp tips, cantilevers should also have optimized spring constants and resonant frequencies. The spring constant should be lower than the spring constant of interatomic

forces (10N/m). The desired resonant frequencies are also above acoustic frequencies (20kHz) in order to minimize the influence of external acoustic noise. Cantilevers with higher resonant frequencies also enable faster scanning rates.

The spring constant  $k$  and resonant frequency  $f$  of a rectangular cantilever of width  $w$ , thickness  $t$  and length  $l$  is given by:

$$k = \frac{Ewt^3}{4l^3} \quad f = \frac{1}{2\pi} \sqrt{\frac{k}{m}} \quad (2.1)$$

for rectangular cantilevers, the resonant frequency can be approximated using the cantilever's Young's modulus  $E$  and density  $\rho$  as [16]:

$$f \approx \frac{t}{2\pi l^2} \sqrt{\frac{E}{\rho}} \quad (2.2)$$

During manufacturing, thousands of tips and cantilevers can be produced on a single wafer. Lengths and widths are accurately reproduced from one cantilever to the other, but the thickness can vary. For  $\text{Si}_3\text{N}_4$  cantilevers, this thickness variation across a wafer can even be seen with the naked eye as it manifests itself as variation in color. Changing thickness is most responsible for variations in the cantilever spring constant. By expressing the thickness  $t$  from equation (2.2) and replacing it in equation (2.1), one gets [16]:

$$k \approx f^3 w l^3 \frac{(2\pi\sqrt{\rho})^3}{\sqrt{E}} \quad (2.3)$$

Measuring variations in cantilever's resonant frequency (fig. 2.11) can be a quick and easy way of calibrating the spring constant.

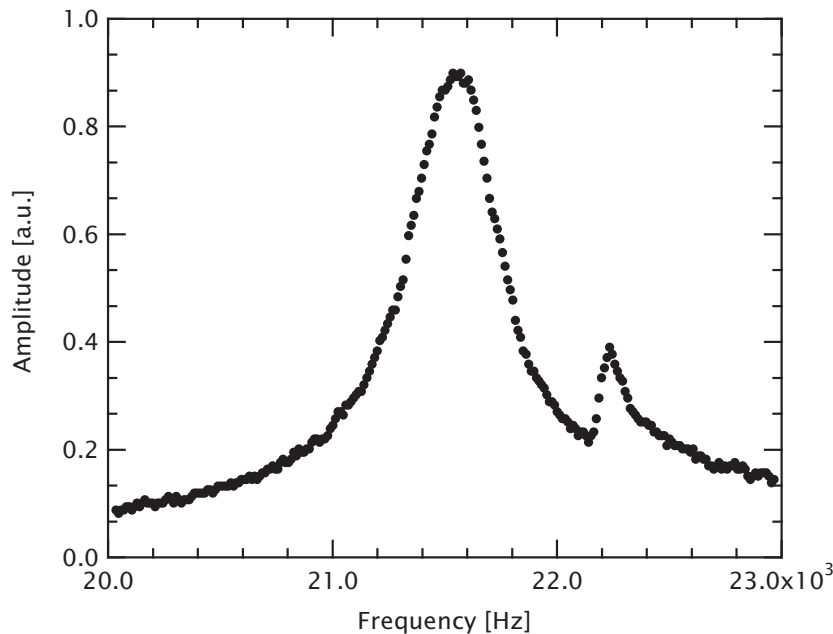


**Fig. 2.11.** Resonance curve of a  $\text{Si}_3\text{N}_4$  microlever from ThermoMicroscopes [17].

Cantilevers can sometimes be coated, for example with a thin metallic layer in order to increase the reflectance. Tips can also be coated with metals for conductive-AFM, ferromagnetic

materials for magnetic force microscopy or even with a diamond-like layer in order to increase resistance to mechanical wearing.

### The scanner

Piezoelectric tubes operating in flexion are commonly used for displacing the sample with respect to the probe (fig. 2.6 on p. 11). Scanners are usually made of PZT ceramics (Pb-Zr-Ti-O). Depending on the piezoelectric type and scanner size and design, the largest area which the scanner can cover can vary from several micrometers to several hundred micrometers. Vertical movements are roughly an order of magnitude smaller. Piezoelectric materials can perform relative movements smaller than atomic diameters but they suffer from three major inherent problems: hysteresis, nonlinearity and creep (fig. 2.12). These problems can be corrected during post-processing, using a precalibrated set of parameters and also during the data acquisition itself by using detectors for tracking the true movement of the scanner and correcting it by a feedback-loop.

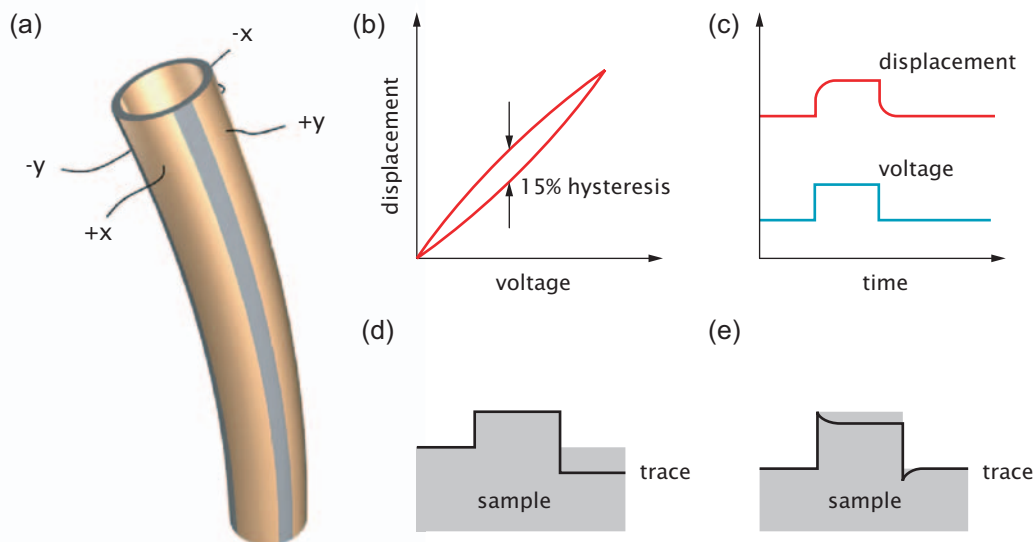


**Fig. 2.12.** (a) A piezo tube scanner [18] (b) hysteresis, (c) creep, and their respective influences on scanning (d) and (e) [19].

## 2.4. Transmission electron microscope

The transmission electron microscope (TEM), developed in 1932 by Knoll and Ruska in Germany is the first scientific instrument to rely on the wavelike nature of matter (electrons) for its operation. The underlying design of a TEM has a lot in common with light microscopes, encompassing a source of “light” (electrons), condenser and objective lenses. Higher resolution is achieved by using matter waves for imaging. Electrons are focused and deflected using magnetic lenses, usually in the form of magnetically soft iron cores, surrounded with copper coils and water-cooled. Electrostatic lenses were used in the first TEM, but they were quickly replaced with magnetic ones as they proved to be superior.

There are two main types of electron sources in use today: thermionic and field-emission sources. Thermionic sources rely on hot (2700K) tungsten filaments or lanthanum hexaboride

(LaB<sub>6</sub>) crystals heated to 1700K. Field-emission sources are sharp tungsten tips, maintained at room temperature from which electrons are extracted by the high electric field around the tip, producing a very bright, coherent and small-diameter beam. Operation of the sources themselves and the need to minimize electron scattering from gas molecules demands that TEMs operate under conditions of high or even ultrahigh vacuum.

High voltage between the emitter and the cathode accelerates electrons to typical energies of 80–300keV. The sample is illuminated with an electron beam using condenser lenses. The resulting image, representing a 2D projection of the sample, is magnified by the objective lens and the projector lens before being collected on a fluorescent screen, photographic paper or a CCD camera. The wavelength of electrons accelerated to 100keV is 4pm. Unfortunately, the main limiting factor in TEM resolution is not the electron wavelength but the aberrations due to electromagnetic lenses that result in a 1Å resolution for state-of-the-art microscopes.

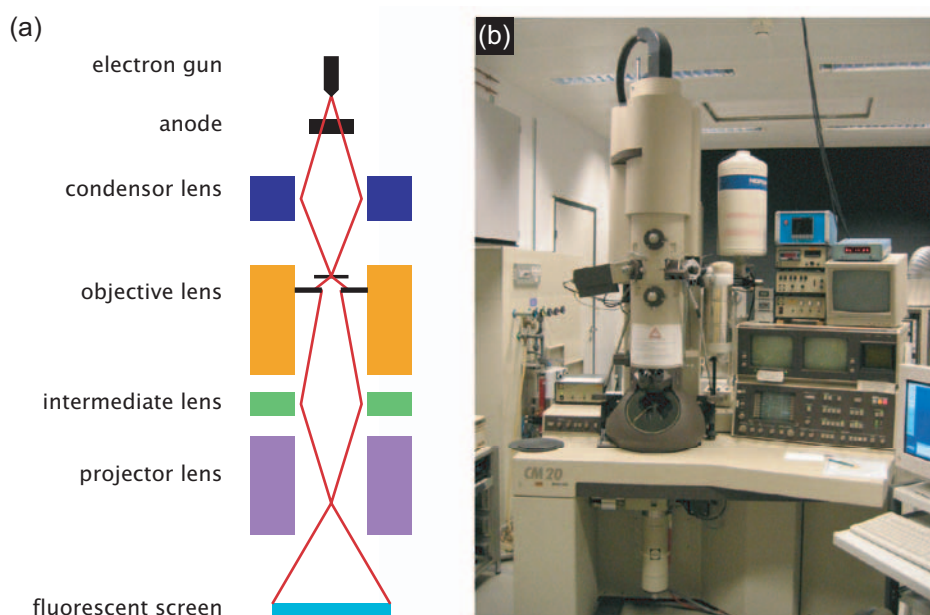


**Fig. 2.13.** (a) A simplified schematic drawing of the main components of a transmission electron microscope. (b) Philips CM20 electron microscope at CIME, EPFL.

In classical light microscopy, the image contrast results from different parts of the specimen absorbing light differently. In TEM, electron absorption is minimal and image contrast is due to electron scattering. Bright-field TEM images are composed of direct, unscattered electrons while dark-field images and diffraction patterns are formed by scattered electrons.

Apart from Bragg diffraction on crystalline planes, the dominant mechanism of electron scattering is Rutherford scattering. The corresponding cross-section is a function of atomic number  $Z$ , the mass or the density and sample thickness. Scattering at high angles ( $>5^\circ$ ) is determined by the atomic number only, serving as basis for  $Z$ -contrast imaging. At lower angles, the scattering depends both on the sample density and thickness, giving rise to mass-density contrast. Thanks to the dual wave-charged particle nature of electrons, TEMs not only provide images but can also yield a wealth of secondary signals like X-rays, Auger electrons and light [20].

Today, TEMs constitute a very efficient tool for material characterization by numerous methods like direct observation, electron diffraction, electron energy loss spectroscopy (EELS) and electron holography.

Carbon nanotubes have been discovered using a TEM in the carbon soot produced during electric arc discharge between two electrodes [21] (fig. 2.14a-c). Details of their microstructure have also been first studied using electron microscopy and diffraction [22] (fig. 2.14d).

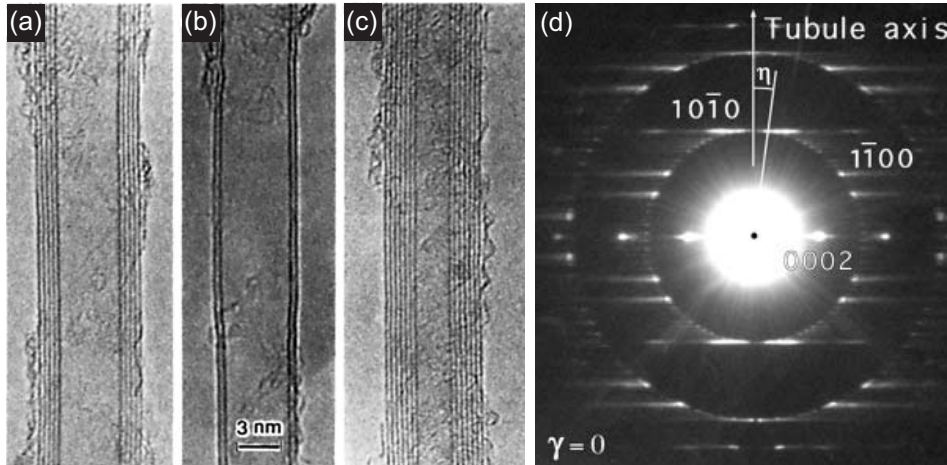
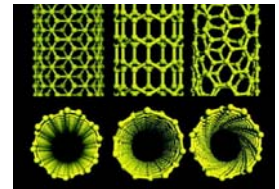


**Fig. 2.14.** (a)-(c) Bright field TEM images of multiwalled carbon nanotubes from Iijima's seminal paper [21]. (d) Electron diffraction pattern from a typical multiwalled carbon nanotube [23].



# 3

## *Physical properties of carbon nanotubes*



### 3.1. Introduction

The basic crystalline forms of elemental carbon, shown here on fig. 3.1, diamond, graphite and amorphous carbon have been known for quite some time. In 1986, with the discovery of  $C_{60}$  by Kroto and Smalley [24], a new form of carbon has been added to the list. The  $C_{60}$  molecule is a representative of a whole new class of molecules, the fullerenes.

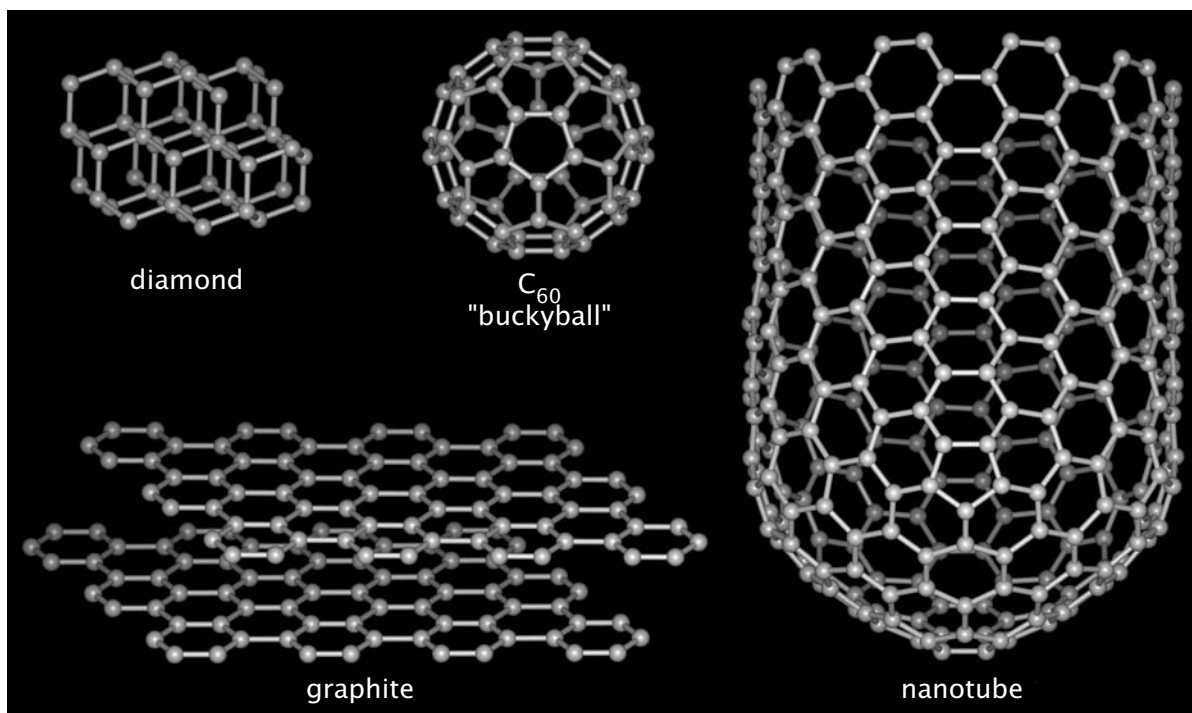
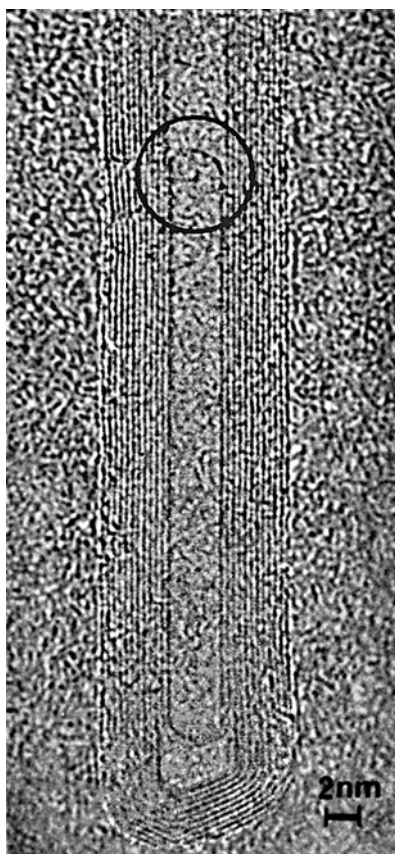


Fig. 3.1. Crystalline forms of carbon [25].

Such a wealth of existing carbon atom arrangements is made possible by a variety of hybridizations – configurations of the electronic states of carbon atoms.

Carbon nanotubes (CNTs) are the newest forms of carbon discovered in 1991 by S. Iijima [21]. This date in fact corresponds to the first paper in which their structure and importance was fully recognized. There are claims of their earlier observation. The first clear TEM images with genuine nanotubes were also made by Iijima, already in 1979 [26] (fig. 3.2).



Owing to their remarkable properties, this discovery has opened whole new fields of study in physics, chemistry and materials science. Nanotubes possess a unique combination of small size (diameters ranging from  $\sim 1$  to 50 nm with lengths up to several mm [27]), low density – similar to that of graphite, high stiffness, high strength and a broad range of electronic properties from metallic to p and n doped semiconducting. The field of their potential applications is immense, including reinforcing elements in high strength composites, electron sources in field emission displays and small X-ray sources, ultra-sharp and resistant AFM tips with high aspect ratios, gas sensors and as components of future nanoscale electronics. In addition, they represent a very popular system for studying fundamental physical phenomena on the mesoscopic scale. Following advances in manufacturing and processing, it is likely they will be integral to many devices that we use in our everyday life.

**Fig. 3.2.** TEM image of a “graphitic structure” from a 1980 paper by S. Iijima [26].

## 3.2. Basic morphologies and the synthesis

From the structural point of view, carbon nanotubes can be thought of as rolled-up single sheets of graphite, graphene. They can be divided into two distinct groups. The first to be discovered, multiwalled carbon nanotubes (MWNT), exhibit a Russian doll-like structure of nested, concentric tubes, fig. 3.3a and b.

The interlayer spacing can range from 0.342 to 0.375 nm, depending on the diameter and number of shells comprising the tube [28]. For comparison, the interlayer spacing in graphite is 0.335 nm. This suggests a relatively weak interaction between individual shells, confirmed by studies of mechanical and electronic properties of CNTs.

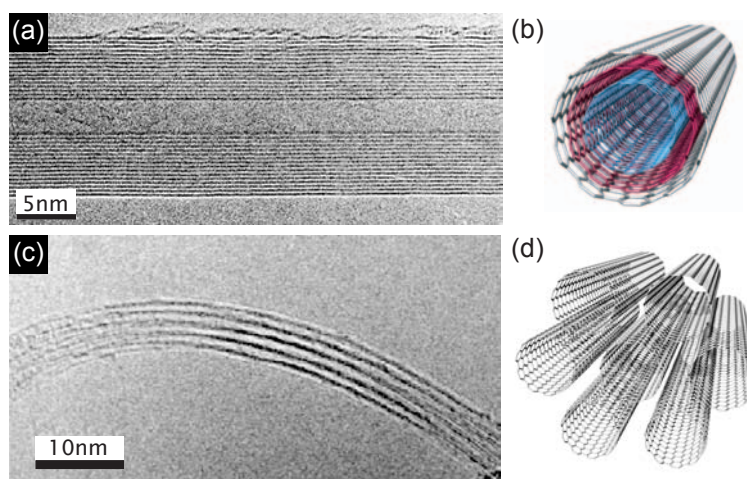


**Fig. 3.3.** Two basic morphologies of carbon nanotubes with corresponding schematic drawings. (a) TEM image and (b) a schematic drawing of a multiwalled nanotube. (c) TEM image and (d) a schematic drawing of a bundle (rope) of single-walled nanotubes.

The second type of carbon nanotubes is in the basic form of a rolled-up graphitic sheet – a single-walled CNT (SWNT). During the production, their diameter distribution is relatively narrow, so they often bundle up in the form of crystalline “ropes” [29], fig. 3.3d, where the single tubes are held together by van der Waals interaction.

### ***Arc-discharge growth***

There are several distinct classes of production methods. The earliest is based on the cooling of carbon plasma generated by the evaporation of solid carbon sources. In the arc-discharge method, which was originally used for synthesis of  $C_{60}$  [30], carbon is evaporated by a plasma of inert gas, usually helium or argon, ignited by a high current (in the range of 100A) passing through opposing carbon electrodes (fig. 3.4a). As the electrodes evaporate, their length decreases but the distance between them is kept constant.

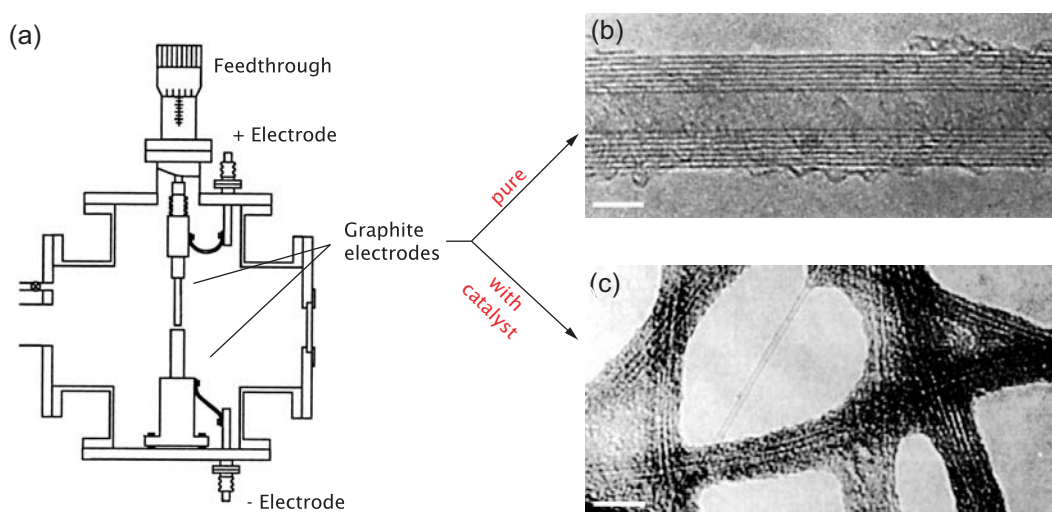


**Fig. 3.4.** (a) The arc-discharge method. MWNT nanotubes are produced when using pure graphitic electrodes and SWNT ropes when using electrodes containing a small amount of catalyst particles. (b) One of the first images of a MWNT [21]. (c) One of the first reported images of SWNT ropes [31].

Upon cooling, soot containing multiwalled nanotubes is formed on the cathode [21]. Fullerenes are produced along with nanotubes. After production, they are predominantly found in the soot deposited on the cooled growth-chamber walls. High quality MWNTs can be produced using this method by controlling the growth conditions like the inert gas pressure and the arcing current. The growth by-products are usually multilayered graphitic particles and fullerenes. If the anode is filled by a small percentage of metal catalysts [31], for example cobalt or iron particles, SWNT bundles as those on fig. 3.4b can form.

### **Laser-ablation method**

Another way of producing high quality CNTs from carbon plasma is by laser ablation [29]. In this method, intense laser pulses are used to ablate a carbon target containing 0.5% of nickel and cobalt (fig. 3.5). The target is placed into a furnace heated to 1200°C. During laser ablation, a flow of inert gas is passed through the chamber, carrying the nanotubes to be collected on a cold collector. The produced SWNTs are mostly in the form of bundles (ropes) consisting of several SWNTs closely packed into hexagonal crystals and held together by van der Waals interactions (fig. 3.1c and d, fig. 3.5b), with a typical intertube distance of 0.33 nm [32].

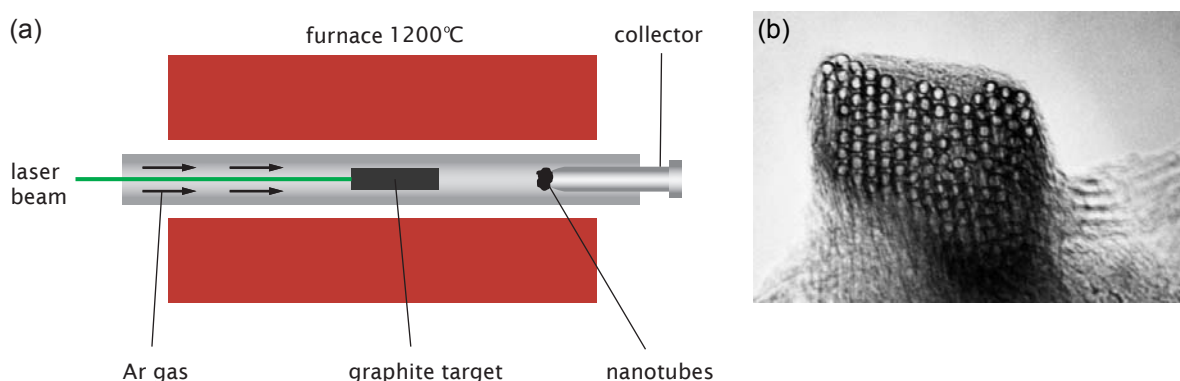


**Fig. 3.5.** (a) Synthesis of carbon nanotube ropes by laser ablation of a graphitic target in a furnace. Carbon nanotube bundles like the one on (b) are collected on the cooled collector [29].

It is generally considered that these methods produce CNTs of higher quality, albeit in very small quantities and without the possibility of scaling up to industrial production.

### **CVD growth**

More promising in this respect are other production methods based on chemical vapor deposition (CVD), a method that has been extensively used for the production of carbon fibers in the past 20 years. It involves flowing a hydrocarbon gas through a tube furnace over a catalyst material [33]. Key parameters controlling the growth are the hydrocarbon species, gas pressure and flow rate, catalyst and growth temperature. Methane or acetylene mixed with nitrogen and/or hydrogen are usually used as the carbon source and carrier gas. CNTs grow on the catalyst which is in the form of iron, nickel or cobalt nanoparticles dispersed on a support material such as alumina or zeolite. This method offers the possibility of controlling the growth of nanotubes by patterning the catalyst [34] and is therefore more suitable for producing nanoscale structures with integrated CNTs. Pillars of aligned MWNTs [35] as well as MWNT bundles with lengths in the millimeter range [27] have been produced using this method. Application of an electric field [36]

or fine control over the gas flow [37] can also result in the growth of nanotubes in a desired direction, bridging prefabricated structures on substrates (fig. 3.7).

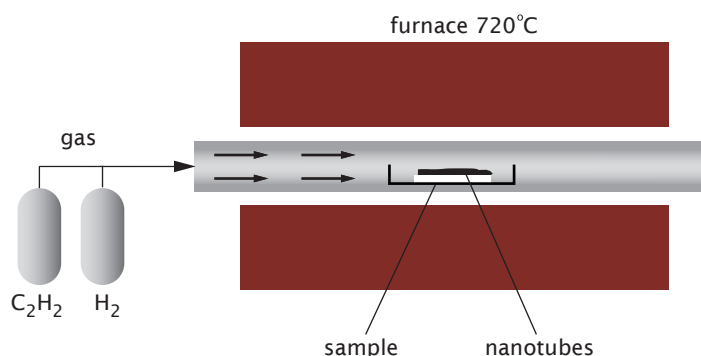


**Fig. 3.6.** Chemical vapour deposition (CVD) based growth of carbon nanotubes.

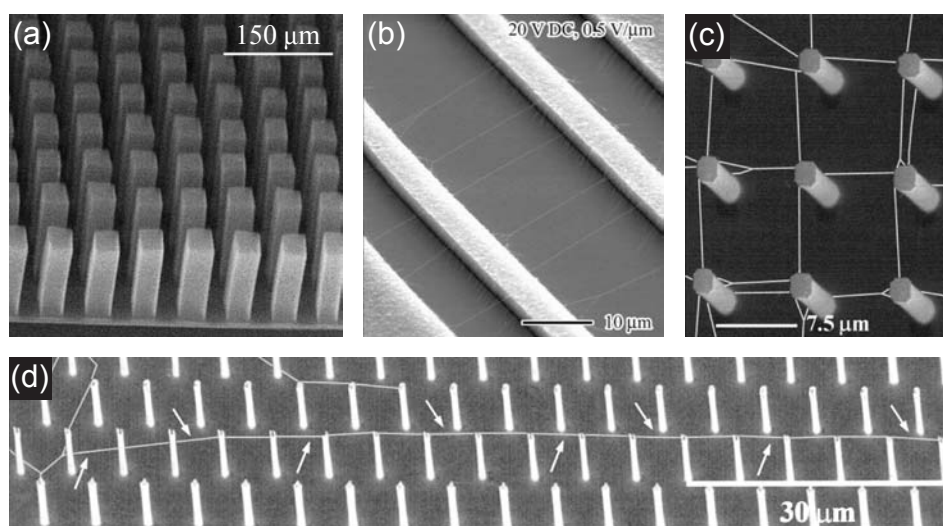


**Fig. 3.7.** (a) Pillars of self-aligned MWNTs [35]. (b) Electric field alignment of growing nanotubes [36] between electrodes. (c) and (d) gas flow alignment of growing nanotubes between prefabricated pillars [37].

The main disadvantage of CVD methods is the higher concentration of defects than in the case of arc-discharge or laser ablation growth methods, which can significantly diminish the mechanical properties of carbon nanotubes [38].

### **Chemical purification**

Typical by-products of SWNT growth by arc-discharge and laser ablation include fullerenes, graphitic polyhedrons with enclosed metallic particles and amorphous carbon in the form of particles or overcoating on the sidewalls of nanotubes (fig. 3.8a). They should all be removed before further investigations. Many different purification schemes have been developed, aiming at oxidizing the amorphous carbon, removing the catalytic particles and retaining only the tubes. In the first attempts, nanotubes were heated to 700°C in air, burning away the graphitic particles and nanotube ends (fig. 3.8b). Unfortunately, the small difference in oxidation rates of particles and tubes resulted in little control over the purification and yields below 1%. Attempts based on oxidation in acidic solutions like  $\text{KMnO}_4$  [39] or nitric acid [40] have given much better yields (<40%) since the solvent-based oxidation is slower and more homogeneous. Oxidation of

nanotubes in solution results in the attachment of many  $-OH$  and  $-COOH$  functional groups on the surface [39], which can change the reactivity and chemical nature of nanotubes.

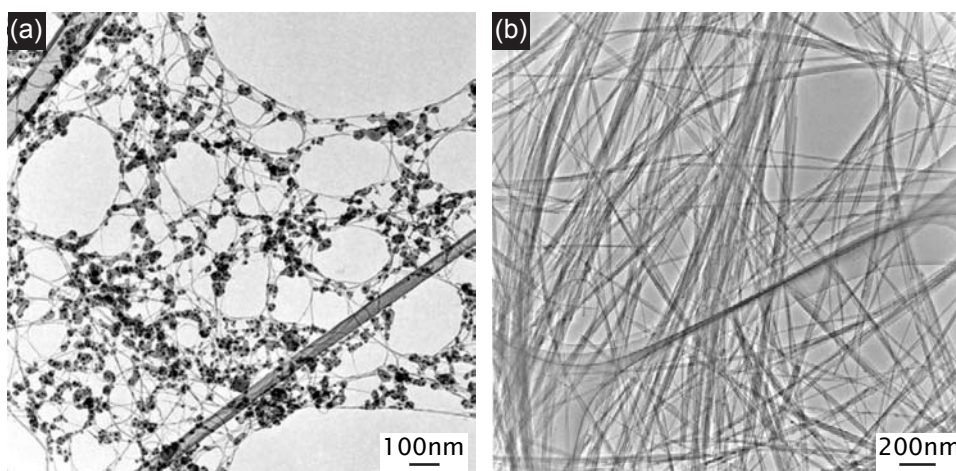


**Fig. 3.8.** (a) Low-magnification TEM image of SWNTs produced using Co as a catalyst. The dark particles correspond to codeposited Co catalyst particles protected by an amorphous carbon layer. (b) TEM image of a purified material [41].

### **Mechanical purification**

The most difficult problem in carbon nanotube purification is separating the metallic particles and carbon nanotubes. Transition metal particles, necessary for SWNT synthesis are mostly surrounded by graphitic layers. Very aggressive chemical purification using acids is needed in order to remove these protective graphitic layers before the metallic particle is reached.

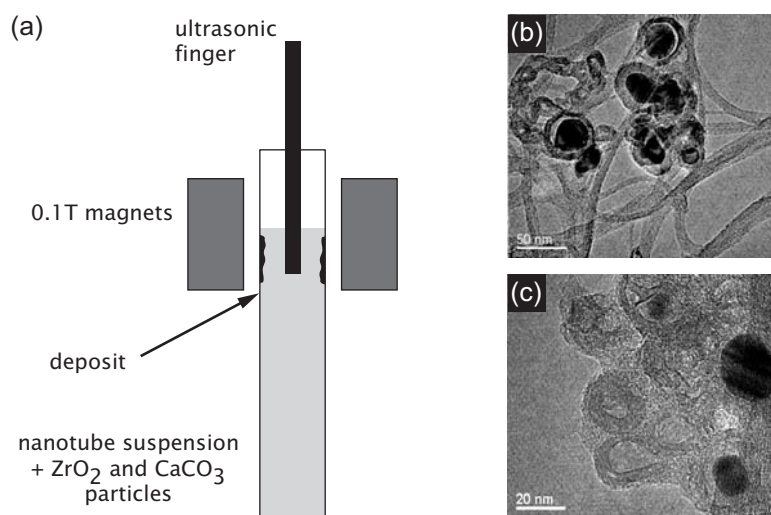


**Fig. 3.9.** (a) Schematic drawing of the mechanical purification scheme. (b) SWNT with magnetic particles enclosed in graphitic shells before and (c) after 24 hours of sonication in the presence of hard particles [42].

The presence of these ferromagnetic particles overwhelms the magnetic response and prevents the intrinsic magnetic properties of carbon nanotubes from being measured. By sonicating a mixture of carbon nanotube suspension and hard inorganic nanoparticles like  $ZrO_2$  and  $CaCO_3$  placed in a magnetic field (fig. 3.9), the ferromagnetic particles can be effectively removed. Hard inorganic particles can eject the metallic core from the graphitic shells (fig. 3.9b and c). The ferromagnetic impurities form a deposit trapped close to the magnets. Subsequent electron-spin

resonance (ESR) measurements have demonstrated that the presence of ferromagnetic particles in the purified material was negligible.

### 3.3. Nanotube chirality

SWNTs can be described as single sheets of graphite (graphene), rolled into a cylindrical, one-dimensional shape with axial symmetry and having diameters between 0.7–10 nm. The atomic structure can be classified according to the chiral vector  $\vec{C}_h$  or chiral angle  $\theta$ . A graphene sheet is shown in fig. 3.10 together with the unit vectors  $\vec{a}_1$  and  $\vec{a}_2$  of the hexagonal lattice. The “rolling-up” is described by the chiral vector whose length corresponds to the tube’s circumference. The chiral vector can be expressed as:

$$\vec{C}_h = n\vec{a}_1 + m\vec{a}_2 \equiv (n, m) \quad (3.1)$$

where integers  $n$  and  $m$  represent the chiral indices. The chiral angle  $\theta$  describes the “twist” in the nanotube lattice. The limiting cases that correspond to chiral angles of 0 and 30° are especially interesting and are referred to as “zig-zag” ( $n, 0$ ) and “armchair” ( $n, n$ ) nanotubes, fig. 3.11.

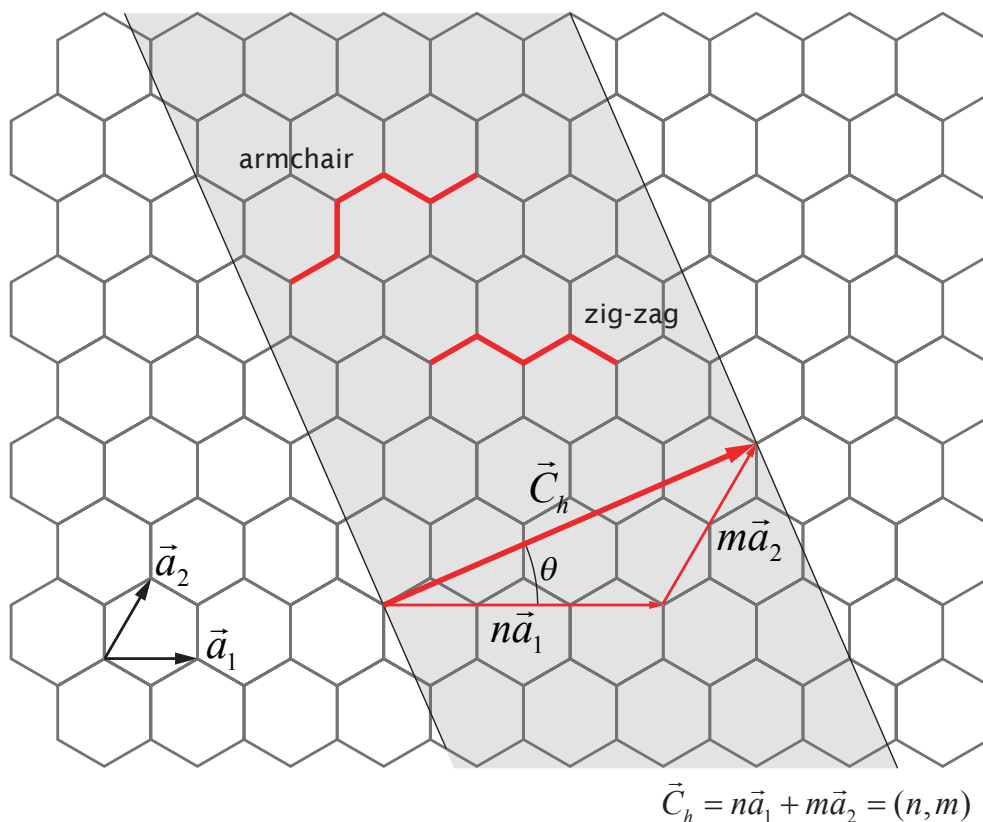


**Fig. 3.10.** Schematic diagram of nanotube formation by “rolling-up” a graphene sheet.

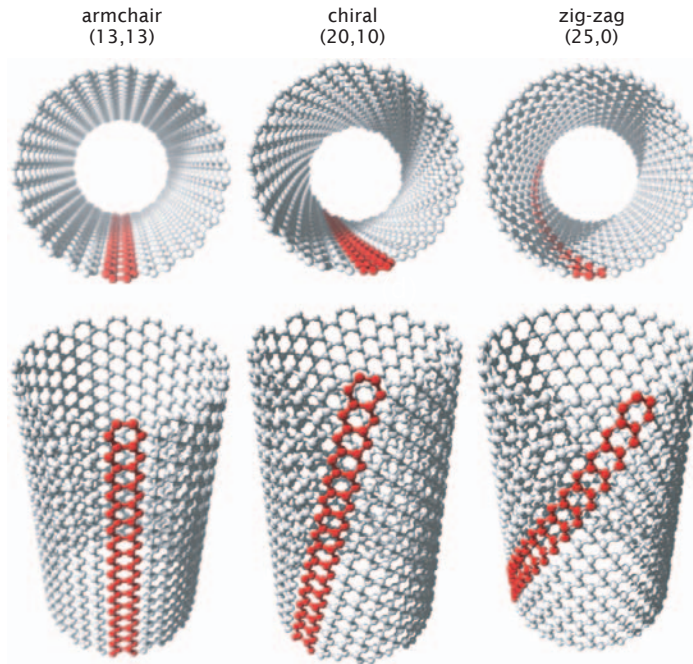


**Fig. 3.11.** Schematic illustrations of the structure of an armchair, chiral and zig-zag carbon nanotubes

The diameter  $d$  of a carbon nanotube is given by  $L/\pi$  where  $L$  is its circumferential length:

$$d = L/\pi, \quad L = |\vec{C}_h| = a\sqrt{n^2 + m^2 + nm} \quad (3.2)$$

where  $a=2.49\text{\AA}$  is the lattice constant of graphite. The nearest neighbor distance between carbon atoms in graphite is  $1.42\text{\AA}$ .

The chirality of a carbon nanotube has a significant influence on its properties. Electronic properties can be semiconducting or metallic, depending on the chirality. Armchair,  $(n, n)$  tubes are metals, tubes with indices that satisfy the relation  $n-m=3i$  where  $i$  is a nonzero integer are small-gap semiconductors because of curvature effects, and all the others are large-gap semiconductors [43, 44] (next section). From the mechanical point of view, strength and the Poisson's ratio show the most pronounced chirality dependence, while the Young's modulus is practically independent of chirality (section 3.5. on p. 29).

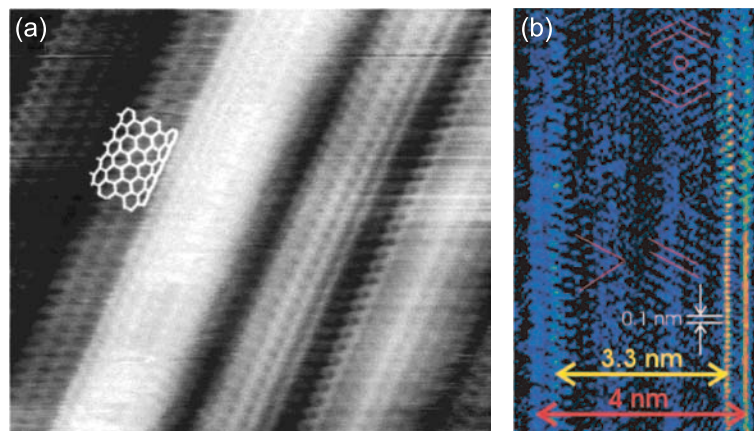


**Fig. 3.12.** (a) An atomically resolved STM image of a carbon nanotube rope [45]. (b) An atomically resolved image of a double-walled CNT reconstructed from an electron diffractogram obtained using a TEM [46].

Nanotube chirality can be experimentally determined either directly from atomically resolved STM [45] or TEM [46] images (fig. 3.12) or from electron diffraction patterns [22, 47].



Carbon nanotubes are always produced with a distribution of diameters and chiralities over which there is no real control. As a consequence, semiconducting p and n tubes are produced along metallic ones and even a small change of diameter can drastically alter their electronic properties from metallic to semiconducting. This is a serious obstacle for applications in electronic devices. One possible solution would be to gain a complete control over the diameter distribution during the production by using catalytic particles of a well-determined size. The other would be to separate different tubes after production. A promising separation procedure based on dielectrophoresis has recently been reported by Krupke et al. [48] who managed to increase the abundance of metallic tubes in a solution from 30% to 80% in a single step. Another recently reported procedure makes use of a chemical reaction in which covalent chemical functionalization is controlled by the electronic properties of carbon nanotubes [49] with metallic tubes reacting much faster to diazonium than semiconducting ones. Functionalization can be reversed by using a heat treatment that completely restores the pristine electronic properties of nanotubes.

### 3.4. Electronic properties

Major characteristics of the electronic properties of carbon nanotubes can be recovered using a simple tight-binding model and taking into account only the  $\pi$  orbitals of the graphene sheet [44]. Due to curvature, there is some mixing of carbon p and s orbitals, but in the first order approximation, this can be neglected. The 2D energy dispersion for the  $\pi$  bands of graphite is plotted in fig. 3.13 and given by:

$$E(k) = \pm t \left[ 1 + 4 \cos\left(\frac{\sqrt{3}k_x a}{2}\right) \cos\left(\frac{k_y a}{2}\right) + 4 \cos^2\left(\frac{k_y a}{2}\right) \right]^{1/2} \quad (3.3)$$

where  $t$  is the nearest-neighbor overlap integral, with a value of  $(2.6 \pm 0.2)$ eV, experimentally determined using an STM [50]. The valence and conduction bands touch at six distinct K-points which define the first Brillouin zone. As the graphene sheet is rolled-up to form a cylinder (fig. 3.10 on p. 25), confinement in the radial direction will impose quantization of the wave vector with the boundary condition:

$$\vec{C}_h \cdot \vec{k} = 2\pi q \quad (3.4)$$

where  $q$  is an integer. The carbon nanotube energy bands can be visualized by cutting the 2D energy dispersion shown in fig. 3.13 in directions expressed in equation (3.4). If one of these bands passes through either of the K points, the nanotube will be metallic – otherwise it will be semiconducting. The condition for metallic tubes is therefore:

$$\vec{C}_h \cdot \vec{k}_F = 2\pi q \quad (3.5)$$

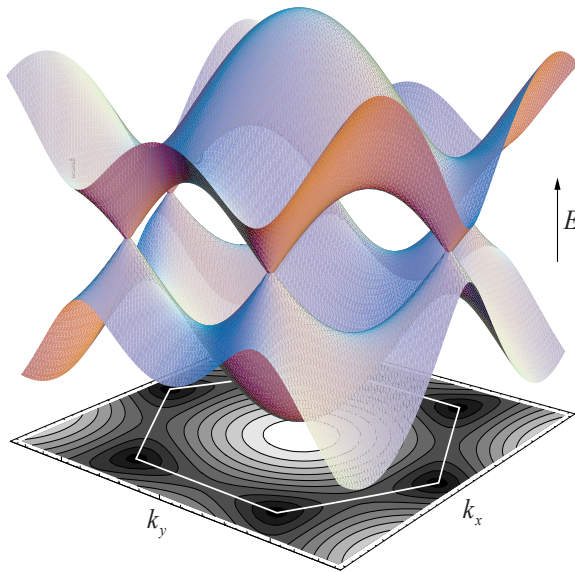


**Fig. 3.13.** Three-dimensional view of the graphene  $\pi$  band and its 2d projection.

As an example, the allowed subbands of two zigzag tubes, (9,0) and (10,0) together with their energy dispersions are shown on fig. 3.14. The (9,0) tube is metallic, but none of the (10,0) tube's subbands contain a K point, so this tube is semiconducting. To the first order,  $(n,m)$  nanotubes will be metallic when  $n-m=3i$  where  $i$  is an integer, otherwise they will be semiconducting. The energy gaps of semiconducting tubes depend inversely on diameter as  $1/d$ . Due to curvature effects ( $\pi$ - $\sigma$  band mixing), a small gap will open in the case when  $i$  is nonzero, with a  $1/d^2$  dependence [51, 52], so strictly speaking, only isolated, noninteracting armchair tubes will be metallic. All the other tubes will be either large or small-gap

semiconductors. A small gap can also open in the case of armchair tubes inside bundles, due to intertube interactions [52].

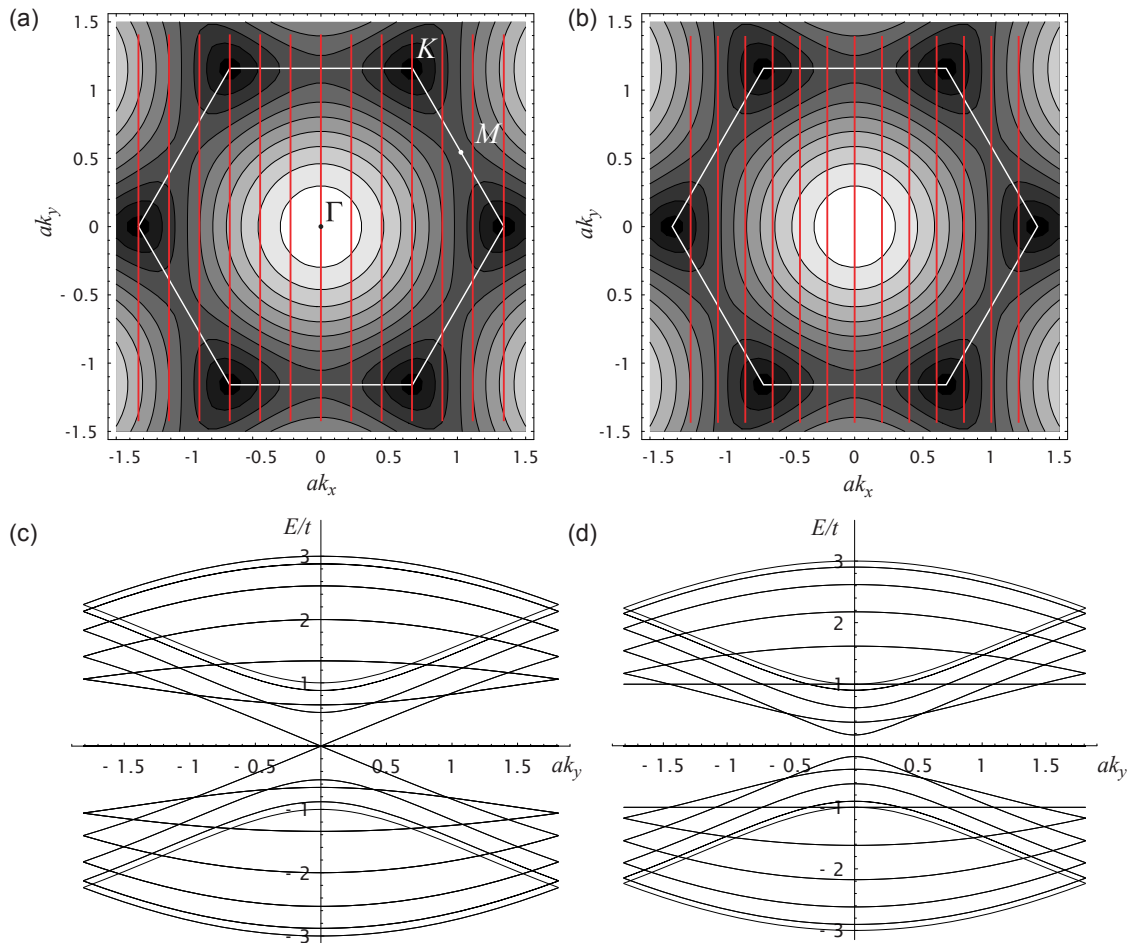


**Fig. 3.14.** (a) Allowed subbands for a (9,0) carbon nanotube and a (b) (10,0) carbon nanotube together with their respective energy bands and dispersions (c) and (d) [53].

### 3.5. Mechanical properties

The mechanical properties of carbon nanotubes are closely related to those of graphite. Strong  $sp^2$ -hybridized in-plane bonds ( $\sigma$ -bonds), 1.42 Å long, give them an exceptionally high Young's modulus while out of the plane  $\pi$ -bonds, responsible for the main features of the electronic properties, govern the weak, van der Waals interlayer binding.

One of the first reported theoretical studies of the elastic properties of carbon nanotubes was performed by Lu [32] using an empirical pair potential. In this model, the atomic interactions near the equilibrium structure are approximated by the sum of pairwise harmonic interatomic potentials. The force constants are empirically determined from fitting to measured elastic constants and phonon frequencies. The interwall interaction in MWNTs and SWNT ropes was modelled by summing pairwise van der Waals interactions:

$$U(r) = 4\varepsilon \left[ \left( \frac{\sigma}{r} \right)^{12} - \left( \frac{\sigma}{r} \right)^6 \right] \quad (3.6)$$

with the parameters  $\sigma=0.34\text{nm}$  and  $\varepsilon=12\text{meV}$ . The parameters used in this model were developed for intraplane interactions in graphite, and therefore do not take into account changes in bond rehybridization due to changes in diameter. The Young's modulus was calculated from the second derivative of the strain energy density with respect to strains (equation (4.15) and discussion on p. 37). The nanotube's wall thickness was chosen to be equal to the interwall distance in MWNT ( $t=0.34\text{nm}$ ), close to the interlayer distance in graphite (0.335 nm). The Young's modulus was found to be 0.97 TPa, and practically independent (with small variations on the third decimal place) of the tube's chirality and diameter (in the range 0.68–27 nm). Lu's calculations for MWNTs have also shown little variation with the number of walls. Furthermore, by minimizing the total intertube interaction in SWNT ropes, he found that the equilibrium lattice constant  $a_0$  and the cohesive energy per atom  $E_0$  scale with the SWNT radius as:

$$a_0 = 2R + 3.2\text{Å} \quad E_0 = \frac{61.5\text{meV}}{\sqrt{R[\text{Å}]}} \quad (3.7)$$

For a typical rope consisting of (10,10) SNWTs this gives  $a_0=16.8\text{Å}$  and  $E_0=23\text{meV}$ . Such a cohesive energy is comparable with a  $C_{60}$  solid. The density of a SWNT rope is only  $1.3\text{gcm}^{-3}$ , half the density of graphite. The Young's modulus was 0.8 TPa for a rope composed of (5,5) ropes and decreased with diameter down to 0.56 TPa for (10,10) ropes.

Hernández et al. [54] have theoretically studied the mechanical properties of carbon and hybrid  $B_xC_yN_z$  nanotubes using a non-orthogonal tight-binding scheme. They found a typical value of 1.22 TPa for the Young's modulus of SWNT, with a small dependence on the tube diameter. This dependence is noticeable only for tubes with diameters below 1.2 nm. The diameter-independent value is rapidly obtained for nanotubes with diameters above 1.2 nm (fig. 3.15). The limiting value of the Young's modulus as a function of tube's diameter is reached from below, which is consistent with the expectation that tubes of higher curvature (smaller diameters) will have weaker bonds due to rehybridization, resulting in decreased Young's modulus. Carbon nanotubes also had the highest Young's modulus of all the tubes that had been considered (C, BN,  $BC_3$ ,  $BC_2N$ ,  $C_3N_4$ , CN). Ab initio calculations of the Poisson's ratio  $\nu$ , the ratio between the radial compression and axial elongation upon the application of an axial stress,

reveal a slight decrease with the tube radius [55], from  $\nu=0.15$  for (10,0) tubes down to  $\nu=0.12$  for (4,4) and a stronger dependence on chirality with  $\nu=0.19$  for (10,10) tubes.

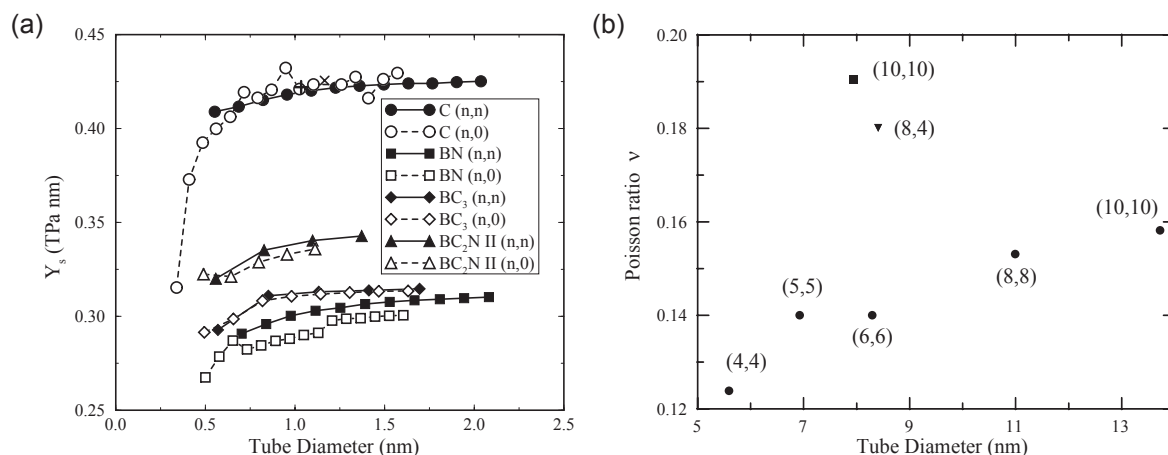


**Fig. 3.15.** (a) Young's modulus as function of diameter for C, BN, BC<sub>3</sub> and BC<sub>2</sub>N nanotubes as calculated from tight-binding simulations [54]. (b) Poisson's ratio dependence on the tube diameter, from ab-initio calculations [55].

The mechanical response of carbon nanotubes to large deformations and the associated morphological changes were first studied by Yakobson et al. [56] using molecular dynamics (MD) simulations. With properly chosen parameters, this analytical tool can predict nanotube behavior not only at small deformations but also beyond the linear response.

In simulations of bending, nanotubes have been found to be susceptible to buckling above a critical curvature  $K_c = (0.155 \text{ nm})d^{-2}$  determined by the tube diameter  $d$ . Experimental and theoretical studies by Iijima et al. [57], show that nanotube bending can be completely reversible up to angles in excess of  $110^\circ$  despite the formation of complex kink shapes. Wong et al. have also observed buckling in lateral deformation of MWNTs by AFM [58].

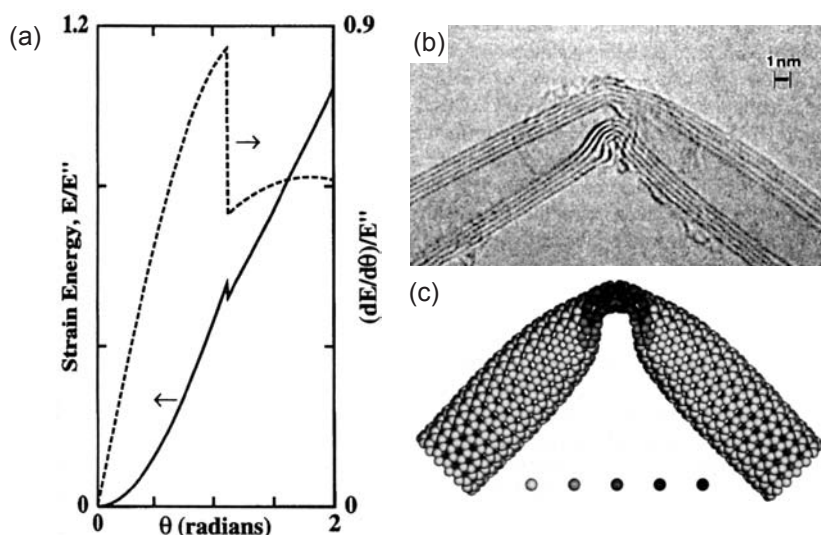


**Fig. 3.16.** The strain-energy curve for the bending of a (13,0) nanotube switches from harmonic to linear at the buckling point at the buckling angle of cca  $57^\circ$ . The force (dashed line) drops and remains almost constant [56]. (b) TEM micrograph of a buckled nanotube. (c) MD simulation of a buckled nanotube [57].

The behavior of carbon nanotubes under large axial strains has also been investigated using both first-principle methods and classical molecular dynamics simulations. Beyond a critical value of 5% axial tension, the nanotube relaxes its excess strain via the Stone-Wales

transformation [59], a  $90^\circ$  rotation of the C–C bond around its center (fig. 3.17) which produces two pentagons and two heptagons coupled in pairs (5-7-7-5).

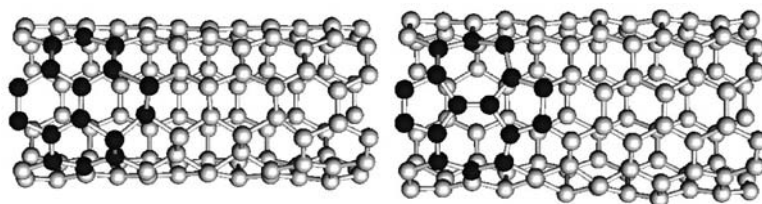


**Fig. 3.17.** Above 5% longitudinal strain, the nanotube can relax excess strain through Stone-Wales transformation [60].

At zero strain, the energy of a (10,10) nanotube containing a Stone-Wales defect is 2.34 eV higher than the ideal one. At 10% strain, the energy of a defective structure is 1.77 eV lower than the ideal. This demonstrates that the Stone-Wales defect is very effective in reducing the tensile strain, since two heptagons can be stretched more than the hexagons, while keeping a C–C bond length that is close to the ideal one. This relaxation effect is most effective in armchair tubes, but it is also favorable in zig-zag tubes with diameters below 1.1 nm [61]. Moreover, simulations have shown that the formation of a Stone-Wales defect is a reversible process [60], with the nanotube recovering its hexagonal network after the strain of 10% had been released. After the formation of a Stone-Wales defect, either brittle cleavage or plastic flow is possible, depending on tube symmetry, applied tension and temperature [61]. Final strain before breaking of a nanotube was calculated to be 17% [62].

High strain-rate MD simulations of the breaking of nanotubes were performed by Yakobson et al. [63]. For very small strains, Hooke's law was reproduced with the strain energy being a parabola in the vicinity of  $\varepsilon=0$  (fig. 3.18a). However, at a certain high level of strain, the energy dropped dramatically and the qualitative behavior changed: it varied irregularly and grew very slowly. Within the Hookean range of strain, and even at larger strains where the stress-strain relation deviates from linear, no bond breaking was observed. At a certain critical level, one of the C–C bonds broke, leading to the formation of distinct atom chains, spanning two tube fragments (fig. 3.18b), with only one chain surviving at higher strains.

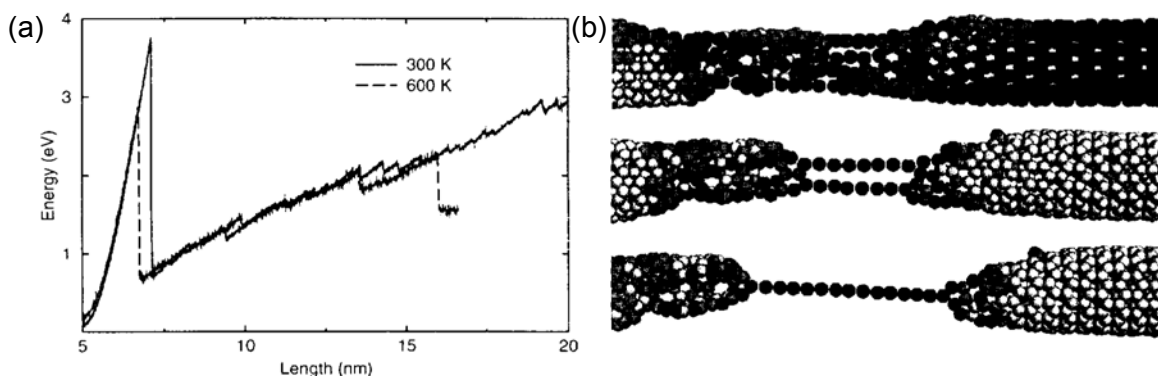
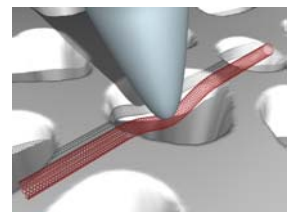


**Fig. 3.18.** (a) Energy-deformation curves for large axial deformations of nanotubes. (b) At large deformations, the structure starts to desintegrate into single chains of carbon atoms [63].



# 4

## *Mechanical measurements on individual nanotubes*



### 4.1. Introduction

Superior mechanical properties are only one of the interesting aspects of carbon nanotubes. Due to their high Young's modulus and strength, they might one day find applications as reinforcing elements in composites, or main components of tough yet light fibers. On the nanoscale, better mechanical properties mean more performant and robust nanomechanical components and also easier handling.

The development of mechanical measurements on nanoscale objects was in great part motivated by the exceptional properties of carbon nanotubes. It is also a dynamic field where discoveries motivate improvements in experimental methods, leading to even more interesting results. Experiments involving nanotubes thus reflect the progress made in the scanning-probe, electron microscopy and other related techniques that enable a growing number of scientists to perform experiments on the nanoscale.

Potential applications of carbon nanotubes as electronic elements in future computer circuitry are at present less certain due to the inability to control their semiconducting properties. Emergent materials, like nanowires, seem to be a more promising candidate [64], unless nanotubes can be separated according to their chirality, which seems to be possible [48, 49]. Once separated, they could either be used directly or as templates for the growth of new tubes, with a well determined chirality [65]. As far as the mechanical properties are concerned, nanowires will not easily match those of carbon nanotubes [58].

Unlike electronic or thermal properties, mechanical properties seem to be adequately described by classical laws even at the nanoscale. Unusual behavior is however possible yet predictable using simulations: rippling or Stone-Wales transformation are only some of the examples. In order to relate to the macroscopic world or computer simulations, the elastic properties of carbon nanotubes are usually described using terms "borrowed" from the continuum theory of elasticity like the Young's and the shear moduli. This may seem

inappropriate at first sight. However, it is not only a convenient way of reporting data, but is also accurate, at least to the first degree. The consistency between a huge amount of experimental and theoretical data, together with some of the mechanical properties being comparable to those of graphite prove this.

## 4.2. Theoretical considerations

### *Linear theory of elasticity*

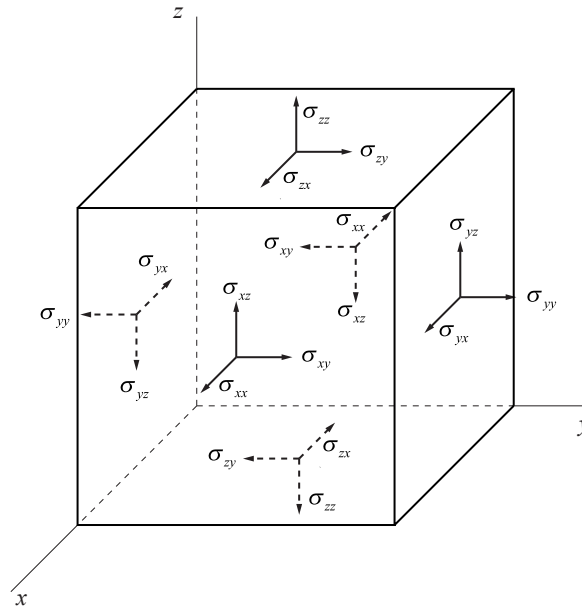


**Fig. 4.1.** Stress components in a loaded body.

Let us consider a volume element like the one shown on fig. 4.1. The surface forces are represented by the product of stress components and the areas on which they act. The stress components  $\sigma_{xx}$ ,  $\sigma_{yy}$  and  $\sigma_{zz}$  will be positive when directed in the positive  $x$ ,  $y$  and  $z$  directions. The nine stress components can be written down as a tensor:

$$\boldsymbol{\sigma} = \begin{pmatrix} \sigma_{xx} & \sigma_{xy} & \sigma_{xz} \\ \sigma_{yx} & \sigma_{yy} & \sigma_{yz} \\ \sigma_{zx} & \sigma_{zy} & \sigma_{zz} \end{pmatrix} \quad (4.1)$$

From the requirement of static equilibrium, three pairs of the shearing stresses are equal, so the tensor in equation (4.1) is symmetric and can be simplified to:

$$\boldsymbol{\sigma} = \begin{pmatrix} \sigma_{xx} & \sigma_{xy} & \sigma_{xz} \\ \sigma_{xy} & \sigma_{yy} & \sigma_{yz} \\ \sigma_{xz} & \sigma_{yz} & \sigma_{zz} \end{pmatrix} \quad (4.2)$$

The internal energy density variation  $\delta U_0$  associated with straining is given by:

$$\delta U_0 = \sigma_{xx} \delta \varepsilon_{xx} + \sigma_{yy} \delta \varepsilon_{yy} + \sigma_{zz} \delta \varepsilon_{zz} + 2\sigma_{xy} \delta \varepsilon_{xy} + 2\sigma_{yz} \delta \varepsilon_{yz} + 2\sigma_{xz} \delta \varepsilon_{xz} \quad (4.3)$$



Consequently, stresses can be expressed as:

$$\begin{aligned}\sigma_{xx} &= \frac{\partial U}{\partial \varepsilon_{xx}} & \sigma_{yy} &= \frac{\partial U}{\partial \varepsilon_{yy}} & \sigma_{zz} &= \frac{\partial U}{\partial \varepsilon_{zz}} \\ \sigma_{xy} &= \frac{1}{2} \frac{\partial U}{\partial \varepsilon_{xy}} & \sigma_{yz} &= \frac{1}{2} \frac{\partial U}{\partial \varepsilon_{yz}} & \sigma_{zx} &= \frac{1}{2} \frac{\partial U}{\partial \varepsilon_{zx}}\end{aligned}\quad (4.4)$$

The Hooke's law asserts that each of the stress components is a linear function of the components of the strain tensor:

$$\begin{aligned}\sigma_{xx} &= C_{11}\varepsilon_{xx} + C_{12}\varepsilon_{yy} + C_{13}\varepsilon_{zz} + C_{14}\varepsilon_{xy} + C_{15}\varepsilon_{xz} + C_{16}\varepsilon_{yz} \\ \sigma_{yy} &= C_{21}\varepsilon_{xx} + C_{22}\varepsilon_{yy} + C_{23}\varepsilon_{zz} + C_{24}\varepsilon_{xy} + C_{25}\varepsilon_{xz} + C_{26}\varepsilon_{yz} \\ &\vdots \\ \sigma_{yz} &= C_{61}\varepsilon_{xx} + C_{62}\varepsilon_{yy} + C_{63}\varepsilon_{zz} + C_{64}\varepsilon_{xy} + C_{65}\varepsilon_{xz} + C_{66}\varepsilon_{yz}\end{aligned}\quad (4.5)$$

where the 36 coefficients  $C_{11}$  through  $C_{66}$  are called elastic constants. They are symmetrical, which decreases the number of distinct elastic constants down to 21 in the most general case. Depending on the symmetry of the particular system being deformed, this number can be further decreased.

The strain energy density of a material obeying the Hooke's law is:

$$\begin{aligned}U_0 &= \frac{1}{2} C_{11} \varepsilon_{xx}^2 + \frac{1}{2} C_{12} \varepsilon_{xx} \varepsilon_{yy} + \dots + \frac{1}{2} C_{16} \varepsilon_{xx} \varepsilon_{yz} + \\ &+ \frac{1}{2} C_{12} \varepsilon_{xx} \varepsilon_{yy} + \frac{1}{2} C_{22} \varepsilon_{yy}^2 + \dots + \frac{1}{2} C_{26} \varepsilon_{yy} \varepsilon_{yz} + \\ &+ \frac{1}{2} C_{13} \varepsilon_{xx} \varepsilon_{zz} + \frac{1}{2} C_{23} \varepsilon_{yy} \varepsilon_{zz} + \dots + \frac{1}{2} C_{36} \varepsilon_{zz} \varepsilon_{yz} + \\ &\vdots \\ &+ \frac{1}{2} C_{16} \varepsilon_{xx} \varepsilon_{yz} + \frac{1}{2} C_{23} \varepsilon_{yy} \varepsilon_{yz} + \dots + \frac{1}{2} C_{36} \varepsilon_{yz}^2\end{aligned}\quad (4.6)$$

From this general form it is clear that the Hooke's law corresponds to a lowest order development of strain energy. It will therefore be valid for small strains, independent of the interaction between the atoms in the material, as every potential function can be approximated with a parabola around its local minimum.

If the orientations of crystals and grains constituting the material are randomly distributed, it will display the same material properties in all directions. It will therefore behave as an isotropic material, and the strains and strain energies will only depend on the principal strains  $\varepsilon_1$ ,  $\varepsilon_2$ , and  $\varepsilon_3$ . Accordingly, the equation (4.6) can be written as:

$$\begin{aligned}U_0 &= \frac{1}{2} C_{11} \varepsilon_1^2 + \frac{1}{2} C_{12} \varepsilon_1 \varepsilon_2 + \frac{1}{2} C_{13} \varepsilon_1 \varepsilon_3 + \\ &+ \frac{1}{2} C_{12} \varepsilon_1 \varepsilon_2 + \frac{1}{2} C_{22} \varepsilon_2^2 + \frac{1}{2} C_{23} \varepsilon_2 \varepsilon_3 + \\ &+ \frac{1}{2} C_{13} \varepsilon_1 \varepsilon_2 + \frac{1}{2} C_{23} \varepsilon_1 \varepsilon_2 + \frac{1}{2} C_{33} \varepsilon_3^3\end{aligned}\quad (4.7)$$

By symmetry, the choice of the principal axes is arbitrary. Hence,  $C_{11}=C_{22}=C_{33}=C_1$  and  $C_{12}=C_{23}=C_{12}=C_2$ . Consequently, the strain energy density can be expressed in the form:

$$U_0 = \frac{1}{2} \lambda (\varepsilon_1 + \varepsilon_2 + \varepsilon_3)^2 + G (\varepsilon_1^2 + \varepsilon_2^2 + \varepsilon_3^2)\quad (4.8)$$

where  $\lambda = C_2$  and  $G = (C_1 - C_2)/2$  are Lamé's elastic coefficients.  $G$  is in fact the shear modulus. Returning to Cartesian coordinates we obtain:

$$U_0 = \frac{1}{2} \lambda (\varepsilon_{xx} + \varepsilon_{yy} + \varepsilon_{zz})^2 + G (\varepsilon_{xx}^2 + \varepsilon_{yy}^2 + \varepsilon_{zz}^2 + 2\varepsilon_{xy}^2 + 2\varepsilon_{xz}^2 + 2\varepsilon_{yz}^2) \quad (4.9)$$

Together with (4.4) this yields Hooke's law for a linear isotropic material in the form:

$$\begin{aligned} \sigma_{xx} &= \lambda e + 2G\varepsilon_{xx} & \sigma_{yy} &= \lambda e + 2G\varepsilon_{yy} & \sigma_{zz} &= \lambda e + 2G\varepsilon_{zz} \\ \sigma_{xy} &= 2G\varepsilon_{xy} & \sigma_{xz} &= 2G\varepsilon_{xz} & \sigma_{yz} &= 2G\varepsilon_{yz} \end{aligned} \quad (4.10)$$

where  $e \approx \varepsilon_{xx} + \varepsilon_{yy} + \varepsilon_{zz}$  is the classical small-displacement cubical strain. By inverting equations (4.10) we obtain:

$$\begin{aligned} \varepsilon_{xx} &= \frac{1}{E} (\sigma_{xx} - \nu\sigma_{yy} - \nu\sigma_{zz}) & \varepsilon_{xy} &= \frac{1+\nu}{E} \sigma_{xy} \\ \varepsilon_{yy} &= \frac{1}{E} (\sigma_{yy} - \nu\sigma_{xx} - \nu\sigma_{zz}) & \varepsilon_{xz} &= \frac{1+\nu}{E} \sigma_{xz} \\ \varepsilon_{zz} &= \frac{1}{E} (\sigma_{zz} - \nu\sigma_{xx} - \nu\sigma_{yy}) & \varepsilon_{yz} &= \frac{1+\nu}{E} \sigma_{yz} \end{aligned} \quad (4.11)$$

where

$$E = \frac{G(3\lambda + 2G)}{\lambda + G} \quad \nu = \frac{\lambda}{2(\lambda + G)} \quad (4.12)$$

are the Young's modulus  $E$  and Poisson's ratio  $\nu$ , the ratio of the compression in transversal direction to the axial elongation. For a stress tensor having only the  $\sigma_{xx}$  component, equation (4.11) reduces to the Hooke's law for tension:

$$\varepsilon_{xx} = \frac{1}{E} \sigma_{xx} \quad \varepsilon_{yy} = -\frac{\nu}{E} \sigma_{xx} \quad (4.13)$$

while the connection between the Young's modulus  $E$  and the shear modulus  $G$  is given by:

$$E = \frac{2G}{(1+\nu)} \quad (4.14)$$

The continuum isotropic theory of elasticity allows Poisson's ratios in the range from  $-1$  to  $1/2$ , due to the requirement that the moduli must be positive.

### 4.3. Continuum models and nanotubes

The direct applicability of concepts like the Young's modulus, that have been developed for describing large-scale structures on the nanoscale could be puzzling at the first sight. Electronic and thermal properties at this scale display behavior in the realm of quantum physics, yet the classical laws seems to be adequate for describing the mechanical properties. The reason why the Hooke's law still holds at the nanoscale is simple and fundamental. The Hooke's law is based on the fact that any smooth potential can be approximated by a parabola for small displacements around the equilibrium position. The same holds for interatomic potentials, regardless of the

particular potential or its numerical value, and for the undeformed nanotube, the interatomic potentials are at the minimal values. The biggest potential difficulty in applying continuum-based models on nanotubes are inconsistencies which can arise from definitions of nanotube geometry, in particular the “thickness” of the graphene sheet.

Apart from the definition as a proportionality factor between the stress and strain (equation (4.13) on p. 36), the Young’s modulus can alternatively be defined using the stress energy:

$$E_{Young} = \frac{1}{V_0} \left. \frac{\partial^2 E}{\partial \varepsilon^2} \right|_{\varepsilon=0} \quad (4.15)$$

where  $V_0$  is the equilibrium volume and  $E$  the strain energy. This definition is more convenient for theoretical modeling and simulations. In the case of a single-walled nanotube, this (and any other definition in fact) requires adopting a convention in order to define  $V_0$ , which for a hollow cylinder is given by  $V_0 = 2\pi LRt$  where  $L$  and  $R$  are the tube’s length and radius respectively, and  $t$  the tube’s thickness. Different conventions have been adopted: Yakobson et al. took the extent of  $\pi$ -orbitals,  $t=0.066$  nm [56]. This definition yielded spectacular values of roughly 5 TPa for the Young’s modulus of carbon nanotubes. Lu proposed another convention, one which is in widespread use today, choosing the interlayer separation of graphite as the nanotube’s thickness ( $t=0.34$  nm). This gave a more reasonable value of 0.97 TPa for the Young’s modulus, which is in good agreement with the  $C_{11}$  elastic constant of graphite (1.06 TPa in the basal plane) [32].

## 4.4. Overview of experimental results on nanotubes

### ***Mechanical resonance excitation inside a TEM***

First measurements of the mechanical properties of carbon nanotubes were based on measuring the amplitude of thermally induced vibration inside a TEM [66]. MWNTs were fixed at one end. The other, free end was vibrating due to the thermal excitation of the nanotube’s mechanical resonant modes. As the vibrational frequency was high enough compared to the acquisition time, the free end appeared blurred on the TEM images, fig. 4.2. The nanotube was modelled as a stochastically driven resonator and the  $E_{Young}$  estimated from its Gaussian vibrational profile whose standard deviation  $\sigma$  is given by:

$$\sigma^2 = \frac{16L^3 k_B T}{\pi E_{Young} (D^4 - D_{int}^4)} \sum_n \beta_n^{-4} \approx 0.4243 \frac{L^3 k_B T}{E_{Young} (D^4 - D_{int}^4)} \quad (4.16)$$

where  $L$  is the cantilevered beam’s length,  $k_B$  the Boltzmann constant ( $1.38 \times 10^{-23}$  J/K),  $T$  the temperature,  $E_{Young}$  the Young’s modulus,  $D$  and  $D_{int}$  the nanotube inner and outer diameters respectively and  $\beta_n$  a numerical constant for vibrational mode  $n$ .

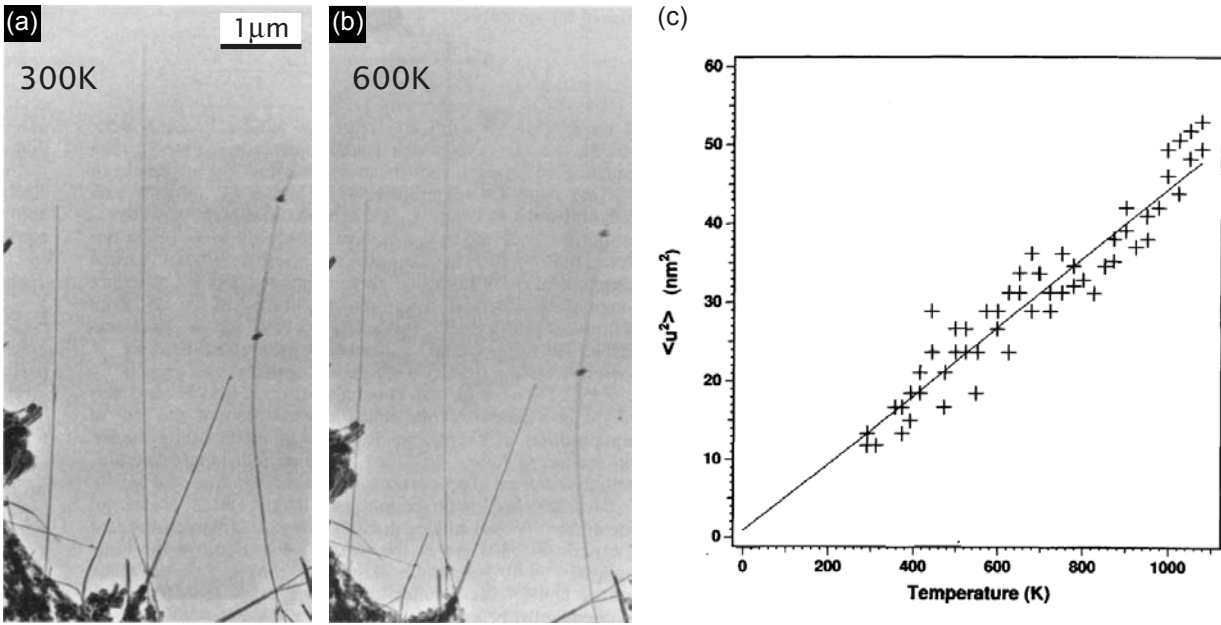


**Fig. 4.2.** TEM image of a cantilevered MWNT showing blurring at the tips due to thermally excited vibration at the free end. Images were recorded at different temperatures (a) 300 K (b) 600 K. (c) Plot of the mean-square vibration amplitudes versus temperature for a 5.1  $\mu\text{m}$  long, 16.6 nm thick nanotube. The effective  $E_{\text{Young}}$  was  $3.7 \pm 0.2 \text{ GPa}$  [66].

From a series of measurements performed as a function of temperature (fig. 4.2c)  $E_{\text{Young}}$  in the 0.4–4 GPa range was obtained, with an average value of 1.8 GPa. Similar measurements were performed on SWNTs [67] where the average value of  $1.25 \pm 0.35 \text{ TPa}$  was obtained. Although the individual measurements are subject to large error bars (20–60%), this was the first attempt to measure the mechanical properties of nanotubes. The method is also simple to implement, requiring only a TEM equipped with a heating stage and could be applied to other nanowire materials as long as the tip blurring effect is obvious. The biggest problem with this method is the reliance on a rather subjective, human criteria when judging the tip blurring. A variation of this method has been applied to BN nanotubes [68].

Another method based on exciting the mechanical resonance of nanotubes inside a TEM has been demonstrated by Poncharal et al. [69]. MWNTs were directly excited using an AC electric field and the  $E_{\text{Young}}$  was calculated from the frequencies of the first two resonant modes. Nanotubes were fixed on a specially designed TEM holder equipped with a piezo translation stage. Electrically contacted nanotubes were then brought to a distance of 5–20  $\mu\text{m}$  from a grounded counterelectrode. When a static potential  $V_s$  is applied to the wire, the tube becomes electrically charged and is attracted to the counterelectrode. The induced charge is proportional to the applied voltage and is equal to  $\alpha V_s$ . The force exerted on the nanotube is essentially concentrated at the tip. It is given by the product of the induced charge and the electric field ( $\beta V_s$ ), and is therefore equal to  $F = \alpha \beta V_s^2$ . Application of an additional time-dependent voltage  $V(t) = V_d \cos(\omega t)$  to the nanotube causes a time-dependent force  $F(t)$  given by the expression:

$$\begin{aligned}
 F(t) &= \alpha \beta \left[ V_s + V_d \cos(\omega t) \right]^2 = \\
 &= \alpha \beta \left[ V_s^2 + 2(V_s + V_d \cos(\omega t)) + \frac{1}{2} V_d^2 \cos(2\omega t) + \frac{1}{2} V_d^2 \right]
 \end{aligned} \tag{4.17}$$

By adjusting the frequency  $\omega=2\pi\nu$ , tubes can be resonantly excited (fig. 4.3) and the bending modulus  $E_{bending}$  can be calculated from the resonant frequency using a formula from the Bernoulli-Euler analysis of cantilevered elastic beams:

$$\nu_j = \frac{\beta_j^2}{8\pi} \frac{1}{L^2} \sqrt{(D^2 + D_{int}^2)} \sqrt{\frac{E_{bending}}{\rho}} \quad (4.18)$$

where  $D$  is the outer diameter,  $D_{int}$  the inner diameter,  $\rho$  the density,  $\beta_j$  a constant for the  $j^{\text{th}}$  harmonic:  $\beta_1=1.875$  and  $\beta_2=4.694$ .

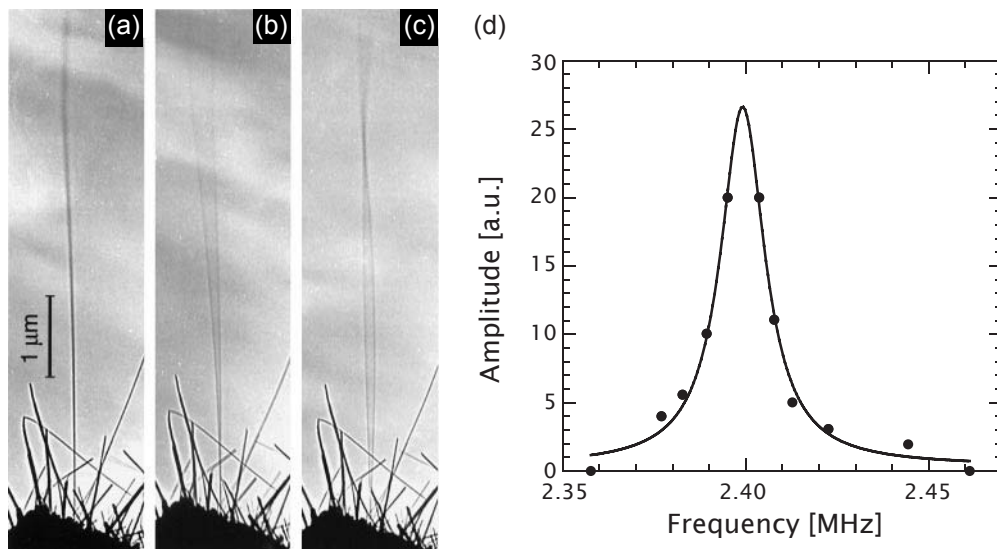


**Fig. 4.3.** Mechanical response of a nanotube to an applied periodic potential. (a) In the absence of a potential the tip vibrates slightly due the thermal excitation. (b) Resonant excitation of the fundamental mode of vibration ( $\nu_1=530$ kHz). (c) Resonant excitation of the second harmonic ( $\nu_2=3.01$ MHz).  $E_{bending}$  of this nanotube was 0.21TPa. (d) Resonant lineshape for another nanotube [69].

For nanotube diameters below 10 nm, a typical value of 1TPa was obtained for  $E_{bending}$ , while it dropped to 100GPa for thicker tubes. This dramatic drop is associated with the appearance of rippling, a wave-like distortion shown in fig. 4.4 which seems to be energetically more favorable for thicker tubes.

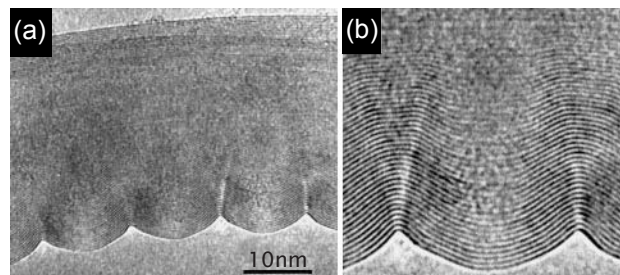


**Fig. 4.4.** (a) High-resolution TEM image of a bent nanotube showing a characteristic wavelike distortion – rippling. (b) Magnified view of the region shown in (a) [69].

### Lateral deformation by AFM

Setups in which the mechanical properties of nanotubes can be directly probed by applying a known force are usually based on AFMs. The first quantitative measurement of the Young's modulus of MWNTs (and SiC nanorods) using this setup was reported by Wong et al. [58]. MWNTs were first randomly dispersed on a flat surface of MoS<sub>2</sub> single crystals that were used because of their low friction coefficient and exceedingly flat surface. Friction between the tubes and substrate was further reduced by performing the measurements in water. Tubes were pinned on one side to this substrate by a deposition of an array of square pads through a shadow mask, fig. 4.5a-c.

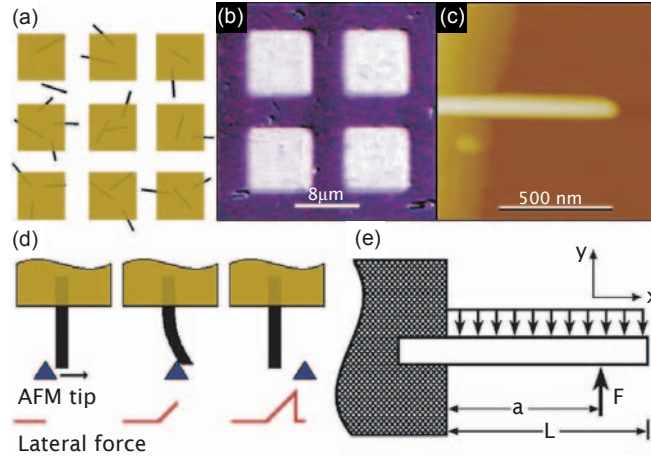


**Fig. 4.5.** (a) Nanotubes are dispersed on a substrate and pinned down by SiO pads. (b) Optical micrograph of the sample. (c) AFM image of a SiC nanorod protruding from the pad. (d) The tip moves in the direction of the arrow. The lateral force is indicated at the bottom. During bending the lateral force increases, until the point at which the tip passes over the beam which snaps back to its initial position. (e) The beam of length  $L$  is subjected to a point load  $F$  at  $x=a$  and friction force  $f$  [58].

AFM was used to locate and characterize the dimensions of protruding tubes. The beam was deformed laterally by the AFM tip, until at a certain deformation the tip would pass over the tube, allowing the tube to snap back to its relaxed position. During measurements, lateral force-distance curves were acquired at different positions along the chosen beam, fig. 4.5d and e. Maximum deflection of the nanobeam can be controlled to a certain degree by the applied normal load, and in this way tube breaking can be avoided or achieved in a controlled manner. The applied lateral load  $F$  in terms of lateral displacement  $y$  at the position  $x$  along the beam is given by the equation:

$$F(x, y) = 3E_{Young} I \frac{y}{x^3} + \frac{f}{8} \left( x - 4L - 6\frac{L^2}{x} \right) \quad (4.19)$$

where  $E_{Young}$  is the Young's modulus of the beam,  $I$  the second moment of the cross-section, equal to  $D^4/64$  for a solid cylinder of diameter  $D$  and  $f$  the unknown friction force, presumably small due to the experimental design. The lateral force, fig. 4.6a is known only up to a factor of proportionality because the AFM lever's lateral force constant wasn't calibrated for these measurements. This uncertainty and the effect of friction were eliminated by calculating the nanobeam's lateral force constant:

$$\frac{dF}{dy} \equiv k = \frac{3\pi D^4}{64x^3} E_{Young} \quad (4.20)$$

The mean value for the Young's modulus of MWNTs was  $E_{Young} = 1.3 \pm 0.6$  TPa, similar to that of diamond ( $E_{Young} = 1.2$  TPa). For larger deformations, discontinuities in bending curves were also observed, attributed to elastic buckling of nanotubes [57].

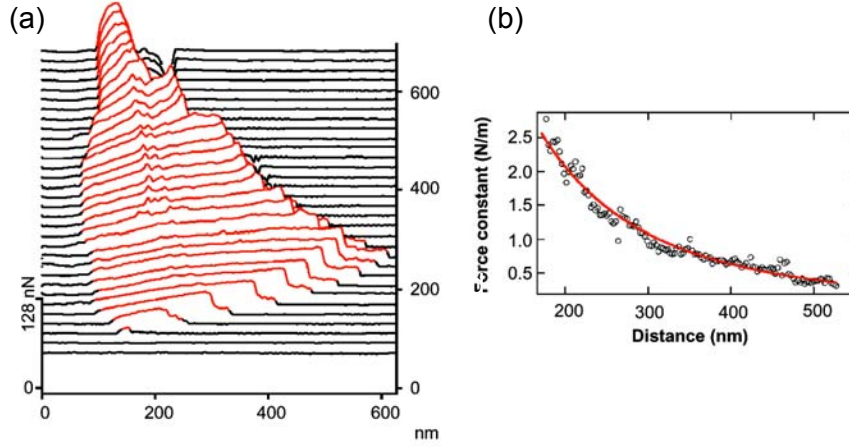


**Fig. 4.6.** (a) A series of lateral force-distance curves for different positions along a MWNT. (b) The lateral spring constant as a function of position on the beam. The curve is a fit to equation (4.20) [58].

Walters et al. pinned ropes of single-walled nanotubes beneath metal pads on an oxidized silicon surface, then released them by wet etching, fig. 4.7a. The SWNT was deflected in the lateral direction using an AFM tip, fig. 4.7b. As the suspended length is on the order of  $1 \mu\text{m}$ , the SWNT rope can be modeled as an elastic string stretched between the pads. Upon deformation, all of the strain goes into stretching. In the simple case of a tube lying perpendicular to the trench and the AFM tip deforming the tube in the middle, the force  $F$  exerted on the tube by the AFM tip is given by the expression (p. 130):

$$F = 2T \sin \theta = 2T \frac{2x}{L} \approx \frac{8kx^3}{L_0} \quad (4.21)$$

where  $T$  is the tension in the string,  $L_0$  its equilibrium length,  $k$  the spring constant and  $x$  the lateral deflection in the middle. Using this setup Walters et al. deformed SNWT ropes to the maximal strain of  $5.8 \pm 0.9\%$  and determined a lower bound of  $45 \pm 7$  GPa on the tensile strength, assuming a value of 1.2 TPa for the Young's modulus.

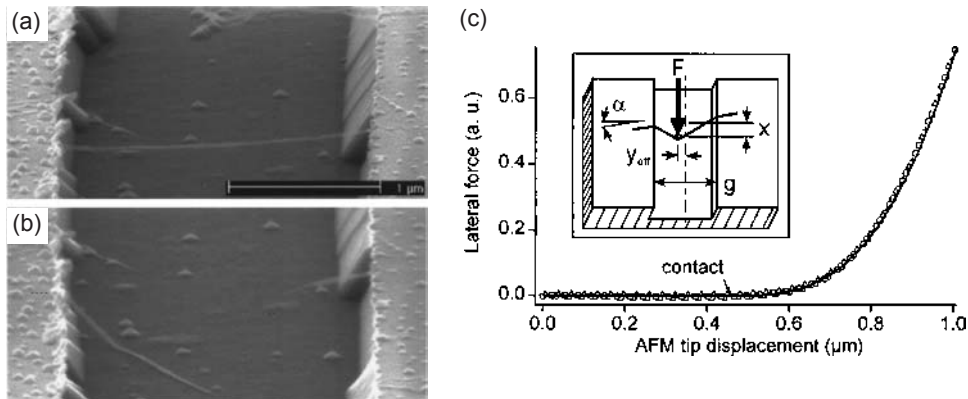


**Fig. 4.7.** (a) SEM image of a SWNT rope suspended over trench in silicon before and (b) after being deformed. (c) Lateral force on a single-walled nanotube rope as a function of AFM tip displacement [70].

### Normal deformation by AFM

In a series of demanding experiments, Salvétat et al. measured the Young's modulus of isolated SWNTs and SWNT ropes [71], MWNTs produced using different methods [38] and the shear modulus of SWNT ropes [72]. The experimental setup that made measurements possible on such a wide range of CNT morphologies involved measuring the vertical deflection of nanotubes bridging holes in a porous membrane (fig. 4.8).

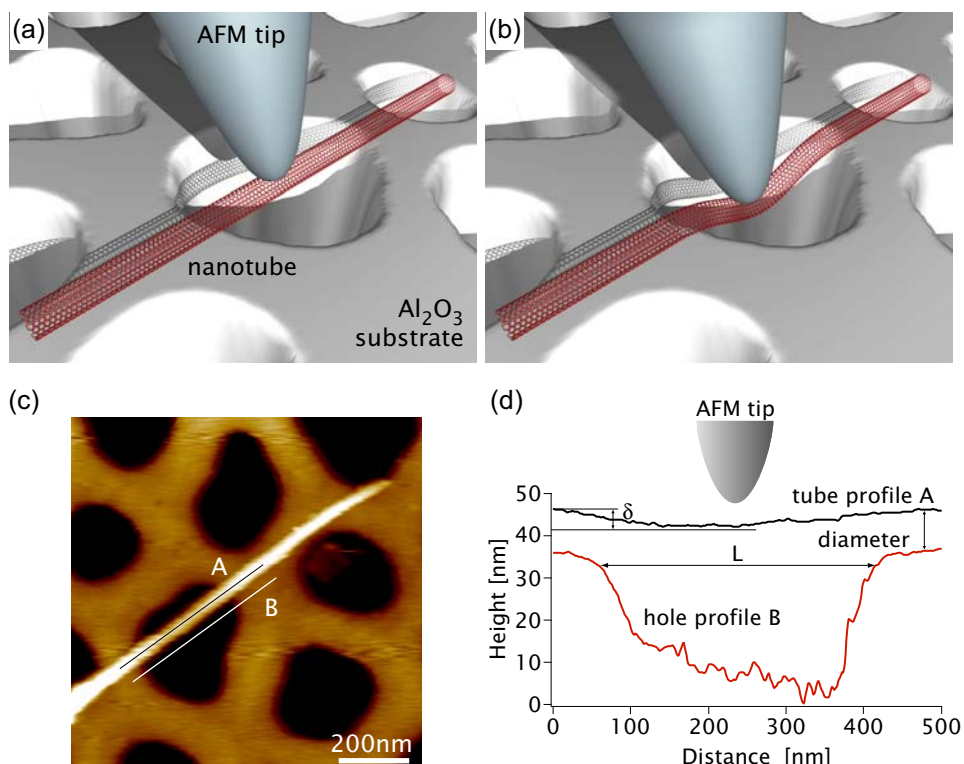


**Fig. 4.8.** (a) Schematic drawing of a carbon nanotube deposited on a porous Al<sub>2</sub>O<sub>3</sub> substrate. (b) During AFM imaging in contact mode, the tube deforms under an applied normal force and this deformation will be recorded as local height in the corresponding AFM image. (c) An AFM image of a 10 nm thick SWNT bundle on a porous substrate. (d) Subsequent analysis of linescans over the tube (A) and the hole (B) yields the nanotube's physical dimensions together with the deformation in the middle [38, 71, 72].

In this measurement method, CNTs are dispersed in an organic solvent, for example in ethanol and deposited on the surface of a well-polished alumina (Al<sub>2</sub>O<sub>3</sub>) ultrafiltration membrane. Tubes adhere to the surface due to van der Waals interaction, occasionally spanning holes (figs 4.8c and 4.9a). After a suitable nanotube has been found, a series of contact-mode AFM images are taken under increasing loads: every image corresponds to the surface (and the tube) under a given normal load. Extracted linescans across the tube, like the one on fig. 4.8c, reveal the vertical deformation, fig. 4.9b. For the range of applied normal loads, the midpoint deflection of a thin, long nanotube under a nominal point load  $F$  can be fitted using the clamped beam formula [73] (see also p. 138):

$$\delta = \frac{FL^3}{192E_{Young}I} \quad (4.22)$$

where  $L$  is the suspended length and  $I$  the second moment of the cross-section, equal to  $d^4/64$  for a solid cylinder of diameter  $D$  [73].



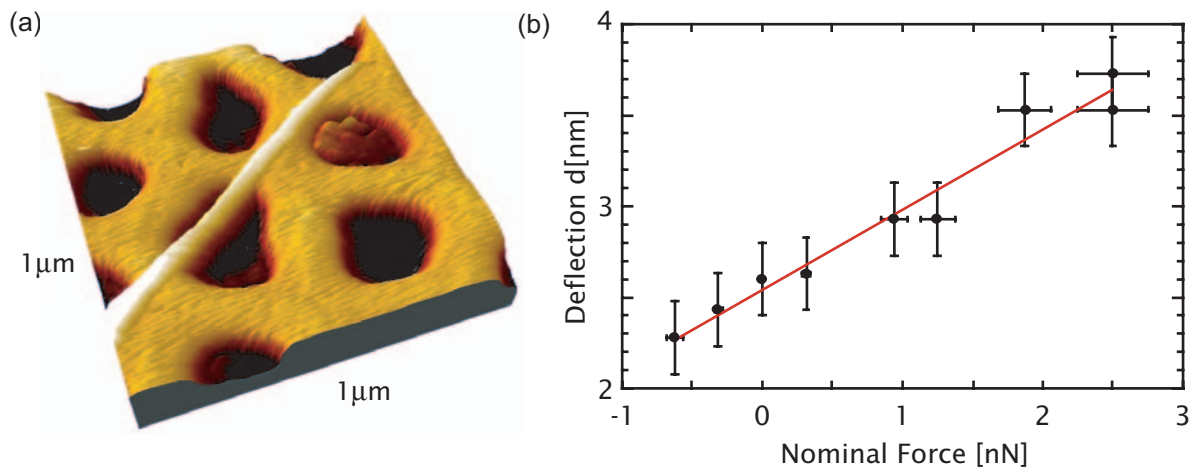


**Fig. 4.9.** (a) AFM image of a 10nm thick SWNT bundle lying on a porous alumina filter. This is a 3D representation of the AFM image in fig. 4.8c. (b) Measured dependence of vertical deflection on the applied nominal force [71].

The fitted line in fig. 4.9b doesn't pass through the origin because the force acting on the nanotube is not equal to the nominal force alone: it contains an additional constant term coming from the attractive force between the AFM tip and the tube. The tube's deflection should also contain a constant term arising from static deformation of the tube provoked during deposition on the substrate's surface.

This variable load imaging technique is advantageous for obtaining quantitative information as one is assured that the AFM tip is in the desired location when deforming the tube. Equation (4.22) is only valid if the tubes adhere well to the substrate, confirmed by the fact that the images reveal no displacement of the parts of the tube in contact with the membrane.

Using this technique, Young's modulus of  $1.0 \pm 0.5$  TPa was found for SWNTs. Values for MWNTs show a strong dependence on the amount of disorder in the graphitic layers – an average value of  $E_{Young} = 870$  GPa was found for the arc-discharge grown tubes, while the catalytically grown MWNTs, known to include a high concentration of defects can have a Young's modulus as low as 12 GPa [38].

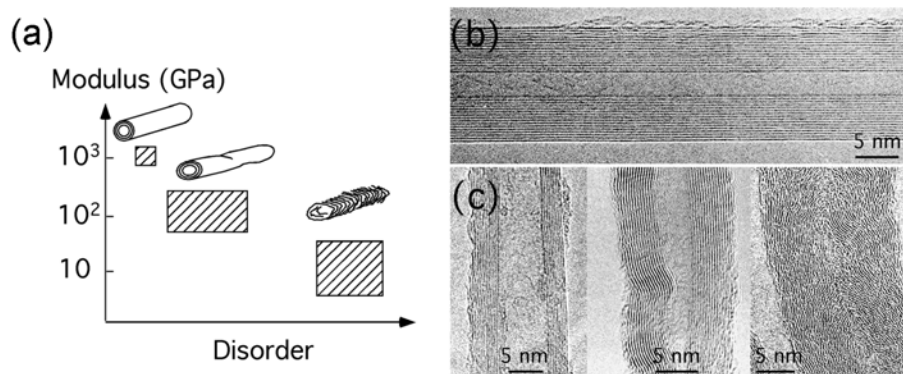


**Fig. 4.10.** (a) A map of the Young's modulus of MWNT, depending on the amount of disorder in their structure. Low-quality nanotubes have a Young's modulus that can be as low as 12 GPa. (b) TEM image of an arc-discharge grown CNT. (c) CVD grown carbon nanotubes of different quality [71].

For the deflection of SWNT ropes, an additional term in the bending formula has to be taken into account because of the influence of shearing between the tubes comprising the rope. Single CNTs are held together in the tube only via the weak, van der Waals interaction. As a consequence, ropes behave as an assembly of individual tubes and not as a compact, thick beam.

In the model, the entire nanotube bundle is treated as a single anisotropic cylinder. The Young's modulus  $E_{Young}$  corresponds to the "stretchiness" of nanotubes. The shear modulus  $G$  describes the intertube sliding. In no way does it represent the shear modulus of single nanotubes – it is called the shear modulus because it plays the same role in the bending of nanotube bundles as the shear modulus in the bending of macroscopic tubes.

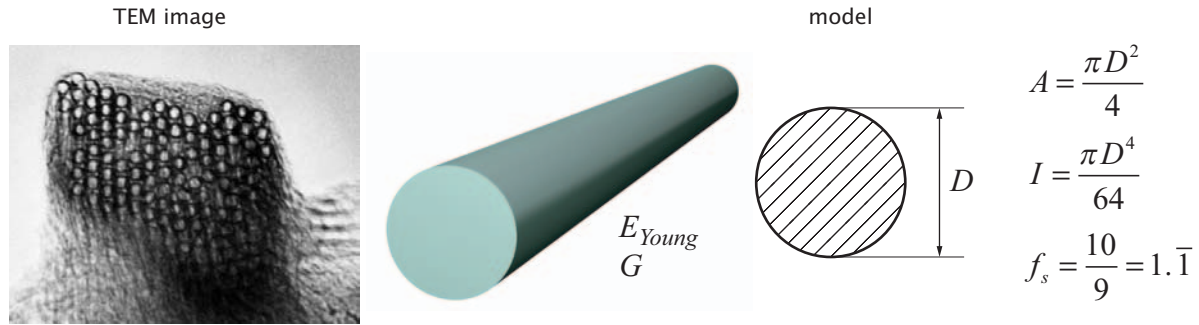


**Fig. 4.11.** Carbon nanotube bundles (TEM image on left) are modelled as anisotropic cylinders. The Young's modulus  $E_{Young}$  corresponds to the "stretchiness" of nanotubes. The shear modulus  $G$  describes intertube sliding. The bundle diameter  $D$  is directly measured and the cross-sectional area  $A$ , second moment of the area  $I$  and the shape-factor  $f_s$  calculated using the formulas on the right-hand side.

The deflection can be modeled as a sum of deflections due to bending and shearing [73] (see also p. 139):

$$\delta = \delta_{bending} + \delta_{shearing} = \frac{FL^3}{192E_{Young}I} + f_s \frac{FL}{4GA} = \frac{FL^3}{192E_{bending}I} \quad (4.23)$$

where  $f_s$  is the shape factor, equal to  $10/9$  for a cylinder,  $G$  the shear modulus and  $A$  the area of the beam's cross-section.  $E_{bending}$  is the effective bending modulus, equal to the Young's modulus when the influence of shearing can be neglected (for thin, long ropes).

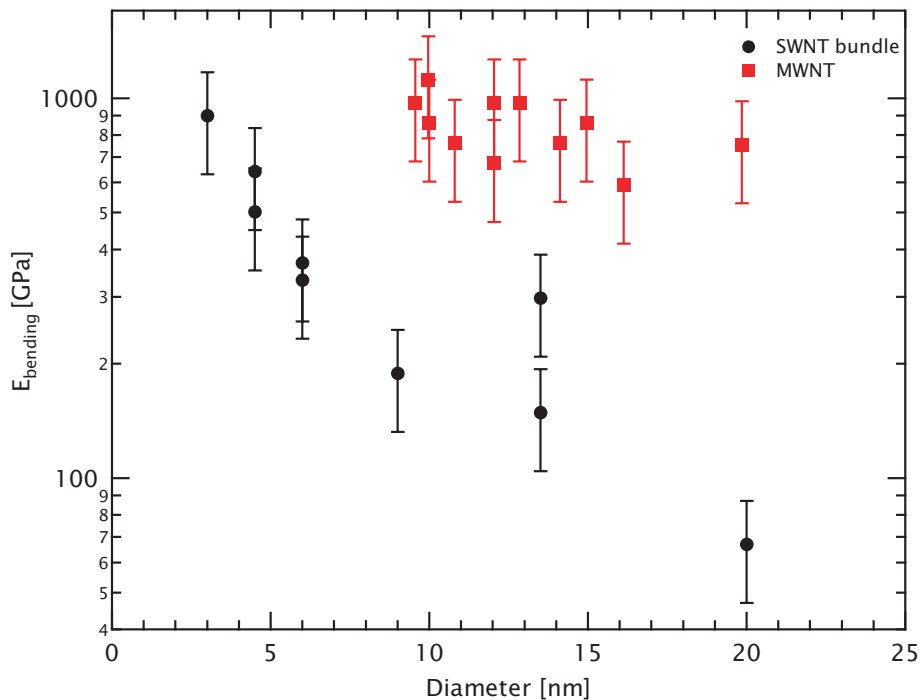


**Fig. 4.12.** Values of the bending modulus for 12 SWNT ropes of different diameters. The measured  $E_{bending}$  of thin ropes corresponds to  $E_{Young}$ , while for thick ropes one obtains the value of shear modulus  $G$  [72]. MWNT data is for arc-discharge grown tubes [38].

The Young's and the shear modulus can thus be extrapolated by measuring the  $E_{bending}$  of an ensemble of ropes with different diameter to length ratios – for thin ropes one obtains the value of the Young's modulus, while for the thick ones, the  $E_{bending}$  approaches the value of  $G$  on the order of 1 GPa – fig. 4.12.

The main advantage of this measurement method is its ease of implementation and large versatility. The measurement process itself consists of taking AFM images and there are no special requirements on the environment, so it should in principle be feasible to perform this kind of measurements using a reasonably good AFM – operating in air, controlled atmosphere or even under liquid for biological applications.

### **Radial deformation by AFM**

Apart from measuring the Young's and shear modulus, AFM was also used for measurements of the radial elastic modulus and tensile strength by the Ruoff group. The radial elastic modulus of MWNTs was measured by Yu et al. by performing nanoindentation on MWNTs using an AFM operating in tapping-mode below the cantilever's resonant frequency [74]. MWNTs were dispersed in 2-butanone and deposited on SiO<sub>2</sub> patterned using e-beam lithography. In tapping mode imaging, the probe is oscillated with the amplitude  $A_0$  above the sample surface. The probe strikes the sample at the bottom of each oscillation cycle, leading to a decrease of oscillation amplitude  $A$ . The surface is tracked by maintaining a constant cantilever oscillation amplitude at a set-point  $S=A/A_0$ . For operation below the cantilever's resonant frequency, the average tapping force  $F_{av}$  can be described with a semiempirical formula [74]:

$$F_{av} = \frac{1}{2} k_c (1 - S) \frac{A_0(f)}{Q\beta} \quad (4.24)$$

where  $k_c$  is the cantilever's force constant,  $Q$  its quality factor, and  $\beta$  the off-resonance parameter defined as:

$$\beta = \frac{A_0(f)}{A_0(f_0)} \quad (4.25)$$

where  $A_0$  is the free cantilever amplitude achieved at different frequencies. Silicon cantilevers with a nominal spring constant of  $k_c=50\text{N/m}$  and a quality factor  $Q=377$  were used. The cantilever was oscillated with a free amplitude  $A_0=26\text{nm}$  at the frequency corresponding to  $\beta=0.03$ . Height profiles and corresponding images of a MWNT (fig. 4.13) clearly show a reversible decrease of height as a consequence of increasing the average tapping force. Corresponding stress-strain curves are shown on fig. 4.14, with strain defined as  $\varepsilon=(H_0-H)/H_0$ , where  $H_0$  and  $H$  denote the original and deformed height, respectively. Different plots on fig. 4.14 correspond to different sections of the nanotube. Variations of the radial deformability are attributed to the presence of defects such as a locally decreased number of shells (fig. 4.14b). The radial elastic modulus of MWNTs can be estimated using the Hertz model for the indentation of a soft cylinder by a rigid sphere (in this case the AFM tip) [75].

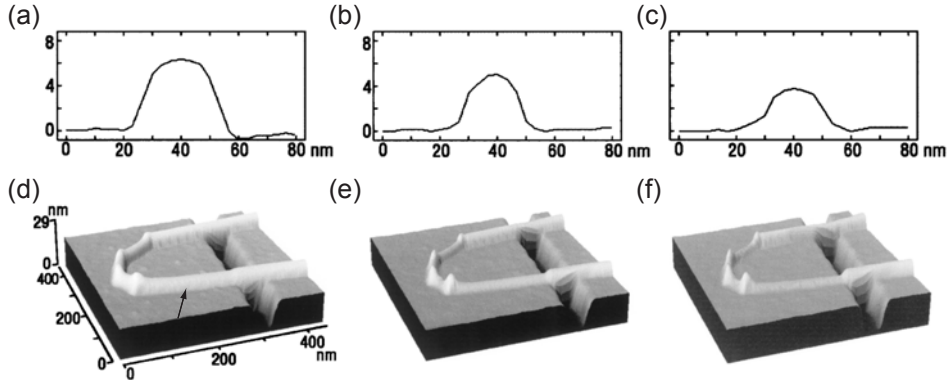


**Fig. 4.13.** Deformation of a MWNT (linescans and corresponding AFM images) deposited on a Si substrate under an AFM cantilever operating in tapping-mode and at different setpoints. Linescans were taken perpendicularly to the tube, at the position denoted with an arrow in (d). Setpoints  $S/S_0$  were 1.0 for (a), 0.7 for (b) and 0.5 for (c) [74].

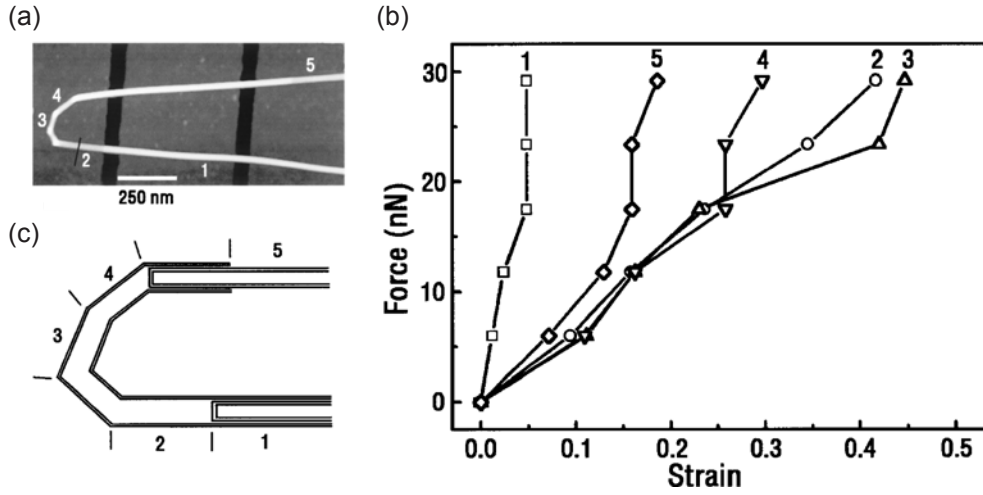


**Fig. 4.14.** (a) AFM image of a MWNT deposited on a  $\text{SiO}_2$  substrate. (b) Force-strain curves obtained for different sections in (a), based on height measurements in images acquired at different set points (c) Schematic of the MWNT structure based on the deformabilities of its various sections [74].

The total deformation  $\delta$  in the contact area can be expressed as:

$$\delta = K(k') \left( \frac{A+B}{RE(k')} \right) \left[ \frac{3kF}{2\pi} \left( \frac{1-\nu_{ip}^2}{E_{ip}} - \frac{1-\nu_{NT}^2}{E_{NT}} \right) \right]^{2/3} \quad (4.26)$$

where

$$A = \frac{1}{R_{ip}}, \quad B = \frac{1}{2R}, \quad \frac{1}{R} = \frac{1}{R_{ip}} + \frac{1}{R_{NT}}, \quad k' = \sqrt{1-k^2} \quad (4.27)$$

and the numerical constant  $k$ , determined by the radii  $R_{ip}$  and  $R_{NT}$ , is the solution of equation:

$$\frac{B}{A} = \frac{(1/k^2)E(k') - K(k')}{K(k') - E(k')} \quad (4.28)$$

where  $K(k)$  and  $E(k)$  are elliptic integrals:

$$K(k) = \int_0^{\pi/2} \sqrt{1 - k^2 \sin^2 \theta} d\theta, E(k) = \int_0^{\pi/2} \frac{1}{\sqrt{1 - k^2 \sin^2 \theta}} d\theta \quad (4.29)$$

The MWNT is considered as a uniform, isotropic and rubberlike solid cylinder characterized by the Poisson's ratio  $\nu_{NT}=0.5$ .  $R_{tip}$  was 24 nm as determined from the apparent widening of the nanotube due to tip convolution. Since the radial elastic modulus  $E_{NT}$  of MWNT was expected to be smaller than that of the silicon AFM tip, the total deflection  $\delta$  is almost exclusively due to the deformation of the cylinder. Under such circumstances the strain is equal to  $\varepsilon=\delta/2R_{NT}$ . Equation (4.26) can then be used to generate the force-strain curves similar to those used to describe the deformability of the MWNT. The observed behavior (fig. 4.13) can be reproduced using the values of  $E_{NT}$  ranging from 0.3 to 4 GPa.

### ***Tensile loading inside a SEM***

Finally, the first direct measurements of the elastic properties of CNTs that haven't relied on the beam or stretching string setup involved deforming MWNTs [76] and SWNT ropes [77] under axial strain. This was achieved by identifying and attaching opposite ends of MWNTs or SWNT ropes to two AFM tips, all inside a SEM.

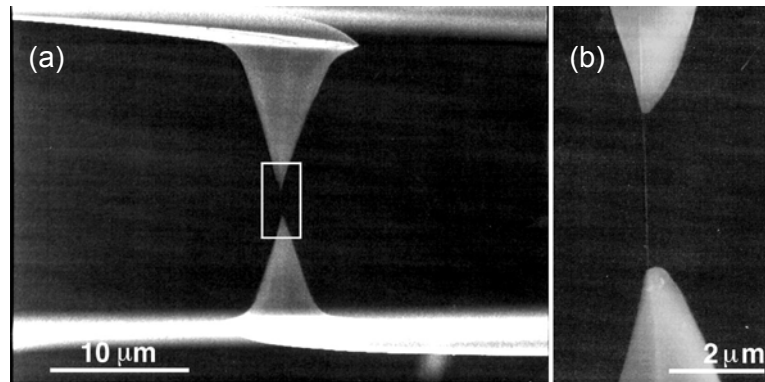


**Fig. 4.15.** (a) A SEM image of a MWNT mounted between two opposing AFM tips. (b) A close-up of the region indicated by a rectangle in (a) [76].

One tip was integrated with a rigid cantilever with a spring constant above 20 N/m and the other was compliant (0.1 N/m), fig. 4.15. The rigid lever was then driven using a linear piezomotor. On the other end, the compliant lever bent under the applied tensile load. The deflection of the compliant cantilever – corresponding to the force applied on the nanotube – and the strain of the nanotube were simultaneously measured. The force  $F$  is calculated as  $F=kd$  where  $k$  is the spring constant of the flexible AFM lever and  $d$  its displacement in the vertical direction. The strain of the nanotube is  $\delta L/L$ , fig. 4.16. From the stress-strain curves obtained in this fashion, fig. 4.16b,  $E_{Young}$  ranging from 270–950 GPa were found. Examinations of the same broken tubes inside a TEM revealed that nanotubes break with the “sword in sheath” mechanism, where only the outer layer appears to have carried the load. After it breaks, pullout of inner shells follows. An average bending strength of 14 GPa and axial strengths up to 63 GPa were found.

Firm attachment of nanotubes to AFM tips was ensured by a deposition of carbonaceous material induced by the electron beam concentrated in the contact area [78].

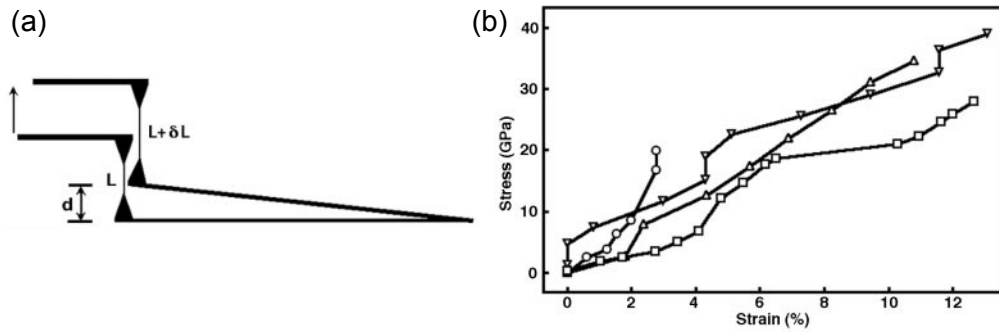
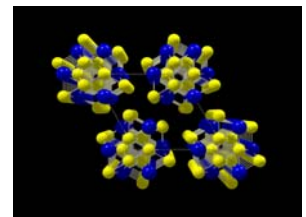


**Fig. 4.16.** (a) Principle of the experiment performed by Yu et al. As the rigid cantilever is driven upwards, the lower, soft cantilever bends by the amount  $d$  and the nanotube is stretched by  $\delta L$ . As a result, the nanotube is strained by  $\delta L/L$  under the action of force  $F=kd$ , where  $k$  is the elastic constant of the lower AFM lever. (b) Plot of stress vs. strain curves for different individual MWNTs [76].

# 5

## *Molybdenum disulphide (MoS<sub>2</sub>) nanotubes*



### 5.1. Introduction

The discovery of C<sub>60</sub> fullerenes [24] in 1986 and carbon nanotubes [21] in 1991 as new forms of crystalline carbon has opened whole new fields of research in physics, chemistry and materials science thanks to their interesting properties and a wide range of potential applications. With the discovery of tungsten disulphide (WS<sub>2</sub>) and molybdenum disulphide (MoS<sub>2</sub>) fullerene-like nanoparticles and tubular structures [79], followed with the synthesis of boron nitride (BN) nanotubes [80], it was realized that fullerenes and carbon nanotubes represent only a small subset of a wide class of layered materials that can form C<sub>60</sub>-like particles, tubes and other interesting morphologies.

Similarly to graphite, these layered materials are characterized by weak, van der Waals interaction between neighboring layers, allowing easy, low strength shearing [81]. Therefore it almost came as no surprise that MoS<sub>2</sub> nanoparticles behave as exceptional solid-state lubricants [82], with a very low friction coefficient (between 0.008 and 0.01) and excellent wear resistance [83]. These interesting tribological properties can be a good indication of their mechanical properties. The low value of the friction coefficient in the case of nanoparticles points to interesting mechanical properties of MoS<sub>2</sub> nanotubes. From these results, a low resistance of nanotubes to sliding within the bundles is expected, together with a relatively flexible structure.

MoS<sub>2</sub> can be synthesized in a large variety of forms: particles, nanotubes [79], multiwall nanotubes [84] and also in the form of ropes, ribbons and thin microtubes several μm in diameter and millimeters in length [85]. They can also be produced in batches of uniform diameter and electronic properties in contrast to carbon nanotubes, which are always grown as mixtures of metallic and semiconducting tubes with a huge dispersion of band-gap values. Before building functional and reliable electronic devices out of them, carbon nanotubes have to be sorted according to their electronic properties. Their richness in form, together with unique physical

properties promises potential applications for MoS<sub>2</sub> nanotubes going beyond those of carbon nanotubes.

## 5.2. Physical properties of MoS<sub>2</sub> nanostructures

### *Structure of MoS<sub>2</sub> nanotubes*

The most stable form of layered MoS<sub>2</sub> consists of a metal layer sandwiched between two sulphur layers (space group P63/mmc), fig. 5.1b. These triple layers are stacked on each other, similarly to graphite, by van der Waals interactions and separated by 6.15 Å. Tubular structures can form, just like in the case of graphite, by wrapping-up of this triple layer in the shape of a cylinder. The wrapping-up can be described in terms of primitive 2d-lattice vectors, leading to definitions of chiralities, armchair (fig. 5.1c) and zigzag (fig. 5.1d) tubes analogous to those in the case of carbon nanotubes (for more on the chiralities of carbon nanotubes, see p. 25).

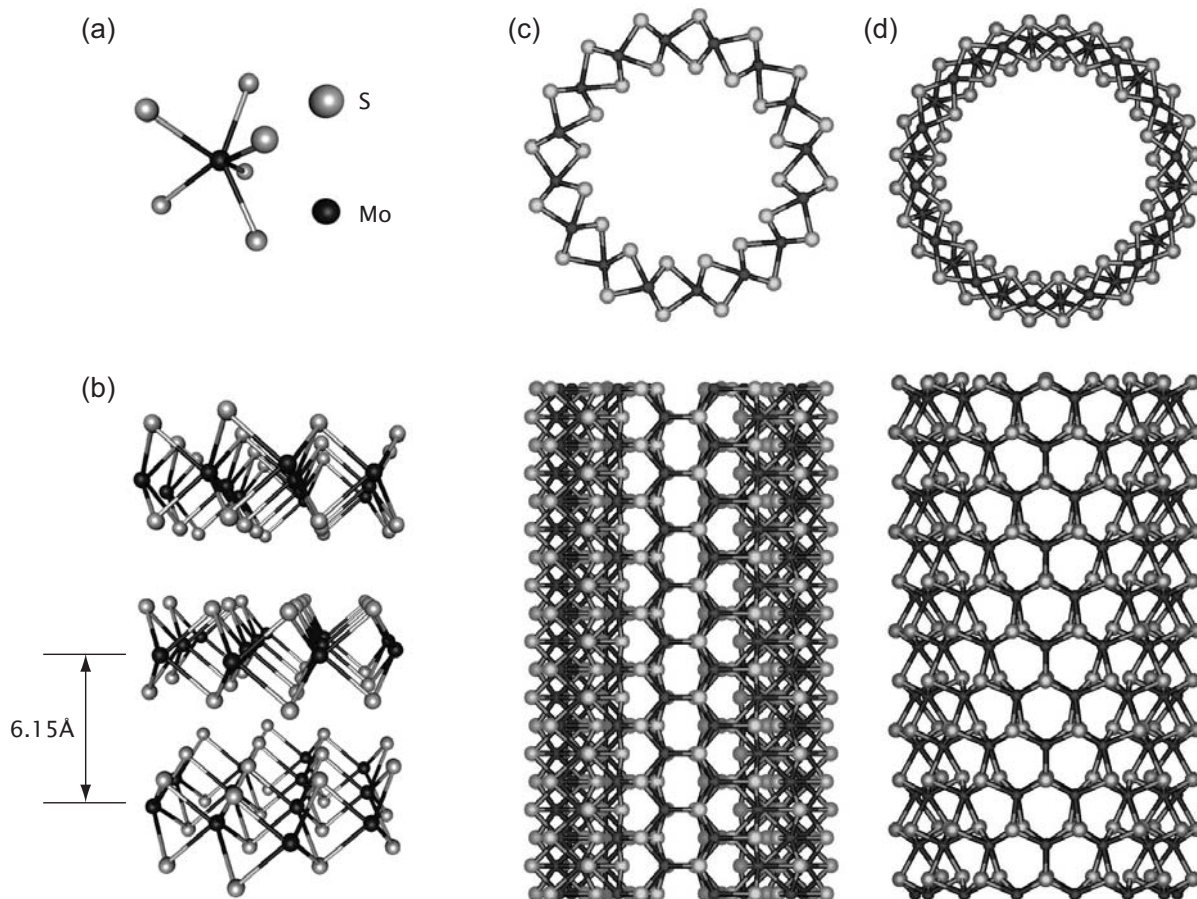


**Fig. 5.1.** (a) A single Mo atom in the MoS<sub>2</sub> structure. (b) Schematic drawing of the MoS<sub>2</sub> layer stacking. (c) Armchair (8,8) (left) and zig-zag (14,14) MoS<sub>2</sub> nanotube [86].



### Basic electronic properties of MoS<sub>2</sub> nanotubes

The band structure of MoS<sub>2</sub> nanotubes can be derived from the electronic structure of the single MoS<sub>2</sub> layer. Band structure of zigzag ( $n,0$ ) tubes resembles that of the corresponding carbon nanotubes, though they are all expected to be semiconducting, unlike the ( $3n,0$ ) carbon nanotubes which are metallic. Contrary to CNTs, their bandgap increases with increasing tube diameters, remaining smaller than the band-gap for the single layer or the bulk material. Armchair MoS<sub>2</sub> nanotubes are all expected to have a moderate direct gap, together with a small indirect gap, which is expected to decrease with increasing diameter. This suggests that zigzag MoS<sub>2</sub> nanotubes could be used for optoelectronic applications in luminescing devices, which is not the case with carbon nanotubes [86].

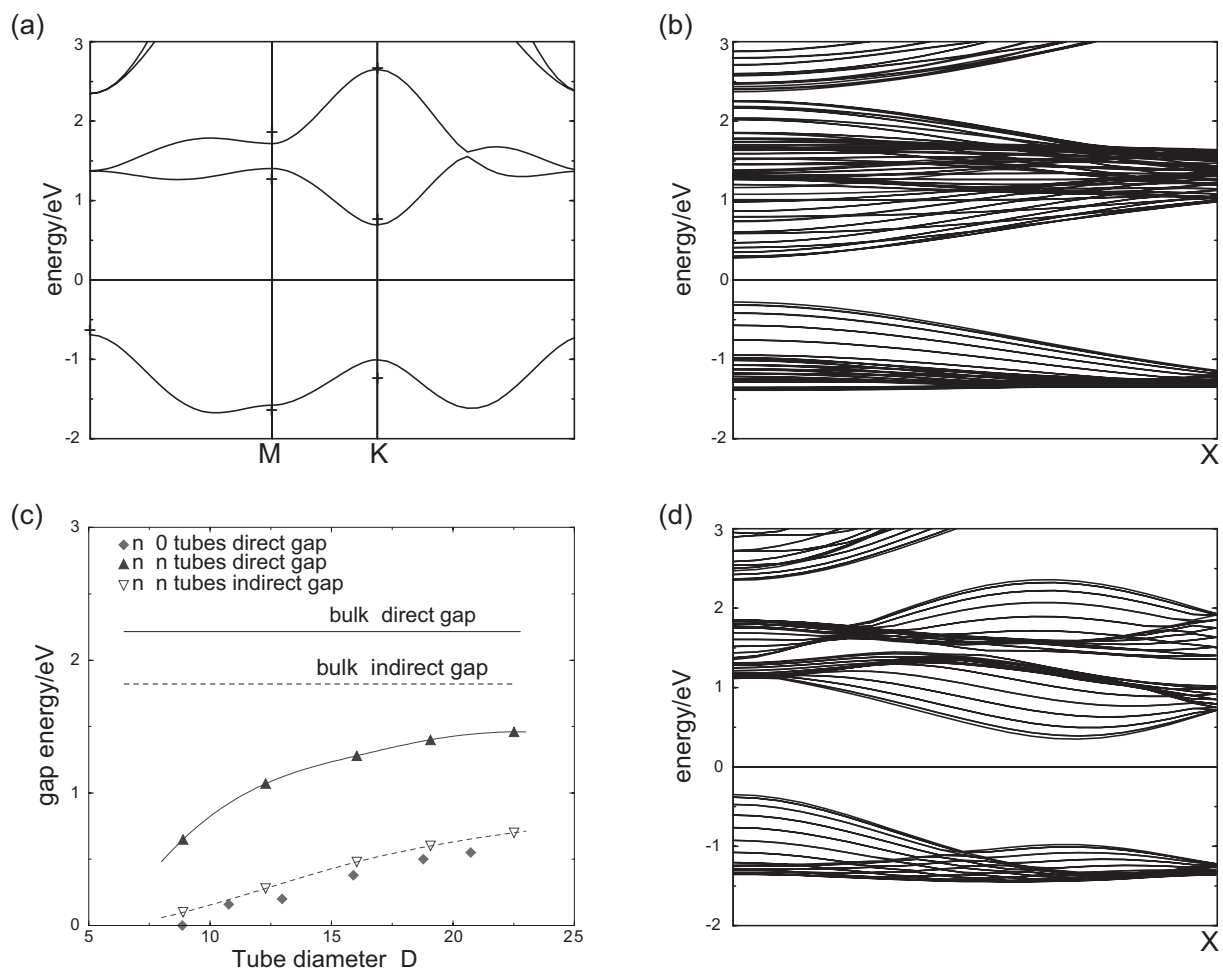


**Fig. 5.2.** (a) Calculated band structure near the Fermi energy for a MoS<sub>2</sub> triple layer (fig. 5.1b). The energy is given relative to the Fermi energy. (b) Calculated band structure for a (22,0), zig-zag MoS<sub>2</sub> nanotube. (c) Calculated band structure for a (14,14), armchair MoS<sub>2</sub> nanotube [86].

### Tribological properties of MoS<sub>2</sub> nanoparticles

MoS<sub>2</sub> and WS<sub>2</sub> are characterized by weak (van der Waals) interatomic interaction between their layered structures which allows easy shearing between neighboring planes [81]. Hollow nanoparticles of these materials (fig. 5.3) can be synthesized in chemical reactions between a

precursor in the form of metal-oxide nanoparticles and H<sub>2</sub>S, resulting in an onion-like structure [87].

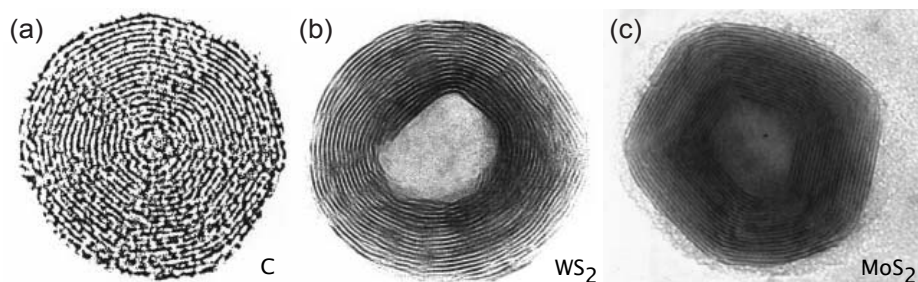


**Fig. 5.3.** TEM images of nanoparticles: (a) carbon onion (b) WS<sub>2</sub> nanoparticle (c) MoS<sub>2</sub> nanoparticle. The distances between the fringes are 3.35Å, 6.18Å and 6.2Å, respectively [87, 88].

Thin films of nanoparticles can also be deposited using an arc-discharge technique. Friction coefficient and wear measurements for these films [82, 83] have demonstrated their superior properties as solid state lubricants. Tribological tests performed using a ball-flat tribometer and a disk-block tester (fig. 5.4) for higher loads and sliding velocities, revealed a friction coefficient  $\mu$  as low as 0.008, with a very low wear rate and virtually no change in the friction coefficient even after  $2.4 \times 10^5$  rubbings in the test apparatus. Such superior tribological properties MoS<sub>2</sub> nanoparticles owe to the low strength of interlayer shearing, absence of dangling bonds which keeps them from sticking to metallic surfaces and easy deformability between corrugations.

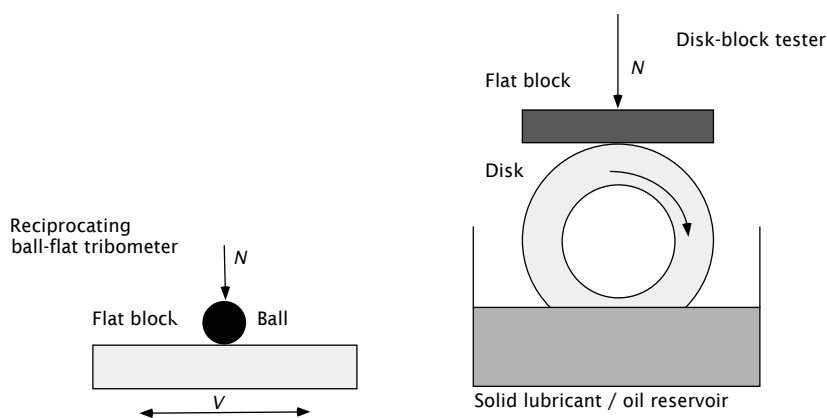


**Fig. 5.4.** Schematic drawing of the experimental setup used to characterize the tribological properties of MoS<sub>2</sub> nanoparticles. (a) A ball-flat tribometer. (b) A disk-block tester [82].

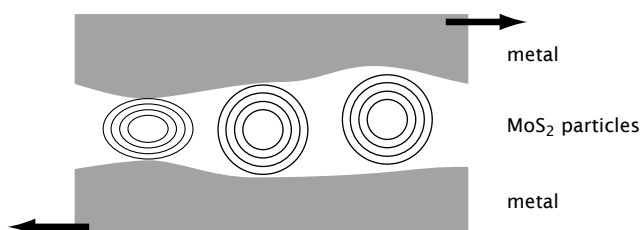


**Fig. 5.5.** Drawing of the action of solid lubricant (MoS<sub>2</sub>) particles between two corrugated metallic plates. Besides rolling, particles can also be squeezed between the corrugations.

MoS<sub>2</sub> nanoparticles have already found practical commercial applications as additives to oil-based lubricants and coatings on automotive parts and tools. The low value of friction between neighboring layers of MoS<sub>2</sub> makes these nanotubes also interesting for future nanoscale mechanical systems like bearings.

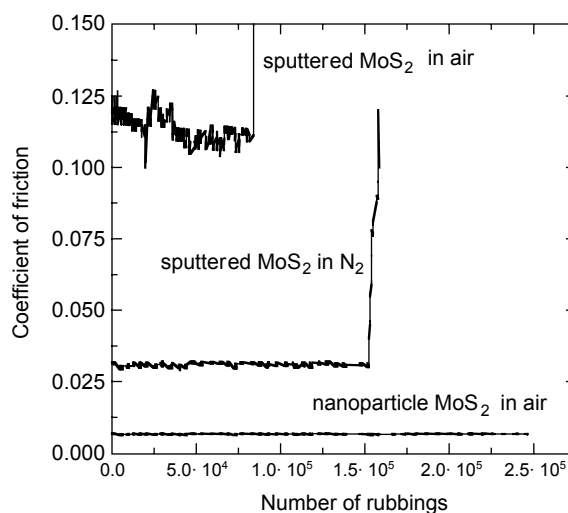


**Fig. 5.6.** The coefficient of friction as a function of time for different types of MoS<sub>2</sub> layers in ambient conditions and under dry nitrogen [83].

### 5.3. Synthesis of subnanometer-diameter MoS<sub>2</sub> nanotubes

The single-walled MoS<sub>2</sub> nanotubes used in this study were grown by a catalyzed transport method in the group of Prof. D. Mihailović from Ljubljana. C<sub>60</sub> (5 weight %) was added to bulk MoS<sub>2</sub> powder in the transport tube as a catalyst and iodine was used as a transport agent. The reaction ran for 22 days at 1010 K in an evacuated silica ampoule at a pressure of 10<sup>-3</sup> Pa with a temperature gradient of 6 K/cm. Approximately 15% of the starting material formed MoS<sub>2</sub> nanotubes. Nanotubes grow in the form of bundles, which can contain up to 10<sup>6</sup> individual tubes, with identical diameters and variable lengths (fig. 5.7) [89]. The structure was elucidated by means of a high resolution transmission electron microscope (HTREM). Images of bundles show highly ordered hexagonal packing of identical nanotubes with a regular stacking arrangement within bundles, with a center-to center distance between the tubes of 0.96 nm. The bundles are composed of (3,3) armchair MoS<sub>2</sub> nanotubes, with iodine atoms inserted in voids between the nanotubes, forming 1D rows along the bundle axis. The closest sulfur atoms on adjacent nanotubes are separated by 0.35 nm, which corresponds approximately to their van der Waals diameters. The distance between sulfur and molybdenum atoms in the nanotube is almost the same as the corresponding distances in bulk crystals, despite the large curvature. The unit cell of the hexagonal close-packed nanotubes within a bundle is 0.40 nm along the bundle axis and 0.96 nm perpendicular to the bundle axis.

The presence of C<sub>60</sub> in the growth process is essential – the nanotubes do not grow in their absence. It seems to play a role of a growth promoting catalyst, as electron energy loss spectroscopy (EELS) analysis indicates that it doesn't get incorporated into the bundle structure.

The mechanism of growth is not clear at this time, but the uniformity of the final product seems to suggest that C<sub>60</sub> could play the role of a template during the growth process.

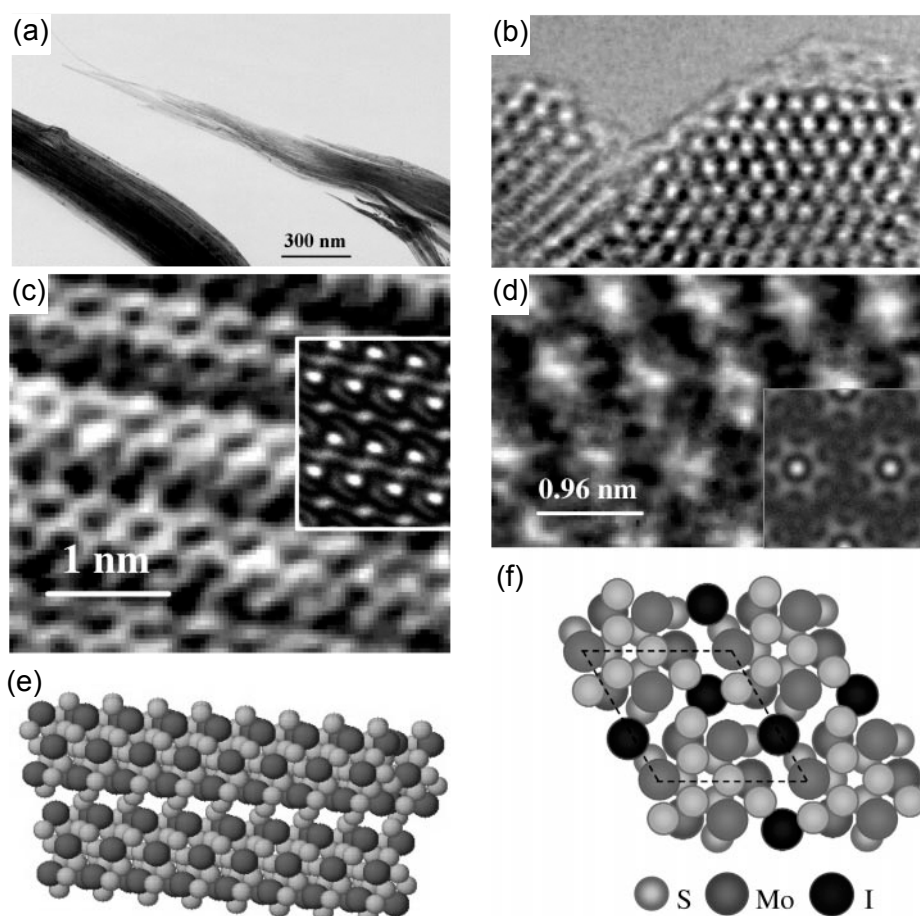


**Fig. 5.7.** Morphology of MoS<sub>2</sub> nanotubes. (a) A strand of MoS<sub>2</sub> nanotube bundles. (c) High-resolution TEM image of a nanotube bundle. (e) Model structure of the tube. (b) TEM image of the cross section of a bundle. (d) High-resolution view of the structure. (f) The model structure in the direction perpendicular to the nanotube axis [89].

## 5.4. Results: AFM and TEM observations

MoS<sub>2</sub> ropes composed of individual nanotubes, all with the same diameter, have been dispersed in absolute ethanol using a dip-probe sonicator operating at moderate power. The resulting suspension, stable during several hours, has been used to prepare samples for TEM by placing a drop on a copper grid coated with holey carbon. They were imaged under an acceleration voltage of 200kV in a Philips CM20 microscope. TEM images like the one in fig. 5.8 reveal a highly ordered structure (fig. 5.8, inset), with average distance between the contrast fringes of 0.88nm. The overall amount of impurity particles seems to be very low, especially when compared with as-produced carbon nanotubes, which reduces the need for post-processing before using this material. There is no visible damage that could be attributed to sonication. Longer exposures to an intense electron beam of this energy can produce observable damage (fig. 5.9).

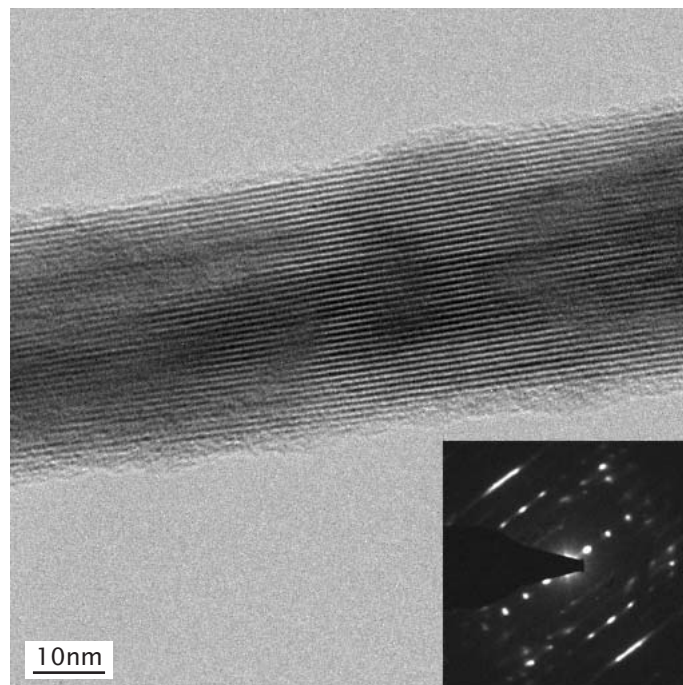


**Fig. 5.8.** TEM image of a MoS<sub>2</sub> nanotube bundle with a corresponding diffraction pattern. Distance between the fringes is 0.88nm [90].

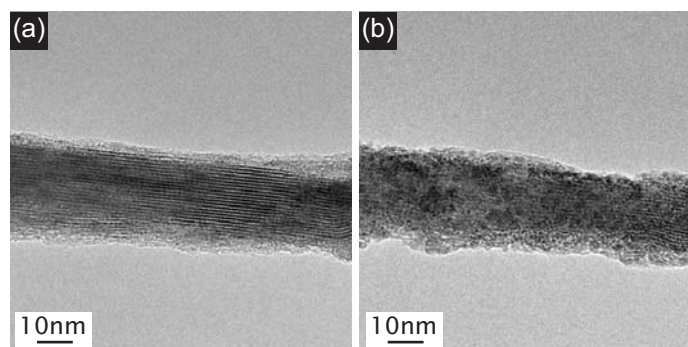


**Fig. 5.9.** The effect of electron-beam irradiation inside a TEM on MoS<sub>2</sub> nanotube bundles. (a) A bundle of single-walled MoS<sub>2</sub> nanotubes before and (b) after 10 minutes under a focused electron beam.

Samples for AFM studies have been prepared in a similar way: the suspension of MoS<sub>2</sub> nanotubes prepared by sonication was deposited on a polished alumina ultrafiltration membrane.

AFM imaging was performed using a Thermomicro M5 [17] operating in contact mode and with cantilevers having a spring constant in the 0.03–0.1 N/m range. A series of images taken over a surface of 100 μm, apart from the presence of bundled MoS<sub>2</sub> tubes, revealed a new morphology of MoS<sub>2</sub> nanotubes: rings (fig. 5.10). The observed diameters ranged from 450 nm–2.8 μm. Rings were formed of bundles having 4–15 nm in diameter.

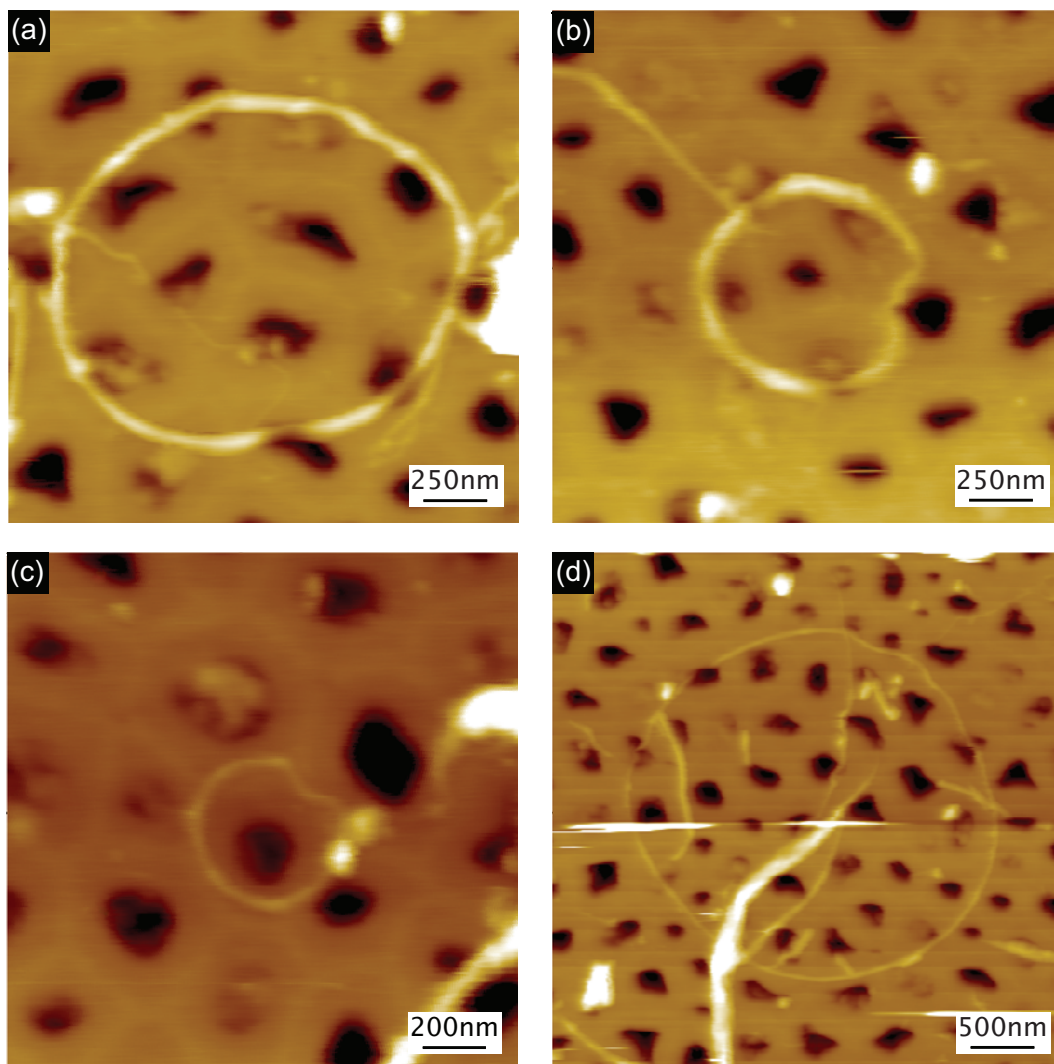


**Fig. 5.10.** AFM images of four different MoS<sub>2</sub> nanotube rings, with diameters between 450 nm and 2.8 μm. They are formed of bundles with diameters ranging from 4 to 15 nm.

Similar structures have been known to appear in the case of carbon nanotubes [91], with distinct formation mechanisms: during the growth process, in which case they form seamless rings and also during the dispersion process. In the latter case, CNT ropes wrap around gas bubbles formed in the agitated liquid and the rope's ends are held together only by adhesion. The energy gained by adhesion has to be superior to the energy cost involved with straining the rope. Carbon nanotube rings served as an interesting testing ground for studies of electron localization in mesoscopic structures [92]. The rings observed in our case most probably form during sonication, and their stability seems to be further increased by adhesion to the Al<sub>2</sub>O<sub>3</sub> substrate.

## 5.5. Results: shear and Young's moduli

Measurements of the bending modulus of MoS<sub>2</sub> nanotube ropes were performed using a Thermomicro M5 [17] atomic force microscope operating in contact mode. V-shaped Si<sub>3</sub>N<sub>4</sub> sharpened cantilevers (commercial name microlevers) with nominal spring constants ranging between 0.03 and 0.1 N/m were used in this study. The cantilever's spring constant were calibrated by measuring their resonant frequency in air [16]. Samples were prepared by depositing MoS<sub>2</sub> nanotube ropes from a suspension in absolute ethanol onto a surface of a polished alumina ultrafiltration membrane. By chance, nanotubes span pores (fig. 5.11a) and are held in place by surface adhesion. This was confirmed by their resistance to repeated AFM imaging. Nanotubes that were selected for measurements did not move over the surface during

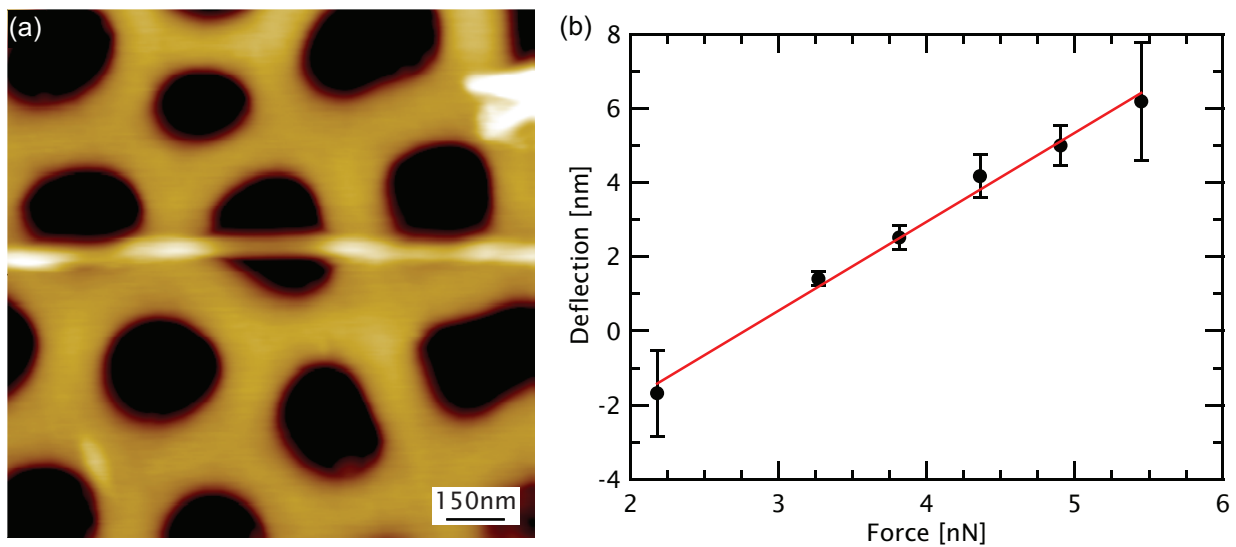


**Fig. 5.11.** (a) AFM image of a MoS<sub>2</sub> nanotube rope on the surface of an Al<sub>2</sub>O<sub>3</sub> membrane. (b) A typical deflection vs. force curve extracted from a series of AFM images acquired under varying normal load [90].

the experiment. Deformations were observed only on their suspended parts. In cases where the adhesion is not strong enough, tube sliding prevents stable imaging, so these tubes are automatically eliminated from the rest of the measurement process. When a suitable nanotube bundle is found, a series of images under varying load is taken. Subsequent image analysis reveals the deflection of the suspended part's middle point, fig. 5.11b (see also p. 42). The reversibility and linearity of these curves indicates that nanotube bundles deform elastically. The tube's deflection  $\delta$  at the middle-point under the normal load  $F$  can be fitted using the clamped beam formula [73] (see also p. 139):

$$\delta = \delta_B + \delta_S = \frac{FL^3}{192E_{Young}I} + f_s \frac{FL}{4GA} = \frac{FL^3}{192E_{bending}I} \quad (5.1)$$

and is in general a sum of  $\delta_B$  – deflection due to bending of tubes which is governed by the Young's modulus  $E_{Young}$  and  $\delta_S$  – deflection due to intertube sliding (shearing), governed by the shear modulus  $G$ . This choice of parameters is analogous to the mechanical description of carbon nanotube bundles on p. 44.  $L$  is the tube's length,  $A$  the cross-section,  $I$  the second moment of the cross-sectional area and  $f_s$  a numerical shape factor, equal to 10/9 for a cylinder (see also the geometrical model, fig. 4.11 on p. 44). The deflection length  $L$  is directly measured from the

AFM images. The tube's diameter  $D$  is determined from the tube's height, which is a more accurate measure of the tube's diameter than the apparent width, because of the tip convolution effect. For isotropic, long and thin beams the second term in equation (5.1) coming from shearing can in general be neglected. In this case, however, tribological measurements on MoS<sub>2</sub> nanoparticles indicate that the value of the shear modulus  $G$  is expected to be much lower than the  $E_{Young}$ .

A single deformation experiment yields an effective value  $E_{bending}$  – the bending modulus, dependent on the tube's geometry, which would be equal to  $E_{Young}$  if the influence of shearing was neglected. For thin and long bundles – ideally a single isolated nanotube –  $E_{bending}$  would correspond to  $E_{Young}$ . On the other hand, the values for short and thick bundles would correspond more closely with the shear modulus  $G$ . By performing measurements on bundles with varying diameters, composed of a different number of single-walled MoS<sub>2</sub> nanotubes, the values of  $E_{Young}$  and  $G$  can be determined.

With this goal in mind, measurements on 12 MoS<sub>2</sub> bundles were performed, with the summary of results given in table 5.1 and on fig. 5.12.

Tube No.	Diameter D [nm] ±5%	Length L [nm] ±15%	$E_{bending}$ [GPa] ±50%
1	16	188	9
2	8	172	158
3	10	228	100
4	16	214	18
5	6	210	120
6	17	258	9
7	14	362	58
8	14	301	200
9	9	294	150
10	20	283	8
11	11	265	140
12	17	291	28

**TABLE 5.1.** Diameter  $D$ , length  $L$ , and the effective, bending modulus  $E_{bending}$  of MoS<sub>2</sub> ropes measured during this study.

The bending modulus  $E_{bending}$  of MoS<sub>2</sub> nanotube bundles follows the same general behavior as the bending modulus of carbon nanotube ropes observed by Salvétat et al. [72]. For small values of the  $D/L$  ratio, the bending modulus of bundles approaches the value of the Young's modulus of an isolated tube. As the  $D/L$  ratio increases, the bending modulus decreases because of the growing influence of intertube sliding (shearing) on the elastic response of the bundle. The value of the shear modulus can be determined more precisely if equation (5.1) is rewritten and the bending modulus  $E_{bending}$  expressed as follows:

$$\frac{1}{E_{bending}} = \frac{1}{E_{Young}} + \frac{1}{G} \frac{10}{3} \frac{D^2}{L^2} \quad (5.2)$$



From the plot of  $E_{bending}$  as a function of the aspect ratio, the shear modulus can directly be determined as the slope of the data points.

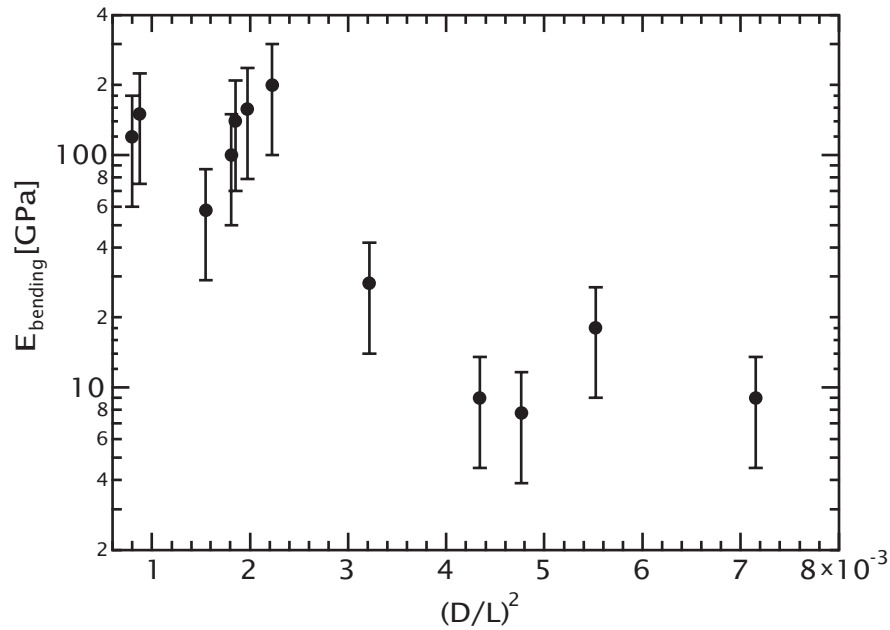


**Fig. 5.12.** Bending modulus  $E_{bending}$  of  $\text{MoS}_2$  nanotube bundles as a function of their aspect ratio  $D/L$  in the suspended beam geometry.

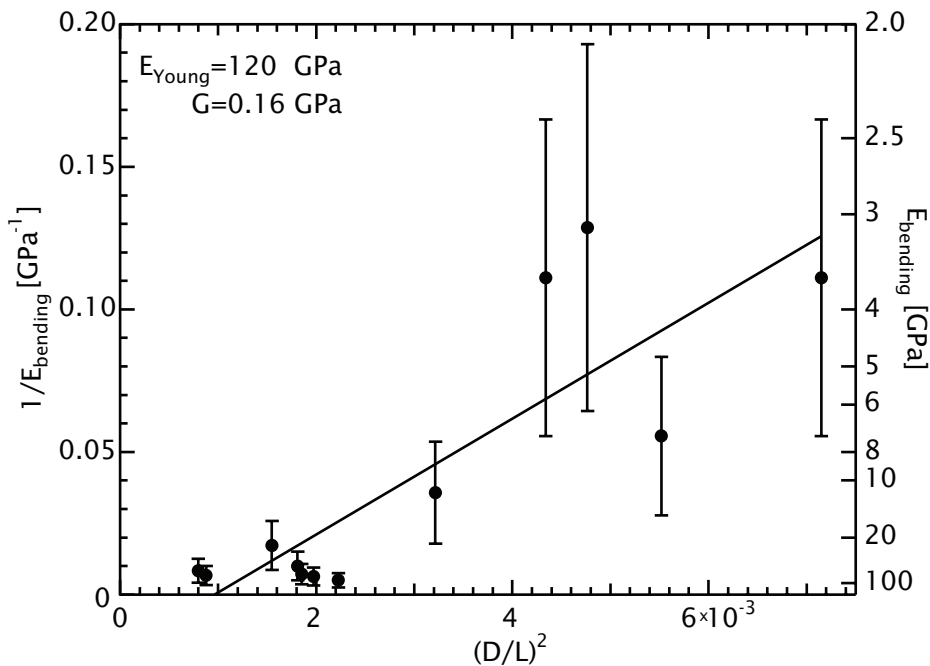


**Fig. 5.13.** A plot of the inverse bending modulus as a function of the bundle's aspect ratio. The shear modulus is the inverse of the lineslope and is equal to  $G=0.16$  GPa [90].

From the linear fit, according to equation (5.2), the numerical value for the intertube shear modulus in  $\text{MoS}_2$  bundles is:

$$G = (0.16 \pm 0.05) \text{ GPa} \quad (5.3)$$

The value of the Young's modulus could in principle be determined from equation (5.2) as the inverse of the intercept between the fitted line and the abscissa on fig. 5.13. Due to systematic

errors and large uncertainty of single measurements ( $\pm 50\%$ ) the intercept is unfortunately negative. The lower limit for the Young's modulus of isolated, single-walled MoS<sub>2</sub> nanotubes could also be estimated by taking the value of the bending modulus  $E_{bending}$  for the bundle with the lowest D/L ratio. From table 5.1, this is the case for the tube no. 5, so the lowest estimate for the Young's modulus is:

$$E_{Young} \geq (120 \pm 60) \text{ GPa} \quad (5.4)$$

a value which is in close agreement with the value of 160 GPa for the Young's modulus obtained from nanoindentation experiments on MoS<sub>2</sub> films [93]. Values for the shear and the Young's modulus of MoS<sub>2</sub> nanotubes can be put into perspective by comparing them with a similar material, carbon nanotube bundles, table 5.2.

Material	Young's modulus E [GPa]	Shear modulus G [GPa]
Graphite	1060	4.5
Carbon SWNT ropes	1200	1–10
MoS <sub>2</sub> ropes	120	0.16
Steel	210	
Aluminium	70	
Kevlar	140	

**TABLE 5.2.** Comparison of the Young's and shear moduli for graphite, carbon, MoS<sub>2</sub> ropes and several engineering materials. For graphite, the in-plane Young's and the interplane shear moduli are given [90].

The Young's modulus of MoS<sub>2</sub> nanotubes was calculated by Dr. Gábor Csányi (University of Cambridge) who performed simulations using density-functional calculus (DFT). Simulated MoS<sub>2</sub> nanotubes were stretched, the structure allowed to relax and the Young's modulus was calculated from the stress energy as:

$$E_{Young} = \frac{1}{V_0} \left. \frac{\partial^2 E}{\partial \varepsilon^2} \right|_{\varepsilon=0} \quad (5.5)$$

where  $V_0$  is the equilibrium volume and  $E$  the strain energy (see also p. 37). A theoretical stress-strain diagram is shown on fig. 5.14.

These calculations found a value of 97 GPa for the Young's modulus, within the error of the experimental results. A value of the intertube shear modulus could not have been calculated due to the low shearing forces.

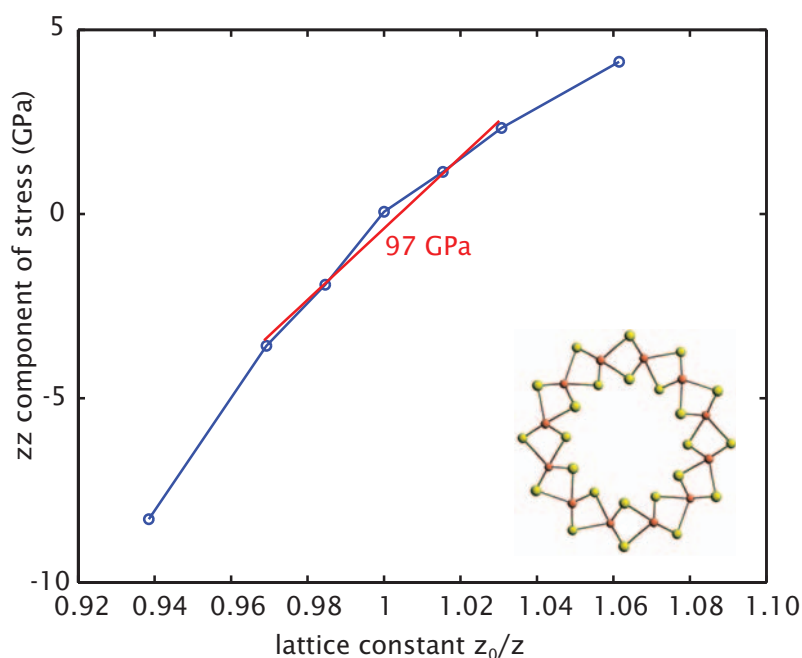


**Fig. 5.14.** Calculated stress-strain diagram for a simulated MoS<sub>2</sub> nanotube, yielding Young's modulus of 97 GPa [94].

## 5.6. Conclusions

The Young's modulus of MoS<sub>2</sub> nanotubes is an order of magnitude lower than that of carbon nanotubes which holds the record. Still, this value is comparable to that of commonly used engineering materials, indicating that this material could be used in nano-electromechanical devices. Their feasibility is to be determined.

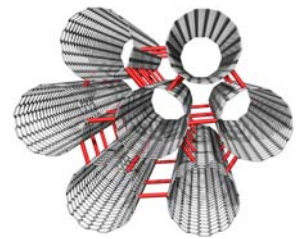
The value of the shear modulus is far more surprising, because it is one order of magnitude lower than that of carbon nanotube bundles. This is due to weak interaction between the sulphur atoms on the outer layer of nanotubes. Such a weak interaction could be an interesting point in further studies of the physical properties of MoS<sub>2</sub> nanotubes because it indicates the tubes comprising the rope are very weakly coupled, and that these tubes could prove to be an interesting playing ground for studying fundamental physical phenomena in 1D and weakly coupled systems. From the practical point of view, such a low value of intertube shearing could make these tubes valuable for building nano-bearings.

Superior tribological properties of MoS<sub>2</sub> nanoparticles are deeply connected with their mechanical properties. Low value of shearing modulus makes them prone to sliding with little friction, while the relatively low value of the Young's modulus imparts a high deformability. High hopes for C<sub>60</sub> fullerene molecules as an ideal lubricating agent have failed at this point: although they can easily slide on planes, the high stiffness of the fullerene cage makes it difficult for them to squeeze past corrugations, and renders them inappropriate for lubrication.



# 6

## *Irradiation-induced crosslinking of SWNT bundles*



### 6.1. Introduction

The field of carbon nanotubes and the mechanical properties on the nanoscale is inarguably on the forefront of modern physics. Carbon nanotubes with their Young's modulus comparable to that of diamond (on the order of 1TPa) have a tremendous potential as the ultimate fiber. Before producing composites with carbon nanotubes, two major obstacles need to be overcome: large scale production and the extremely low shear modulus of carbon nanotubes, on the order of 1–10GPa [72], reflecting the fact that single nanotubes interact only via van der Waals interaction. This low shear modulus is a serious weakness of carbon nanotubes. Because of it, bundles of carbon nanotubes behave as a loose bunch of individual tubes and not as a compact object. In particular, macroscopic objects like the “bucky-paper” or carbon nanotube fibers [95] are extremely compliant, with the Young's modulus in the low GPa range, due to their weak inter-tube interaction.

The obvious solution to the problem of shearing is to introduce links between the tubes. In the ideal case these links should be covalent carbon-carbon bonds only, because of their high strength. One of the possible ways to achieve this would be to use electron-beam irradiation.

When an energetic charged particle interacts with the atoms of the target, the energy transfer can take place in several mechanisms. They can be divided in two major categories, depending on whether they lead to atom displacements or to excitations:

1. Knock-on effects – lead to atomic displacements
  - atomic displacements in the bulk
  - atomic displacements on the surface (sputtering)
2. Excitations
  - localized electronic excitation or even ionization of atoms
  - collective electronic excitations (plasmons)

- vibrational excitations – phonons (heating)
- bond breaking and/or crosslinking
- secondary emission of photons – visible light or X-rays
- secondary emission of Auger electrons

The cross-sections for these processes behave differently as a function of the incoming particle energy and strongly depend on the target's local structure and electronic properties. In general, with increasing particle energy, excitations decrease in importance, while knock-on effects increase. Cross-sections and transferred energies are higher for heavier particles like ions than for electrons. Excitations are substantial in insulators where ionization can play the dominant role. On the other hand, ionization is strongly suppressed in metals due to conduction electrons that can screen and neutralize ions on the timescale of 1 fs. Radiation damage in metals is therefore limited to knock-on displacements.

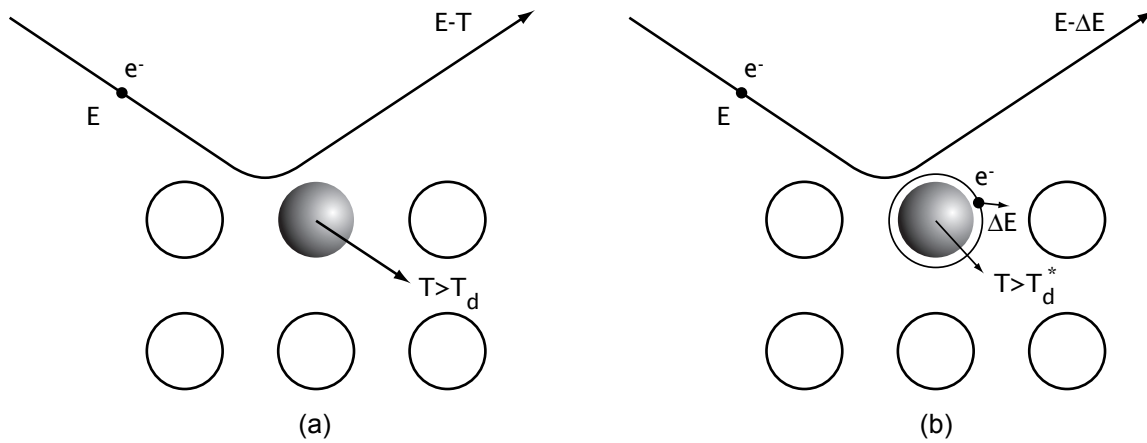


**Fig. 6.1.** Atomic displacement mechanisms by an electron of energy  $E$ : (a) Knock-on, a direct momentum transfer during a collision. The transferred energy  $T$  has to be greater than threshold energy  $T_d$  for the displacement to occur. (b) Radiolysis, in which the incoming electron excites at first the target's electronic states. This excitation can further lead to atomic displacements if the electronic excitation is not screened or relaxed [96].

## 6.2. Irradiation effects on solids

### Excitations

*Phonon excitation* is mainly caused by inelastic scattering of the incoming particles by target atoms. It leads to heating, which is a function of the scattered particle's mean free path. The rise in specimen temperature  $T$  may be calculated by solving the radial form of the differential equation for heat conduction given by:

$$\frac{1}{r} \frac{\partial}{\partial r} \left( r \frac{\partial T}{\partial r} \right) + \frac{1}{\kappa} \frac{j}{e} \left( \frac{dU}{dz} \right) = 0 \quad (6.1)$$

where  $\kappa$  is the thermal conductivity of the sample [96]. For a flat film of uniform thickness, thermally anchored to a good conducting medium at the periphery  $r=s$ , the maximum temperature rise in the centre of an irradiated area of radius  $b$  is

$$\Delta T_{\max} = \frac{i}{e} \frac{(dU/dz)}{2\pi\kappa} \left( \frac{1}{2} + \ln \frac{a}{b} \right) \quad (6.2)$$

As the radiative heat loss is neglected, this calculation represents the upper bound. The temperature rise is proportional to the total incident beam current and not to the current density and there is no sample thickness dependence. The order of magnitude of heat conductivity in carbon films is 0.1 W/mK which gives a temperature rise of 15 K for a total beam current of 30 nA.

*Electronic excitations* such as intraband or interband excitations are in the eV range. They are significant in insulators and to a lesser extent in semiconductors. Excited states can lead to local bond instabilities and rearrangement – a phenomenon called radiolysis (fig. 6.1b). Metals and graphite are immune to this type of damage due to the screening of excited states by conduction electrons.

*Plasmons* are collective electronic excitations. Their dissipation causes heating but little structural damage.

*Ionization* is of importance in insulators and semiconductors where the lifetime of excited electrons is long enough to cause irreversible bond breaking. In metals, ionization is practically instantaneously quenched, on the  $10^{-15}$  s timescale, after which local perturbations in electric charge are removed. The interchange of electrons with the nuclei is slow compared with the spreading of electronic energy, and the dissipation of energy occurs on a timescale which is small compared to the lattice vibration period.

The generation of X-rays or Auger electrons behaves similarly to ionization damage. For light elements such as carbon, Auger dominates over X-ray emission. In carbon,  $K\alpha$  X-ray and Auger excitations lead to an energy loss of the projectiles of 284 eV: the cross-section is lower than for plasmon excitations.

The inelastic scattering cross-section for all these processes decreases slowly with increasing beam energy and increases with the atomic number of the specimen material. No primary damage is caused in metals, but preexisting atomic defects can be affected – for example irradiation-induced recombination can occur.

### ***Knock-on displacements***

Atom displacements by direct momentum transfer occur by collisions of energetic electrons or ions with the nuclei of the target atoms that happen on the typical timescale of  $10^{-21}$  s [96]. On such a short timescale, screening effects of electrons can be neglected. The collision of a non-relativistic electron or ion with a nucleus can be treated using a simple Coulomb potential. The angular dependence of the transferred energy  $T$  in the geometry shown on fig. 6.2 is given by the formula:

$$T(\theta) = T_{\max} \cos^2(\theta) \quad (6.3)$$

where  $\theta$  is the angle between the incoming particle's initial motion and the direction in which the knocked nucleus is scattered.  $T_{\max}$  is the maximum energy which can be transferred in this process in a head-on collision ( $\theta = 0$ , particle is deflected backwards).

Maximum energy transfer from a relativistic particle of energy  $E$  and rest mass  $m$  to an immobile nucleus of mass  $M$  is given by:

$$T_{max} = \frac{2ME(E + 2mc^2)}{(m + M)^2c^2 + 2ME} \quad (6.4)$$

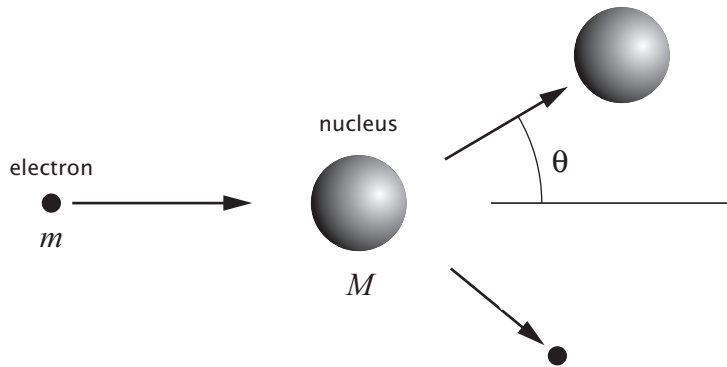


**Fig. 6.2.** Scattering geometry for a light particle of mass  $m$  scattering on an atomic nucleus of mass  $M$ .

The minimum energy transferred to the atom which is required to produce a vacancy-interstitial pair that doesn't spontaneously recombine is called the threshold energy  $T_d$ . This threshold energy depends on the direction of collision with respect to the target's crystal lattice and bond energy. In close-packed structures, the displacement can involve serious perturbation of the bonding of ten or more neighboring atoms, so  $T_d$  can be much higher than the energy of a single bond.

Atomic displacement is possible even with atoms whose energies are below the threshold in some special cases, for example in a two-stage displacement process. In that case, a light impurity atom (e.g. adsorbed hydrogen) struck by an electron displaces a lattice atom in a collision with a high momentum transfer. Another sub-threshold displacement mechanism is surface sputtering, in which surface atoms are ejected under the influence of incoming projectile particles. As the surface atoms are less tightly bound than bulk ones, the corresponding threshold energies are lower. Calculated and experimentally measured values for the displacement threshold in different carbon-based structures are cited in table 6.1.

Material - type of defect	Threshold energy $T_d$ [eV]
Amorphous carbon	10
isolated SWNT (simulation)	17 [97]
SWNT – next to a vacancy (simulation)	15 [97]
MWNT – interstitial creation (simulation)	15 [97]
diamond	30 (lower limit) [98]

**TABLE 6.1.** Threshold energies for the creation of defects in various forms of carbon.



### Displacement cross-section and displacement rate

The atom displacement rate  $p$  (expressed in displacements per atom in second – dpas<sup>-1</sup>) is a function of cross-section  $\sigma$  and beam current density  $j$ :

$$p = \sigma j \quad (6.5)$$

An analytical approximation by McKinley and Feschbach [99] of the relativistic, Mott formula is appropriate for displacement of light elements such as carbon. For an isotropic displacement energy this gives:

$$\sigma = \frac{4Z^2 E_R^2}{m^2 c^4} \pi a_0^2 \left( \frac{1 - \beta^2}{\beta^4} \right) \left\{ \left( \frac{T_{\max}}{T_d} \right) + 2\pi\alpha\beta \sqrt{\frac{T_{\max}}{T_d}} - \right. \\ \left. - (\beta^2 + \pi\alpha\beta) \ln \frac{T_{\max}}{T_d} + 2\pi\alpha\beta - 1 \right\} \quad (6.6)$$

where  $Z$  is the atomic number of the displaced atom,  $E_R$  the Rydberg energy (13.6eV),  $\alpha_0$  hydrogen atom's Bohr radius ( $5.2 \times 10^{-11}$  m),  $\beta = v/c$  and  $\alpha = 1/137$ . It could seem at first sight that  $\sigma$  would increase with increasing atomic number, however due to momentum conservation the energy transfer (equation (6.4)) is lower for heavier target atoms. Only at very high projectile energies ( $E \gg E_d$ ) can a higher displacement rate be expected for heavier atoms. The cross-section  $\sigma$  from equation (6.6) is plotted in fig. 6.3 for the case of carbon, as a function of threshold energy  $T_d$  and electron kinetic energy  $E$ .

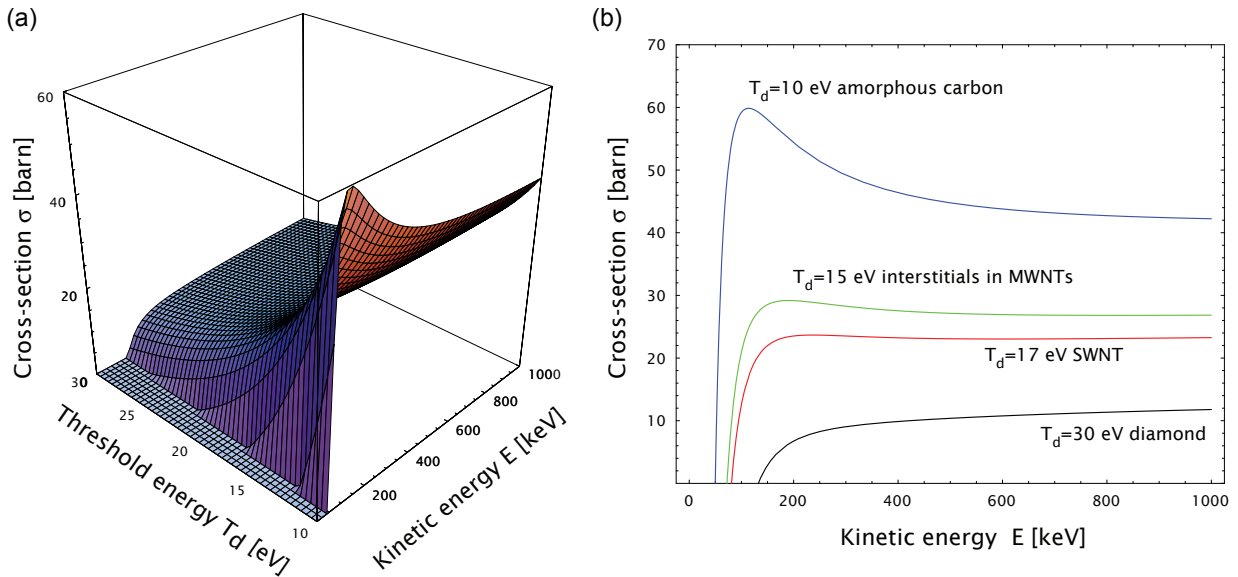


**Fig. 6.3.** (a) Cross-section for elastic scattering of relativistic electrons by carbon atoms according to the McKinley-Feschbach approximation (equation (6.6)) of the Mott formula for scattering. (b) Cross-sections from (a) plotted for characteristic values of the displacement threshold in various forms of carbon. 1barn =  $10^{-28}$  m<sup>2</sup>.

The condition for elastic displacement  $T_{\max} > T_d$  and equation (6.4) on p. 66. will define the minimal kinetic energy  $E_d$  (fig. 6.4) that the incoming electron must have in order to produce irradiation damage.

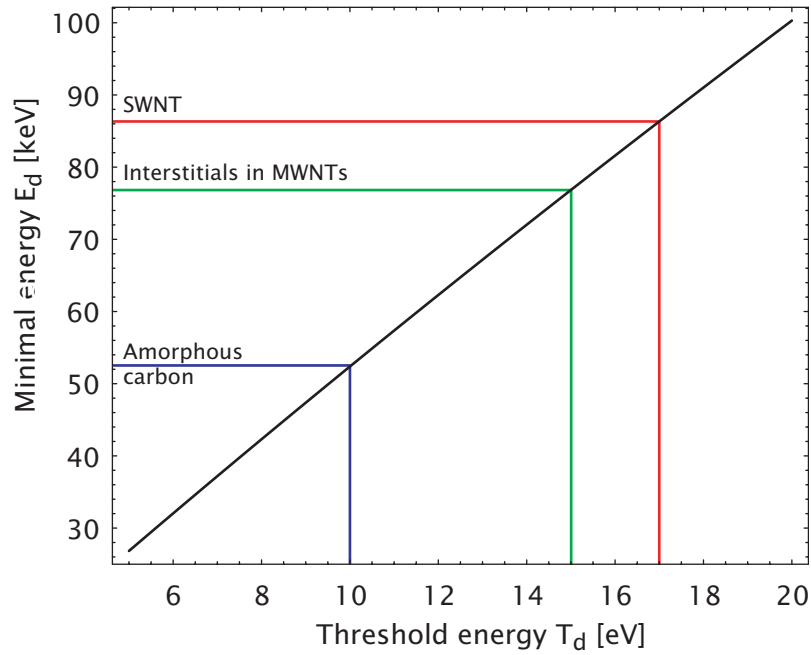


**Fig. 6.4.** Minimal kinetic energy  $E_d$  necessary for ejecting carbon atoms from various forms of carbon.

When the maximal transfer energy satisfies the condition  $T_{max} > 2T_d$ , the ejected atom itself will have enough energy to displace other atoms and cascades will occur. The total number of displacements  $N$  per primary displacement has to be corrected [100] according to:

$$N = \left( 1 + \ln \frac{T_{max}}{T_d} \right) \quad (6.7)$$

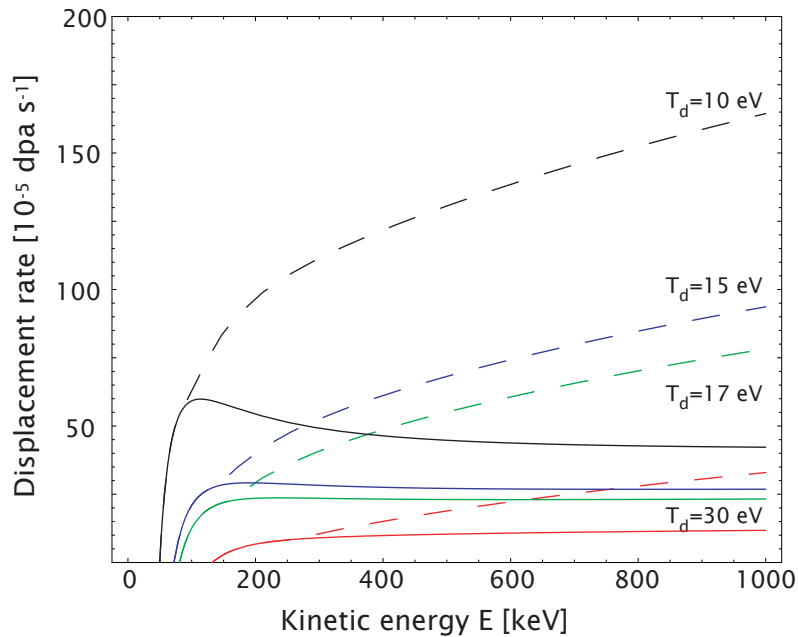


**Fig. 6.5.** Displacement rates of carbon atoms in elastic collisions with incoming electrons of the kinetic energy  $E$ , for different values of displacement threshold  $T_d$ . An electron current of  $1 \text{ A cm}^{-2}$  is assumed. Dashed lines represent the correction due to cascades.

Assuming a current density of  $1 \text{ A cm}^{-2}$ , and a displacement threshold  $T_d = 15 \text{ eV}$ , characteristic for interstitial creation in MWNTs [97], this gives  $9 \times 10^{-5} \text{ dpas}^{-1}$  under irradiation with  $80 \text{ keV}$  electrons. For this value of the displacement threshold, cascades occur above  $144 \text{ keV}$ . Irradiation with  $200 \text{ keV}$  electrons provokes  $40 \times 10^{-5} \text{ dpas}^{-1}$  with and  $30 \times 10^{-5}$  without taking cascades into account.

### 6.3. Irradiation effects on carbon nanostructures

#### Graphite

Graphite is the basic structure underlying carbon nanostructures, and therefore presents the basis for understanding their physical properties, including behavior under particle beam irradiation. Graphite has been extensively studied since 1950s because of its use as a moderator in nuclear reactors. Macroscopic measurements on graphite irradiated using particles like neutrons, protons and electrons revealed several irradiation effects: large strains (growth parallel to c-axis and contraction within the basal planes), increases in c-axis thermal and electrical conductivity. These effects largely result from lattice disorder and structural changes associated with irradiation and depend largely on irradiation temperature, flux, dose and type of source [101].

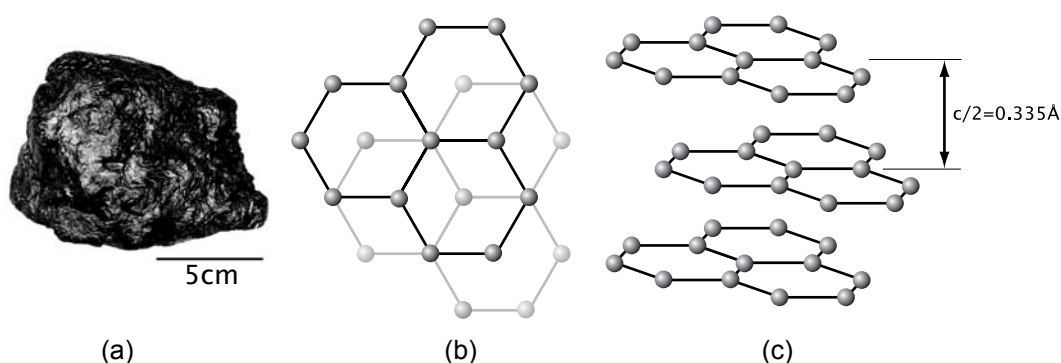


**Fig. 6.6.** (a) A lump of hexagonal graphite (b) Top-view of graphitic basal planes. (c) Sideview of the graphitic structure.

Due to the presence of conduction electrons which rapidly quench ionization and electronic excitations, the behavior of graphite under irradiation is governed by knock-on atomic displacements. Atoms knocked from the graphite lattice by projectile particles produce interstitial and vacancy defects (Frenkel pairs). Because of the large anisotropy of the graphitic lattice, the displacement within the basal planes is difficult, while the displacement into channels between the basal planes is facilitated, with several stable interstitial positions.

Their configuration has been a subject of intense theoretical work during the several last decades. Until recently, it remained unclear whether the interstitial forms covalent bonds to one or both adjacent planes, or if it migrated as an unbound atom between the graphitic layers. Free interstitials have been assumed to have a migration energy of  $0.1 \text{ eV}$  or below, making them mobile even at room temperatures. Two or more mobile interstitials can combine and form a less mobile cluster. This agglomerate can then act as a seed onto which other atoms will bind. Further aggregation pushes the adjacent planes apart and eventually leads to the formation of a new lattice plane, fig. 6.7.

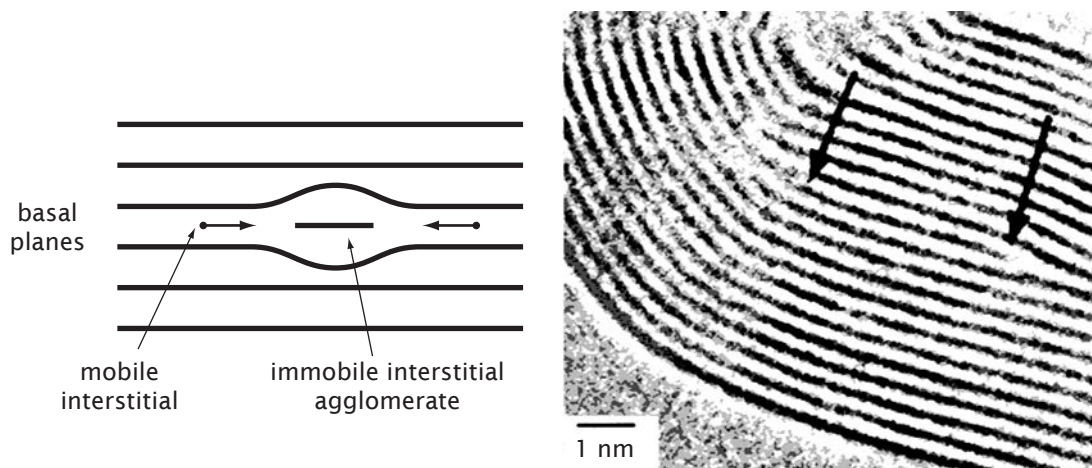


**Fig. 6.7.** (a) Agglomeration of mobile interstitials between the basal planes of graphite. A new plane is eventually created which leads to macroscopically observed swelling of graphite. (b) High resolution transmission electron micrograph showing the appearance of a new plane in an irradiated graphitic nanoparticle [100].

Such agglomeration stops at higher temperatures, above 300°C [102], because of the annealing of interstitial-vacancy pairs due to the increased mobility of interstitials. The jump frequency  $n$  of an interstitial carrying-out thermal diffusion is:

$$n = n_0 e^{-E_M/k_B T} \quad (6.8)$$

With the attempt frequency  $n_0$  having an order of magnitude  $n_0 \approx 10^{14} s^{-1}$  and a migration energy of  $E_M = 0.86 eV$  [103] this gives  $n \approx 3 s^{-1}$  at 50°C and  $n \approx 3 \times 10^6 s^{-1}$  at 300°C. This six-order increase in mobility explains the experimentally observed annealing characteristics.

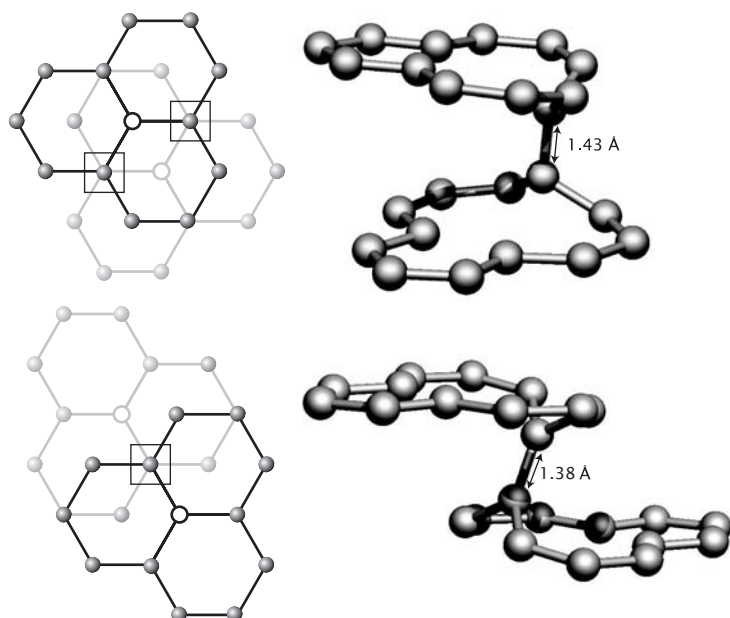


**Fig. 6.8.** Two possible types of crosslink-promoting divacancies in graphite, with their respective spatial models. Possible bonds are shown with squares. Corresponding bond lengths are 1.43Å and 1.38Å [104].

Vacancies themselves were often considered to be planar defects with ideal, threefold symmetry. Recent theoretical modeling based on density-functional calculations has demonstrated that in fact two of the atoms surrounding a vacancy form a weak bond and displace the third neighbor out of the graphitic layer by about 0.7Å [104]. This vertical displacement confers a greater tendency for inter-plane interactions around vacancies. Furthermore, two vacancies from neighboring graphene sheets can join into a metastable divacancy (fig. 6.8) with bridging bonds of 1.43Å and 1.38Å in length. For comparison, the  $sp^3$  bond is 1.57Å long, while the  $sp^2$  bond is 1.42Å

long. Interstitials can also form crosslinks between graphitic layers.

Previous work has shown that the most stable state is that of an interstitial sitting above a bond center, about half-way between the layers, forming two covalent bonds. Another stable state forms when the surrounding lattice is slightly sheared. A fourfold coordinated defect is formed, fig. 6.9. Such a basal shearing will not be spontaneously created within perfectly crystalline graphite, because of the high energy associated with it. Interstitial atoms will more likely be attracted to existing basal dislocation which exist in high densities in most types of graphite [101] with a shift of exactly  $-0.71 \text{ \AA}$ . There are therefore two possible ways of connecting atomic planes within graphite, one involving two vacancies on opposite sides and another with an interstitial atom acting as a bridge.

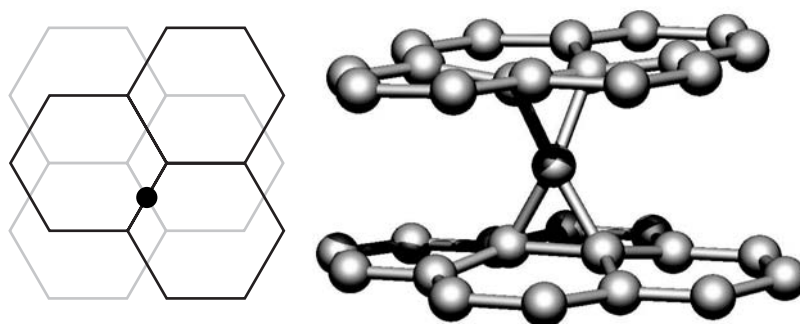


**Fig. 6.9.** The fourfold coordinated interstitial that can occur when the basal planes are shifted by half a bond length ( $-0.71 \text{ \AA}$ ) from their equilibrium configuration [104].

Crosslinking defects of this kind will play an important part in explaining the occurrence of nanotube crosslinking.

### **Formation of carbon onions under irradiation**

Graphitic planes also display a tendency towards bending and curving under irradiation, due to the introduction of pentagons and heptagons into their structure. Under certain conditions, they can even close into spherical graphitic onions, fig. 6.10 [106]. Carbon onions are composed of concentric, spherical graphite layers that form during electron or ion-beam irradiation of amorphous or graphitic carbon. They present one of the earliest examples of building nanostructures using electron-beam irradiation. At temperatures above  $600^\circ\text{C}$ , annealing of radiation-induced defects leads to the formation of coherent shells. The variation in possible sizes is huge: from a two-shell configuration such as  $\text{C}_{60}@\text{C}_{240}$  with a diameter of  $1.4 \text{ nm}$  up to onions with hundreds of shells and diameters in the micron range.

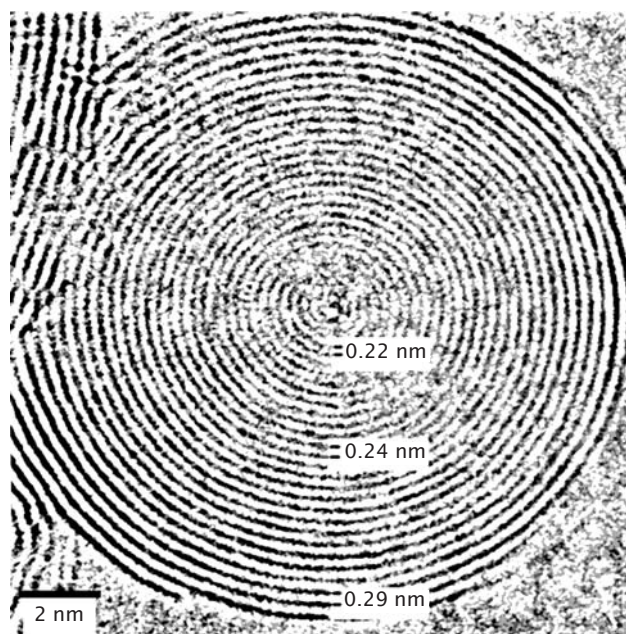


**Fig. 6.10.** A carbon onion formed under electron irradiation at  $700^\circ\text{C}$ . The distance between successive shells increases towards the centre due to increasing pressure [105].

Carbon onions form under electron beam with energies above 100keV, intensities on the order of  $100\text{Acm}^{-2}$  and irradiation times of several minutes [107]. The threshold energy was found to be slightly below 100keV [108], showing that atomic displacements are responsible. Onions that have developed under room-temperature irradiation contain a considerable amount of defects and are not stable under continuous irradiation. At temperatures above  $300^\circ\text{C}$ , in situ annealing prevents the formation of defect agglomerates. Onions with perfectly coherent shells show a decrease in distance between shells that becomes more pronounced towards the centre of the onions. The spacings between the shells are much smaller than those between the layers of graphite ( $0.335\text{nm}$ ). In some cases a decrease, from  $0.28\text{nm}$  close to the surface down to  $0.22\text{nm}$  in the center, has been observed (fig. 6.10). These spacings correspond to pressures that could be on the order of  $100\text{GPa}$ .

When two graphene sheets approach well below the equilibrium distance of  $0.335\text{nm}$ , a change of the bonding character from  $\text{sp}^2$  to  $\text{sp}^3$  is expected. With decreasing distance, more and more  $\text{sp}^3$  interlayer links can be formed, presumably only for a short time and contribute to the mutual attraction of graphene layers. Studies by electron energy-loss spectroscopy indicate that this is indeed the case [109].

### ***Transformation from onions to diamond under irradiation***

Carbon onions that have been self-assembled at elevated temperatures have very regular shells with decreasing interlayer spacing in the middle (fig. 6.10), an indication of increased pressure in their interior. Under prolonged exposure to electron beam irradiation, crystalline diamond starts to nucleate in their center, fig. 6.11. Temperatures above  $600^\circ\text{C}$ , beam intensities in excess of  $100\text{Acm}^{-2}$  and electron energies of at least  $200\text{keV}$  are needed to start diamond nucleation after 1 h of exposure. From these parameters and equations (6.5) and (6.6), assuming a cross section of  $\sigma=20\text{barn}$ , around 50 irradiation-induced displacements in the average are needed until diamond nucleation takes place.

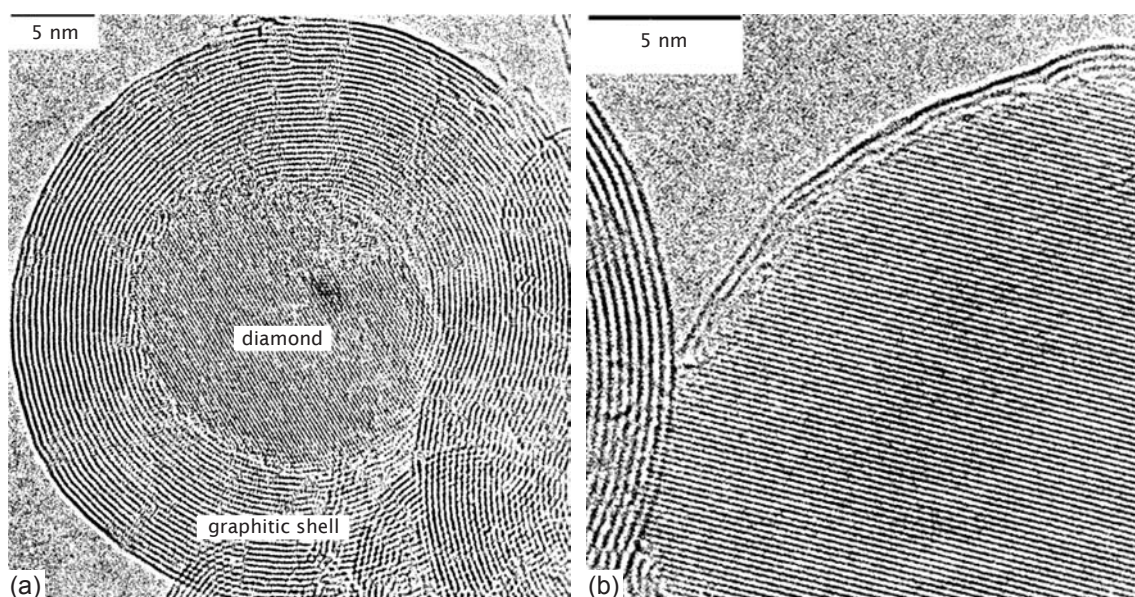


**Fig. 6.11.** (a) A carbon onion with a nanocrystalline diamond core. (b) A diamond crystal formed from a carbon onion. The transformation is almost complete [102].

The nucleation is most probably due to high pressure in the center and is facilitated by the high curvature and decreased distance between the graphitic shells in the center which leads to an appearance of  $sp^3$  bonding between the shells. Once nucleated, the cubic diamond crystals grow at the expense of surrounding graphitic shells while subjected to continuous irradiation [105]. Growth proceeds almost isotropically, without favoring a certain crystallographic direction and continues until almost the whole graphitic onion has been converted to diamond, fig. 6.11b. The maximum size of diamond is therefore only limited by the size of the onion – largest diamonds produced in this way were almost 100nm in diameter.

It has also been shown that this phenomenon of conversion from graphite to diamond is not limited to carbon onions, or even curved graphitic planes. The transformation can be induced by an electron beam even on a simple interface between planar graphite and diamond [110].

### ***Irradiation effects on carbon nanotubes***

In the first years following the discovery of carbon nanotubes in 1991 by S. Iijima [21], most of the research was limited to structural studies using transmission electron microscopes. Very soon, it was discovered that prolonged exposure of carbon nanotubes to the electron beam can lead to irreversible shape changes. Ajayan et al. [111] and Kiang et al. [112] have shown that nanotubes develop ripples and eventually break under intense irradiation.

The most probable mechanism by which isolated single-walled nanotubes damage is by direct, knock-on collisions of incoming electrons with the carbon atoms which break the carbon-carbon  $sp^2$  bonds. Value of the threshold energy  $T_d$  strongly depends on the direction of the incoming electron. Obviously, the smallest value is expected for the radial displacement in the direction perpendicular to the nanotube's surface, and highest for in-plane displacements. According to tight-binding molecular dynamics simulations performed on (5,5) nanotubes, the threshold energy can vary from 17eV for ejections normal to the nanotube's surface up to 43.5eV for ejections that occur in-plane [97]. With such a threshold value, ballistic displacements in the direction perpendicular to the tube's surface are possible with electrons whose kinetic energy is above the threshold value of 86keV [113].

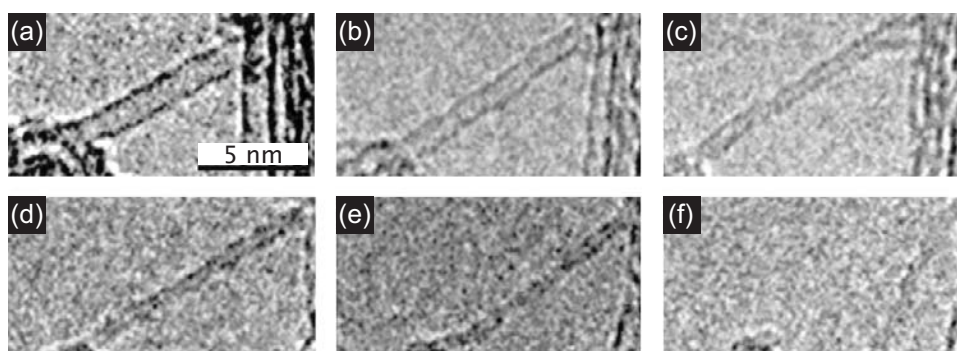


**Fig. 6.12.** An isolated SWNT exposed to a low-intensity ( $1Acm^{-2}$ ) 200keV electron beam. Atom extraction from the surface leads to a series of surface reconstructions in which the nanotube diameter decreases from the original value of 1.4nm (a) to 0.4nm (f) before eventually breaking [114].

Irradiation on carbon nanotubes with particle beams has been shown to provoke structural changes like shrinking and breaking [114], collapse into ribbons [97], coalescence [115], amorphization [116] or junction formation [117]. The fate of nanotubes under irradiation is determined by particle energy, flux and the temperature at which the nanotubes are maintained.

Prolonged exposure of isolated single-walled nanotubes to a low-intensity electron flux ( $0.1\text{--}1\text{ Acm}^{-2}$ ) with the energy of  $200\text{ keV}$  can lead to nanotube shrinking due to atom loss from the tube surface (fig. 6.12) [114]. Atom loss from the nanotube surface creates vacancies which can cluster into larger holes in the structure that are energetically unstable due to a large number of dangling bonds. The system tends to rearrange itself. As a consequence, the tube can shrink from the initial diameter of  $1.4\text{ nm}$  down to  $0.4\text{ nm}$  before eventually breaking after half an hour of irradiation.

Tight-binding molecular simulations of the slow, homogeneous extraction of carbon atoms from the lattice have shown that most of the vacancies heal as two-coordinate carbon atoms (green in fig. 6.13(a)) and try to recombine, forming a highly defective carbon network. The structure eventually rearranges and stabilizes as a disordered  $sp^2$  network around five, six and seven-membered rings, as seen on fig. 6.13(b) showing a  $(10,10)$  nanotube that has lost half of its atoms to irradiation. The cohesive energy of this reconstituted network is reduced by  $0.55\text{ eV/atom}$  compared to a perfect  $(5,5)$  nanotube of the same diameter. A large number of defects is of the 5-7 type (Stone-Wales [59], see also fig. 3.17 on p. 31) which are otherwise formed during plastic deformation of carbon nanotubes [60]. This suggests that they may play a larger role in the way carbon nanotubes respond to external stress and topological changes.

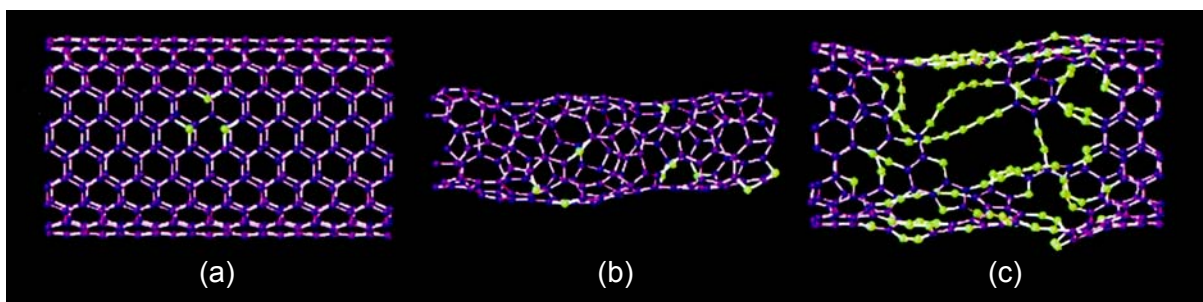


**Fig. 6.13.** (a) A simulated  $(10,10)$  nanotube after an extraction of one carbon atom. Atoms with a coordination number lower than 3 are shown in green. (b) After 200 atoms have been randomly removed, the nanotube's lattice reconstructs and the diameter shrinks. Although the nanotube surface is highly defective, the network is still roughly cylindrical with a mean diameter of  $0.7\text{ nm}$ . (c) A  $(10,10)$  nanotube after an inhomogeneous, fast extraction of 80 carbon atoms. The network is unable to reconstruct into a disordered  $sp^2$ -network as in (b) [114].

When the atom extraction proceeds at a faster rate and in an inhomogeneous fashion, the defective surface is not able to reconstitute as a disordered network, but instead creates linear chains of carbon atoms, carbynes, connecting undamaged regions of the nanotube, fig. 6.13(c). A similar situation can occur when a nanotube is pulled in tension [61].

Nanotubes of sufficiently large diameters, namely multiwalled carbon nanotubes, can respond to irradiation damage by collapsing, indicating a mechanical weakening of their structure. If the irradiation damage is anisotropic, damaged portions of the tube weaken, so that the elastic energy cost of squashing a tube is smaller than the gain in cohesive energy.

Crespi et al. managed to provoke such a structural collapse using electron beams with energies of  $800\text{ keV}$  and fluxes of  $2 \times 10^{19}\text{ ecm}^{-2}\text{ s}^{-1}$  [97]. Essentially the same effect can be reproduced when irradiating the tubes with a  $200\text{ keV}$  electron-beam and an order of magnitude lower flux of  $2.5 \times 10^{18}\text{ ecm}^{-2}\text{ s}^{-1}$  [118]. The electron beam energy therefore doesn't seem to play a crucial role, as long as it's above the threshold value.



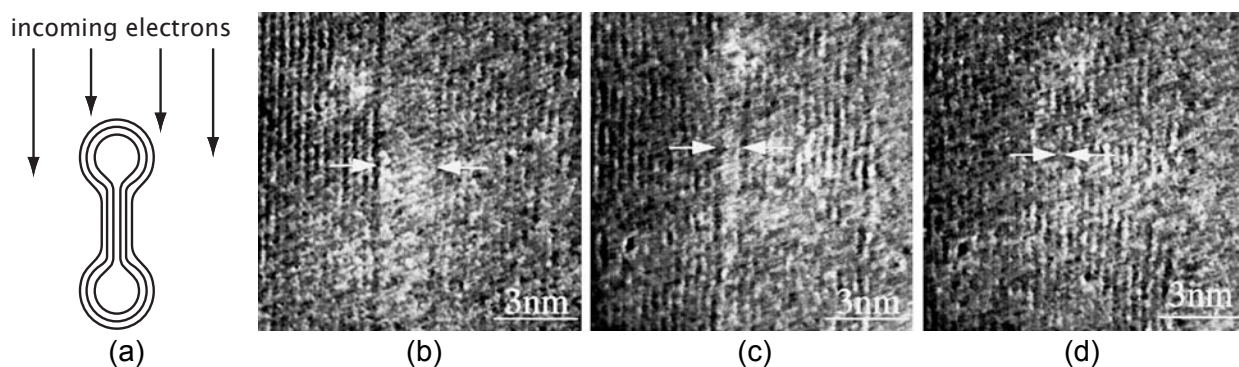


**Fig. 6.14.** (a) Schematic drawing of a MWNT collapse under electron irradiation. Due to anisotropy of the threshold energy, atom extraction and weakening proceeds faster in regions perpendicular to incoming electrons. This provokes gradual squashing. (b) A MWNT irradiated with 800keV electrons after 10s. (c) The same tube after 70s and after (d) 100s [97].

The squashing itself occurs in the direction perpendicular to the incoming beam. Lattice fringes along the sides of the tube remain clear, indicating that the tube damages faster in the regions facing the beam. Tight-binding molecular dynamics simulations have confirmed that the threshold value for knock-on ejections of carbon atoms strongly depends on the direction and angle of ejection, table 6.2 and fig. 6.15. Displacements within the nanotube's plane can cause significant distortions in positions of up to 10 neighboring atoms during the ejection process, so the displacement threshold in this plane is expected to be large, especially when it coincides with a bond direction. In contrast to tangential electrons, an impulse transfer in the radial direction allows the atom to escape with minimum distortion of the local environment. The 17eV displacement threshold in this direction is only moderately larger than the sum of the bonds broken during this process. After moderate damage, a significant amount of atoms is located next to vacancies. Displacement thresholds for all directions are reduced and remain anisotropic. As a consequence the damaging starts to accelerate as the irradiation proceeds. Simulations on double-walled nanotubes, namely a (5,5) tube inserted in a (8,12) tube, indicate that the threshold for  $sp^2$  bond breaking for impulse transfers in the radial direction is 15eV – lower than in the case of an isolated tube. Multiwalled tubes are therefore prone to damage for electron energies above 76 keV (see fig. 6.4 on p. 68).

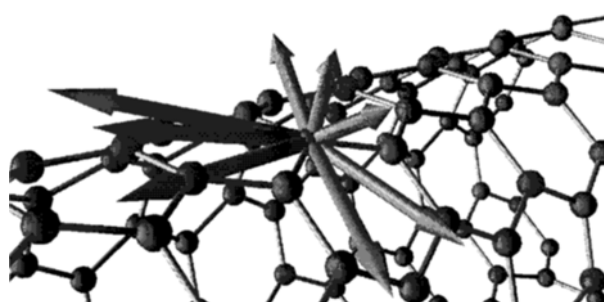


**Fig. 6.15.** Graphical representation of the displacement energy anisotropy for a (5,5) carbon nanotube [97]. Numerical values are given in table 6.2.

Angle $\theta$	Displacement energy [eV]	Displacement energy next to a vacancy [eV]
tangential		
0	>35	15
$\pi/4$	43.5	
$\pi/3$	36	
$\pi/2$	40.5	31
$3\pi/4$	>36	
$5\pi/6$	41	
$\pi$	33	23
radial		
0	17	15
$\pm\pi/4$	19	
$-\pi$	19	

**TABLE 6.2.** Threshold energies for atom ejections from a perfect (5,5) nanotube. Tangential escape refers to directions within the local tangent plane with  $\theta=0$  referring to motion towards the nearest neighbour in the circumferential direction. Radial escape refers to ejections in the plane that slices circumferentially through the tube with  $\theta=0$  referring to the radially outward direction.

When exposed to an electron beam, nanotubes can not only shrink, but also coalesce. The driving force for this process is still the same as in the case of nanotube shrinking: energy minimization through dangling bond saturation. When the tubes are assembled into bundles, coalescence is energetically more favorable because it also minimizes the strain energy, so that the process goes in the direction of diameter increase. Terrones et al. have shown that nanotubes comprising a rope can coalesce when exposed to 1.25 MeV electron beams and heated to 800 °C [115]. Under such irradiation conditions, each carbon atom can be displaced once every 100 s, on the average, implying a current density of 20 A cm<sup>-2</sup>. At this temperature, interstitial carbon atoms created during irradiation are highly mobile, leading to the annealing of vacancy-interstitial pairs, before interstitial aggregates could form. Thanks to this mechanism, carbon nanostructures that have been heated during irradiation exhibit a lower number of defects. Observations of the coalescence process show that they can occur on varying time-scales.

For example, the event depicted on fig. 6.16 occurred faster than the time resolution (0.1 s) of the real-time video camera that was used to record the experiment. Other events, taking place over 10 min have also been observed, giving insight into the intermediate stages of merging. Initially, two tubes coalesce rapidly into a larger cylinder of double the circumference. Subsequently, this coalesced tube establishes a link with a neighboring tube of a smaller diameter. After a while, this bridge develops into a dumb-bell-like configuration. This kind of processes was frequently observed on the edge of the bundle, probably because the coalescence requires free space. Tight-binding molecular dynamics simulations was used to investigate the dynamics of nanotube coalescence. The simulation starts with the creation of 20 atomic

vacancies in two adjacent (10,10) nanotubes, fig. 6.16c. After 100ps, a connection between the tubes is formed, fig. 6.16d, and the structure is annealed via a zipper-like mechanism.

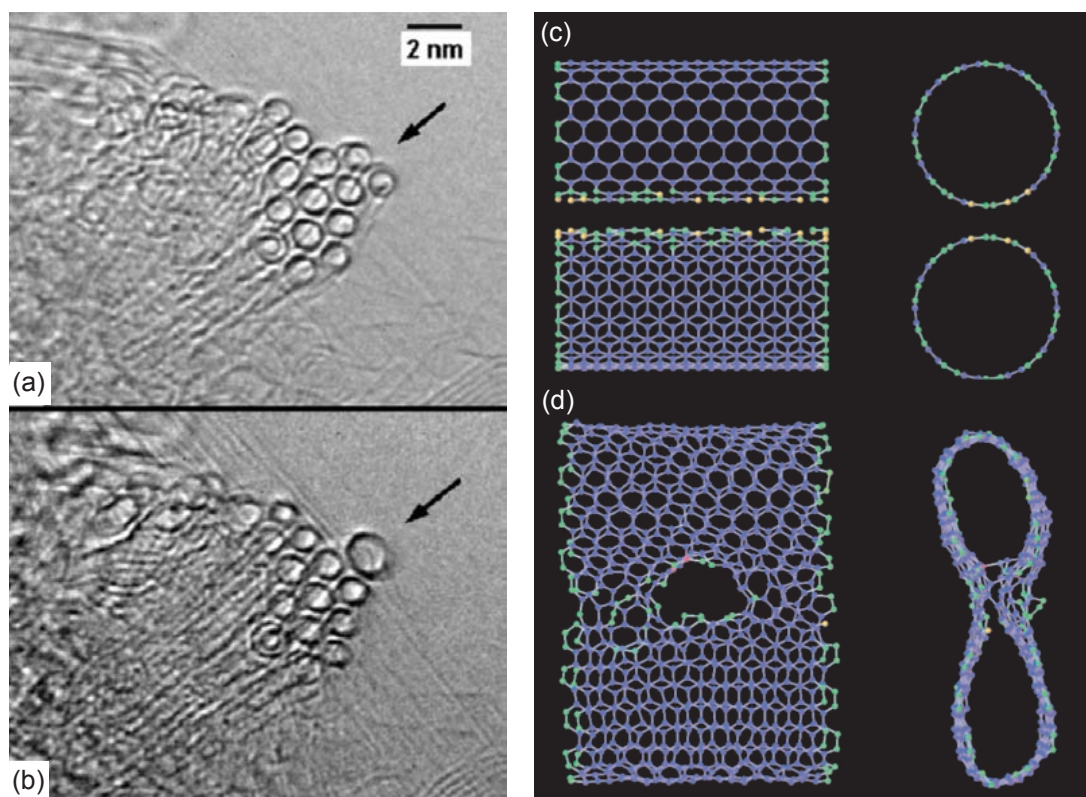


**Fig. 6.16.** (a) HRTEM image of a nanotube bundle before and (b) after a couple of seconds under a high-intensity 1.25MeV electron beam. (c) Molecular dynamics simulation of a coalescence of two (10,10) nanotubes. (d) Formation of a connection between the neighbouring nanotubes and the beginning of the “zipping” mechanism [115].

The coalesced tube still exhibited a few remaining dangling bonds, but the small number of two- and four-coordinated atoms indicates that the annealed network is essentially an  $sp^2$  hexagonal network. Although they have the dominant role, vacancies are not the only type of defects that can lead to nanotube coalescence. Stone-Wales defects [59] (fig. 3.17 on p. 31) can also cause the tubes to approach each other and eventually coalesce.

Nanotube coalescence has also been exploited for building multiterminal nanotube structures. Junctions consisting of a pair of crossed individual single-walled nanotubes were irradiated with 1.25MeV electrons at 800°C with a beam current of  $10\text{Acm}^{-2}$  [117]. After a few minutes of irradiation, their merging was observed at the point of contact, resulting in a structure with the shape of the letter “X”, fig. 6.17. These X-junctions can be further irradiated in well defined spots in order to break-away one of the junctions by sputtering, thus creating “Y” and “T” junctions. However, the tubes in junctions appear defective and electrical characterization of these devices will be needed in order to assess their potential usefulness and the extent to which irradiation induced damage influences the tube’s electronic properties.

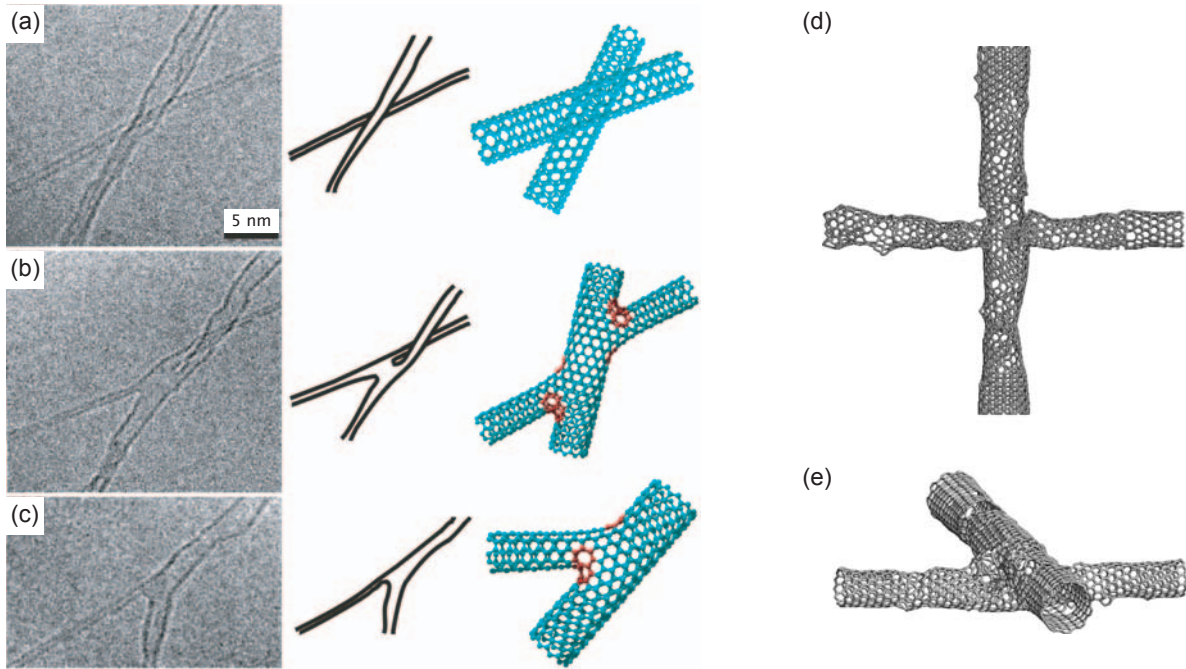


**Fig. 6.17.** TEM images, sketches and molecular models of junctions formed when two crossing nanotubes (a) are irradiated with 1.25MeV electrons at 800°C. Heptagonal rings are shown in red. (b) The same junction as in (a) after 60s of irradiation. (c) After longer exposures to the electron beam, one of the arms has disappeared due to sputtering and a three terminal junction was formed [117]. (d) Molecular model of an irradiated carbon nanotube junction. (e) Sideview of the same model as in (d) [119].

The influence of irradiation on the electronic properties of carbon nanotube bundles was first studied by the Avouris group [120]. Carbon nanotube bundles were irradiated inside a sputtering machine using an  $\text{Ar}^+$  ion beam with an energy of 500 eV. Monte-Carlo simulations predict that  $\text{Ar}^+$  ions can penetrate into carbon nanotubes up to a typical depth of 6 nm. Under the sputtering conditions that were used ( $\text{Ar}^+$  ion flux  $1.5 \times 10^{15} \text{ m}^{-2} \text{ s}^{-1}$  during 20 s), one defect was created per 1000 atoms. Most of the bundle was protected by a mask, except for a 200 nm long exposed area. Gold electrodes were subsequently deposited over the damaged portions of the tube.

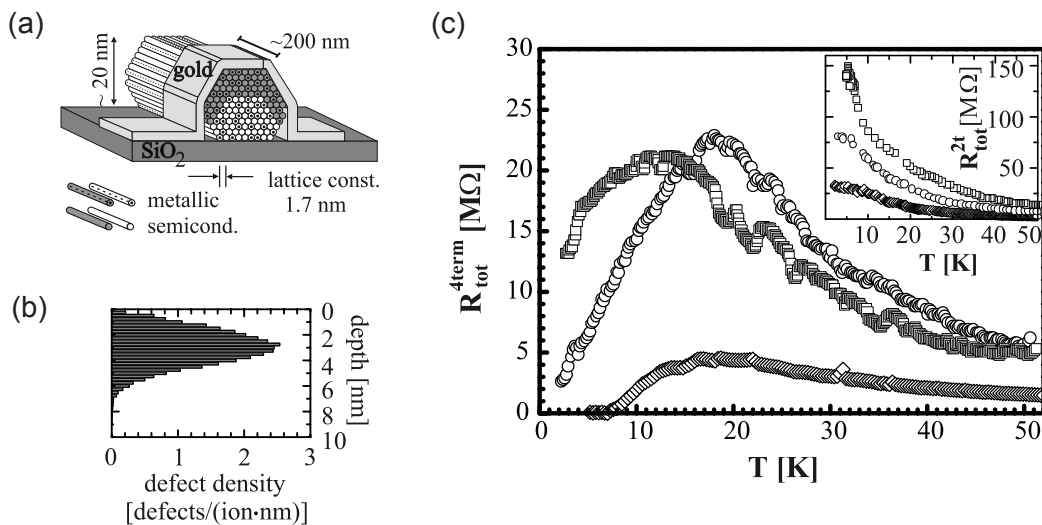


**Fig. 6.18.** (a) Schematic of a section of a rope (a) together with a simulation of the defect distribution introduced by sputtering (b). Shading marks the damaged tubes. Part (c) shows four (4t) and two (2t) terminal resistances versus temperature for three different samples [120].

The structural integrity of tubes was preserved to a high extent, but the electrical resistance of single tubes on the surface was found to have increased by a factor of 1000 – from several k $\Omega$  to several M $\Omega$ .

In this case, the irradiation was used solely to locally increase the electrical resistivity of nanotubes by introducing defects. This setup was then used to study intertube electrical coupling by measuring the two ( $R^{2t}$ ) and four ( $R^{4t}$ ) terminal resistance as a function of temperature. Down to a certain, sample-specific temperature, the current was carried by the damaged metallic tubes at the surface and the resistance was dominated by scattering at defect sites. At the point where the resistance of these damaged tubes became greater than the resistance associated with tunneling between the tubes, the current would start tunneling from damaged into the undamaged tubes in the rope's inside and the overall device's resistance would decrease. From the data, the electrical resistance associated with tunneling was estimated to be in the 2–140M $\Omega$  range. The transfer resistance lied in such a broad range because of a small dispersion in the intertube distance and the exponential dependence of the tunneling resistance on the intertube distance.

Another interesting example of the influence of electron-beam irradiation on carbon nanotubes – though here nanotubes only act as containers – is the coalescence of  $C_{60}$  molecules inside “peapods”, single-walled carbon nanotubes filled with fullerene molecules [121]. They are separated from nanotube walls by the graphitic van der Waals distance of 0.34nm. Neighboring  $C_{60}$  molecules are separated by a distance of approximately 1 nm. When such structures are irradiated with 100keV electrons, the  $C_{60}$  molecules start to coalesce and eventually fuse together forming an inner capsule or sometimes even a whole new nanotube shell [122]. The interlayer distance in such a double-walled nanotube is a uniform 0.3nm. As the bond energy of carbon atoms in  $C_{60}$  is 0.6eV lower than in carbon nanotubes, the coalescence process is much faster than the damaging of the surrounding tubes.

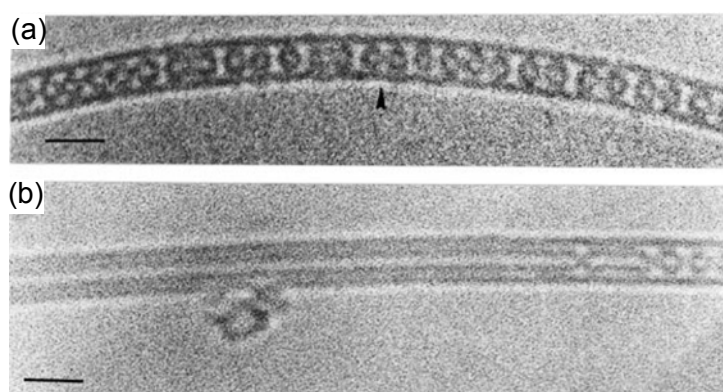


**Fig. 6.19.** (a) HRTEM micrographs of 1.4nm diameter SWNTs that contain a self-assembled chain of  $C_{60}$  molecules. (b) A double-walled nanotube formed after e-beam irradiation. Scale bar is 2nm long [122].

Fullerenes have an even larger tendency towards forming peapods in boron-nitride (BN) nanotubes because of the larger energy gain associated with this process [123]. In this case the  $C_{60}$  molecules also coalesce under electron-beam irradiation, forming a regular carbon nanotube core inside an insulating BN structure.

## 6.4. Results: connecting carbon nanotubes in ropes

### Motivation

Previous measurements of the elastic properties of carbon nanotube bundles have shown that they behave as a bunch of loosely bound individual tubes [72]. Even though each individual nanotube has a Young's modulus ( $E_{Young}$ ) on the order of 1TPa, when they bundle-up into ropes containing hundreds of tubes, they interact with each other only through the van der Waals interaction. As a consequence, when such a rope is deformed, individual tubes prefer to slide with respect to each other, rather than bend, which decreases the efficiency of load distribution over the entire rope diameter. This is reflected in the decrease of the bending modulus ( $E_{bending}$ ), the tube's resistance to bending (defined by equation (6.10) on p. 81) with increasing tube diameter (fig. 6.20).

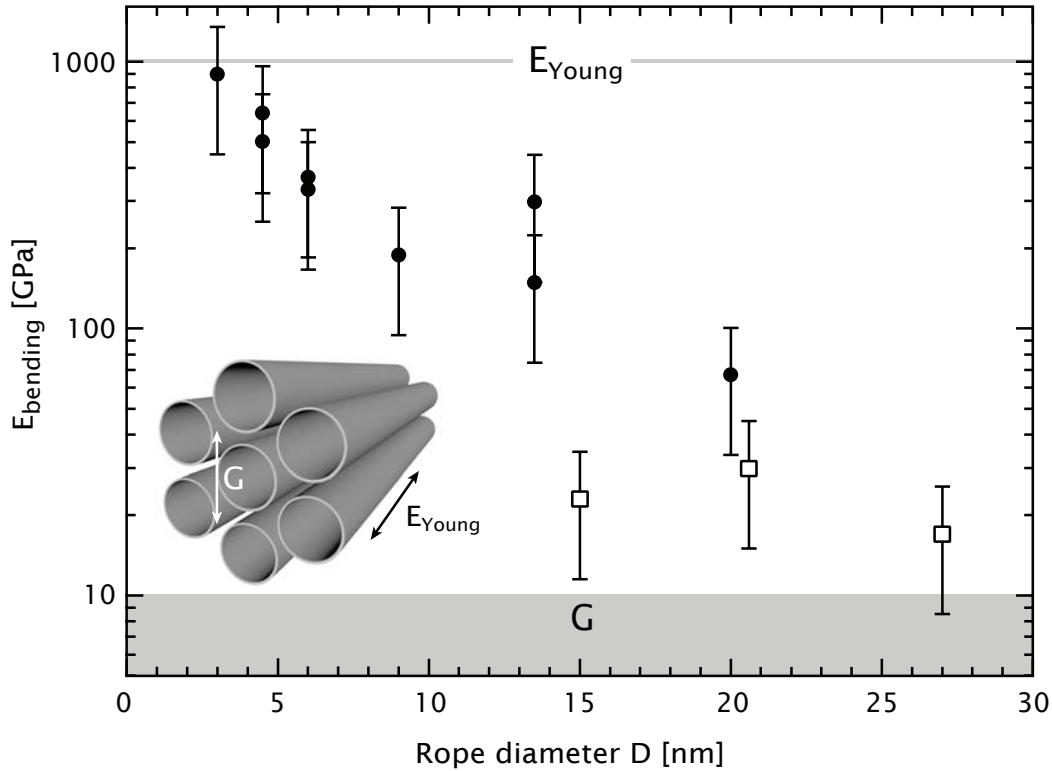


**Fig. 6.20.** Dependence of the bending modulus  $E_{bending}$  of twelve carbon nanotube ropes on the rope diameter. The bending modulus of thin ropes corresponds more closely to the Young's modulus ( $E_{Young}$ ). For thicker ropes, the bending modulus decreases due to sliding between the tubes and approaches the value of the shear modulus ( $G$ ).  $E_{Young}$  can be reached by forming irradiation induced cross-links between the tubes. Open squares show the initial  $E_{bending}$  for ropes used in this study. Black dots represent data taken from [72].

The bending modulus of thin ropes (ideally a single, isolated nanotube) is close to the  $E_{Young}$  of a single-walled carbon nanotube which is 1TPa. As more tubes are added to bundles, the number of tubes contained in the rope ( $N$ ) will increase with the square of the diameter  $D$  ( $N \propto D^2$ ). In the trivial case when the tubes are independent (non-interacting) this means that the bending stiffness  $k$  of the rope would be proportional to  $NE_{Young}$  – hence also increase with  $D^2$ . On the other hand, the bending stiffness  $k$  of homogenous, anisotropic cylinders can be written as:

$$k = \frac{F}{\delta} = 3\pi E_{bending} \frac{D^4}{L^3} \quad (6.9)$$

and therefore scales with  $D^4$ . As a consequence, when the mechanical response of a carbon nanotube rope is modelled supposing that the rope is a homogeneous cylinder, the  $E_{bending}$  will take on an apparent dependence on the rope's diameter. This dependence is purely geometrical in nature and is a direct consequence of the fact that nanotube ropes can't be modelled as homogeneous and isotropic objects. As a first correction, the influence of intertube interaction (or more precisely the lack of it) has to be introduced through the shear modulus  $G$ . The total deformation  $\delta$  of the nanotube bundle under a force  $F$  is then given by the sum of deformation due to beam bending ( $\delta_B$ ) and due to shearing ( $\delta_S$ ) [73] (see also p. 139):

$$\delta = \delta_B + \delta_S = \frac{FL^3}{192E_{Young}I} + f_s \frac{FL}{4GA} = \frac{FL^3}{192E_{bending}I} \quad (6.10)$$

where  $L$  is the tube's length,  $A$  the cross-section,  $I$  the second moment of the cross-sectional area and  $f_s$  a numerical shape factor, equal to 10/9 for a filled cylinder (see also the geometrical model, fig. 4.11 on p. 44). Deflection length  $L$  and the tube's diameter  $D$  are directly measured from the AFM images.

This phenomenon of intertube sliding is, in some respect, analogous to the mechanical behavior of graphite. Single layers of graphite (graphene) have a high interplane modulus. Still, due to the weak, van der Waals interaction between the successive layers, they can easily be peeled off – a phenomenon that enabled the widespread use of graphite in pencils. The same van der Waals interaction is responsible for the apparent weakening of carbon nanotube ropes.

This structural weakness of carbon nanotubes is a serious obstacle in their application as reinforcing elements. It isn't only limited to bundles of single-walled nanotubes. Whenever nanotubes aggregate – be it single or multiwalled – the weak intertube interaction will cause them to easily slide with respect to each other. This is clearly illustrated in the example of macroscopic fibers composed of carbon nanotubes [95]. Very long (hundreds of meters) nanotube fibers can be spun by injecting a suspension of carbon nanotubes in a surfactant solution (for example sodium-dodecyl sulphate – SDS) into polyvinyl alcohol (PVA) (fig. 6.21a). PVA rapidly destabilizes the suspension and a fiber is formed in the direction of the suspension flow.

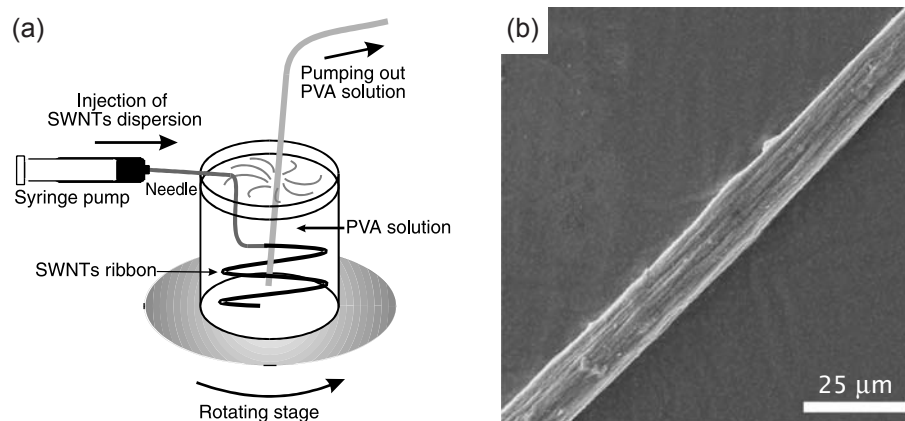


**Fig. 6.21.** Schematic of the setup for producing carbon nanotube fibers. Suspension of purified nanotubes in SDS solution is introduced into a spinning beaker containing PVA. The nanotube suspension is destabilized by PVA and the nanotubes coagulate into fibers aligned with the flow direction. (b) A scanning electron micrograph showing a portion of the nanotube fiber [95].

Carbon nanotubes in such fibers are well aligned with the initial flow direction (fig. 6.21b). Unfortunately, they are connected only via van der Waals interaction or with the help of the intercalated polymer. Their Young's modulus is determined by the intertube coupling and is pretty low – ranging from 15 GPa [95] to 80 GPa [124], depending on the production method (fig. 6.22).

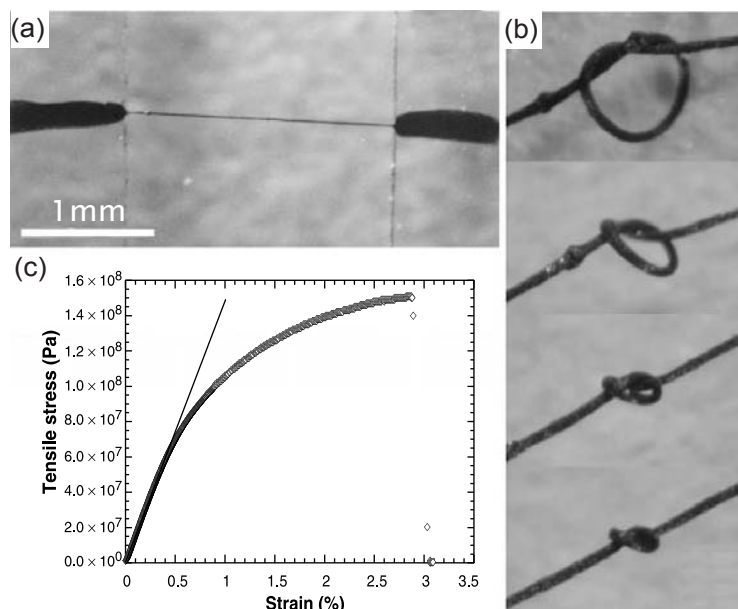


**Fig. 6.22.** (a) A free-standing nanotube fiber. (b) Tying knots indicates the elasticity and strength of the nanotube fiber. (c) Mechanical measurements under tensile loading performed at a strain rate of 1%/min. The modulus deduced at low deformation is about 15 GPa. The fiber exhibits plastic behavior under strong loading [95].

Such low values of the Young's modulus clearly demonstrate the need for finding a reliable way of connecting single carbon nanotubes. If stable connections between carbon atoms could be introduced between neighboring carbon nanotubes in fibers, we would be able to take full advantage of the superior mechanical properties of carbon nanotubes on the macro and not only on the nano-scale. The best mechanical properties would be achieved in the ideal case when the intertube connections would involve only carbon atoms.

Irradiation with charged particle beams was chosen in this thesis as the best possible way of achieving this. At that time, in the beginning of 2000, it seemed less obvious because the results of the Avouris group [120] as well as those of Terrones et al. on nanotube coalescence [115] and junction formation [117] were unknown. Not even after their work was it completely clear in what respect the irradiation damage influences the physical properties of carbon nanotubes.

### ***Experimental setup used in this thesis***

In order to investigate the influence of electron-beam irradiation on the mechanical properties of carbon nanotube bundles, the beam deflection method of Salvétat et al. [72] was applied. Arc discharge-grown carbon nanotube ropes were first mildly purified using HCl and HNO<sub>3</sub> in order to remove any catalytic particles remaining from the production. Subsequent refluxing in H<sub>2</sub>O<sub>2</sub> removed most of the residual amorphous carbon. The purification was mild in order to avoid extensive damage to the tubes, which would have greatly influenced the mechanical measurements.



The method of Salvétat et al. is originally based on deforming carbon nanotubes deposited on a polished alumina ( $\text{Al}_2\text{O}_3$ ) substrate and deforming them using an AFM. Unfortunately, these substrates are rather thick ( $>100\mu\text{m}$ ) and insulating, which posed great difficulties for imaging them in a TEM. In order to avoid problems related to charging and sample thickness, ion-beam milling was used to thin the middle portion of the sample. Nanotubes were then deposited and the thinned region was first scanned using an AFM (Thermomicro M5 [17]) and then a TEM. First results were rather disappointing because the thinned region was too small to contain a significant number of nanotubes. Working with the AFM close to the ion-beam drilled hole was also problematic. The solution to these problems came in the form of nanofabricated  $\text{Si}_3\text{N}_4$  membranes kindly provided by Jürgen Brugger (at that time at the University of Twente, now a professor on EPFL). They were produced by focused ion-beam etching of 500nm thick  $\text{Si}_3\text{N}_4$  membranes.

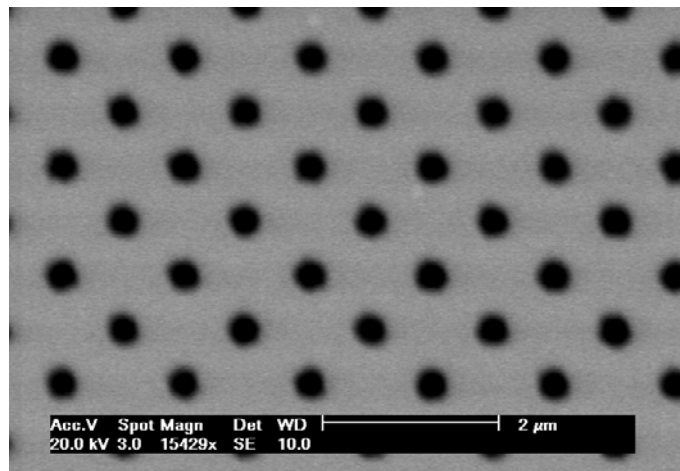


**Fig. 6.23.** SEM micrograph of a  $\text{Si}_3\text{N}_4$  nanosieve produced using a focused ion-beam. The mean hole diameter is around 500nm.

Carbon nanotubes were dispersed in absolute ethanol using ultrasound and deposited on the surface of these  $\text{Si}_3\text{N}_4$  membranes. AFM imaging was performed first, in order to locate tubes suitable for the bending modulus measurements. The sample was then transferred to the TEM for further studies. Locating the same nanotube in TEM and AFM was facilitated by the way the holes were patterned on the substrate, forming a triangular mesh with a distance of  $1\mu\text{m}$  between them. The arrays covered discrete rectangular regions  $100\mu\text{m}$  wide.

### ***Irradiation with 200keV electrons***

TEM and AFM images of the same carbon nanotube bundle are shown on fig. 6.24. TEM imaging gives an additional advantage of checking the tube's morphology for contamination layers and catalytic particles that could influence the mechanical measurements. After the tube has been located, TEM images are taken at low beam intensities. The beam is then focused on the part of the tube bridging a hole. The irradiated area is approximately 500nm in diameter. Electron flux during the irradiation part of the experiment was  $1.35 \times 10^{19} \text{ ecm}^{-2} \text{ s}^{-1}$ , corresponding to a current density of  $2 \text{ Acm}^{-2}$  and a displacement rate of  $8 \times 10^{-4} \text{ dpas}^{-1}$  (assuming a displacement threshold of 15eV, see p. 69). After a typical irradiation time of a couple of minutes, another image of the sample would be taken under low flux and compared to the previous state. The sample would then be transferred to the AFM, and the bending modulus would be measured.

After that, the sample would be returned to the TEM and the whole process repeated. In this way, the same tube could be irradiated and its mechanical properties measured after cumulative, discrete irradiation steps. The TEM part of the experiment was performed using a Philips CM20 TEM on CIME, EPFL.

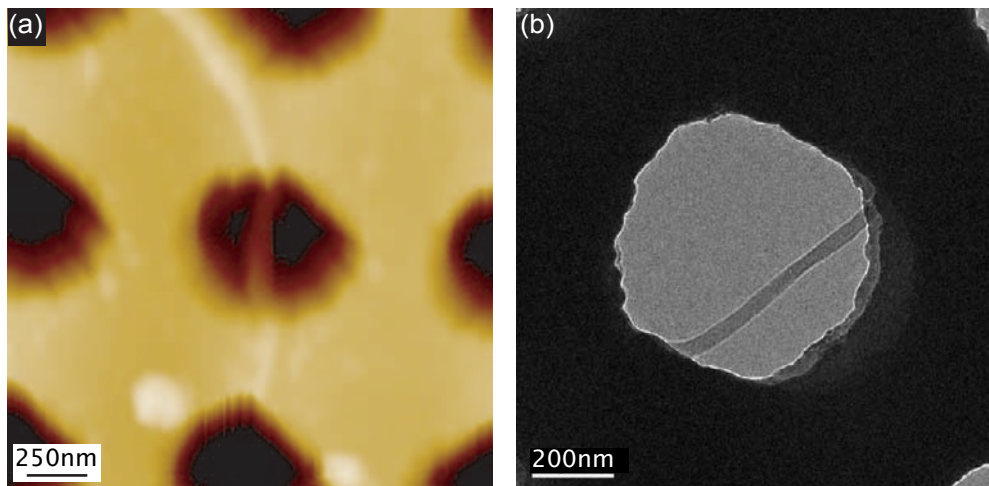


**Fig. 6.24.** (a) An AFM image of a carbon nanotube rope deposited on a Si<sub>3</sub>N<sub>4</sub> membrane. The rope diameter is 21 nm and the suspended length is 603 nm. (b) TEM image of the same nanotube.

TEM images taken at different stages of irradiation (fig. 6.25) revealed to no surprise that tubes become damaged under the electron beam. The measurements of  $E_{bending}$  performed on the same rope (fig. 6.27) reveal a more complex evolution than just a simple amorphisation of the structure. For low dosages, below  $20 \times 10^{20} \text{ e cm}^{-2}$ ,  $E_{bending}$  is monotonically increasing before reaching a plateau or maybe even a peak. The stiffening of the structure is an indication of the appearance of crosslinks between single tubes in the rope. After longer exposures to the electron beam, the radiation damage to the rope finally leads to amorphisation, as seen on TEM images (fig. 6.25). During the entire irradiation, there is a competition between two processes: crosslinking, which increases the shear modulus by introducing stable links between tubes and the damage to the structure which decreases the Young's modulus by introducing defects into the lattice. At sufficiently long exposures, damaging prevails over crosslinking and the rope eventually becomes amorphous.

The precision of measurements unfortunately degrades at high  $E_{bending}$  because of the necessity of using the same cantilever for the force measurements. As the rope becomes stiffer, the slope of the deflection vs. force measurements decreases and approaches the resolution of measurements. This was in fact the biggest experimental problem – not that the stiffening itself was difficult to reproduce from one tube to the other, but that a suitable tube had to be found on which measurements could be performed with reasonable precision and with the same cantilever both in the pristine and crosslinked state.

Another series of TEM images taken under 200 keV reveals in more detail the influence of exposure to the electron beam on the morphology of the carbon nanotube rope (fig. 6.26).

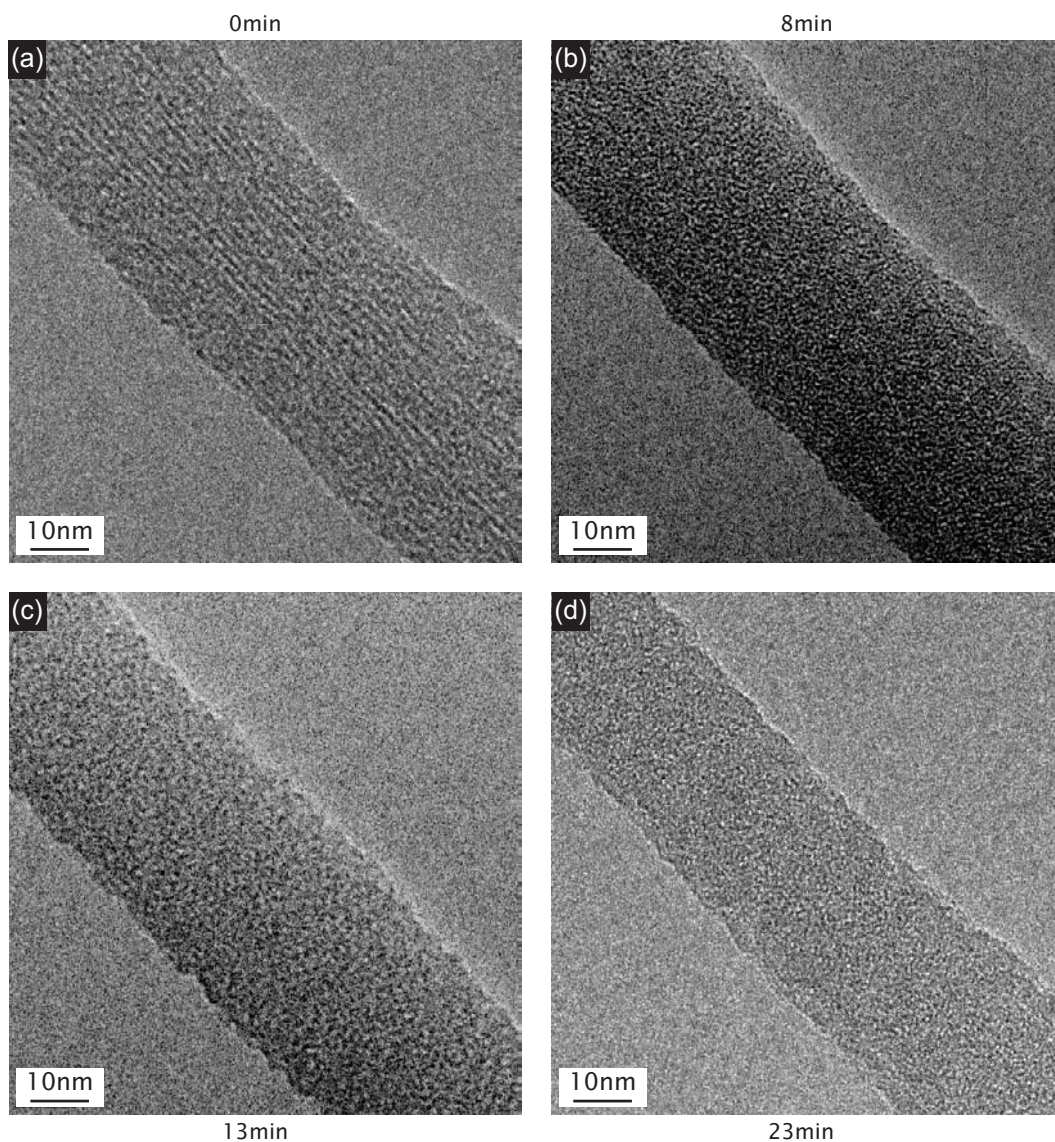


**Fig. 6.25.** The same carbon nanotube rope as on fig. 6.24, after increasing exposure to the electron beam. The initially crystalline rope becomes more and more disordered before being converted into an amorphous fiber after approximately 20 minutes (corresponding to a dose of  $150 \times 10^{20} \text{ ecm}^{-2}$ ).

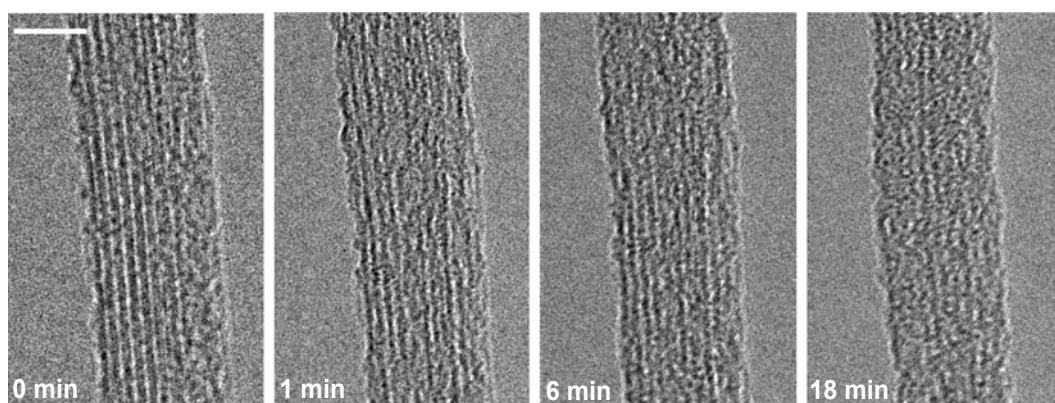


**Fig. 6.26.** Evolution of the morphology of a carbon nanotube rope under intense electron beam irradiation. The acceleration voltage was 200kV with a flux of  $1.35 \times 10^{19} \text{ ecm}^{-2} \text{ s}^{-1}$ . Exposures corresponding to times indicated on the images are (from left to right) 0,  $8.1 \times 10^{20}$ ,  $60 \times 10^{20}$  and  $150 \times 10^{20} \text{ ecm}^{-2}$ . The scale bar is 10 nm long [125].

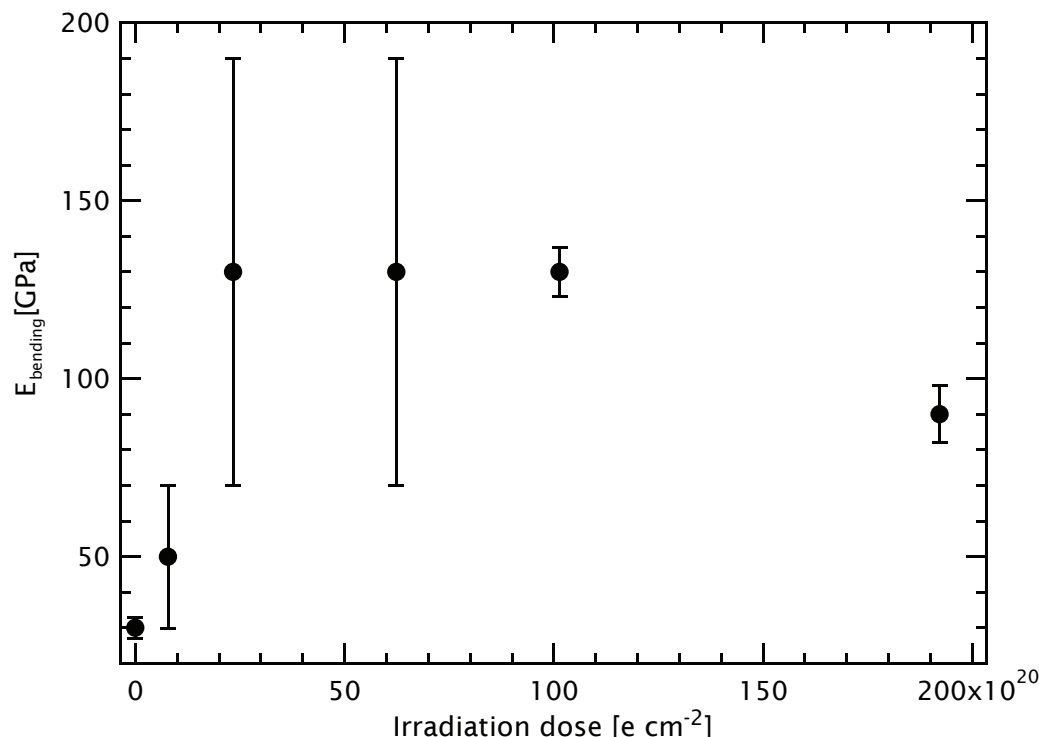


**Fig. 6.27.** Evolution of the bending modulus of a carbon nanotube rope exposed to a 200keV electron beam. The current density was  $2\text{Acm}^{-2}$ . For low doses,  $E_{\text{bending}}$  has increased from 30GPa to 130GPa, indicating the occurrence of crosslinking. Further irradiation decreases the bending modulus due to extensive irradiation damage with the tube eventually becoming amorphous [125].

### ***Irradiation with 80keV electrons***

After successful observation of crosslinking under the influence of 200keV electrons, the mechanisms that could lead to it remained largely unexplained. It was obvious that the process of radiation damage is responsible for the degradation of the  $E_{\text{bending}}$  at high exposures. The nature of crosslinking and its relation to damage was, however not clear. It would be more advantageous if crosslinking was possible to achieve without damaging the lattice. It was also not clear if the crosslinking itself could be reproduced on lower energies without the damage. The crosslinks themselves could have been formed exclusively by carbon atoms, but also from functional groups introduced during the purification. As the intertube distance is equal to  $3.4\text{\AA}$ , twice the van der Waals radius of graphite, it didn't seem plausible that a single  $\text{sp}^3$  bond ( $1.57\text{\AA}$  in diamond) could bridge the intertube gap.

According to the general agreement in the nanotube community based primarily on calculations of Smith et al., carbon nanotubes shouldn't damage under the influence of electrons with energies below a threshold value of 86keV [113]. Using electrons with the energy of 80keV, which is the lowest voltage at which the TEM at our disposal could operate with reasonable resolution, should have eliminated the radiation-induced damaging from the picture.

The experimental setup was identical to that used in the irradiation studies using 200keV electrons, namely a combination of AFM for measurements and TEM for observation and irradiation. Electron flux during the irradiation part of the experiment was  $2.22 \times 10^{18} \text{e cm}^{-2} \text{s}^{-1}$  corresponding to a current density of  $0.4 \text{Acm}^{-2}$  and a displacement rate of  $3.6 \times 10^{-5} \text{dpas}^{-1}$  (assuming a displacement threshold of 15eV, see p. 69)

The first measurement was very encouraging, with a spectacular increase of  $E_{bending}$  from 20 to 750 GPa after only one irradiation session. Further evolution was however quite puzzling at the beginning – the  $E_{bending}$  started to decrease, finally reaching the same value as in the experiment involving 200keV electrons – 90GPa, characteristic for amorphous carbon, fig. 6.28. Corresponding AFM and TEM image of this nanotube are shown in fig. 6.29.

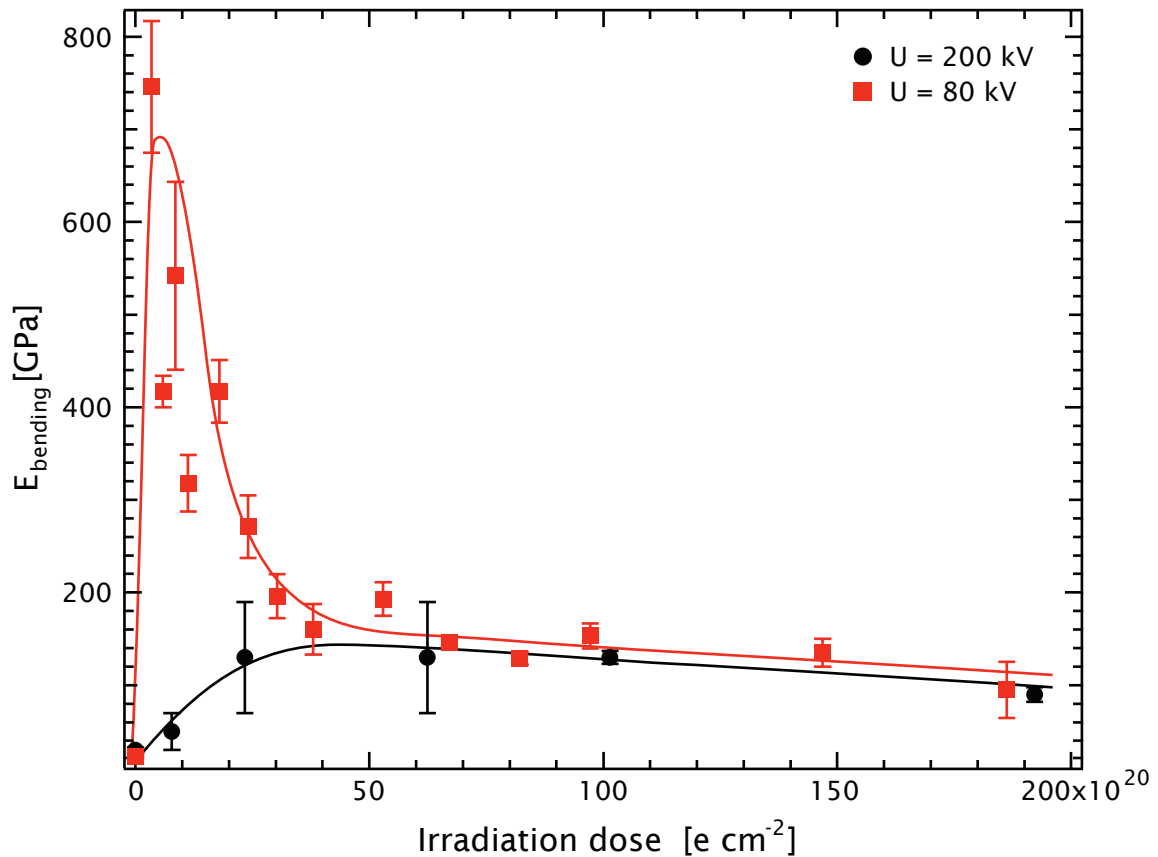


**Fig. 6.28.** Behaviour of the bending modulus  $E_{bending}$  of different carbon nanotube ropes as a function of received dose for two incident electron energies. For 200keV, the bending modulus increases on short exposures due to crosslinking and degrades at higher exposures because of structural damage. The rope irradiated with 80keV electrons shows a much stronger and sharper increase of the bending modulus. Lines are given for clarity [125].

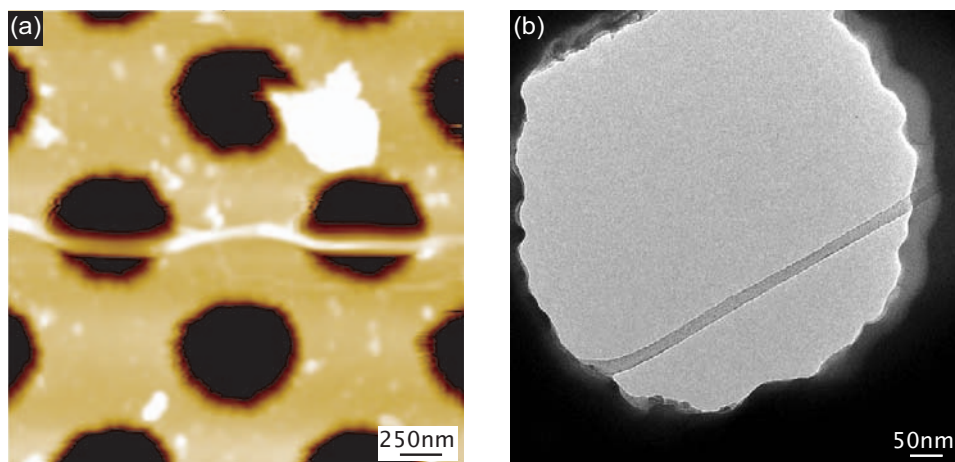


**Fig. 6.29.** (a) AFM image of a carbon nanotube rope spanning two holes on a  $\text{Si}_3\text{N}_4$  membrane. Measurements were performed on the right hole. (b) TEM image of the same nanotube.

According to Smith et al., nanotubes were not supposed to get damaged when using an electron beam with the energy below 86keV [113]. Both the mechanical measurements and the TEM observations (fig. 6.30) clearly show this isn't the case.

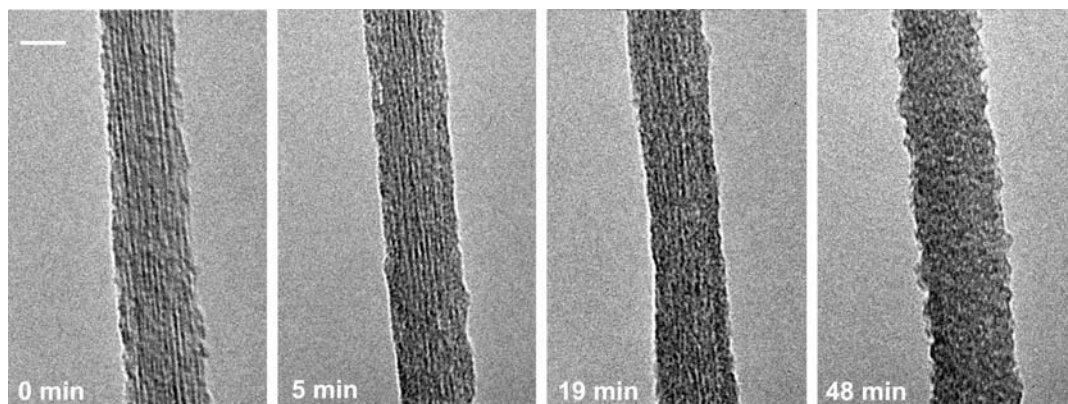


**Fig. 6.30.** Evolution of the morphology of a carbon nanotube rope under intense electron beam irradiation. The acceleration voltage was 80kV and the current density  $0.4\text{Acm}^{-2}$ . Corresponding doses are:  $3.4 \times 10^{20}$ ,  $17 \times 10^{20}$ ,  $67 \times 10^{20}$   $\text{ecm}^{-2}$ . The scale bar is 10nm long.

The carbon nanotube rope got damaged just like under irradiation with 200keV electrons. This 86keV threshold is in reality valid only for ideal and isolated nanotubes without defects. Around defects, the threshold value is lower, due to the lower coordination and the irradiation damaging starts there. Crosslinking introduces local deformations that could also lead to local decrease of the threshold voltage. With every additional crosslink, the area of the tube which is prone to irradiation damage grows and the tube eventually amorphizes. Crespi et al. calculated that the threshold energy for radial displacements in the vicinity of a vacancy is 15eV [97], which corresponds to a threshold voltage of 76.8keV.

Further light on the irradiation-induced crosslinking was shed by Dr. Gábor Csányi (University of Cambridge) who performed simulations using density-functional calculus (DFT) in order to investigate a number of possible bridging configurations.

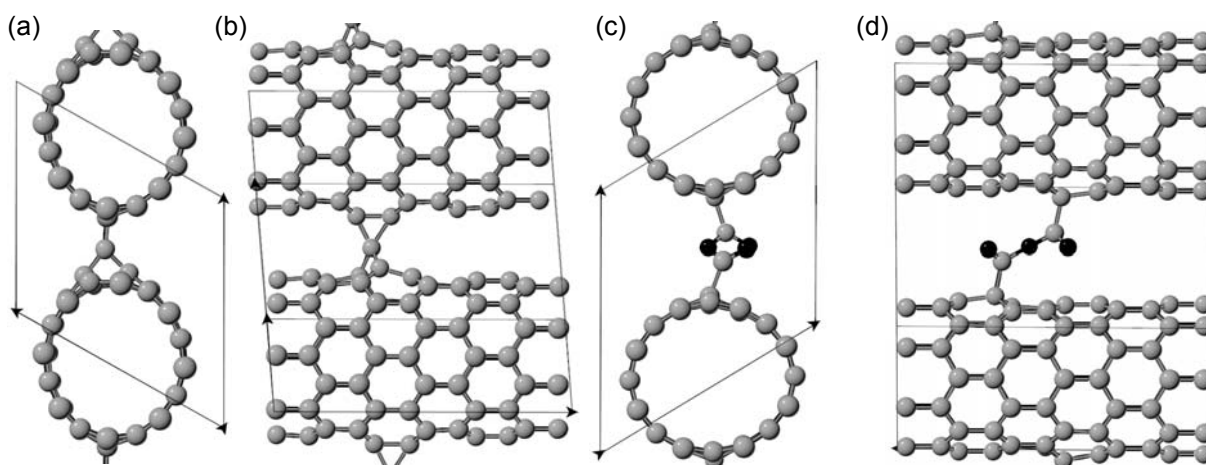


**Fig. 6.31.** Atomic models based on DFT calculations of two different kinds of bridges formed between neighbouring carbon nanotubes. Frontal (a) and side view (b) of a bridge involving carbon atoms formed via a fourfold coordinated interstitial carbon atom. Frontal (c) and side view (d) of an electron-beam irradiation induced chemical reaction between carboxyl functional groups attached to neighbouring nanotubes. Oxygen atoms are shown in black [125].

One possibility for crosslinking is a bridge shown on fig. 6.31a and b, where the connection to the two nanotubes is formed by a fourfold coordinated interstitial carbon atom.

On top, the adatom is on a bond, forming a triangle with angles of  $60 \pm 3$  degrees, and sides of  $1.5\text{--}1.6\text{Å}$ . On the bottom, one of the bonds in the hexagonal network was broken, and the resulting two new bonds are  $1.5 \pm 0.02\text{Å}$  long, with an angle of 88 degrees between them. Two carboxyl groups on neighboring nanotubes can also form a stable crosslink. In the carboxyl bridge shown on fig. 6.31c and d, the C–C bonds to the tubes are  $1.53 \pm 0.01\text{Å}$  long, the C=O bonds are  $1.2 \pm 0.01\text{Å}$  long, and the C–O–C bonds lengths are  $1.38 \pm 0.01\text{Å}$  with an angle of 122 degrees between them. Single carboxyl and hydroxyl groups from which hydrogen would be removed by irradiation did not form crosslinks.

Simulations where carbon nanotubes have been irradiated with  $\text{Ar}^+$  ions [126, 127] also show the possibility of crosslinking via interstitials. Incoming  $\text{Ar}^+$  ion energies were in the  $100\text{--}1000\text{eV}$  range. The maximum energies that could be transferred during collisions with immobile atoms correspond to those of electrons with energies in the  $300\text{keV}\text{--}1.5\text{MeV}$  range. Due to the large mass and size of  $\text{Ar}^+$  ions, the corresponding cross-sections are orders of magnitude larger than in the case of electrons. Their penetration depth is therefore much shorter, on the order of  $10\text{nm}$ . The most common form of defects formed under ion irradiation are atomic vacancies and vacancy-related defects and also topological defects such as Stone-Wales defects [59]. Under low-temperature, low-dose irradiation, vacancies can persist for macroscopically long times. Knocked-off carbon atoms end up as interstitials and give rise to various defects both inside nanotubes and in the inter-tube regions. Some of them act as bridging atoms in the formation of crosslinks, fig. 6.32. Intertube links can also form when the CNT lattice relaxes around vacancies. Both crosslinking mechanisms, via an interstitial atom and with the help of lattice relaxation have been theoretically modelled in irradiated graphite (fig. 6.8 on p. 70) [104].

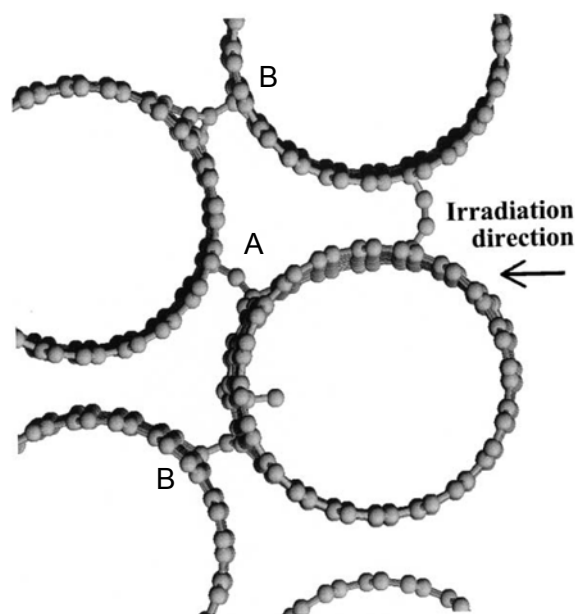


**Fig. 6.32.** A carbon nanotube rope after having been irradiated with  $500\text{eV}$   $\text{Ar}^+$  ions. They can transfer as much kinetic energy as  $1\text{MeV}$  electrons. Intertube links are clearly visible. They can form either via interstitial atoms (A) or through surface relaxation in the vicinity of vacancies (B) [126].

## 6.5. Conclusions

Measurements of the  $E_{bending}$  of carbon nanotubes as a function of irradiation presented in this chapter represent the first measurement of a physical property of nanotubes under irradiation. Both the  $200\text{keV}$  and  $80\text{keV}$  experiment clearly show the appearance of crosslinking between neighboring nanotubes in the rope before amorphization. In the  $80\text{keV}$  case,  $E_{bending}$  reaches  $750\text{GPa}$ ,  $70\%$  of the Young's modulus value of an isolated nanotube. Irradiation of nanotubes was always considered to be a purely destructive process. These measurements show that it could

also be exploited as a remedy for one of the most serious flaws of carbon nanotubes, the weak intertube interaction.

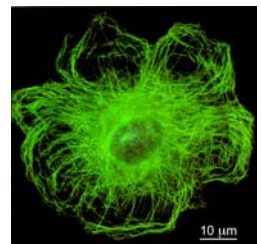
Crosslinking is most probably not due to a local change in atom hybridization from  $sp^2$  to  $sp^3$ , because of a prohibitively large intertube distance. Other possible explanations, corroborated with theoretical modelling include bridge formation via interstitial atoms, lattice relaxation in the vicinity of vacancies and irradiation-induced chemical reaction between functional groups on the nanotube's surface. The latter seems to be less probable, as it requires two chemical groups on opposite nanotubes. The value of 750 GPa for the  $E_{bending}$  also seems to favor bonds that are composed of carbon atoms. Bridge formation as a consequence of lattice relaxation also requires two vacancies on opposite nanotubes. Vacancies are mobile, so they could in principle move on the nanotube's surface until they combine and form a bridge like in the case of graphite (fig. 6.8 on p. 70). By far the most probable way of crosslink formation is by interstitials. They are much more mobile than vacancies, especially at room temperature, and can be created when nanotubes are irradiated using electrons with energies above 77 keV. Simulations show that they can form bridges when in the right position between the tubes, provided they do not recombine with a vacancy first.

These measurements are not only an addition to previous irradiation studies on carbon nanotubes, but also a proof that nanotubes can be crosslinked in this way. The road to industrial and large-scale applications is still long and thorny. Other irradiation sources could be necessary to perform crosslinking on CNT composite ropes. UV light could for example be used to connect nanotubes with intercalated chemical species or gasses. Pure carbon nanotubes could also be crosslinked using radioactive or dedicated cathode-ray sources.



# 7

## *Shear and Young's moduli of microtubules*



### 7.1. Introduction

All living organisms, from the most primitive bacteria to humans are made of cells – the basic unit of living matter. According to the underlying cellular architecture, organisms are divided into prokaryotes (without a nucleus) – bacteria and much more complex eucaryotes (fig. 7.1), with a cell nucleus containing the DNA.

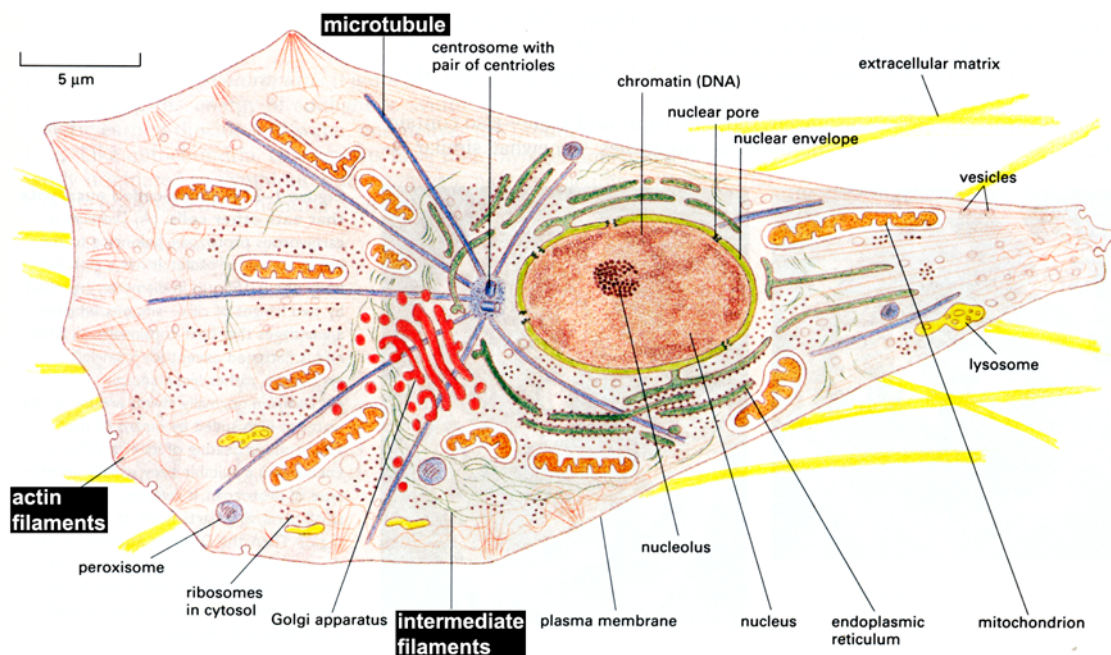


**Fig. 7.1.** Major features of a typical animal eukaryotic cell. Almost the same components are found in plant cells and fungi. Plant cells also contain chloroplasts and vacuols. Their membrane is surrounded by a tough external wall formed of cellulose [128].

Eucaryotes are highly compartmentalized, with specialized structures like the cytoskeleton – a system of protein filaments acting as a mechanical support, and also separate compartments for digestion, secretion, etc.

The supporting structure of eukaryotic cells, the cytoskeleton, contains three major classes of filaments, fig. 7.2, each with a distinct role. Actin filaments are two-stranded helical polymers of the protein actin with a diameter of 5–9 nm and organized into a variety of bundles and networks. Though present throughout the cytoplasm, the cellular interior, they are most abundant just beneath the cellular membrane. Microtubules (MT) are long, hollow cylinders with a diameter of 25 nm, and lengths which can reach tens of micrometers. In living cells, they typically have one end attached to a single structure called a centrosome and located close to the cell's nucleus. They play several vital roles in living cells, like providing mechanical stability, acting as a highly efficient transport network for specialized proteins that can move along them and pulling apart chromosomes containing the cell's genetic material during cell division. From the structural point of view, they are fairly simple polymers of a basic subunit – protein tubulin. Yet, they are already “living” in a sense – they self-organize into networks, grow, shrink and consume energy in the form of GTP (guanosine 5'-triphosphate).

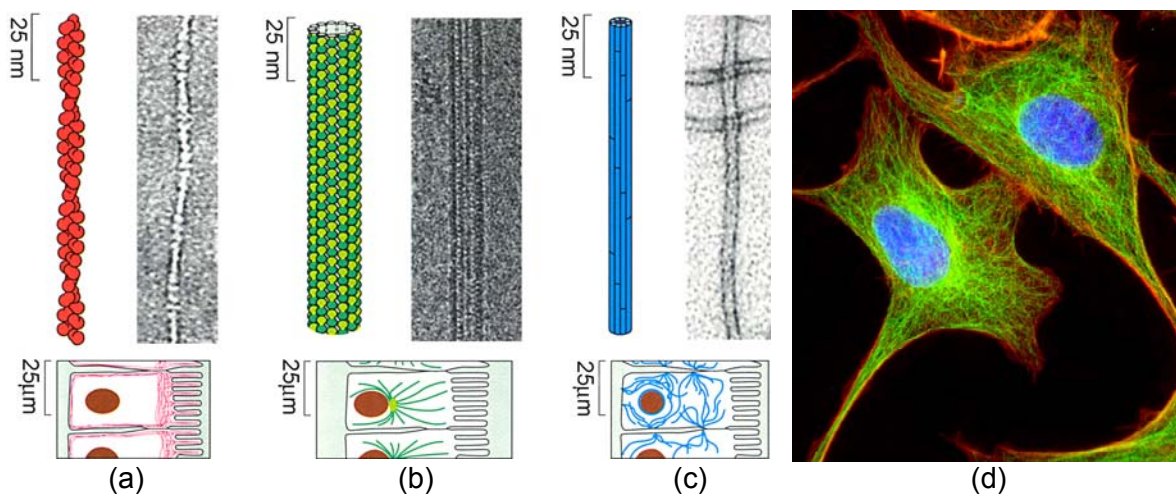


**Fig. 7.2.** Three classes of cytoskeletal filaments. (a) Actin (b) microtubules (c) intermediate filaments [129]. (d) Fluorescently stained epithelial cells. Microtubules are stained green, actin red and the DNA blue [130].

The third cytoskeletal component are the so called intermediate filaments, ropelike fibers with a diameter of around 10 nm. They are made of a whole family of proteins, the intermediate filament proteins such as vimentin and lamin.

The cytoskeletal filaments were first identified by electron microscopy. Since then, the constituent proteins like actin and tubulin have been extracted and chemically purified. Moreover, in relatively simple in-vitro experiments the filaments themselves can self-assemble in a solution of constituting proteins, usually kept at 37°C [131]. Actin and tubulin have also been crystallized and their amino-acid sequences and atomic structures determined.

## 7.2. Microtubule structure

The basic building block of microtubules is the  $\alpha\beta$ -tubulin dimer. These dimers associate head-to-tail to form a linear chain, the protofilament (fig. 7.3). Protofilaments bind laterally, forming a hollow cylinder with a typical diameter of 25nm. The regular head-to-tail longitudinal arrangement of dimers gives microtubules a structural polarity, with two different ends: the plus-end terminated in  $\beta$ -tubulin and the minus end terminated in  $\alpha$ -tubulin. Lateral contacts are formed between  $\alpha$ - $\alpha$  and  $\beta$ - $\beta$  subunits, except for a “seam” of  $\alpha$ - $\beta$  contacts [132]. The dimers are offset by 0.92nm between neighboring protofilaments. In the most usual case, microtubules have 13 protofilaments. However, many other kinds of microtubules have been observed, fig. 7.4e, with the protofilament number varying between 8 and 19 [133-136].

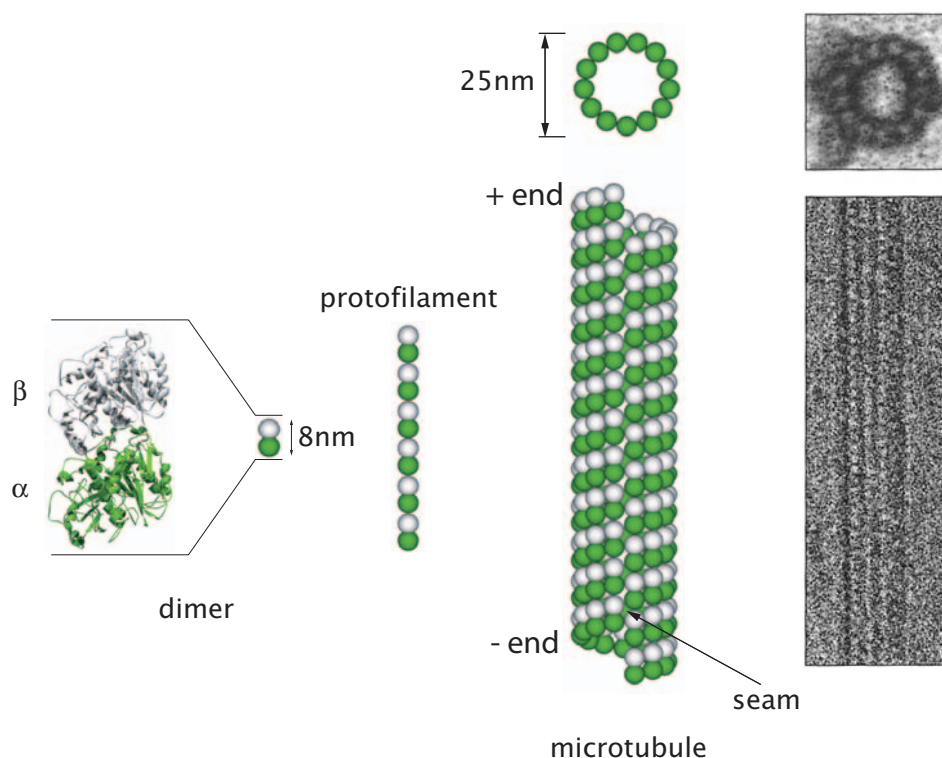


**Fig. 7.3.** (a) The structure of a microtubule and its subunit, the tubulin dimer composed of  $\alpha$  and  $\beta$ -tubulin. Tubulin dimers arrange into protofilaments which form a hollow cylinder – the microtubule. (b) Cryo-TEM image of a microtubule [129].

Different protofilament numbers are often associated with different cell-types – an indication that they might have distinct functions. For example, bovine brain microtubules are almost exclusively composed of 13 protofilament MTs [137], yeast cells have mostly 12 protofilament MTs while the nematode worm *C. elegans* has 11, 13 and 15 protofilament microtubules [135]. Such a diversity of possible lattice configurations is made possible by protofilament skewing, fig. 7.4, so that the lattice continuity is maintained [136]. In the most usual, 13-protofilament microtubule, the lateral path of subunits closes exactly 3 subunits (13:3) above its starting position along the protofilament, giving rise to a 3-start helix organization in which the protofilaments remain parallel to the MT axis. On the other hand, in a 15 protofilament MT, the 3 start monomer helix (15:3) is slightly out of register compared to its ideal position in the 13:3 MT. To correct this mismatch, protofilaments become slightly skewed and “turn” helicoidally around the MT axis (fig. 7.4). Electron microscopy studies have confirmed that significantly

different surface lattices like (14:3) and (15:4) can have essentially the same interprotofilament contacts [138]. This extraordinary ability of the same object, the MT lattice, to accommodate different structures by skewing the protofilaments is indicative of considerable flexibility of the lateral contacts between the protofilaments.

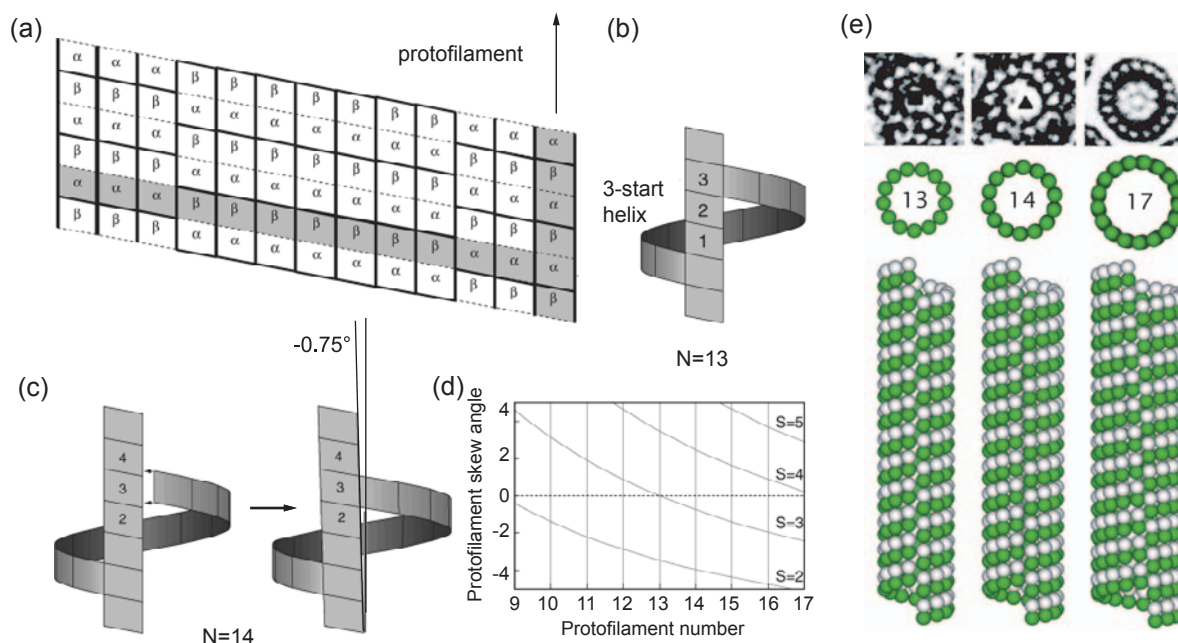


**Fig. 7.4.** (a) Microtubule lattice for 13 protofilaments. Helical representation of a microtubule surface lattice. In a 13:3 microtubule, the left-handed monomer helix closes exactly 3 monomers above its starting position. (c) In 14 protofilament microtubules, the lattice compensates the mismatch by undergoing rotation. (d) Lattice rotation for microtubules with different protofilament and helix start numbers [139]. (e) TEM images and drawings of microtubules with 13, 14, 15 and 17 protofilaments [133].

Microtubules are highly dynamic structures, switching stochastically between growing (with rate  $\sim 1\mu\text{m/s}$ ) and shrinking (with rate  $\sim 10\mu\text{m/s}$ ) which occurs by addition and removal of subunits at the ends of the polymer, both *in vivo* and *in vitro* [140-142], figs. 7.5 and 7.6. Nearby microtubules can grow and shrink independently on each other. As there can be both shrinking and growing microtubules in a given solution or cell, the ensemble as a whole may appear to be in a steady state. The rates and lengths of shortening and growing phases, as well as the frequency of transitions between growth and shortening, depend on factors like the concentration of monomers,  $\text{Mg}^{2+}$  or  $\text{Ca}^{2+}$  ions, GTP, temperature, presence of microtubule-associated proteins (MAP) etc. The behavior of microtubule's ends is radically different: the plus end – terminated in  $\beta$ -tubulin – is more active, with a higher frequency of switching between growing and shrinking, while the minus end (terminated in  $\alpha$ -tubulin) is less active. *In vivo*, this end is connected to the centriole.

Microtubule dynamics was first visualized on the single object-level by Horio et al. *in vitro*, using video enhanced DIC (differential interference contrast microscopy) [140], fig. 7.6. This technique was also used by Fygenon et al. for observing the dynamic behavior of microtubules under a wide range of temperature and tubulin concentration which permitted them to construct a phase diagram of microtubules [141]. For *in vivo* studies, the most widely used technique is fluorescence microscopy [143]. Cryo-TEM studies helped visualize the ends, “caps” of growing and shrinking microtubules. Growing microtubules had straight, blunt ends, fig. 7.5a. Individual, coiled protofilaments could be seen at the ends of shrinking microtubules [144], fig. 7.5b,

indicating that the lateral interaction between the protofilaments plays a vital role in microtubule stability and dynamics.

The time-evolution of a whole ensemble of microtubules can easily be studied by measuring the light absorbance in the UV range, at 340nm, which gives a good estimate of the amount of polymerized tubulin [145]. During in-vitro experiments, microtubules are most often assembled using tubulin dissolved in a buffer at pH 6.9 at a typical concentration of 5mg/ml. The optimal temperature for assembly from mammalian tubulin is 37°C [131].

The dynamic behavior of microtubules is based on binding and hydrolysis of GTP by tubulin subunits. Each tubulin monomer binds one molecule of GTP. The straightening of protofilaments occurs by “zipping” of adjacent protofilaments via lateral contacts, and the effect of GTP hydrolysis could be explained as the “unzipping” of protofilaments by weakening of lateral contacts between them.



**Fig. 7.5.** TEM images of (a) polymerizing and (b) depolymerizing microtubules [144].

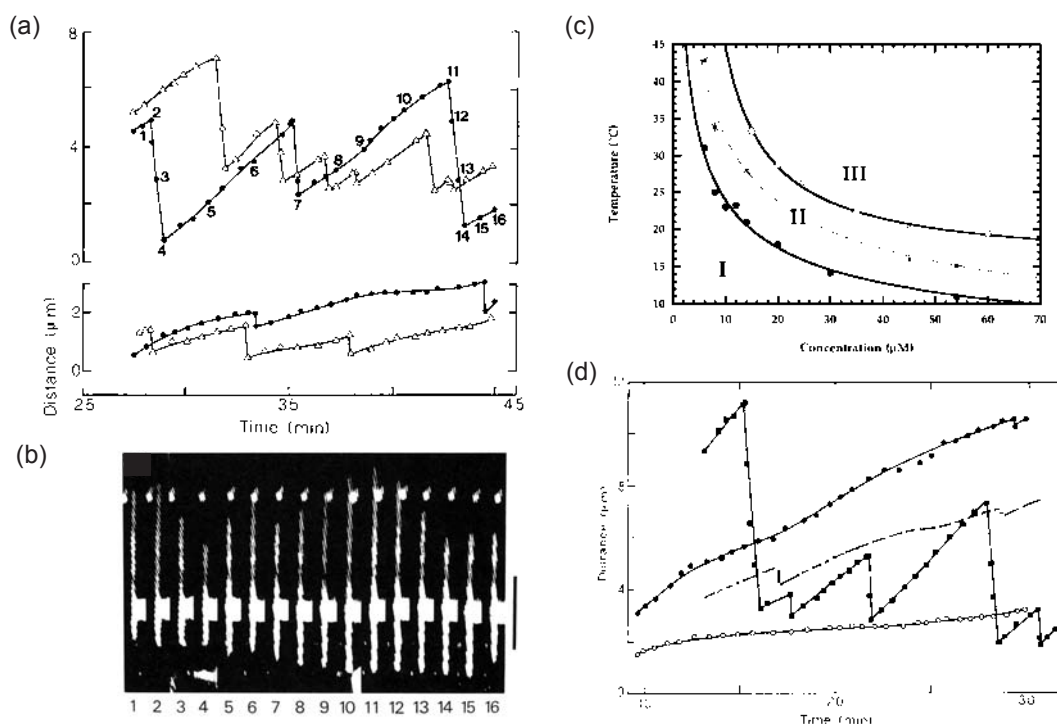


**Fig. 7.6.** Length fluctuations of the plus (above) and minus (below) ends of a dynamic microtubule. (b) A series of DIC microscopy images of fluctuating microtubules [140]. (c) The phase diagram of microtubule assembly. (d) Effect of MAPs on length fluctuations of a microtubule [141]. Filled symbols correspond to the plus end, while the empty to minus ends. Circles are without MAPs and rectangles with MAPs [140].

In vivo, microtubules are often “decorated” by proteins that bind to them. These are collectively called microtubule-associated proteins (MAP). They are responsible for stabilizing microtubules against disassembly and also for the interaction between microtubules and other cellular components.

A very special kind of proteins associated with microtubules and actin filaments are the motor proteins. They bind to the filaments and use the energy derived from ATP hydrolysis to move along them, carrying cargo in form of vesicles or cellular organelles. They can also act as actuators or form superstructures together with their filaments. In the case of microtubules, these structures can propel cells, or pull apart chromosomes. There are two types of microtubule motor proteins: kinesins, moving towards the plus-end and dyneins directed to the minus end.

### ***High-resolution structure of tubulin and microtubules***

There are five classes of tubulin proteins. The two most important are  $\alpha$  and  $\beta$ -tubulin forming the dimer which is the basic building block of microtubules. Other tubulins,  $\gamma$ ,  $\delta$ , and  $\epsilon$  are mostly responsible for microtubule nucleation and replication [146].

The structure of the tubulin dimer was obtained at 3.7 Å resolution by electron crystallography of zinc-ion induced 2D crystals, “zinc-sheets” [147] and refined to 3.5 Å resolution [148]. As the protein structure was obtained from the polymerized form, the crystallographic model included information on the longitudinal and lateral contacts between the dimers. The longitudinal contacts are very similar between monomers within one dimer and between adjacent dimers, while there is a slight difference between  $\alpha$ - $\alpha$  and  $\beta$ - $\beta$  lateral contacts. Each tubulin monomer is a compact ellipsoid of approximate dimensions 46×40×65 Å (height, depth and width).

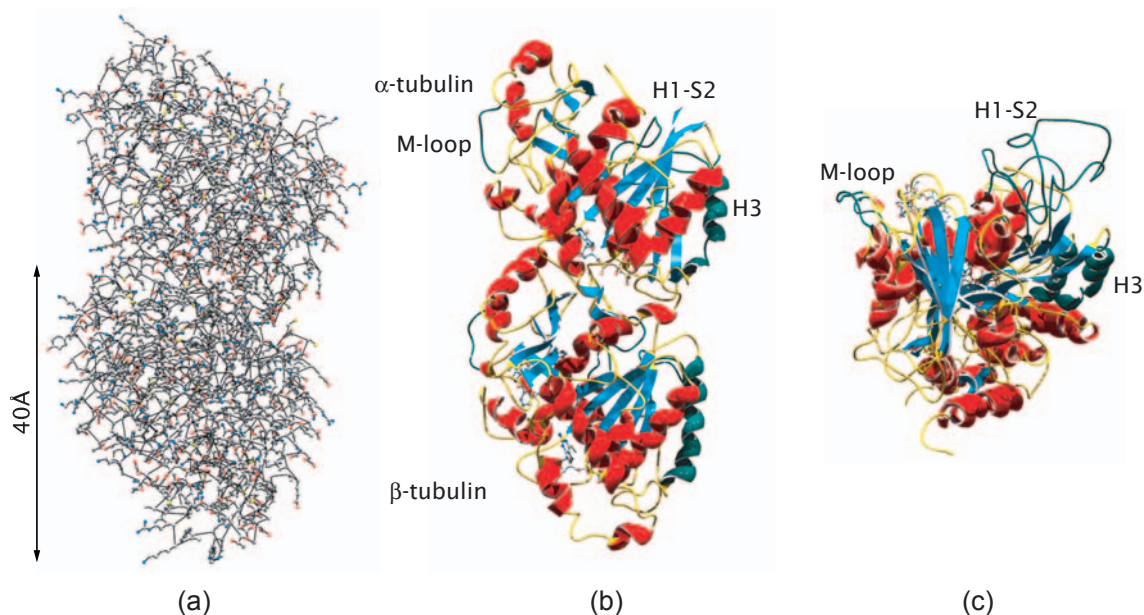


**Fig. 7.7.** (a) The atomic structure of the  $\alpha\beta$ -tubulin dimer. (b) The corresponding ribbon diagram of the  $\alpha\beta$ -tubulin dimer. Structural elements participating in lateral contacts between the protofilaments are colored green. (c) Top-view of the  $\alpha\beta$ -tubulin dimer [147-150].

By docking the structure of tubulin into a 20Å density map of the microtubule, a model has been obtained showing how the crystallographic tubulin model [147] is positioned and oriented in microtubules. This has also enabled identifying regions of lateral and longitudinal contact between the dimers. The fitting was later improved using 14Å [138] and 8Å [150] reconstructions of the microtubule’s surface.

The microtubule’s surface is characterized by protofilaments composed of practically indistinguishable subunits. Protofilaments are separated by deep grooves with holes in the microtubule’s surface, having a 10Å diameter, fig. 7.8.

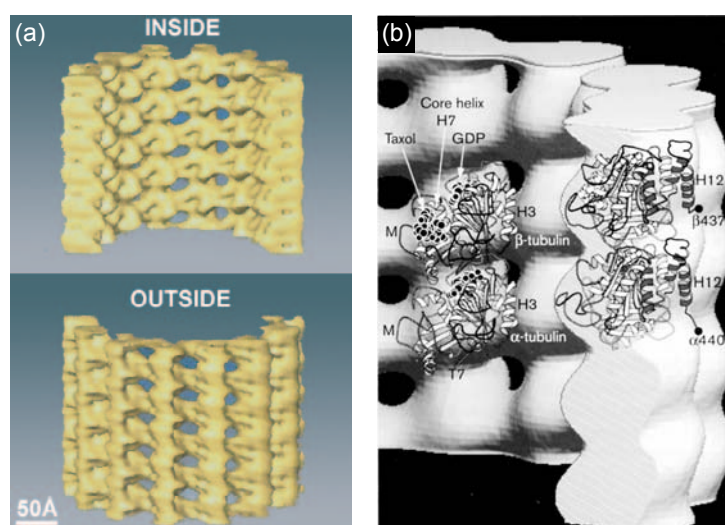


**Fig. 7.8.** (a) 3D reconstruction of the microtubule's surface based on cryo-TEM images [138]. (b) 3D structure of the tubulin dimer superimposed on a 20 Å resolution surface reconstruction of a microtubule [151].

Longitudinal interfaces between the tubulin subunits are topologically very similar. They are very extensive and complementary in shape, with a total surface of about  $3000\text{Å}^2$  completely buried upon the dimer formation and polymerization. Van der Waals interactions are therefore important. Both polar and hydrophobic interactions contribute to the binding between the monomers inside a dimer and between the dimers, with the intradimer interaction having a small electrostatic component. The intradimer interaction is therefore stronger than the interdimer one. Lateral contacts between protofilaments are dominated by the interaction of the M-loop with the helix H3 and a part of the H1-S2 loop, fig. 7.7b and c. Based on residue charges in those regions, the interaction is likely to involve an important electrostatic contribution [149]. Almost all cold- and temperature-sensitive mutations localize on the polymerization surfaces, both longitudinal and lateral [152]. Lateral interactions are therefore central in explaining the dynamic instability of microtubules.

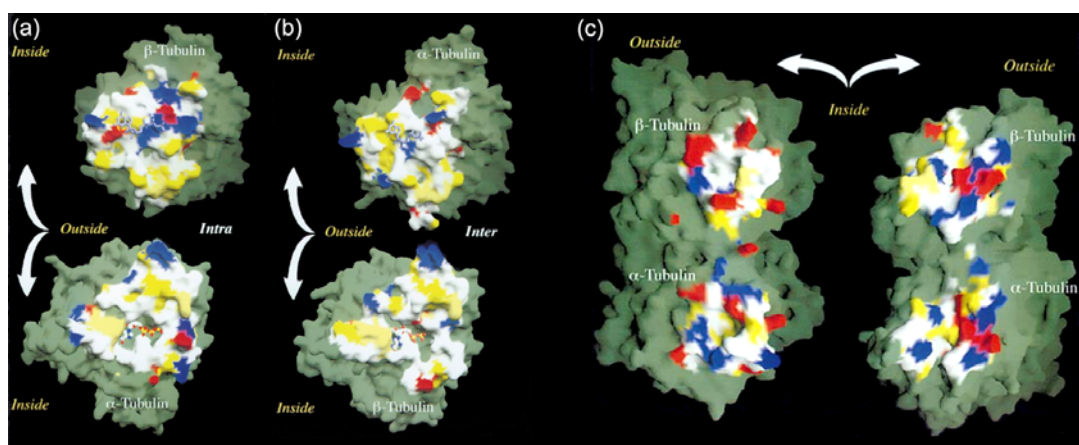


**Fig. 7.9.** Contact surfaces between the monomers [149]. The interacting surfaces are colored according to their charge character: blue negative, red positive and yellow for hydrophobic residues. Longitudinal contact interfaces (a) within the dimer (b) between dimers. (c) Lateral contact interfaces.

### 7.3. Review of previously published results

The complex dynamics of microtubules and other cytoskeletal elements plays a key role in cell division, motility, and determination of cell shape. Their elastic properties and interaction with the cell membrane are crucial in understanding cell morphology. Quantifying the mechanical properties of microtubules would directly provide necessary parameters for modelling and explaining the mechanical properties of cells, and structures like sensory hair cells and sperm tails. Precise measurements of the Young's and the shear modulus could also provide deeper insight into structural changes provoked under the influence of various physical conditions such as temperature or chemical agents, for example drugs like the anticancer drug taxol.

Experimental attempts at determining the elastic properties of microtubules date back to 1983 [153]. In spite of increasing level of sophistication, there are many conflicting results available in the literature.

Almost all the previously published papers report the elastic properties of microtubules in terms of flexural rigidity. The authors also suppose that microtubules can be modelled as elastic, isotropic cylinders in order to model microtubule deformation. In that case, the flexural rigidity would be a real material property, independent of length and could be written in terms of  $EI$ , where  $E$  is the Young's modulus and  $I$  the second moment of the cross-sectional area. In order to facilitate comparison between the results of this thesis, the Young's modulus was calculated by dividing the reported values of flexural rigidity by  $1.67 \times 10^{-32} \text{m}^4$ .

#### **Thermal fluctuations**

The history of mechanical measurements on microtubules began in 1983, when Mizushima-Sugano et al. [153] analyzed dark-field microscope images of microtubules deposited from a solution onto coverslips. Microtubules were modelled as flexible polymer chains undergoing thermally induced fluctuations in shape. The mean-squared end-to-end distance  $\langle R^2 \rangle$  of a chain is related to its contour length  $L$  as [154]:

$$\langle R^2 \rangle = 2 \frac{e^{-\lambda L} - 1 + \lambda L}{\lambda^2} \quad (7.1)$$

where  $\lambda$  is the inverse of the characteristic length determined by the flexural rigidity  $\varepsilon$  and the temperature  $T$  as:

$$\lambda = \frac{k_B T}{2\varepsilon} \quad (7.2)$$

with the Boltzmann constant  $k_B$ . The assumption that adsorbed microtubules can be modelled as semiflexible chains is a very brave one, as it implies that upon adsorption the whole chain gets stuck to the surface at the same time. In a much more realistic depiction, the binding of the microtubule would start at the portion that comes into contact with the coverslip and then proceed during a certain time in which the nonbound portions would undergo Brownian movement. There could also be other sources of microtubule bending like convective currents in the liquid.

Furthermore, the authors assumed that there was no sliding between the protofilaments and therefore, the flexural rigidity could have been written as  $EI$  where  $I$  is the second moment of



inertia of the cross-section. This gave a typical value of the Young's modulus of microtubules  $E=100\text{MPa}$ .

Thermal fluctuations in microtubule shape were also used by Gittes, Mickey and Howard [155, 156] to measure the Young's modulus of microtubules. A solution containing microtubules was squeezed between two coverslips with a distance between surfaces that was smaller than  $3\mu\text{m}$ . Images of thermally fluctuating microtubules were recorded using a dark-field optical microscope and digitized. The microtubule shape was parametrized as the local tangential angle  $\theta(s)$  at every point  $s$  along the arc length. The shape  $\theta(s)$  can be Fourier-decomposed into vibration modes:

$$\theta(s) = \sum_{n=0}^{\infty} \theta_n(s) = \sqrt{\frac{2}{L}} \sum_{n=0}^{\infty} a_n \cos\left(\frac{n\pi s}{L}\right) \quad (7.3)$$

where  $L$  is the microtubule's length. Up to three modes could be resolved, each giving an independent result on the flexural rigidity. Fig. 7.10 shows an example of such a decomposition.

The equipartition theorem, which states that each harmonic mode has a mean energy of  $1/k_B T$ , implies that the mean square vibration amplitude of the  $n$ -th mode will be:

$$\langle (a_n - a_n^0)^2 \rangle = \frac{k_B T}{EI} \left(\frac{L}{n\pi}\right)^2 \quad (7.4)$$

where  $a_n^0$  denotes the vibration amplitude in the absence of applied or thermal forces, and is zero if the relaxed filament is straight.

The thermal bending of flexible polymers is commonly discussed in terms of the three-dimensional persistence length  $L_p = EI/k_B T$ , which is the arc length above which the angle  $\theta(s)$  becomes uncorrelated:

$$\langle \cos \Delta\theta(s) \rangle = e^{-s/L_p} \quad (7.5)$$

Using equation (7.4), the persistence length can be written as:

$$L_p = \frac{L^2}{n^2 \pi^2 \langle (a_n - a_n^0)^2 \rangle} \quad (7.6)$$

The microscope and the imaging system also contribute to the variances with their own noise, effectively displacing each point on the filament by a random distance  $\varepsilon_k$ . The measured mean square vibration amplitude will then be:

$$\langle (a_n - a_n^0)^2 \rangle = \left(\frac{L}{n\pi}\right)^2 \frac{k_B T}{E_y I} + \frac{4}{L} \langle \varepsilon_k^2 \rangle \left[ 1 + (N-1) \sin^2\left(\frac{n\pi}{2N}\right) \right] \quad (7.7)$$

where  $N$  denotes the number of segments into which the microtubule is divided during image analysis. A typical plot of the variance of the mode amplitude for different modes is given in fig. 7.11. From a series of measurements performed on microtubules of lengths  $24\text{--}68\mu\text{m}$ , an average value for the Young's modulus of  $1.9\text{GPa}$  was found with apparently no length dependence.

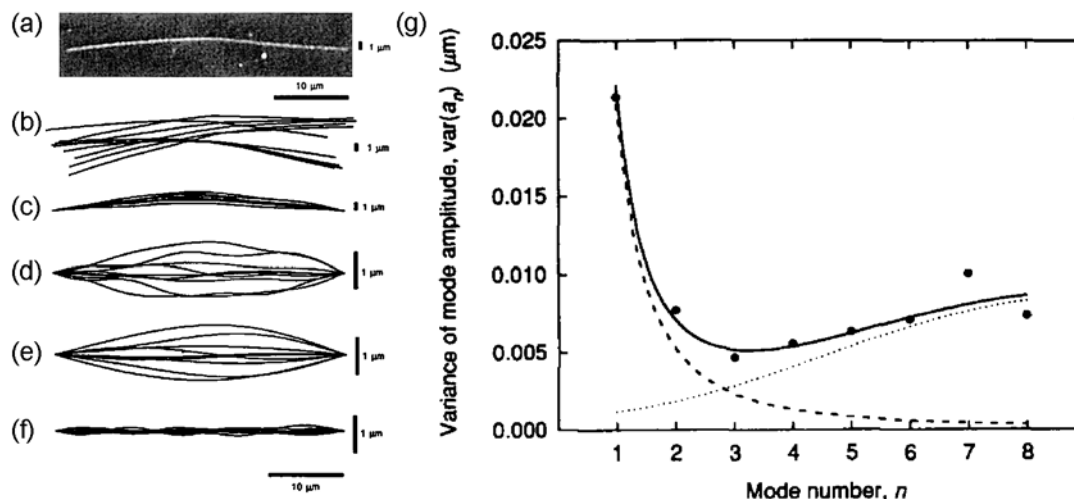


**Fig. 7.10.** (a) Fluorescence image of a thermally fluctuating microtubule. Every 10s positions of a set of 8 points along the microtubule were digitized. Ten such sets are shown in (b). The shape was Fourier decomposed into bending modes. (c) Reconstruction of microtubule shapes from the Fourier modes. (d) Same as (c) but after a subtraction of an average shape and multiplication by 3. (e) Reconstruction of a microtubule's shape from the first two modes only (f) contributions of the remaining higher modes [155]. (g) Variance of the Fourier coefficients of each mode, plotted against the mode number [156].

### Hydrodynamic flow

First measurements on microtubules performed by observing their deformation under an application of a controlled force were carried out by Venier et al. [157]. They assembled microtubules on axoneme pieces (isolated from sea urchin sperm tails) adhering to a glass coverslip, directly in the measurement chamber and during the experiment. This technique was adopted by several other groups. The buffer surrounding microtubules was flown past them with a determined flow-rate, causing microtubules to bend, as can be seen on fig. 7.11.

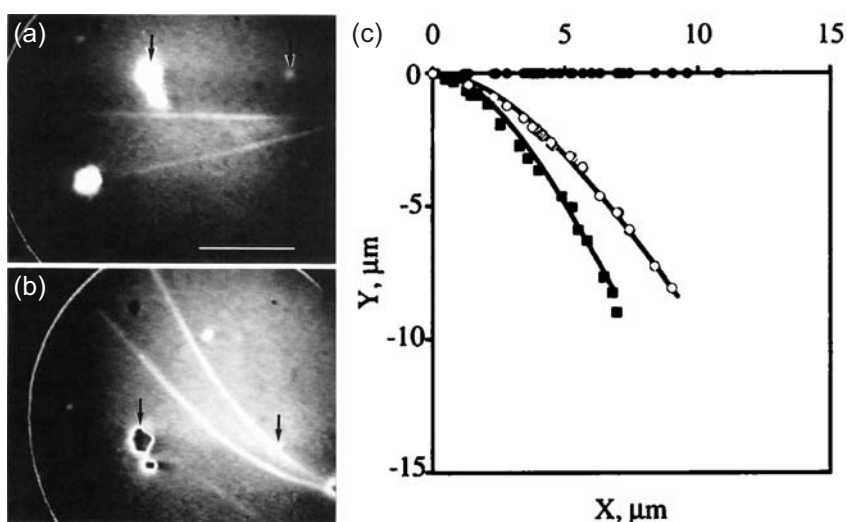


**Fig. 7.11.** (a) Dark-field images of microtubules in the absence of hydrodynamic flow. (b) Same microtubules bend in a flow of buffer. The flow rate was  $40\mu\text{l}/\text{min}$ . The scale bar is  $5\mu\text{m}$  long. (c) Plot of the microtubule deflection at different positions along their lengths [157].

The microtubule feels a uniform force  $f$  acting along its length, given by the Navier-Stokes equation:

$$f = \frac{4\pi\eta v}{\ln(L/2D)} \quad (7.8)$$

where  $\eta$  and  $v$  are the fluid's viscosity and velocity, respectively.  $L$  is the microtubule length and  $D$  the diameter.

The velocity of the buffer flowing through the measurement cell was evaluated by recording the movement of particles in the flowing buffer observed at a given focal length. Fluid velocities were measured at different depths within the solution and increased linearly with the distance from the glass surface in the 0–5  $\mu\text{m}$  range.

The shape of the bent microtubule was described by the equation for small bending of isotropic beams [73]:

$$y = \frac{fL^4}{24EI} \left[ \left( \frac{x}{L} \right)^4 - 4 \left( \frac{x}{L} \right)^3 + 6 \left( \frac{x}{L} \right)^2 \right] \quad (7.9)$$

The microtubule's shape was recorded using a DIC microscope, analyzed and fitted to equation (7.9) as shown on fig. 7.11. The microtubule was assumed to be an isotropic cylinder, yielding an average result for the Young's modulus of  $500 \pm 100$  MPa. The thermally induced fluctuations of the microtubule's free end were also recorded. The persistence length  $L_p$  was calculated from the deviation  $l$  of the microtubule's end from the mean position using the expression:

$$\langle l^2 \rangle = \frac{2}{3} \frac{L^3}{L_p} \quad (7.10)$$

The average persistence length was found to be  $2200 \pm 200$   $\mu\text{m}$ , and the corresponding Young's modulus was  $550 \pm 50$  MPa, similar to the result obtained using hydrodynamic flow. Influence of instrument noise was not considered as in the study of Gittes et al. [155].

### **Optical tweezers**

Controlled force can also be applied to microtubules using optical tweezers. They consist of a laser beam that can be focused by the objective lens of a standard light microscope which can be simultaneously used to observe a given object. Felgner et al. used a combination of optical tweezers [158] and hydrodynamic flow [159].

Microtubules were polymerized from axonemes attached to a coverslip via poly-L-lysine. During the experiment, the microtubule's free end is trapped by means of an optical tweezer, like the one schematically drawn on fig. 7.12a. The stage is moved in a direction perpendicular to the initial shape of the microtubule which bends as a consequence of this movement (fig. 7.12b). After switching off the laser power, the microtubule relaxes.

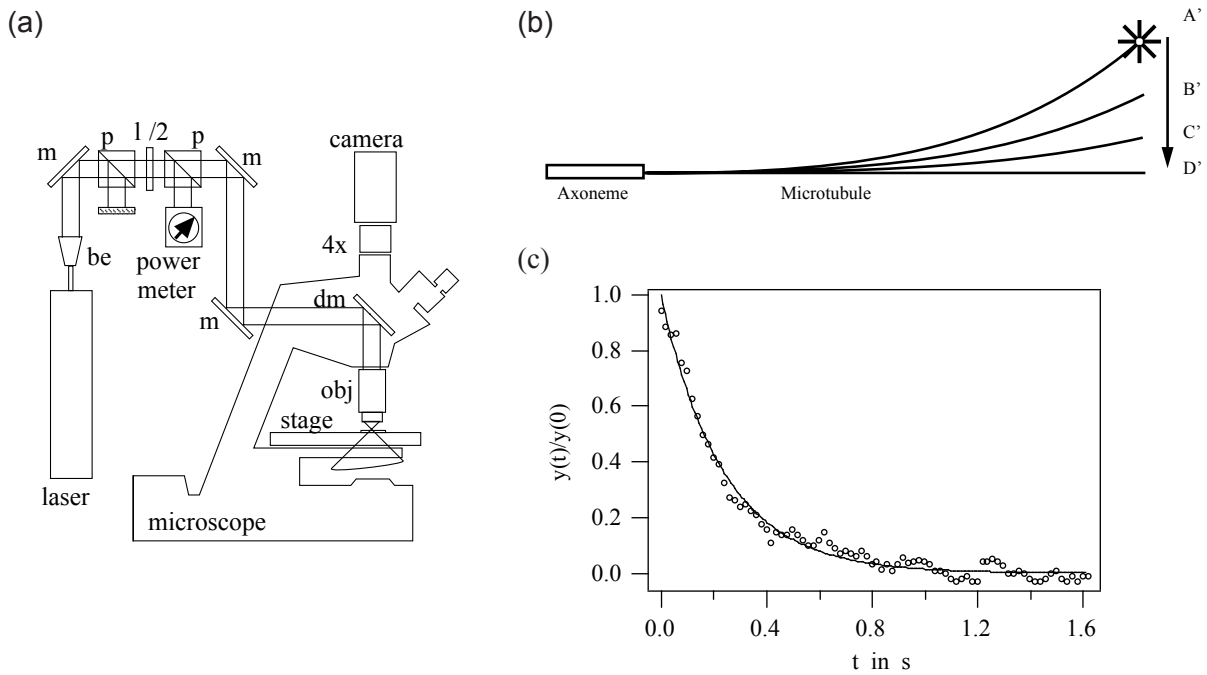


**Fig. 7.12.** (a) Schematic diagram of the optical tweezer setup used by Felgner et al. for measuring the Young's modulus of microtubules. (b) The free end of a microtubule is held by the optical tweezers. The stage is moved in the vertical position and the laser beam turned off. Microtubule relaxes to its initial form. (c) Position of a relaxing microtubule's end plotted versus time [159].

The authors suppose that the fluid velocity changes linearly along the microtubule length from  $v=0$  at fixed end to  $v$  at the free end. The force per unit length is given by [157]:

$$f = \frac{2\pi\eta v}{\ln(L/2D)} \quad (7.11)$$

The deflection of a microtubule under a load linearly varying from  $f=0$  at  $x=0$  to  $f=f_m$  at  $x=L$  is:

$$y(x) = \frac{f_m L^4}{120EI} \left[ \left( \frac{x}{L} \right)^5 - 10 \left( \frac{x}{L} \right)^3 + 20 \left( \frac{x}{L} \right)^2 \right] \quad (7.12)$$

Together with (7.11) this yields for the deflection at the free end:

$$y(x) = \frac{11\pi\eta v_m L^4}{60EI \ln(L/2D)} \quad (7.13)$$

The relaxation of the microtubule's free end (fig. 7.12c) can be described by an exponential decay:

$$\frac{y(\tau)}{y(0)} = e^{-EI\tau} \quad (7.14)$$

The microtubule's length varied between 6.1 and 14  $\mu\text{m}$ . The Young's modulus deduced from the exponential relaxation of the microtubule was  $220 \pm 50$  MPa.

Proximity of the coverslip and its influence on the viscous drag was not taken into account as in the work of Venier et al. [157].

### Atomic force microscope

The atomic force microscope was first used for measuring the Young's modulus of microtubules by Vinckier et al. in 1996 [160]. Microtubules were absorbed on APTES ((3-aminopropyl)-triethoxysilane) treated silicon oxide surface. Mechanical measurements were based on indenting a microtubule with an AFM tip positioned at its middle (fig. 7.13a and b). Microtubules were fixed using glutaraldehyde. The surface with the deposited microtubules was imaged under buffer using an AFM both in contact and in tapping mode. When a suitable microtubule was found, the AFM tip was positioned on top of the microtubule. A reference force-distance curve was then taken on the hard substrate and subtracted from subsequent measurements, fig. 7.13c.

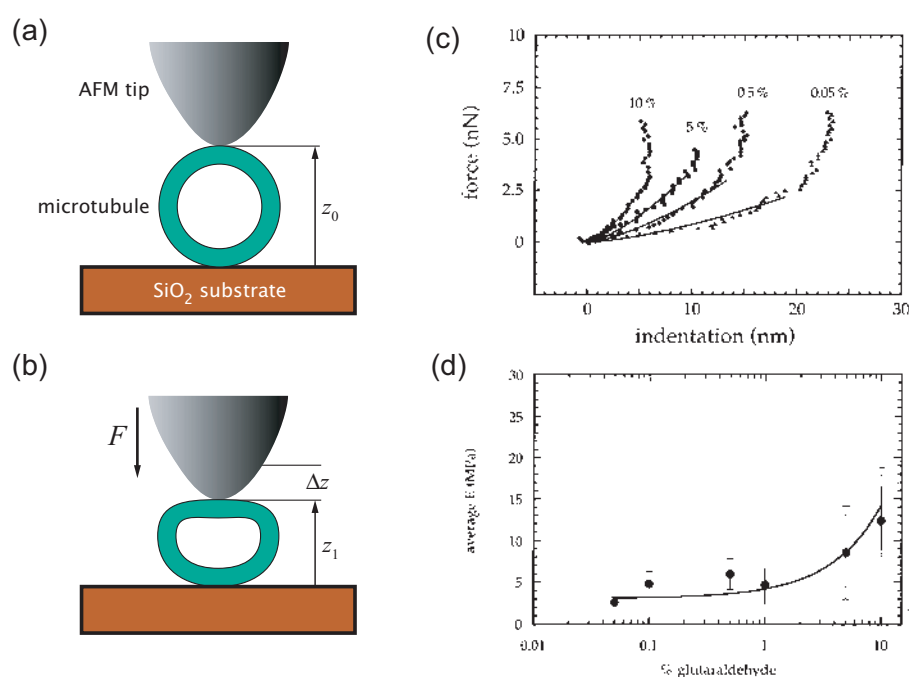


**Fig. 7.13.** (a) Schematic drawing of microtubule nanoindentation. (b) The microtubule deforms by  $\Delta z$  under normal force  $F$ . (c) A series of indentation curves acquired for different glutaraldehyde concentrations. (d) Plot of the Young's modulus calculated using the Hertz model as a function of glutaraldehyde concentration [160].

Experimental data was analyzed using the Hertz formula for the indentation of a soft sphere (the microtubule) by a hard one (the tip). The force  $F$  producing an indentation  $\Delta z$  can be written as:

$$F = \frac{4}{3} \frac{\sqrt{RE}}{1-\nu^2} (\Delta z)^{3/2} \quad (7.15)$$

where  $E$  is the Young's modulus,  $\nu$  the Poisson's ratio, and  $R$  the AFM tip's curvature. The Poisson's ratio was assumed to be 0.5, the highest possible value, characteristic for rubber-like materials, while the tip's radius was estimated by means of a calibration sample to be  $50 \pm 20$  nm.

Mechanical measurements were performed as a function of glutaraldehyde concentration. Fitting to equation (7.15) clearly shows that glutaraldehyde increases the Young's modulus, fig. 7.13d, with values of the Young's modulus ranging from  $2.6 \pm 0.6$  MPa for a glutaraldehyde concentration of 0.05%,  $4.7 \pm 2.3$  MPa for 1% and  $12.3 \pm 6.5$  MPa for 10%. The observed dependence of the Young's modulus on glutaraldehyde concentration was then used to

extrapolate the Young's modulus that would correspond to the absence of glutaraldehyde, yielding a hypothetical value of  $3.1 \pm 0.5$  MPa for unfixed microtubules.

By the time this thesis was mostly written, an interesting new contribution to the mechanical measurements on microtubules had been published by de Pablo et. al. [161]. They performed measurements on microtubules stabilized using taxol. Microtubules were deposited on APTES coated glass and imaged using an AFM operated in jump-mode [162]. In this mode, topographical images are constructed by approaching the AFM tip in every point of the image until a predetermined setpoint is reached. The tip is then retracted and moved in the lateral direction before approaching the surface again. This effectively eliminates lateral forces during imaging.

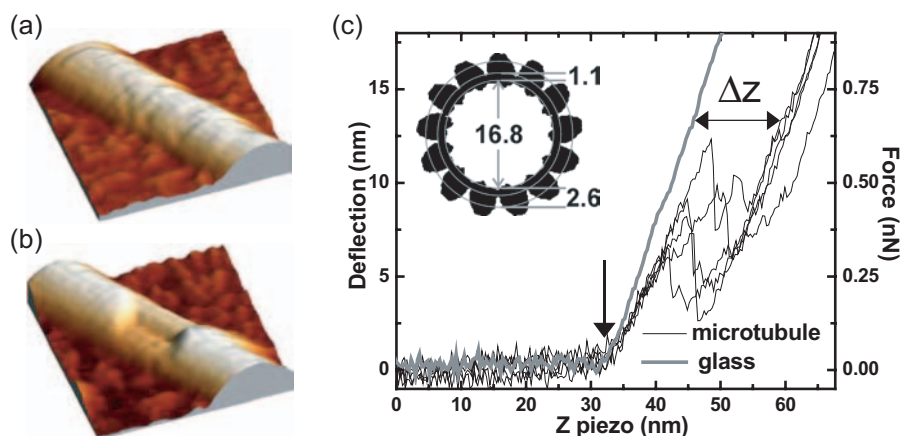


**Fig. 7.14.** (a) AFM image of a microtubule before and (b) after indentation measurements. Irreversible damage occurs after the acquisition of <5 force-distance curves. (c) A set of force-distance curves obtained on a microtubule. The inset shows the finite element model used to fit the data [161].

Several force-distance curves were acquired on a well determined portion of microtubules before it would locally collapse, fig. 7.14. The data was fitted using an elaborate finite element model, consisting of 12609 plates and taking into account the fine surface structure of microtubules, determined by cryo-TEM imaging (fig. 7.8 on p. 97). From such a model, they found that a Young's modulus on the order of 1 GPa could fit the experimental data. The mechanical model is probably accurate to a high degree, but it lacks robustness, as each particular experimental situation would need the 12609-plate model to be solved separately.

## Summary

The history of mechanical measurements on microtubules is long and confusing. First measurements were performed as early as 1983, yet every new experiment seemed to add to the general confusion surrounding the results.

Calculating the Young's modulus by estimating the persistence length using static images only is not without caveats. It is a very tempting idea that one could measure the rigidity of a material by taking only a snapshot of it [163]. Yet, there are many reasons why a filament can have a particular shape at one moment, without changes in mechanical properties. Fluid flow-rates can change, protein conformations also, additional stresses can occur during freezing or sample preparation [164] which could all lead to the false conclusion that it's the material property that changes and not only the shape.

Dynamic recording of microtubules' shape fluctuations is a much better way of deducing their material properties without deforming them on purpose. With considerate modelling, this can even grow into a sophisticated tool, as demonstrated by the Howard group [155, 156]. Their effort proves to which lengths one has to go in order to “measure” the Young's modulus of microtubules by imaging alone.

Technique	MT type	Temperature [°C]	Length [ $\mu\text{m}$ ]	E	Authors
Thermal fluctuations	MAPs	25	10–40 $\mu\text{m}$	100MPa	Mizushima-Sugano et al. [153]
Thermal fluctuations	taxol	25	25–65	1.2GPa	Gittes et al. [155]
Thermal fluctuations	taxol	25–37	24–68	1.9GPa	Mickey et al. [156]
Hydrodynamic flow	GDP	37	10–20	0.5 – 1.7GPa	Venier et al. [157]
Optical tweezers	taxol, MAPs	25°C	6.1–14	220MPa	Felgner et al. [159]
AFM	taxol, glutaraldehyde	25°C	–	3MPa	Vinckier et al. [160]
AFM – jump mode	taxol	25°C	–	1 GPa	de Pablo et. al. [161]

**TABLE 7.1.** A comparison between the most significant results on microtubule elasticity. Numbers correspond to results for microtubules assembled from pure tubulin.

The direct way of measuring the Young's modulus of microtubules is by measuring their deformation under the application of known, reasonably well calibrated forces. This is straightforward to achieve using the usual instruments for manipulating nanoscale objects like fluid flow, optical tweezers and an atomic force microscope.

## 7.4. Results: elastic deformation by AFM

The basic experimental setup used for measuring the mechanical properties of microtubules during this thesis was based on the method first used by Salvétat et al. for measuring the Young's and shear moduli of carbon nanotubes [72] (see also p. 42). Working with microtubules required additional improvements of this method. All the measurements had to be performed in the liquid environment, not only to slow down the degradation of proteins but also to prevent the structural collapse of microtubules which occurs during air-drying [165]. This demanded a more appropriate method of binding the microtubules to the substrate than relying on van der Waals interaction which was sufficient in the case of nanotubes. The dynamic instability of microtubules had to be blocked, in order to prevent them from disassembling in the course of measurements that could sometimes last longer than 10 hours.

### Surface functionalization

The optimal buffer for imaging microtubules would be the one that is used for their assembly *in vitro*, with a pH of 6.9. At this pH, the surface of microtubules is negatively charged [166]. The simplest method of binding them to a surface would be to choose a positively charged flat surface and rely on Coulomb interaction to hold the microtubules in place.

Another method of microtubule immobilization could rely on some kind of a chemical reaction between microtubules and functionalized surfaces.

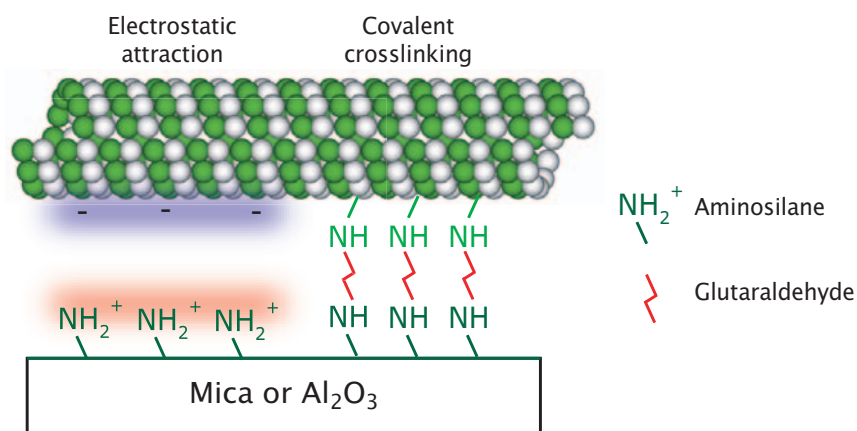


**Fig. 7.15.** Schematic drawing of different approaches to microtubule immobilization on surfaces.

Both these approaches would start with the chemical functionalization of the substrate. One of the most common methods was the one first described by Lyubchenko et al. who used it for chemical functionalization of muscovite mica (chemical formula  $\text{KAl}_2(\text{AlSi}_3)\text{O}_{10}(\text{OH})_2$ ) [167]. In this protocol, the amino groups of (3-aminopropyl)-triethoxysilane (APTES) are covalently bound to a freshly cleaved mica surface. This surface becomes positively charged in a water solution up to a pH of 10.5. Negatively charged DNA strands strongly adhere to this kind of surfaces.

This surface modification technique, shortly silanization, was used to change the surface charge of  $\text{Al}_2\text{O}_3$  membranes and make them a suitable substrate for performing mechanical measurements on microtubules in liquid. Prior to the procedure, pieces of polished  $\text{Al}_2\text{O}_3$  membranes were cleaned first in isopropanol, then in ultrapure water – both in an ultrasonic bath during 10 minutes. A 2l glass desiccator was prepared and 30  $\mu\text{l}$  of APTES were placed at its



bottom, fig. 7.16. Clean pieces of  $\text{Al}_2\text{O}_3$  membranes were mounted at the top of the desiccator, which was then closed end briefly evacuated. The desiccator was purged with argon and the reaction allowed to proceed for 2 hours. After that, the substrates were ready for use. They could also be stored for up to one month in a dry desiccator.

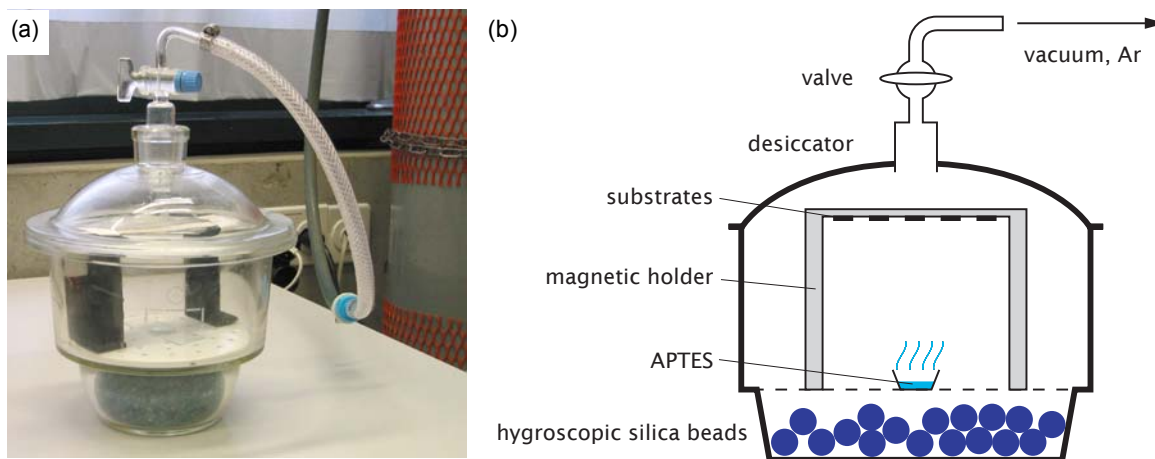


**Fig. 7.16.** (a) A photograph of the setup used for substrate silanization. (b) Schematic drawing of the same setup.

Microtubules adhere electrostatically to  $\text{Al}_2\text{O}_3$  membranes treated in this way. An additional step can also be performed in the sample preparation, by putting the substrates into a 1% solution of glutaraldehyde which is allowed to chemically react with the silanized surface for 10 min. After that, the sample is rinsed with ultrapure water. Immediately after adding the protein-containing solution, the amino-groups on the protein surface will react with the glutaraldehyde which will effectively act as a crosslinker between the silanized surface and the protein, fig. 7.17.

Both methods gave similar results in terms of microtubule adhesion and mechanical properties, so the electrostatic method was adopted for the sake of simplicity.

### Microtubule preparation

Bovine brain tubulin, both purified to 99% and MAP-containing, was purchased from Cytoskeleton Inc. in the form of lyophilized powder [169]. In the case of pure tubulin, lyophilized protein was dissolved in a buffer containing 80mM Na-PIPES (piperazine-N,N'-bis[2-ethanesulfonic acid]), 1mM  $\text{MgCl}_2$ , 1mM EGTA (ethylene glycol-bis( $\beta$ -aminoethyl ether)-N,N,N',N'-tetraacetic acid), 10% glycerol, pH

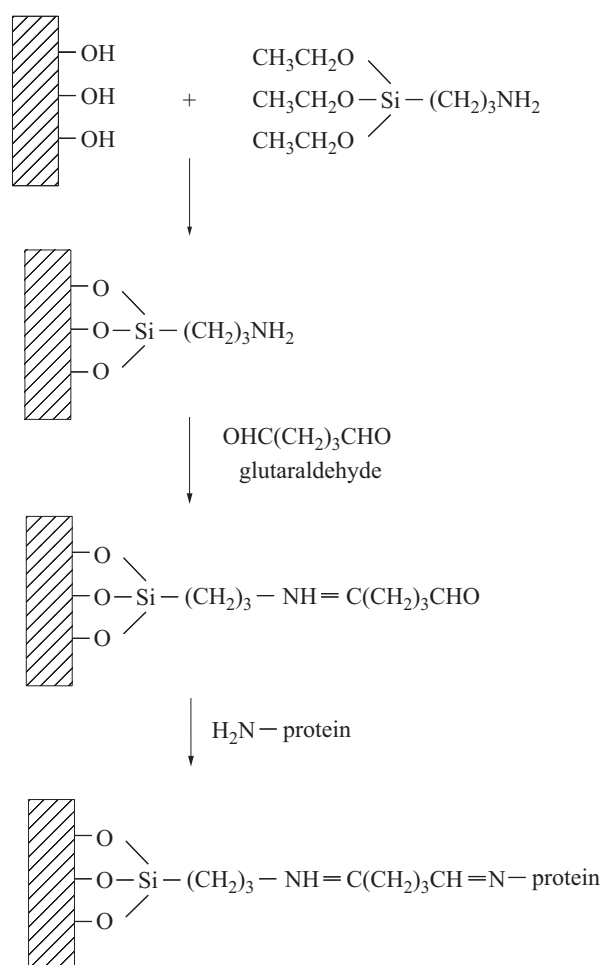


**Fig. 7.17.** Silanization and subsequent protein binding [168]

6.9. Addition of glycerol decreases the critical concentration for tubulin assembly that would otherwise be 10mg/ml. The final concentration of tubulin was 5 mg/ml. The test tube containing the solution was immersed into a mixture of water and ice. After the tubulin dissolves, GTP is added to a final concentration of 1mM. The solution, having a typical volume of 50 $\mu$ l is then transferred into a quartz cuvette which is placed into a UV spectrophotometer heated to 37°C. The absorbance at 350nm [145] was recorded as a function of time (fig. 7.18) using a Cary50 spectrophotometer from Varian, acting as a check of polymerization dynamics.

A typical absorbance curve, shown here on fig. 7.18, consists of three distinct regions, corresponding to different phases of microtubule assembly. During the first phase, dimers form by the binding of  $\alpha$  and  $\beta$ -tubulin. In the next phase, dimers assemble into microtubules, while during the last stage a steady state is reached in which microtubule growth and shrinkage are in equilibrium.

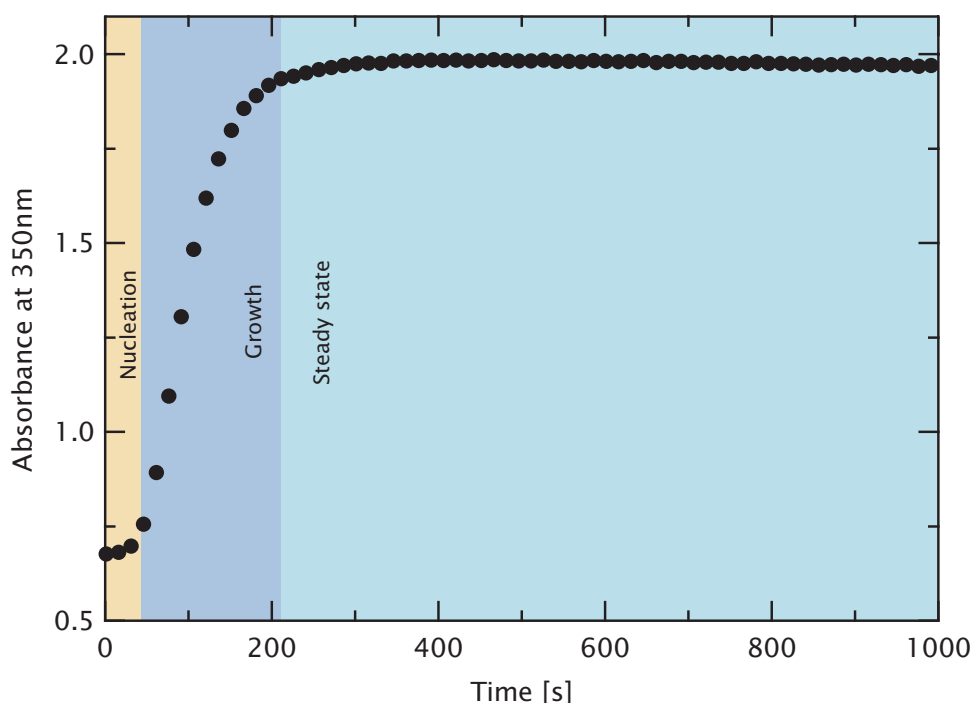


**Fig. 7.18.** Absorbance at 350nm of a solution maintained at 37°C containing assembling microtubules.

During the steady state, the length distribution of microtubules changes, with microtubules becoming longer on the average and the overall distribution broadening as the assembly proceeds. For the elastic measurements, the assembly can be blocked anytime during the last stage. This was done by adding glutaraldehyde to final concentrations ranging from 0.5–1% during 1–5 minutes. Glutaraldehyde fixation was stopped by the addition of a TRIS buffer (100mM tris(hydroxymethyl)-aminomethane hydrochloride in water) with pH 6.9. The solution was then centrifuged during 10min at 8000rpm (6000g) in a Sigma 3K18 lab centrifuge in order to separate polymerized microtubules from unpolymerized tubulin. The supernatant containing tubulin was discarded, and the pellet (formed from microtubules on the bottom of the test tube) resuspended in the buffer having the same composition as the one used for polymerization but without glycerol and GTP. The final volume of solution was usually 100 $\mu$ l. This solution was usually diluted 20-fold before a drop of it (10 $\mu$ l) was deposited on top of the substrate. Deposition times ranging from 1–10s were sufficient to produce the right surface coverage by

microtubules. Longer deposition times or denser solutions would result in a crowded surface on which measurements would be too difficult to perform. Centrifugation is also a very important step in sample preparation. Unpolymerized tubulin diffuses faster to the surface than the much heavier microtubules and therefore competes with microtubules for surface attachment. From the as-produced solution, most of the deposited material would in fact be unpolymerized tubulin.

Glutaraldehyde fixation was necessary in order to stabilize the microtubules during long experiments and to promote substrate adhesion. Other potential methods of microtubule stabilization like MAPs or taxol didn't result in microtubules that would strongly adhere to the substrate. This method was widely used for sample preparation in electron microscopy before the development of cryo-electron microscopy. Glutaraldehyde fixation is also occasionally used for preparing protein crystals for structure determination [170], demonstrating that it provides good preservation of protein structure.

Video-enhanced DIC (differential interference contrast) microscopy studies of fixed microtubules reported in the literature have shown the extent of structural changes induced by glutaraldehyde [164]. Fig. 7.19 shows the effect of a 1% glutaraldehyde solution on a single microtubule. As the fixation proceeds, the microtubule gradually bends, forming kinks which increase in degree over time. Observations of the Brownian movement show that the microtubule's flexibility doesn't change appreciably. Therefore, the kinks visible on fig. 7.19 are static and persistent. Increasing the glutaraldehyde concentration increased the rate of bending and kink formation but had no apparent effect on its degree or on the final appearance of microtubules.

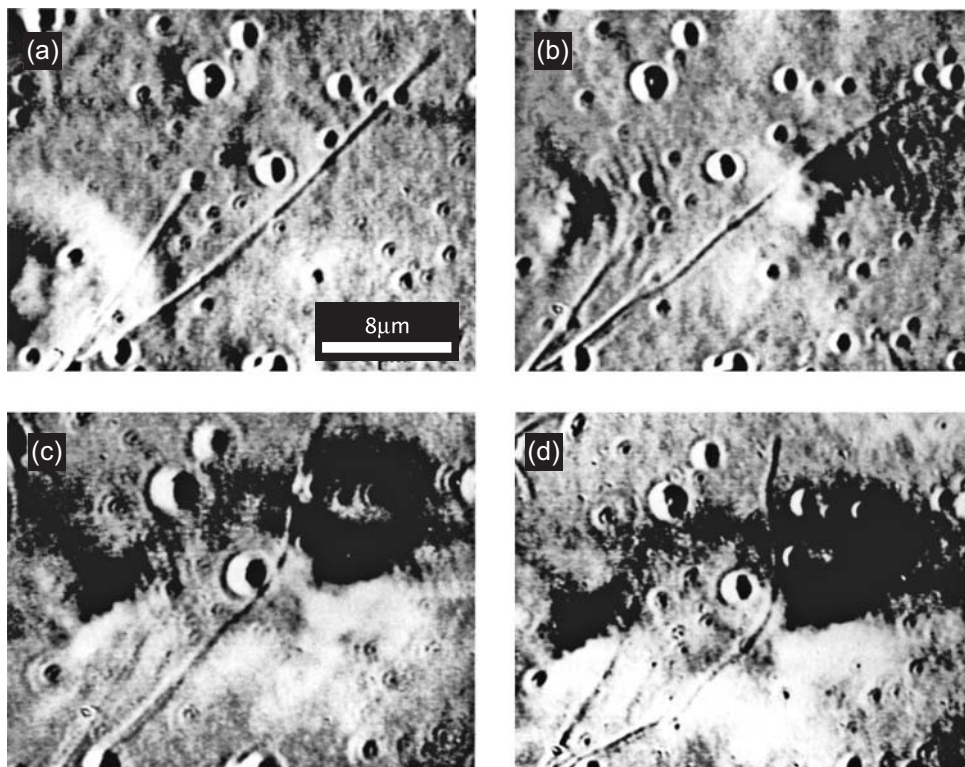


**Fig. 7.19.** DIC microscopy images of microtubules fixed with a 1% glutaraldehyde solution. (a) microtubule grown from an axoneme 2 seconds after exposure to glutaraldehyde (b) same microtubule after 6 min20s (c) 9min52s (d) 16min10s [164].

The microtubule fine structure seems to be preserved in general, as confirmed by the fact that glutaraldehyde-fixed microtubules support kinesin movement on their surface [171]. Local conformational change of tubulin inside microtubules can cause the release of bound nucleotides (GTP and GDP). Studies performed by Himes et al. [172] show the dynamics of nucleotide release from microtubules upon fixation with different concentrations of glutaraldehyde, indicating conformational changes of tubulin monomers induced by glutaraldehyde. At a concentration of 0.5% no observable loss occurs in the first 4 minutes upon fixation and less than 5% in the 8 minutes following the fixation. This demonstrates that the local changes in structure of tubulin monomers are negligible during the first 4 minutes following glutaraldehyde exposure. The only systematic study of glutaraldehyde on the mechanical properties of microtubules, performed by Vinckier et al. using an AFM (see p. 103) shows a stiffening of microtubules by a factor of 2 when fixed with 0.5% glutaraldehyde.

### Measurement setup

Mechanical measurements on microtubules were all performed using a Thermomicro M5 AFM [17]. While this microscope is not the first choice for working in liquid and on biological samples, it offers several significant advantages for this kind of measurements. Its hardware-linearized scanner is essential for repeated imaging of the same,  $1\mu\text{m}\times 1\mu\text{m}$  area of the sample. The inverted, scanned probe design, fig. 7.20, also enables the addition of a temperature controller beneath the sample.

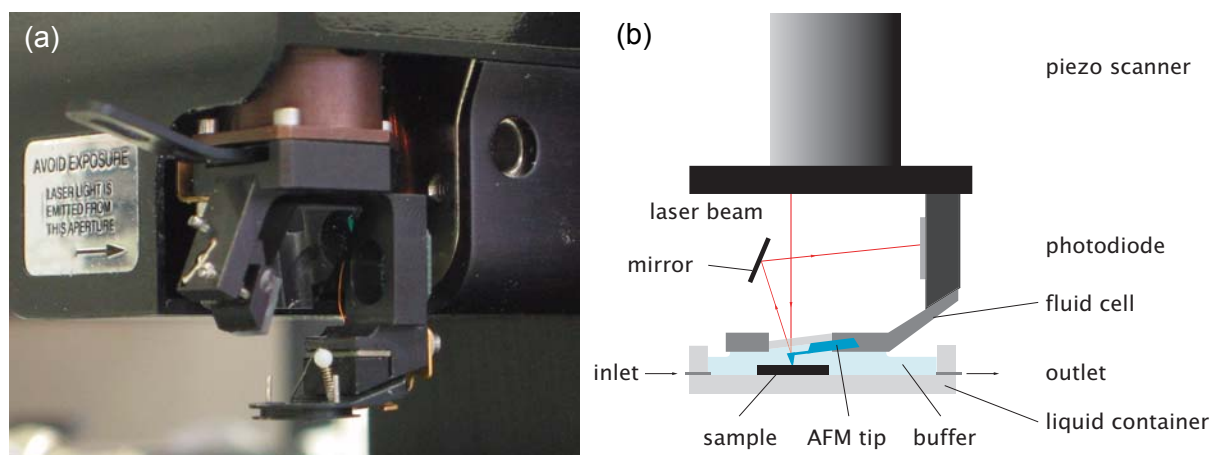


**Fig. 7.20.** (a) A photograph of the AFM head with the fluid cell (b) schematic drawing of the setup used for measurements in liquid.

The fluid cell was of the open type, in order to enable large displacements over the sample, which was sometimes necessary when searching for a microtubule suitable for mechanical measurements. The sample was most of the time firmly held at the bottom of a Petri-dish filled with buffer. AFM imaging was performed using silicon-nitride sharpened microlevers, type C from Park Scientific [17], with a typical spring constant of  $0.01\text{N/m}$ , calibrated by measuring their resonant frequency in air [16]. Metallized cantilevers proved to be useless, because they were very sensitive to temperature changes due to a difference in coefficients of heat expansion. Microtubules were deposited on APTES-functionalized alumina membranes (p. 106) and imaged

in contact mode under varying loads. Their deformation was extracted from the images and fitted using the clamped beam formula:

$$\delta = \frac{FL^3}{192E_{bending}I} \quad (7.16)$$

The analysis is analogous to that first used for carbon nanotubes by Salvétat et al. (see p. 42). An example of a microtubule imaged under two different force setpoints, on the order 100 and 150 pN is shown on fig. 7.21. The total force can include a constant term corresponding to adhesion. As the model is linear, only relative forces and deformations need to be measured. The deformations are also measured with respect to some easily recognized image feature and correspond therefore with relative microtubule deformations.

### ***Bending modulus***

The nature of the microtubules' mechanical response was determined at the beginning of the study. Fig 7.22 shows a typical deformation-force curve. In the range of the applied forces, the deformation is linear within the experimental error. Furthermore, the deformation is reversible, with loading and unloading curves having the same slope, and the microtubule recovering the initial shape after the mechanical measurement. This proves that under these conditions the microtubule behaved as linearly elastic material, justifying the choice of equation (7.16). The fact

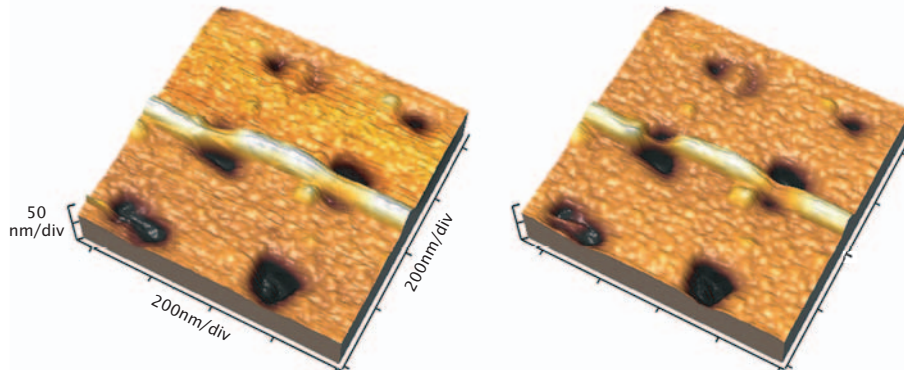


**Fig. 7.21.** Microtubule under two different loading forces. (a) Imaged with a force setpoint of 100pN (b) imaged with a setpoint of 150pN.

that microtubules behave as clamped beams is supported by the observation that AFM imaging in the direction perpendicular to the microtubules' local shape doesn't displace them in the lateral direction. Of course, this wasn't always the case: not all microtubules were perfectly held in place on the functionalized substrate. They were however swept away by the AFM tip after only an image or two. The imaging itself provided a satisfactory test of whether the microtubule-surface interaction was strong enough. The issue of boundary conditions was further clarified using finite element analysis (see p. 122).

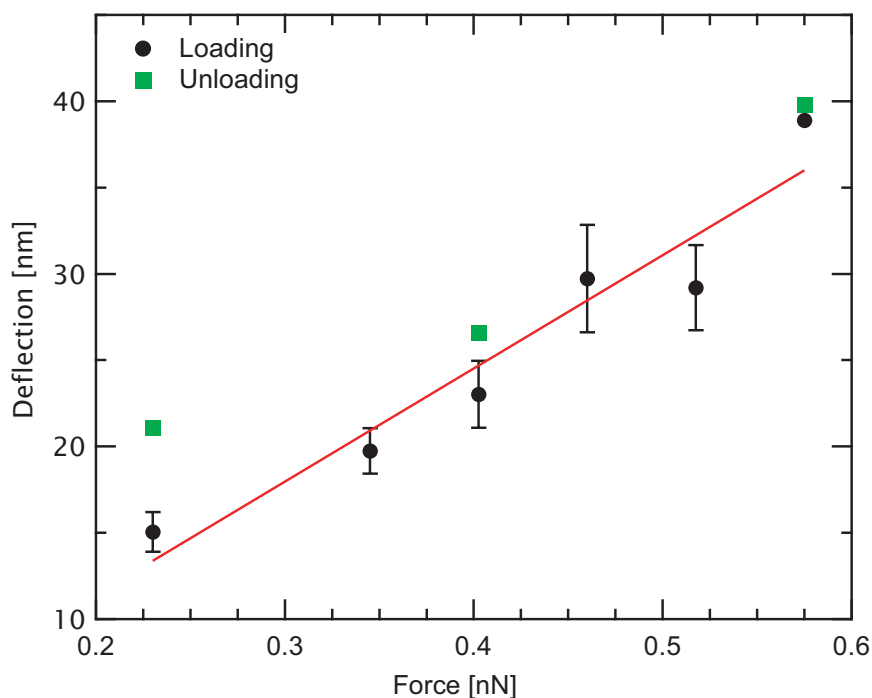


**Fig. 7.22.** Deformation of a microtubule. The suspended length was 144nm, and the bending modulus  $14 \pm 7$ MPa.

As expected from structural data based on electron microscopy [138, 149, 150] (see also p. 96) and TEM images of disassembling microtubules (fig. 7.5 on p. 95), microtubules are most probably mechanically anisotropic. The bending modulus  $E_{bending}$  in equation (7.16) is therefore an equivalent elastic modulus introduced to facilitate comparison between results. It would be equal to the Young's modulus only if shear deformations could be neglected.

Typical values of the  $E_{bending}$  measured on microtubules assembled from pure tubulin were in the range of 1–20MPa. Two measurements on microtubules with MAPs, fixed with glutaraldehyde, with values of 4 and 10MPa also fall in this range, yielding no conclusion on the influence of MAPs. Such a wide spread of individual measurements could be explained by the relatively high error of each particular measurement, estimated to be around 50% due to the uncertainty in determining the suspended length. However, the most probable reason is the same as for the much bigger spread in the values reported in the literature – microtubules' mechanical anisotropy introducing a length dependence into the values of  $E_{bending}$ , just as in the case of carbon and  $\text{MoS}_2$  nanotubes.

The most reliable way of avoiding systematic errors is to perform measurements on the same tube, using the same cantilever and varying the microtubule's surrounding in a controlled fashion. The absolute value of  $E_{bending}$  would then still be determined within 50%, but the relative changes could be measured much more accurately. This kind of measurements would then give a better picture of changes in microtubule's mechanical behavior than a comparison between different tubes, suspended on different holes and measured with different cantilevers.

First series of experiments performed in this way dealt with the influence of glutaraldehyde on the bending modulus of microtubules. Microtubules that were initially fixed with 0.5% were first

measured in the usual buffer. The liquid was then replaced with a buffer containing up to 10% glutaraldehyde. Results are collected in table 7.2.

MT n.	L [nm]±15%	$E_{bending}$ [MPa]±50%				
		0.5%	1%	2%	5%	10%
7	137	14	9	14	6	11
8	149	10	8	8	-	-
9	172	-	4	10	2	2
10	130	2	-	-	-	2
11	140	5	-	-	-	3
12	174	5	-	-	-	4

**TABLE 7.2.** Bending modulus  $E_{bending}$  measured in buffers containing varying concentrations of glutaraldehyde.

There doesn't seem to be a reproducible and homogeneous dependence of the bending modulus on the concentration of glutaraldehyde, in contradiction to measurements of Vinckier et al. [160] who found that the stiffness of microtubules increases with glutaraldehyde concentration (fig. 7.13 on p. 103). In fact, it seems that  $E_{bending}$  most probably doesn't change. Due to the duration of the experiment itself with 30–60 min needed for each measurement, all the binding sites on the microtubule's surface saturate with glutaraldehyde, and the addition of more glutaraldehyde into the solution doesn't change anything.

### Temperature dependence

Microtubule's fluctuations in length, assembly and disassembly are all temperature dependent. The basis for this behavior could be in the mechanical properties, inspiring measurements of the bending modulus as a function of temperature. The best way of performing this kind of measurements was to perform all the measurements on the same microtubule while changing the temperature. During the experiment, the temperature was controlled using a Peltier-element based temperature control stage from Molecular Imaging [173] (fig. 7.23). The sample was placed in a copper liquid container, which was chosen to minimize convective currents inside the buffer due to local temperature differences. Using such a setup, a stability of 0.1°C/hour was achieved.

Thermal dilatations of the microscope's construction due to temperature drift could influence the measurements by modifying the optical path of the laser beam used for detecting cantilever deflections or even simply by deforming the detector itself. The feedback system, which maintains a constant signal on the photodiode, would compensate changes in the signal provoked by thermal dilatation by changing the cantilever's deflection – effectively changing the imaging force. Such a change accumulated during the acquisition of an entire series of images needed for the mechanical measurements would manifest itself as an artificial contribution to the slope of the linear fit like the one on fig. 7.22, p. 112. This effect could be directly observed by measuring the voltage signal corresponding to the unloaded cantilever before and after taking a series of images. The difference in deflection signals from undeformed cantilevers is an indication of temperature drift in the system and can be used as a criteria for checking if the

optimal measurement conditions have been met. This problem could most simply be avoided by disengaging the cantilever from the sample before taking each image, thereby “resetting” the reference voltage corresponding to zero-force. In the worst case, thermal drift would result in the change of the force by the same amount in every image, which is taken care of by the linearity of the applied model.

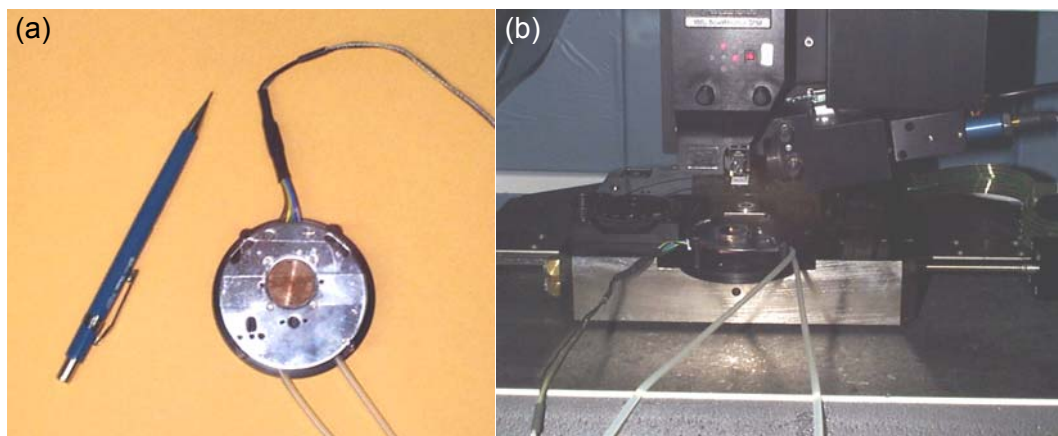


**Fig. 7.23.** (a) The heating stage used to control the sample temperature. (b) The heating stage mounted inside the AFM.

Measurements started at the mammalian physiological temperature of 37°C. The temperature was first lowered in discrete steps and allowed to stabilize during 1 hour prior to mechanical measurements. After the measurements at 5°C had been performed, the temperature was slowly raised to 41°C, and more measurements taken at this temperature and at 42°C, the highest attainable temperature with the heating stage that had been used.

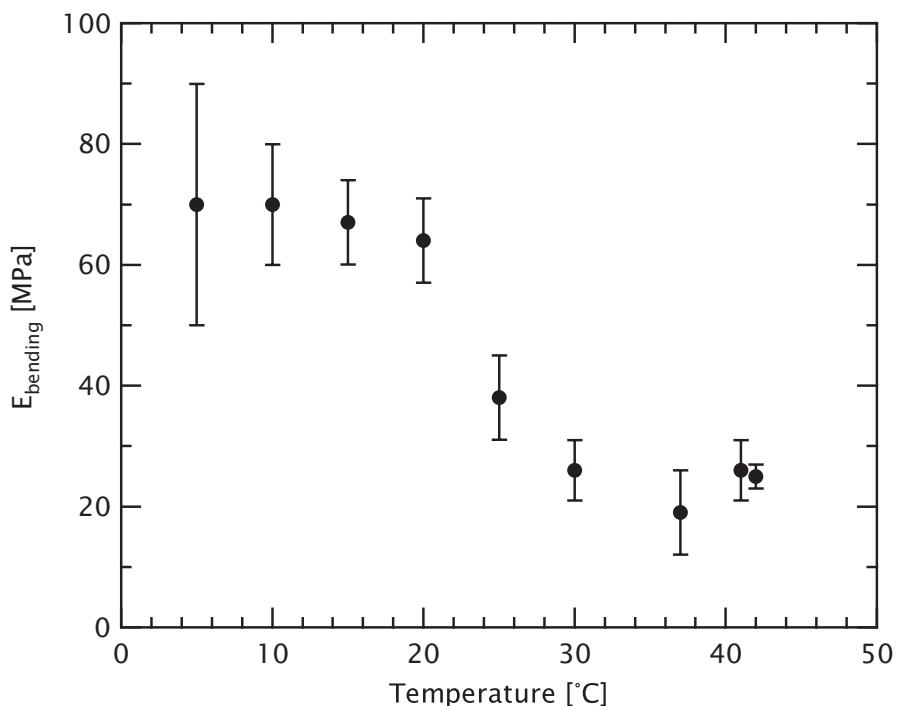


**Fig. 7.24.** Temperature dependence of the bending modulus. Microtubule length was 197 nm. The temperature was first lowered from 37°C to 5°C, then raised [174].

The behavior of  $E_{\text{bending}}$  as a function of temperature, shown on fig. 7.24, exhibits a monotonous and reversible increase with decreasing temperature and possibly a transition



between a stiffer and softer “state” around 25°C which could be reminiscent of glass transitions in polymers. This phenomena is however collective in nature and could hardly be applied to single microtubules.

The main feature of such a temperature dependence was also verified by performing measurements in which microtubules were squeezed in the vertical direction by the AFM tip, in a manner similar to that of Vinckier et al (p. 103).

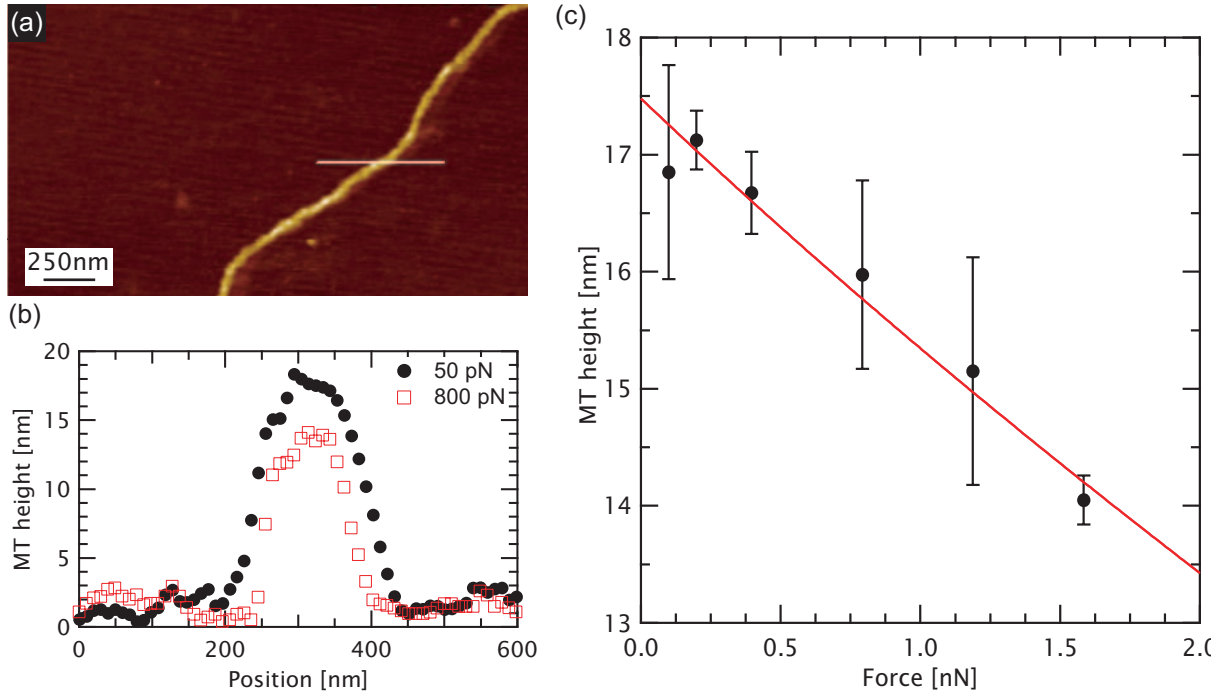


**Fig. 7.25.** (a) AFM image of a microtubule deposited on APTES-functionalized mica. (b) Linescans at the position indicated in (a) taken under two different forces. (c) Microtubules height under different imaging forces was fitted using the Hertz model.

Microtubules were deposited on the surface of APTES-functionalized mica and imaged in contact mode under different forces. Microtubule’s height was extracted from the images, fig. 7.25. The indentation of a microtubule was fitted using the Hertz model for the indentation of an isotropic cylinder by a sphere. Neglecting deformation of the AFM tip, the indentation  $\delta$  can be expressed by:

$$\delta = C(R_{MT}, R_{tip}) \left[ \frac{1-\nu^2}{E_r} F \right]^{2/3} \quad C(R_{MT}, R_{tip}) = K(k') \left( \frac{A+B}{RE(k')} \right) \left( \frac{3k}{2\pi} \right)^{2/3} \quad (7.17)$$

with  $E_r$  being the radial elastic modulus. The geometric factor  $C(R_{MT}, R_{tip})$  is given by:

$$A = \frac{1}{R_{tip}}, \quad B = \frac{1}{2R}, \quad \frac{1}{R} = \frac{1}{R_{tip}} + \frac{1}{R_{MT}}, \quad k' = \sqrt{1-k^2} \quad (7.18)$$

and the numerical constant  $k$ , determined by the radii  $R_{tip}$  and  $R_{NT}$  is the solution of equation:

$$\frac{B}{A} = \frac{(1/k^2)E(k') - K(k')}{K(k') - E(k')} \quad (7.19)$$

where  $K(k)$  and  $E(k)$  are elliptic integrals:

$$K(k) = \int_0^{\pi/2} \sqrt{1 - k^2 \sin^2 \theta} d\theta, E(k) = \int_0^{\pi/2} \frac{1}{\sqrt{1 - k^2 \sin^2 \theta}} d\theta \quad (7.20)$$

For the sake of comparing these results with the work of Vinckier et al., the Poisson's ratio was also assumed to be  $\nu=0.5$ , characteristic of rubberlike, isotropic solids. The tip radius was determined to be 20nm giving a geometric factor  $C=352\text{m}^{1/3}$ . The tip radius itself doesn't have a significant influence: a radius of 50 nm would correspond with  $C=307\text{m}^{1/3}$ .

The temperature dependence of the radial elastic modulus  $E_r$  shows the main feature of the  $E_{bending}$ 's behavior: decreasing of compliance on lower temperatures. The precision of a single measurement is lower in this case, as one has to deal with an elastic regime that is limited to a much smaller deformation range. The model used to fit the data and the choice of the Poisson's ratio is more appropriate for isotropic materials. In the case of strongly anisotropic materials, as might be the case of microtubules, the radial elastic modulus could closely correspond with the interprotofilament shear modulus.

In spite of the model used to fit the data, these experiments independently confirm the validity of measurements reported on fig. 7.24.

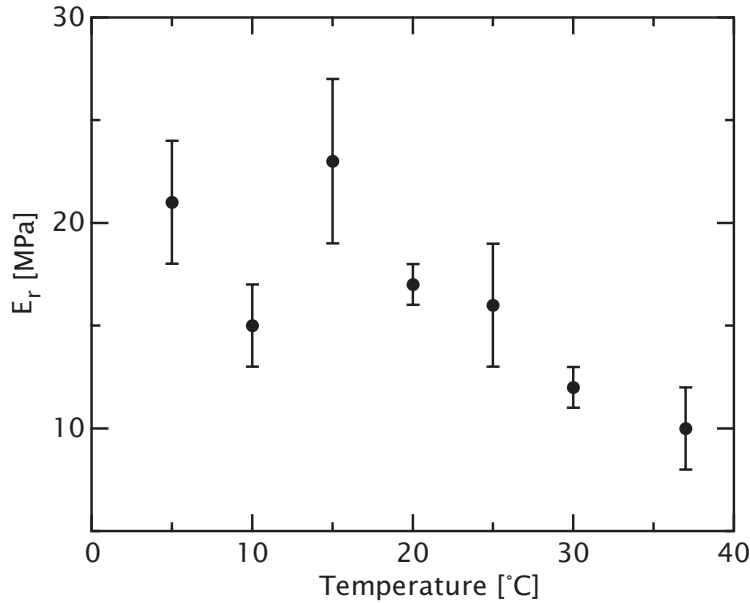


**Fig. 7.26.** Temperature dependence of the radial modulus  $E_r$  of a microtubule

The biological significance of  $E_{bending}$ 's temperature dependence could be found in the disassembly speed of single microtubules. From TEM images of disassembling microtubules [144] (see also fig. 7.5 on p. 95) it has been predicted that single protofilaments “peel-off” from the ends of microtubules. Interaction between the protofilaments, manifested in the shear modulus, would determine how easily protofilaments could be removed, relating the mechanical properties of microtubules to their dynamic behavior. Higher shear modulus would mean a more stable structure and a lower disassembly speed and vice versa. The simplest, empirical comparison between the disassembly speed and the mechanical properties would be to plot the data on fig. 7.24, and superimpose the data of Fygenon et al. [141]. This has been done on

fig. 7.27., clearly demonstrating the physiological relevance of the measured temperature dependence of  $E_{bending}$ .

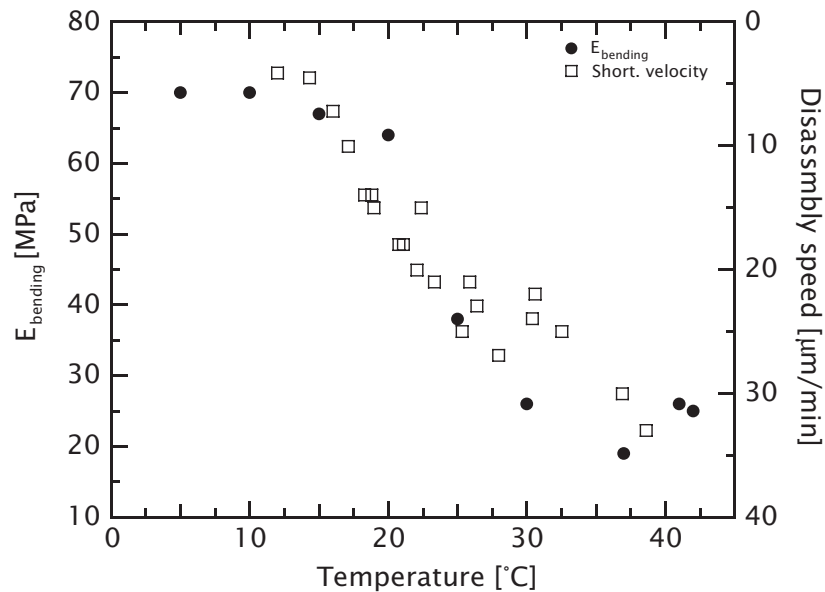


**Fig. 7.27.** Comparison of the temperature behaviour of  $E_{bending}$  and the disassembly speed of microtubules from [141].

### Shear modulus

During the last 20 years of mechanical measurements on single microtubules, they have exclusively been modelled as mechanically isotropic, smooth, homogeneous cylinders (with the exception of the recent paper from de Pablo et al. [161], see also p. 104). There were however numerous indications that this approach was wrong and that microtubules should be considered as anisotropic, with strong interaction between tubulin dimers along protofilaments and a much weaker interaction between neighboring protofilaments. TEM images of disassembling microtubules show protofilaments curving away from microtubules' ends, indicating that the interaction between dimers is much stronger inside the same protofilament. Surface reconstructions, also based on TEM images, show compact protofilaments separated with wide grooves and even helped identify regions of the tubulin protein involved in the inter- and intraprotofilament interactions. The extraordinary ability of microtubules to accommodate various lattice configurations with the protofilament number ranging between 8–17 could also be facilitated by a relatively weak interprotofilament interaction.

In case of an anisotropic mesoscopic object, the first refinement of the mechanical model can be realized by introducing a “shear modulus”. In the case of nanotubes, both carbon and  $\text{MoS}_2$ , this shear modulus takes into account intertube sliding which occurs when nanotube bundles are bent. Low values of the shear modulus give rise to a length-dependent  $E_{bending}$  in both these cases. The same behavior is expected during the deformation of microtubules.

In the model, fig. 7.28, the microtubule is treated as a single anisotropic tube, with external and internal diameters being 25nm and 15nm respectively. These dimensions correspond to 13-protofilament microtubules. The Young's modulus  $E_{Young}$  is the “stretchiness” of microtubules, governed by longitudinal deformations of protofilaments. The shear modulus  $G$  describes the weakening of the structure due to weak lateral connections between the protofilaments. As expected from structural data, the shear modulus  $G$  should be much lower than  $E_{Young}$ .

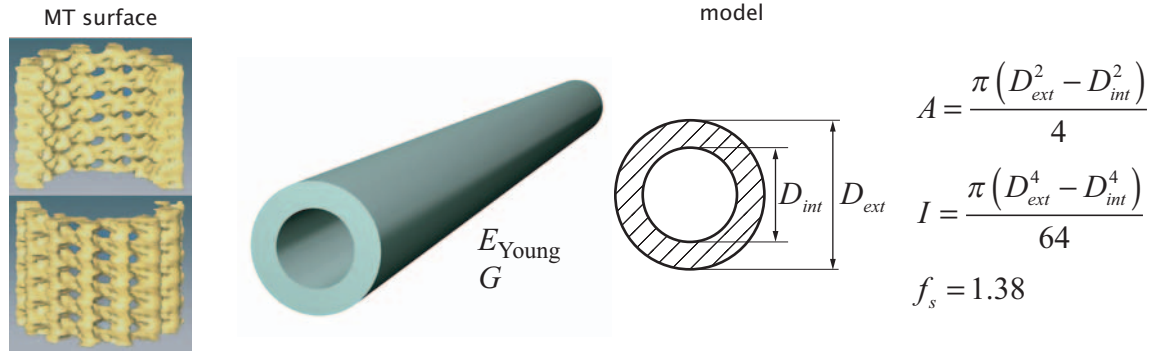


**Fig. 7.28.** Microtubules (TEM-based surface reconstruction on left) are modelled as anisotropic tubes, with external and internal diameters being 25nm and 15nm, respectively. The Young's modulus  $E_{Young}$  corresponds to the "stretchiness" of the microtubule. The shear modulus  $G$  describes the weakening of the structure due to thin connections between the protofilaments. The cross-sectional area  $A$ , second moment of the area  $I$  and the shape-factor  $f_s$  are calculated using the formulas on the right-hand side.

The deformation  $\delta$  of a microtubule deposited on a hole of length  $L$  would be given as the sum of deformation due to pure bending determined by  $E_{Young}$  and shear deformation governed by  $G$  [73] (see also p. 139):

$$\delta = \delta_{bending} + \delta_{shearing} = \frac{FL^3}{192E_{Young}I} + f_s \frac{FL}{4GA} = \frac{FL^3}{192E_{bending}I} \quad (7.21)$$

where  $f_s$  is a shape factor, equal to 10/9 for a filled cylinder and 1.38 for a hollow cylinder corresponding to the geometrical model of a microtubule (fig. 7.28).  $A$  is the area of the microtubule's cross-section.  $E_{bending}$  is the effective, bending modulus, equal to the Young's modulus only when the influence of shearing can be neglected (long microtubules). Equation (7.21) can be simplified as:

$$\frac{1}{E_{bending}} = \frac{1}{E_{Young}} + \frac{1}{G} \frac{3f_s (D_{ext}^2 + D_{int}^2)}{L^2} \quad (7.22)$$

In the case of carbon and MoS<sub>2</sub> nanotubes, the two elastic moduli were determined from an ensemble of measurements on bundles with varying diameters and, to a limited extent, different suspended lengths. This effectively varied the relative weights of bending and shearing terms in equation (7.21). Microtubule diameters are fixed by nature at 25nm in the 13-protofilament case. Apart from varying the protofilament number, which is not perfectly controllable, the only way of extrapolating  $E_{Young}$  and  $G$  from the mechanical response would be to perform measurements using holes of different sizes. It would also be desirable to perform the measurements on the same microtubule, in order to minimize systematic errors.

Such measurements were performed using a special kind of substrate, designed for these mechanical measurements. It was prepared at the University of Basel, in the group of Prof. Schönenberger by B. Babić, with the help of T. Nussbaumer. Silicon was spin-coated with 400nm of poly(methyl methacrylate) (PMMA). Slits with widths varying between 80–170nm were cut into PMMA using electron-beam lithography, and a 20nm thick layer of gold evaporated on top. Microtubules were assembled from pure tubulin, stabilized using 0.5%

glutaraldehyde during 1 minute, centrifuged and deposited on top of the substrate. Fig 7.29a. shows a microtubule spanning four different-sized slits on the substrate.

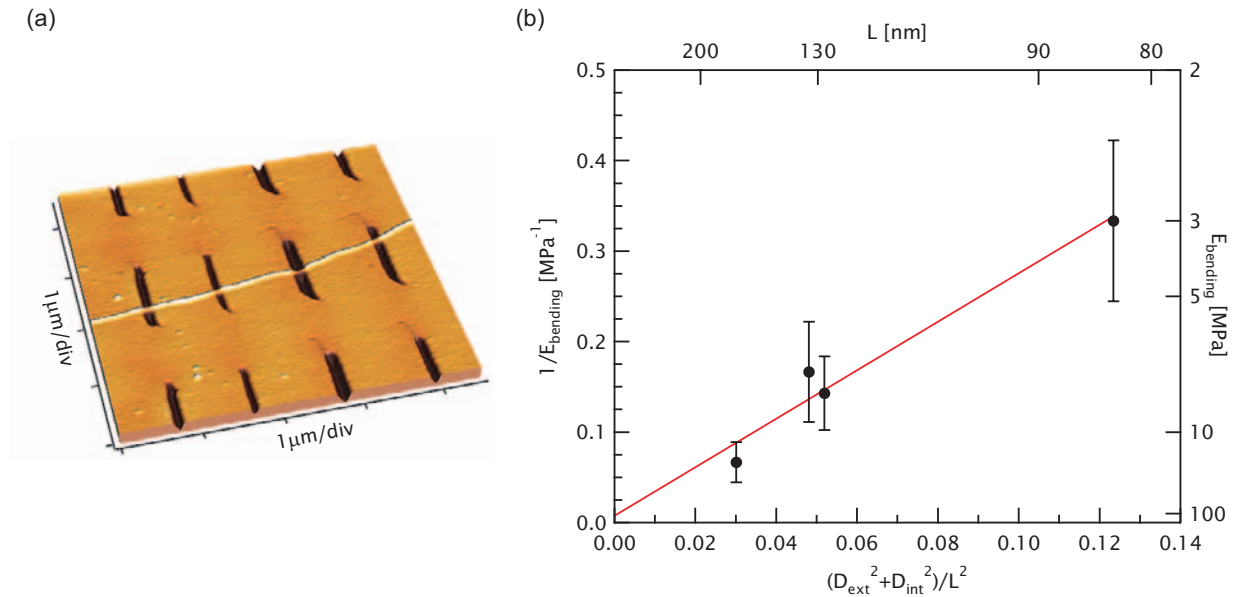


**Fig. 7.29.** (a) Pseudo-3D rendering based on the AFM image of a microtubule deposited on a lithographically tailored substrate. The suspended lengths for the four slits are (from left to right) 133, 83, 168 and 128 nm. (b) Variation of  $E_{bending}$  as a function of suspended length for the microtubule shown in (a). Red line is a fit to equation (7.22), with shear modulus corresponding to the inverse slope and Young's to the inverse segment on the abscissa [174].

Good adhesion between the gold layer on top of the PMMA and the microtubule was assured by the presence of sulphure (from the amino acid cysteine) on the exterior of microtubules. Sulphur and gold form an essentially covalent bond, with a breaking strength of 1.4 nN [175], far above the typical imaging force of 0.2 nN.

The microtubule shown on fig. 7.29a was elastically deformed during AFM imaging in the contact mode. The obtained variation of  $E_{bending}$  with the suspended length, shown on fig. 7.29b, clearly demonstrates the mechanical anisotropy of microtubules. There would be no length dependence for the  $E_{bending}$  of a mechanically isotropic cylinder.

Data was fitted using the equation (7.22), yielding for the values of the shear and the Young's modulus:

$$G = (1.5 \pm 0.3) \text{ MPa} \quad E_{Young} > 130 \text{ MPa} \quad (7.23)$$

In the representation chosen on fig. 7.29b, the shear modulus is proportional to the inverse slope of the fit, while the Young's modulus is the inverse of the segment on the abscissa. The value for  $E_{Young}$  is an extrapolation from the experimental data, and represents only a lower limit. From the statistical point of view, the segment on the abscissa could even be zero, implying a physically impossible infinite  $E_{Young}$ . As all the previous experiments reported in the literature have in fact measured the  $E_{bending}$  on microtubules with varying lengths, the closest value for  $E_{Young}$  would be the  $E_{bending}$  obtained on the longest microtubules. This is the case in the measurements of Mickey and Howard, who obtained the mean value of 1.9 GPa for microtubules with lengths ranging from 24–68 μm, with no apparent length dependence [156] (see also p. 98). In order to determine the Young's modulus of microtubules using an AFM, one would have to increase the suspended

length. Unfortunately, microtubules are so flexible that already with hole sizes used in this study, the microscope has to operate on the highest level of its sensitivity – increasing the hole size would mean further decreasing imaging forces.

Due to the presence of glutaraldehyde, the shear modulus' value represents a higher limit as the glutaraldehyde might increase the interaction between tubulin subunits.

As a consequence of high mechanical anisotropy, the bending measurements on the 100–200nm length scale are much more sensitive to changes in the shear modulus than in the  $E_{Young}$ . As an illustration, let us consider fig. 7.30, the plot of  $E_{bending}$  as a function of shear modulus of a 200nm long microtubule segment, for a range of  $E_{Young}$ . This suspended length was chosen so as to coincide with the length in temperature-dependent measurements of  $E_{bending}$  reported on fig. 7.24, p. 114. For  $G=1.5\text{MPa}$  and  $E_{Young}$  above 130MPa,  $E_{bending} \approx 16\text{MPa}$ , within the experimental error of the high-temperature value of 20MPa. When the temperature is lowered to  $5^\circ\text{C}$ ,  $E_{bending}$  increases by almost a factor of 4, to roughly 70MPa. Such a huge increase can't be explained by an increase of  $E_{Young}$  only – not even in the unlikely event of  $E_{Young}$  reaching 1TPa – the Young's modulus of diamond and carbon nanotubes – would it be enough to provoke such a huge increase in the bending modulus. An increase of  $G$ , up to at least 6.4MPa, in case when  $E_{Young}$  was 2GPa, or even more if it was lower, would be necessary to reproduce the observed behavior. On the other hand, the only results so far reported in the literature even claim a 30% decrease of  $E_{Young}$  on cooling from  $37^\circ\text{C}$  to  $25^\circ\text{C}$  [156]. So, no matter what the temperature behavior of  $E_{Young}$  was, the shear modulus should increase at least by a factor of three to account for the experimental data.

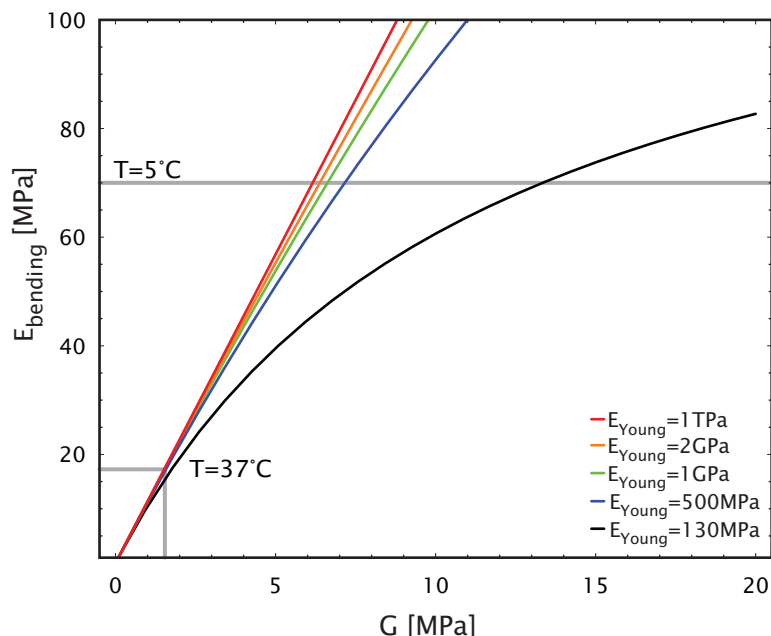


**Fig. 7.30.** Calculated bending modulus as a function of the shear modulus  $G$ , for different values of  $E_{Young}$ . The suspended length was  $L=200\text{nm}$ , corresponding to the length of the microtubule on which the temperature-dependent bending modulus was measured (fig. 7.24 on p. 114.). Horizontal lines indicate possible choices of  $E_{Young}$  and  $G$  which yield the measured  $E_{bending}$  at two characteristic temperatures.

A much more direct and empirical proof can be provided by performing AFM measurements of the shear modulus, this time on different temperatures. Deformation of the same microtubule was recorded on two temperatures,  $37^\circ\text{C}$  and  $7^\circ\text{C}$ , corresponding to high and low-temperature states of the microtubule. The corresponding variation of  $E_{bending}$  is given in fig. 7.31. The slope of

the fit decreases when the temperature is increased, indicating an increase of the shear modulus from  $G=1.9\pm 0.6\text{MPa}$  at  $37^\circ\text{C}$  to  $G=12\pm 7\text{MPa}$  at  $7^\circ\text{C}$ . The uncertainty of the data is unfortunately too big to allow a conclusion on the behavior of  $E_{\text{Young}}$ . There is however no doubt that the shear modulus increases when lowering the temperature.

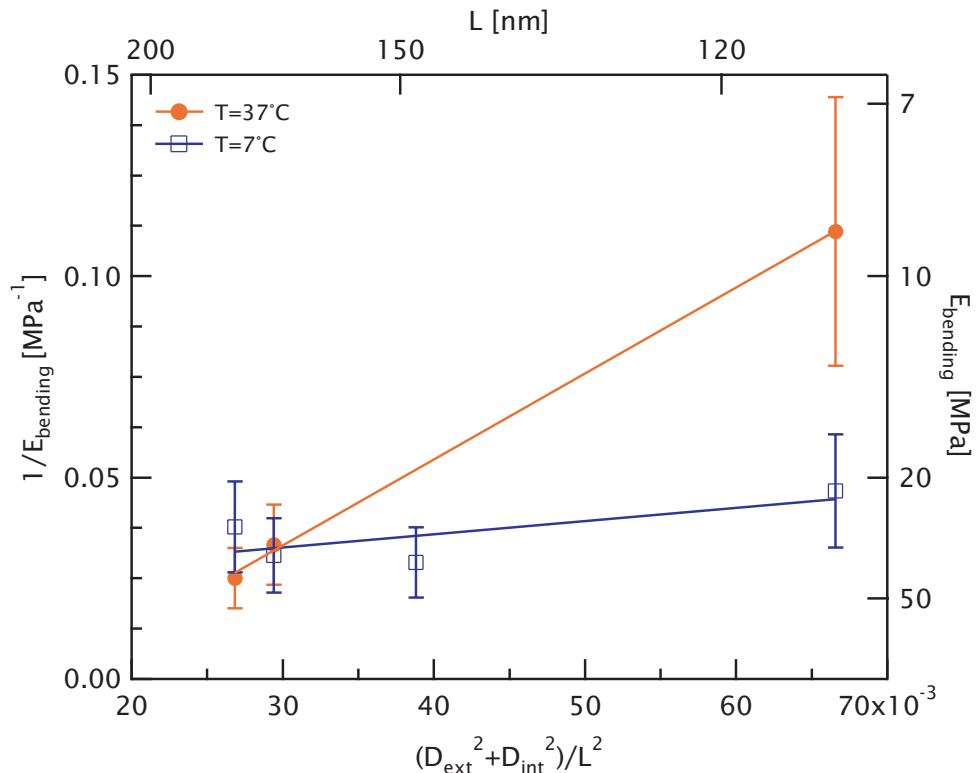


**Fig. 7.31.** Variation of  $E_{\text{bending}}$  as a function of suspended length at two different temperatures.

Such a behavior is intimately connected with the functional properties of microtubules, namely the dynamic instability.

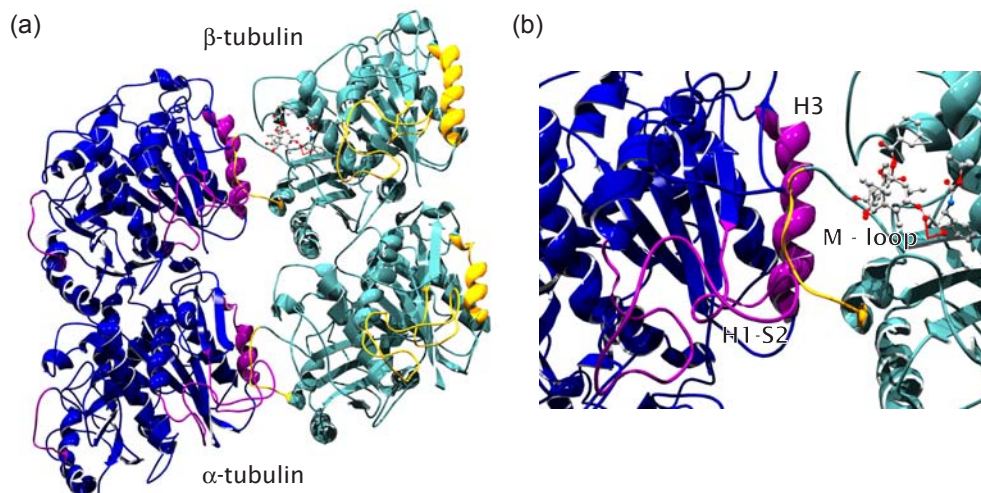


**Fig. 7.32.** Ribbon diagrams of two tubulin dimers, corresponding to neighbouring protofilaments. Protein regions involved in the lateral interaction are colored magenta and orange. (b) Close-up of the lateral contact area.

Simply said, microtubules are mechanically highly anisotropic because a smaller region of the tubulin molecule is involved in the lateral than in the longitudinal binding. Regions of tubulin involved in the interaction between the neighboring protofilaments have been identified by comparing crystallographic data [147] with cryo-TEM images [138, 149, 150], and are shown on fig. 7.32.

Computer simulations of the flexibility of tubulin dimers have identified these regions as being the most flexible [176]. As the motion of these flexible regions is thermally activated, decreasing the temperature would also decrease the fluctuations, allowing the protein to spend more time close to the equilibrium configuration leading to stabilized contact area. This would lead to an experimentally observed increase in the shear modulus.

### ***Finite element analysis***

Using the finite elements method (FEM), the behavior of microtubules under mechanical stress was modelled together with Sándor Kasás [177]. This method consists of building a computer model of an object and simulating its behavior under mechanical stress. The most important question we wanted to address was the influence of boundary conditions on measurements of the shear modulus and the influence of the mechanical anisotropy on the overall shape of a deformed microtubule.

Analytical solutions for interpreting experimental data and simulating MT behavior are available only for a limited number of situations and at a price of dramatic simplifications. They can even cause considerable errors, as the problem of microtubule's mechanical anisotropy clearly demonstrates. Molecular dynamics (MD) would probably be the method of choice, but it is unfortunately not suitable for calculations on structures that can extend up to hundreds of micrometers. Additionally, MD simulations require a huge computational power which is not accessible to the majority of our community.

A very convenient way of modeling microtubules is by building a computer model and simulating its behavior under mechanical stress using FEM. The essence of FEM lies in dividing an object under study into small, discrete elements. The element positions and load distributions are approximated by trial functions that are iteratively refined according to the principle of minimal potential energy [75].

FEM enables to simulate and understand a richer variety of experimental situations than can be analytically solved. This method can also lead the way to building better analytical models by showing which assumptions are safe to make. Contrarily to molecular dynamics, FEM analysis requires less computational power and runs on modern desktop computers. In addition, several user friendly computer packages are commercially available, giving us the opportunity to model complex geometries and analyze their mechanical properties in a relatively short period of time.

Microtubules without MAPs were simulated using the ASDL ANSYS® 5.7 programming language. The dimensions of single tubulin molecules and their connecting angles were set according to Chretien et al. [136]. The model was built of a BEAM4, a 3D uniaxial element with tension, compression, torsion, and bending capabilities. Every element corresponded to a single tubulin molecule. The material constants for each tubulin "molecule" were calibrated by adjusting the model until it behaved as "real" microtubules did under certain circumstances.



Small bending of a 2  $\mu\text{m}$  long model corresponded to the bending of a homogeneous cylinder with a Young's modulus of 2 GPa, according to the results of Mickey et al. [156]. The shear modulus was then adjusted to 1.4 GPa, in a simulation of the mechanical measurements on a PMMA substrate. Such a microtubule could then be used in further simulations in which microtubules were "suspended" above "holes" of different lengths. The solid surface on which the microtubule was lying was simulated by blocking the microtubule's lower protofilaments.

Curves depicting microtubule deformation as a function of applied force all show linear behavior. Varying the hole size reproduced the essential feature of the AFM experiment: dependence of  $E_{\text{bending}}$  on the suspended length (fig. 7.33a).

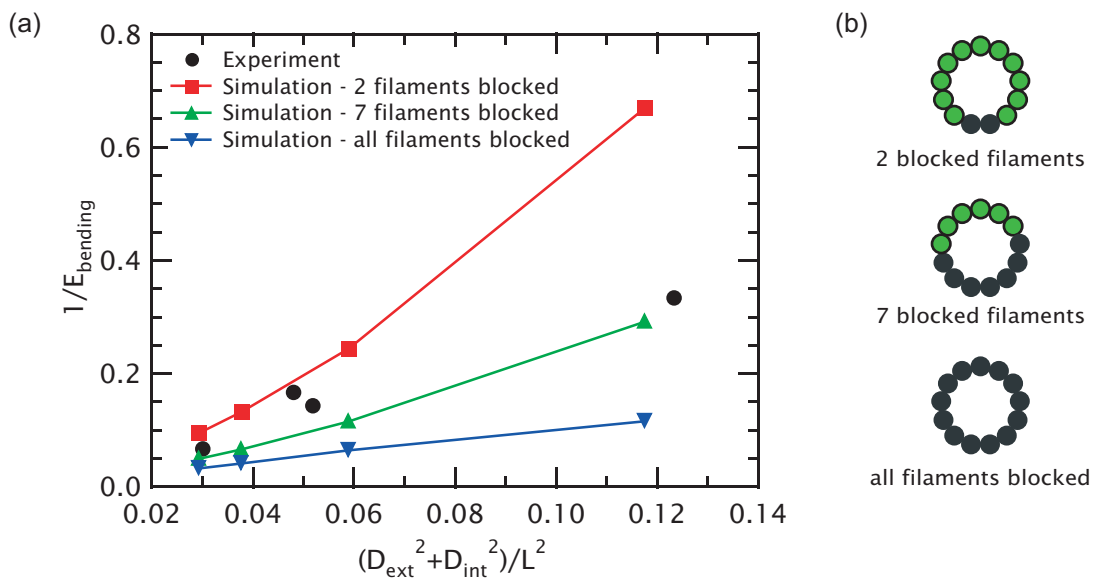


**Fig. 7.33.** (a) Comparison of simulated and the experimental data for the boundary conditions schematically depicted in (b) [177].

The basic assumption of the mechanical model used to fit the data is that microtubules behave as clamped beams. This was tested by changing the number of protofilaments that are blocked by the substrate, allowing for movements of the "upper" protofilaments. Results for the variation of  $E_{\text{bending}}$  as a function of length for 2, 7 and 13 blocked protofilaments are shown on fig. 7.33a. The main criterion for comparisons with the experiment is the overall shape of the curve describing the dependence of  $E_{\text{bending}}$  on MT length. Deviations of this curve from a straight line in fig. 7.33b show how much of the  $E_{\text{bending}}$ 's length dependence is an artifact coming from boundary conditions and how much from real, physical properties of MTs. The absolute numerical values depend on model calibration. As we didn't want our simulations to favor any of the possible extremes in the number of blocked filaments, the shear modulus was calibrated assuming that only the 7 lower protofilaments were bound in the experiment. During calibration, the slope of the linear fit of the simulated points was adjusted to the slope of the experimental values. Because a fixed, predetermined value of the Young's modulus was used, the actual points didn't overlap with the experimental data.

Results where only 2 protofilaments were blocked show a significant deviation, at small suspended lengths, from the experimental data and the behavior described by the expression for the effective bending modulus, equation (7.22) on p. 118. In the case where all the protofilaments have been blocked, which corresponds to the clamped-beam model, the linear dependence of  $1/$

$E_{bending}$  on  $(D_{ext}^2 + D_{int}^2)/L^2$  is completely reproduced, while in the case of 7 blocked protofilaments there is still a deviation at small lengths.

The most significant influence of varying the boundary conditions is the deviation of the mechanical behavior from equation (7.22), while the exact numerical values and their eventual accordance with the experiment depend on model calibration. As the experimental data shows a linear behavior that is qualitatively the same as in the simulation with all protofilaments blocked, the original assumption of a clamped beam is validated. The experimentally observed variation of microtubule's  $E_{bending}$  is therefore physical, and not an artifact coming from changes in the boundary condition from one slit to the other.

To estimate the extent of discrepancy in the mechanical behavior between the isotropic and the anisotropic case, two different “kinds” of MTs were simulated. Isotropic microtubules were simulated by setting the same material constants for all the connections between single “tubulin molecules”, (2GPa each) whereas anisotropic ones had different material constants along and between their protofilaments (2GPa for the Young's modulus and 1.4MPa for the shear modulus). Both MTs were fixed at one of their ends and a given transversal force was applied to their remaining free end. Lengths of both MTs were set to  $2\mu\text{m}$ . The same transversal force induced a 70% larger bending in the anisotropic than in the isotropic MT. Even when the end-deformations are adjusted to be equal, there is a significant difference in the overall shape of the deformed microtubule (fig. 7.34), which could drastically influence estimations of the microtubule's persistence length [153].

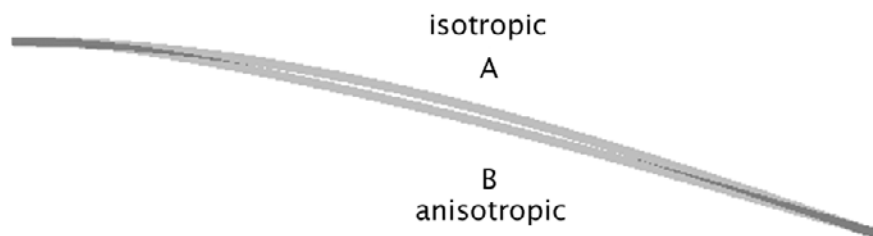


**Fig. 7.34.** Results of two simulation runs in which both MT A and B were fixed at their left ends and deformed by a vertical force acting at their free right end. Both MTs were  $2\mu\text{m}$  long. MT A had the same Young's and shear moduli, whereas MT B, corresponded to the realistic situation, where the shear is much lower than the Young's modulus. The forces applied on MT A and B were different, chosen so as to induce the same maximal deflexion on both MTs. The same force applied in both cases would produce a 70% larger deformation of MT B than MT A [177].

## 7.5. Conclusions

The method of Salvétat et al., originally developed for mechanical measurements on carbon nanotubes has been extended for measurements on microtubules in the liquid environment using surface functionalization. This could in future enable similar measurements to be performed on other cytoskeletal filaments like actin and intermediate filaments.

At this stage, glutaraldehyde fixation couldn't have been avoided – this was the only way of stabilization that worked during long experiments. The fixation time and concentration were chosen in the way to minimally perturb the fine structure of microtubules, as proven by their ability to keep bound nucleotides [172], bind motor proteins [171] and the extent of structural deformations [164]. The presence of glutaraldehyde implies that the obtained values represent the upper limit for the shear modulus. The temperature dependence or the mechanical anisotropy themselves couldn't be artefacts of glutaraldehyde fixation.

The temperature dependence of the bending modulus of microtubules, measured for the first time, shows a surprising behavior, with a factor of four increase when the temperature is decreased from 37°C to 5°C, this change being well reproducible and reversible. This result was further verified using the AFM for performing “indentation” on the surface of a microtubule.

By performing measurements on the same microtubule suspended over holes with varying widths, the shear and Young's moduli were simultaneously determined. This was the first time these two elastic properties were simultaneously measured on a single nanoscale object. Results have verified the initial suspicion that from the mechanical point of view, microtubules behave as anisotropic cylinders, with tubulin subunits being strongly bound along the protofilaments and weakly between them. This gives microtubules flexibility that is length dependent: the mechanical response on length scales associated with the cell size is governed by the high Young's modulus, while the low shear modulus determines deformation on short length scales. This is intimately related with the ambiguous role microtubules play in living cells. On one side, they should be stiff, in order to provide adequate support for the cell – this can be achieved on longer lengths. On the other hand, the protofilaments should be weakly bound, allowing dynamic instability which enables the cellular microtubule network to reorganize when needed (for example during cell division).

By measuring the shear modulus on different temperatures, the stiffening of microtubules on lower temperatures was explained in terms of increasing interaction between the protofilaments, in excellent accord with previously published data on microtubule dynamics. The basis for such a behavior on the molecular level is most probably a decrease in thermally induced shape fluctuations, leading to stronger interaction between the protofilaments.



Three different mesoscopic systems have been studied from the mechanical point of view. MoS<sub>2</sub> nanotubes is a kind of nanotubes that might replace carbon nanotubes because they can be produced with uniform electronic properties. They could also be interesting for scanning-probe applications, especially in biology, because they are chemically more reactive than their carbon counterparts. Before even considering this particular application, their mechanical properties should be investigated. Measurements of their mechanical properties presented in this thesis are the first “single-molecule” measurements performed on them. Bundles of single-walled MoS<sub>2</sub> nanotubes are prone to intertube sliding in the same way as carbon nanotubes. Their Young’s modulus, with a lower limit of 120GPa might not be spectacular as the previously published 1TPa value for the carbon nanotubes, but this is still in the range of common engineering materials in use today. The intertube shear modulus, measured the same way as was done for carbon nanotubes by Salvétat et al. [72], has a value of 160MPa. This is an order of magnitude lower than in the case of carbon nanotubes, already notorious for their easy intertube sliding. This shows that the van der Waals interaction between individual tubes is much weaker in the case of MoS<sub>2</sub>, indicating that MoS<sub>2</sub> nanotubes might manifest the behavior of weakly coupled 1D systems in other physical properties, for example magnetic susceptibility [178].

In the case of carbon nanotubes, a nanoscale “engineering” problem was addressed – how to connect carbon nanotubes together? The measurement method was extended using substrates compatible with imaging inside a transmission electron microscope. This enabled observations of nanotube structure and AFM measurements on the same nanotube, with repeatable and accurate repositioning of the sample both inside the TEM and AFM. Nanotube bundles irradiated with 200keV and 80keV electrons inside a TEM show a dramatical increase of the bending modulus, indicating the onset of crosslinking. Further irradiation decreases the bending modulus. TEM imaging confirmed that this decrease corresponds to structure amorphization. The crosslinking process is much more pronounced when irradiating with 80keV electrons, which is less damaging to the structure in the early stages of irradiation. Theoretical modelling based on DFT

calculations, performed by G. Csányi, shows that the most probable mechanism of crosslinking is bridge formation via interstitial atoms created during irradiation. These results also represent the first qualitative measurements of the irradiation effect on carbon nanotubes. Previous experiments consisted of TEM imaging supported by theoretical calculations. Apart from the academic significance, these findings could also have a profound influence on applying nanotubes as reinforcing fibers as they show the way to connecting carbon nanotubes with the goal of producing strong nanotube fibers. Furthermore, the method of depositing nanotubes on fabricated, patterned membranes could enable a host of related experiments in which TEM, SEM and AFM observations on nanotubes and nanowires could be combined.

Mechanical measurements on the biological equivalent of nanotubes, the microtubules, have revealed new facets of their already fascinating properties. Measurements of the bending modulus on the same microtubule have shown that they behave as a mechanically anisotropic cylinder, in strong contrast to a 20 year old belief that they can be modelled as being mechanically isotropic. In fact, microtubules have a shear modulus that is at least hundred times lower than their Young's modulus, indicating that the tubulin molecules are more strongly bound in the longitudinal than in the lateral direction. These measurements are also the first example where these two mechanical properties have been determined simultaneously on a single mesoscopic object. The temperature dependence of the shear modulus shows good correlation with the dynamic properties of microtubules, the assembly and disassembly speed, indicating that the dynamic behavior of microtubules is strongly influenced by their mechanical properties.

The mechanical measurements performed on microtubules are an introduction to a future systematic study in the field of cellular biophysics. Open questions like the influence of UV light or oxidative stress on the mechanical properties of microtubules could be addressed. The same method could also be applied to the study of other cytoskeletal components: actin and intermediate filaments. The later offers ample opportunity because it has been unjustly ignored by most of the community, so far.

# Appendix: mechanical deformation of beams

## Stretching of beams

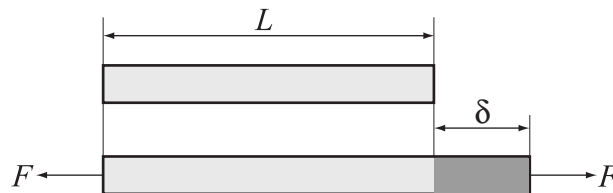


**Fig. A.1.** Elongation of a prismatic bar of initial length  $L$  subjected to an axial loading force

When a prismatic bar like the one on fig. A.1, is subjected to an axial force  $F$ , it will elongate by an amount  $\delta$ . If the force acts at the center of the cross-section, the uniform stress  $\sigma$  will be given by:

$$\sigma = \frac{F}{A} \quad (\text{A.1})$$

where  $A$  is the beam's cross-sectional area. If the bar is made of a homogeneous material, the axial strain will be:

$$\varepsilon = \frac{\delta}{L} \quad (\text{A.2})$$

In addition, if the material is linearly elastic and follows the Hooke's law, equation (4.13) on p. 36, the longitudinal stress and strain will be related by the equation

$$\sigma = E\varepsilon \quad (\text{A.3})$$

where  $E$  is the modulus of elasticity. The preceding equations can then be combined yielding the expression for the elongation  $\delta$  of a bar under an axial force  $F$ :

$$\delta = \frac{FL}{EA} \quad (\text{A.4})$$

The stiffness  $k$  is defined as the force required to produce a unit elongation:

$$k \equiv \frac{F}{\delta} = \frac{EA}{L} \quad (\text{A.5})$$

The flexibility  $f$  is defined simply as the reciprocal of stiffness  $k$ .

In experiments involving nanotubes, this configuration was initially difficult to achieve and was at the end realized by positioning nanotubes at the ends of two opposing AFM tips inside a SEM (see p. 47). A slightly more accessible configuration involved depositing long, thin nanotubes on trenches and deforming them in the perpendicular direction (p. 41). In this case, the nanotube can be treated as a stretched elastic string of a spring constant  $k$  in the geometry shown on fig. A.2. The tension  $T$  inside the string is  $T=k\Delta L$  where  $\Delta L$  is the elongation. The normal component of the force is then:

$$F = 2T \sin \alpha \quad (\text{A.6})$$

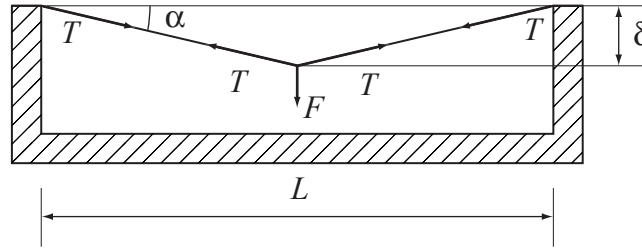


**Fig. A.2.** Stretching of a string suspended above a trench of width  $L_0$ . The point load  $F$  is applied in the middle.

In the simplest case, when the force is applied in the middle, the elongation becomes:

$$\Delta L = 2\sqrt{\left(\frac{L}{2}\right)^2 + \delta^2} - L = L \left[ \sqrt{1 + \left(\frac{2\delta}{L}\right)^2} - 1 \right] \quad (\text{A.7})$$

For small deformations, this simplifies to:

$$\Delta L \approx 2\left(\frac{\delta}{L}\right)^2 \quad (\text{A.8})$$

In this case,  $\sin \alpha$  can also be replaced by  $\tan \alpha = 2\delta/L$  which gives:

$$F = 4\left(\frac{\delta}{L}\right)^3 \quad (\text{A.9})$$

### **Differential equations for beam bending**

In the more general case, the structures under deformation will not only stretch but also bend. In addition to the load applied perpendicularly to the beam's axis, there will also be a torque acting perpendicularly to plane in which the beam is lying, causing the beam to rotate (bend). Finding the deformed beam's shape will involve identifying the reaction forces and couples of



the supports, and solving the differential equation of beam bending for a particular set of boundary conditions (fig. A.3).

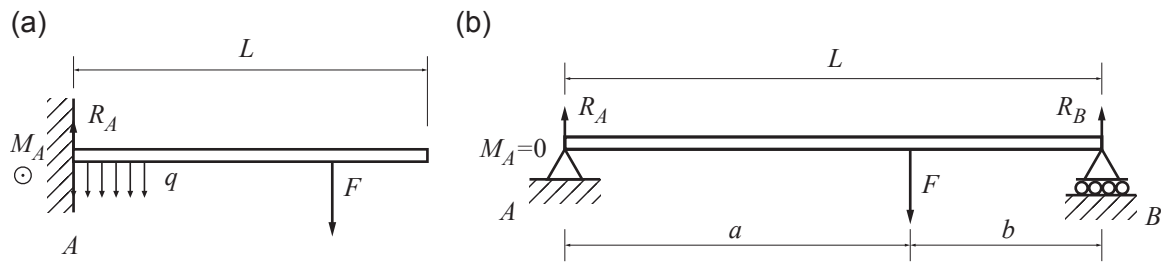


**Fig. A.3.** Examples of beams and the corresponding support forces and torques. (a) Cantilevered beam subjected to a point load  $F$  and a distributed load  $q$ . (b) A simple beam, free to rotate (but not to deflect) in points A and B, subjected to a point load  $F$ .

When a beam is loaded by forces or couples, internal stresses and strains are created. In order to determine them, the internal forces and couples will have to be identified. As an example, we can consider the case of a cantilever beam acted upon by a vertical force  $F$  at its free end, fig. A.4a.

Imagine that we cut through the beam at a cross section  $mn$  located at a distance  $x$  from the free end and isolate the left-hand part of the beam as a free body (fig. A.4b). The free body is held at equilibrium by the force  $F$  and stresses that act over the cut cross section  $mn$ . These stresses represent the action of the right-hand part of the beam on the left-hand part.

It is convenient to reduce the resultant to a shear force  $V$  acting parallel to the cross section and a bending moment  $M$ . The stress resultants in statically determinate beams can be calculated from the conditions of static equilibrium. In the case shown in fig. A.4, the shear force  $V$  and the bending moment  $M$  are  $V = P$ ,  $M = Px$ . The shear force and the bending moment are defined to be positive when acting on the left-hand part of a beam in the directions shown in fig. A.5. On the right-hand side, the directions are reversed.

In order to obtain relationships between the loads on the beam, let us consider an element of a beam cut out between two cross sections that are a distance  $dx$  apart (fig. A.5). In general,  $V$  and  $M$  are functions of distance. For the sake of generality, the load on the top section is supposed to be a distributed load  $q$ . From the equilibrium of forces in the vertical direction ( $\sum F = 0$ ) we get:

$$V - (V + dV) - qdx = 0 \tag{A.10}$$

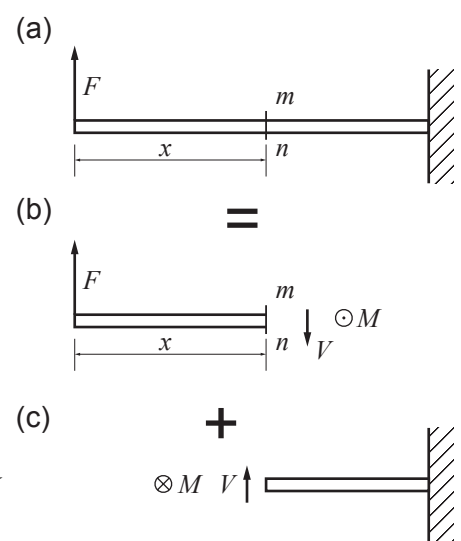


**Fig. A.4.** Stress resultants  $V$  and  $M$ .

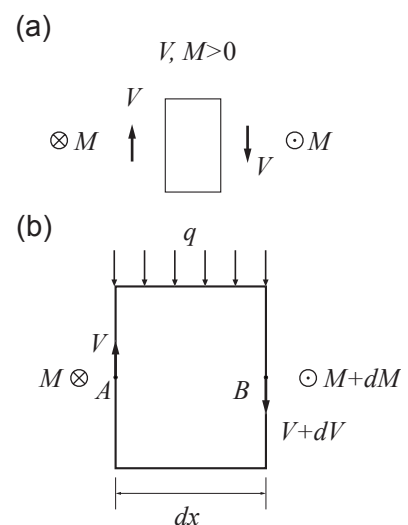


**Fig. A.5.** (a) Sign convention for  $V$  and  $M$ . (b) Element of a beam used in deriving relationships between loads, shear forces and bending moments.

therefore:

$$\frac{dV}{dx} = -q \quad (\text{A.11})$$

As a consequence, if there is no load on a part of a beam, the shear force stays constant.

On the other hand, from the equilibrium condition for the bending moment ( $\sum M = 0$ ), with respect to the point  $A$  (fig. A.5) we get:

$$(M + dM) - M - (V + dV)dx - \underbrace{\int_0^{dx} (q dx')}_{\frac{q(dx)^2}{2}} = 0 \quad (\text{A.12})$$

Neglecting the term containing the square of a differential yields the expression for the bending moment:

$$\frac{dM}{dx} = V \quad (\text{A.13})$$

In the case of a point load being applied on the top face of the segment, equations (A.11) and (A.13) will become:

$$\Delta V = -F, \quad \left. \frac{dM}{dx} \right|_A = V, \quad \left. \frac{dM}{dx} \right|_B = V - F \quad (\text{A.14})$$

Therefore, passing from the left to the right-hand side of the deformed beam and through the point of application of  $F$ , will abruptly change the shear force and the derivative of the bending moment.

In order to obtain the general differential equation for the shape of the deformed beam, we will now consider a cantilevered beam as the one shown on fig. A.6.

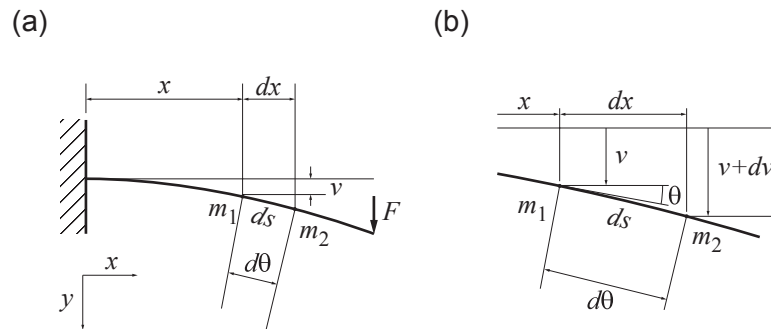


Fig. A.6. (a) Deflection curve of a beam. (b) Middle portion enlarged.

The coordinate systems' origin is at the fixed end. The  $xy$  plane is assumed to be a plane of symmetry and all loads act in this plane, making  $xy$  the plane of bending. The deflection  $v$  of the beam at any point  $m_i$  at distance  $x$  from the origin is the displacement of that point in the  $y$  direction, measured from the  $x$  axis to the deflection curve. Similarly, the angle of rotation  $\theta$  of the beam axis at any point  $m_i$  is the angle between the  $x$  axis and the tangent to the deflection curve (fig. A.6b). With the definition of  $x$  and  $y$  axis as in this case, the rotation angle will be positive when clockwise. The deflection at a second point  $m_2$  at a small distance further along the

curve  $ds$  is  $v+dv$ . Also, the angle of rotation at  $m_2$  is  $\theta+d\theta$ . Intersection of the lines normal to the tangent of the deflection curve will define the center of curvature  $O'$ . The distance from  $O'$  to the curve is the radius of curvature  $\rho$ . As seen on the figure,  $\rho d\theta=ds$ ; hence the curvature  $\kappa$  (a reciprocal of the radius of curvature  $\rho$ ) is given by the equation:

$$\kappa = \frac{1}{\rho} = \frac{d\theta}{ds} \quad (\text{A.15})$$

The slope of the deflection curve is equal to the tangent of the rotation angle  $\theta$ , thus:

$$\frac{dv}{dx} = \tan \theta; \quad \theta = \arctan \frac{dv}{dx} \quad (\text{A.16})$$

The curvature is then

$$\kappa = \frac{d\theta}{ds} = \frac{d(\arctan v')}{dx} \frac{dx}{ds} \quad (\text{A.17})$$

From fig. A.6  $ds^2 = dx^2 + dv^2$ , so

$$\frac{ds}{dx} = \sqrt{1 + \left(\frac{dv}{dx}\right)^2} = \sqrt{1 + (v')^2} \quad (\text{A.18})$$

Also, by differentiation:

$$\frac{d}{dx} \arctan(v') = \frac{v''}{1 + (v')^2} \quad (\text{A.19})$$

by substituting the last two expressions into the equation (A.15) for curvature we get:

$$\kappa = \frac{1}{\rho} = \frac{v''}{[1 + (v')^2]^{3/2}} \quad (\text{A.20})$$

This equation is based on geometric considerations only and applies to a beam of any material. Furthermore, there are no assumptions on the magnitudes of slopes and deflections.

In the case of small deflections, the corresponding curvatures are very small. Under these conditions the angle  $\theta$  is small, so we can make the approximation:

$$ds \approx dx \quad (\text{A.21})$$

Therefore, equation (A.15) becomes

$$\kappa = \frac{1}{\rho} = \frac{d\theta}{dx} \quad (\text{A.22})$$

Also, since  $\tan \theta \approx \theta$ , we can approximate equation (A.16) as follows:

$$\theta \approx \tan \theta = \frac{d\delta}{dx} \quad (\text{A.23})$$

Combining with equation (A.22) we obtain the expression for curvature:

$$\kappa = \frac{1}{\rho} = \frac{d\theta}{dx} = \frac{d^2\delta}{dx^2} \quad (\text{A.24})$$

A small section of the beam that is subjected to couples  $M_0$  will bend (fig. A.7a).

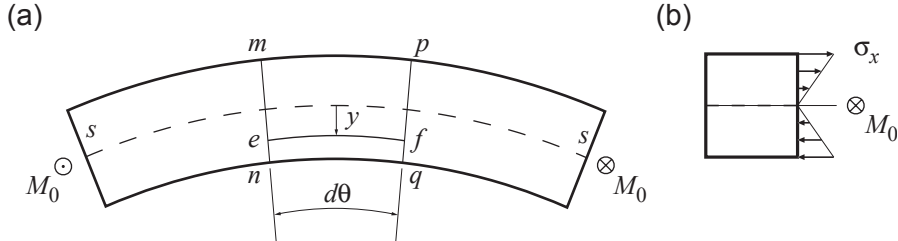


**Fig. A.7.** (a) Deformation of a beam in pure bending produced by couples  $M_0$   
 (b) Distribution of normal stresses  $\sigma_x$  in a beam of linearly elastic material.

The bending moment  $M$  in the beam due to the couples  $M_0$  is negative. Cross sections  $mn$  and  $pq$  will rotate with respect to each other. The upper part of the beam will be in tension and the lower in compression. In the interior of the beam there is a surface which will not change in length, called the neutral surface of the beam. For a beam made of a material that obeys the Hooke's law, this surface will pass through the middle of the beam. After bending, the line  $ef$  at distance  $y$  from the neutral surface will have a length of  $L_1$ :

$$L_1 = (\rho - y)d\theta = dx - \frac{y}{\rho}dx \quad (\text{A.25})$$

As the undeformed length of the line is  $dx$ , the elongation will be  $L_1 - dx$ , or  $-ydx/\rho$ . The corresponding elongation will be:

$$\varepsilon_x = -\frac{y}{\rho} = -\kappa y \quad (\text{A.26})$$

and the corresponding stress will be, according to the Hooke's law:

$$\sigma_x = E\varepsilon_x = -E\kappa y \quad (\text{A.27})$$

with a distribution shown in fig. A.7b. A positive stress  $\sigma_x$  acting on the element  $dA$  produces a negative moment about the  $z$  axis which is a negative contribution to the moment  $M_0$ :

$$dM_0 = -\sigma_x y dA \quad (\text{A.28})$$

Thus, the total bending moment  $M$  will be:

$$M = \int \sigma_x y dA = -\kappa E \int y^2 dA = -\kappa EI \quad (\text{A.29})$$

where  $I$  is the moment of inertia defined as:

$$I = \int y^2 dA \quad (\text{A.30})$$

The curvature therefore becomes:

$$\kappa = \frac{1}{\rho} = -\frac{M}{EI} \quad (\text{A.31})$$

Equation (A.31) is valid regardless of the magnitude of deflections. Combining equation (A.24) which is valid for small deflections, with equation (A.31) yields:

$$\frac{d^2v}{dx^2} = -\frac{M}{EI} \quad (\text{A.32})$$

which is the basic differential equation of the deflection curve of a beam. It can be integrated in each particular case to find the angle of rotation  $\theta$  or deflection  $v$ , provided the bending moment  $M$  is known. If we combine the equation (A.32) with the previously obtained expressions for the bending moment (A.13) and the shear force (A.11), we obtain:

$$EI \frac{d^3v}{dx^3} = -V, \quad EI \frac{d^4v}{dx^4} = q \quad (\text{A.33})$$

### ***Cantilevered beam under a concentrated load***

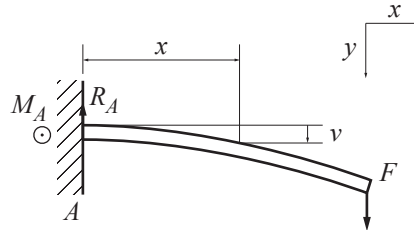


**Fig. A.8.** Beam clamped at one end.

In the case of a cantilevered beam as the one shown on fig. A.8, the bending moment in the static equilibrium is:

$$M = -F(L - x) \quad (\text{A.34})$$

The differential equation (A.32) then becomes:

$$EI \frac{d^2v}{dx^2} = F(L - x) \quad (\text{A.35})$$

The first integration yields:

$$EI \frac{dv}{dx} = -\frac{F(L - x)^2}{2} + C_1 \quad (\text{A.36})$$

The constant of integration  $C_1$  can be found from the condition that the slope of the beam is zero at the support,  $v'(0) = 0$ :

$$v'(0) = 0 \Rightarrow C_1 = \frac{FL^2}{2} \quad (\text{A.37})$$

The second integration yields:

$$EIv = \frac{F(L-x)^3}{6} + \frac{FL^2x}{2} + C_2 \quad (\text{A.38})$$

as the deflection at the support is zero, the constant  $C_2$  is found to be:

$$v(0) = 0 \Rightarrow C_2 = -\frac{FL^3}{6} \quad (\text{A.39})$$

and the equation of the deflection curve becomes:

$$v = \frac{F}{2EI} \left[ Lx^2 - \frac{x^3}{3} \right] \quad (\text{A.40})$$

Total deflection at the free end is then:

$$\delta = \frac{FL^3}{3EI} \quad (\text{A.41})$$

In the case of large deflections, the exact expression for the curvature (A.20) must be used. Thus, the differential equation for the deflection curve becomes:

$$\frac{v''}{[1+(v')^2]^{3/2}} = -\frac{M}{EI} \quad (\text{A.42})$$

The vertical deflection at the end of the cantilever is:

$$\frac{\delta_v}{L} = 1 - \sqrt{\frac{4EI}{FL^2}} [E(k) - E(k, \phi)] \quad (\text{A.43})$$

where  $E(k)$  and  $E(k, \phi)$  are the complete and incomplete elliptic integrals of the second kind, respectively:

$$E(k, \phi) = \int_0^\phi \sqrt{1 - k^2 \sin^2 \theta} d\theta, \quad E(k) = E(k, \pi/2) \quad (\text{A.44})$$

Where  $k$  is the solution of equation:

$$F(k) - F(k, \phi) = \sqrt{\frac{FL^2}{EI}}, \quad \phi = \arcsin \frac{1}{k\sqrt{2}} \quad (\text{A.45})$$

$F(k)$  and  $F(k, \phi)$  are the complete and incomplete elliptic integrals of the first kind:

$$F(k, \phi) = \int_0^\phi \frac{d\theta}{\sqrt{1 - k^2 \sin^2 \theta}}, \quad F(k) = F(k, \pi/2) \quad (\text{A.46})$$

The discrepancy between the approximative and exact solutions to beam bending, plotted on fig. A.9, becomes larger than 10% for deformations characterized by  $\delta/L > 0.42$ .

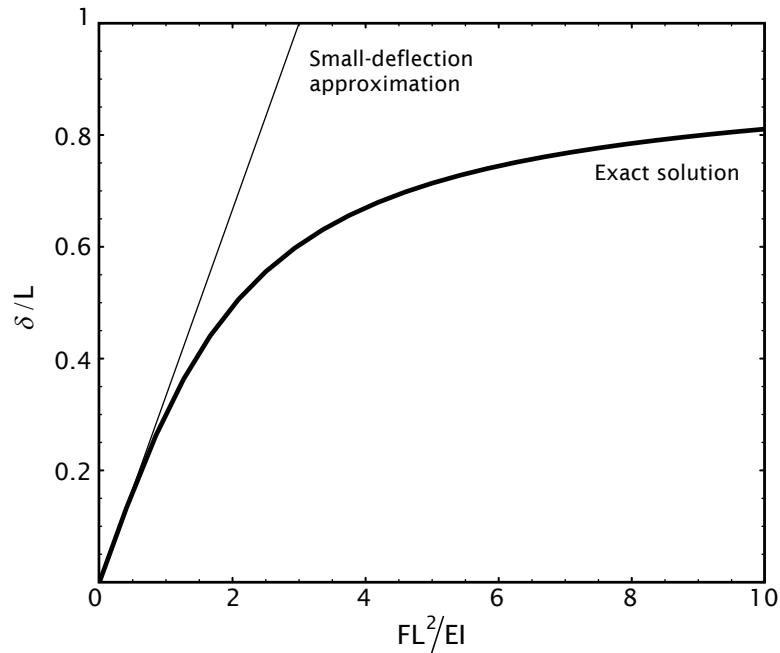


**Fig. A.9.** Large deflection of a cantilever beam with a concentrated load  $F$  at the free end compared with the small-displacement approximation.

### ***Simply supported beam under a concentrated load***

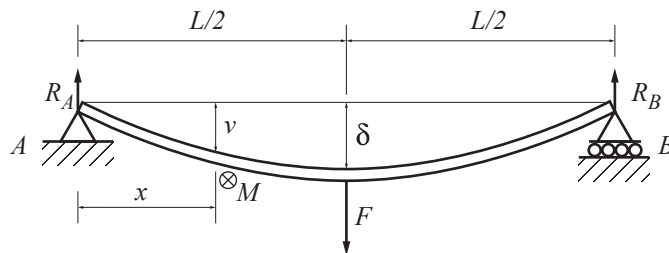


**Fig. A.10.** Simply supported beam loaded in the middle.

The case of the deformation of a simply supported beam loaded in the middle (fig. A.10) can be studied in a similar manner. The beam has to be divided in two parts, and the equation (A.32) solved for each part separately – in this case the solution for the left part of the beam ( $0 \leq x \leq L/2$ ) will be considered. The final solution will be symmetrical with respect to the beam's middle. From the condition for static equilibrium, the bending moment is:

$$M = R_a x = \frac{F}{2} x \quad (\text{A.47})$$

The differential equation (A.32) becomes:

$$EI \frac{d^2 v}{dx^2} = -\frac{F}{2} x \quad (\text{A.48})$$

after the first integration we get:

$$EI \frac{dv}{dx} = -\frac{F}{4} x^2 + C_1 \quad (\text{A.49})$$

and after the second:

$$EIv = -\frac{F}{12}x^3 + C_1x + C_2 \quad (\text{A.50})$$

Integration constants  $C_1$  and  $C_2$  can be found from the boundary conditions. The slope of the deflection curve in the middle will be equal to zero, as well as the deflection at the end, which yields for  $C_1$  and  $C_2$ :

$$C_1 = \frac{FL^2}{16}, \quad C_2 = 0 \quad (\text{A.51})$$

This leads to the expression for the deflection curve:

$$v = \frac{Fx}{48EI}(3L^2 - 4x^2) \quad (\text{A.52})$$

The deflection  $\delta$  at the middle will then be given by:

$$\delta = \frac{FL^3}{48EI} \quad (\text{A.53})$$

### Clamped beam under a concentrated load

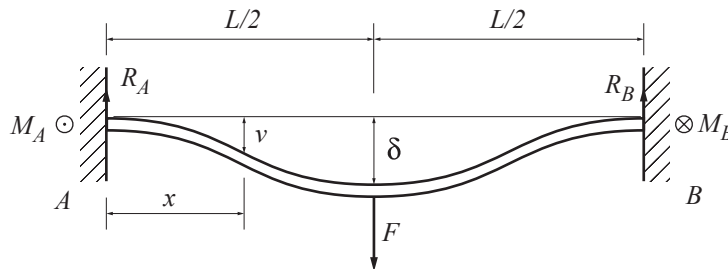


**Fig. A.11.** Deformation of a clamped beam of length  $L$  under the application of a point force  $F$  in the middle of the suspended part.

As the load acts at the midpoint of the beam, the reaction forces and moments are, from the symmetry,  $M_a = M_b$  and  $R_a = R_b = F/2$ . No load acts on the beam in the region between  $x=0$  and  $x=L/2$ , so the differential equation (A.33) becomes:

$$EIv'''' = 0 \quad (\text{A.54})$$



Successive integration yields:

$$EIv''' = C_1 = -V \quad (\text{A.55})$$

$$EIv'' = C_1x + C_2 = -M \quad (\text{A.56})$$

$$EIv' = \frac{C_1x^2}{2} + C_2x + C_3 \quad (\text{A.57})$$

$$EIv = \frac{C_1x^3}{6} + \frac{C_2x^2}{2} + C_3x + C_4 \quad (\text{A.58})$$

The shear force throughout the left-hand side of the beam is equal to  $R_a$ ; hence from equation (A.33) and equation (A.55) we get  $C_1 = -F/2$ . The bending moment at  $x=0$  is  $M_a$ , so from equation (A.56) we get  $C_2 = M_a$ . The two conditions on the slope of the beam ( $v' = 0$  at  $x=0$  and  $x=L/2$ ) yield  $C_3 = 0$  and

$$M_a = \frac{FL}{8} \quad (\text{A.59})$$

Finally, the condition  $v=0$  at  $x=0$  gives  $C_4=0$ . Combining these results leads to the equation of the deflection curve:

$$v = \frac{Fx^2}{48EI}(3L - 4x) \quad \left(0 \leq x \leq \frac{L}{2}\right) \quad (\text{A.60})$$

and the deflection  $\delta$  in the middle:

$$\delta = \frac{FL^3}{192EI} \quad (\text{A.61})$$

### Shear deflections of beams

For greater accuracy, the deflections of beams due to shearing have to be determined and added to the bending deflections. The most convenient way of obtaining beam deflections due to shearing is using the unit-load method, based on the principle of virtual work.

Let us consider a differential element of dimensions  $dx$ ,  $dy$  and  $dz$  (fig. A.12) from the interior of the beam subjected to a unit load.

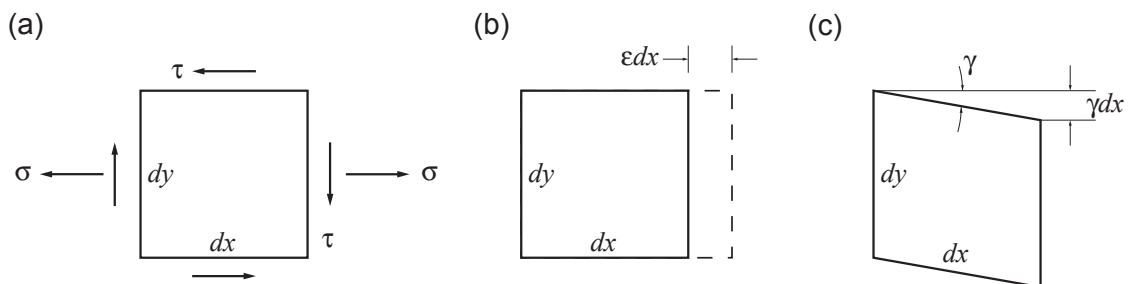


**Fig. A.12.** Element from a beam. (a) Normal stresses  $\sigma$  and shear stresses  $\tau$  act on both sides. (b) Extension of the beam element by the moment  $M_L$ . (c) Shear distortion caused by the shear force  $V_L$ .

The element is deformed due to normal stresses  $\sigma$  and shear stresses  $\tau$  caused by the bending moment  $M_U$  and the shear force  $V_U$  produced by the unit load. These stresses can be calculated from the flexure and shear formulas:

$$\sigma = \frac{M_U y}{I}, \quad \tau = \frac{V_U Q}{Ib} \quad (\text{A.62})$$

where  $Q$  is the first moment of the cross-sectional area and  $b$  the width of the segment.

In the unit-load method, the virtual deformations imparted to the element are chosen to be the same as the deformations caused by the actual loads which produce bending moments  $M_L$  and shear forces  $V_L$ . The corresponding deformations consist of an extensional strain  $\varepsilon$  and shear strain  $\gamma$  (fig. A.12) given by:

$$\varepsilon = \frac{M_L y}{EI}, \quad \tau = \frac{V_L Q}{GIb} \quad (\text{A.63})$$

The internal work of stresses  $\sigma$  and  $\tau$  acting on the differential element is:

$$\begin{aligned} dW_{int} &= (\sigma dydz)(\varepsilon dx) + (\tau dydz)(\gamma dx) = \\ &= \frac{M_U M_L y^2}{EI^2} dx dy dz + \frac{V_U V_L Q^2}{GI^2 b^2} dx dy dz \end{aligned} \quad (\text{A.64})$$

The total internal work is obtained by integrating the preceding expression throughout the volume of the beam:

$$W_{int} = \int \frac{M_U M_L y^2}{EI^2} dx dy dz + \int \frac{V_U V_L Q^2}{GI^2 b^2} dx dy dz \quad (\text{A.65})$$

The following quantities are constant at a given cross section of the beam:  $M_U$ ,  $M_L$ ,  $V_U$ ,  $V_L$ ,  $E$ ,  $G$  and  $I$ , so the preceding integral can be separated into an integration over a cross-sectional area  $A$  and length  $L$  as:

$$W_{int} = \int_L \frac{M_U M_L}{EI^2} \left[ \int_A y^2 dz dy \right] dx + \int_L \frac{V_U V_L}{GI^2} \left[ \int_A \frac{Q^2}{b^2} dy dz \right] dx \quad (\text{A.66})$$

The first term in brackets is the moment of inertia  $I$  and the second is the form factor for shear,  $f_s$ , a constant dependent on the cross-sectional dimensions and shape of the beam, defined as:

$$f_s = \frac{A}{I^2} \int_A \frac{Q^2}{b^2} dA \quad (\text{A.67})$$

where  $dA = dydz$  represents an element of area in the cross section of the beam. The expression for internal virtual work simplifies into:

$$W_{int} = \int \frac{M_U M_L dx}{EI} + \int \frac{f_s V_U V_L dx}{GA} \quad (\text{A.68})$$

Finally, the unit load equation for the deflection  $\Delta$  is obtained by equating external work (equal to  $1 \cdot \Delta$ ) with equation (A.68) for internal work:

$$\Delta = \int \frac{M_U M_L dx}{EI} + \int \frac{f_s V_U V_L dx}{GA} \quad (\text{A.69})$$

In case of a clamped beam, the bending moment and shear force due to actual load can be obtained from equations (A.55) and (A.56):

$$M_L = \frac{FL}{8} - \frac{Fx}{2}, \quad V_L = \frac{F}{2} \quad (\text{A.70})$$

The unit load acting at the middle of the beam produces the following bending moments and shear forces:

$$M_U = \frac{L}{8} - \frac{x}{2}, \quad V_U = \frac{1}{2} \quad (\text{A.71})$$

Substitution of these quantities into equation (A.69) yields the expression for the deflection  $\delta$  at the midpoint of the beam:

$$\begin{aligned} \delta &= \frac{2}{EI} \int_0^{L/2} \left( \frac{FL}{8} - \frac{Fx}{2} \right) \left( \frac{L}{8} - \frac{x}{2} \right) dx + \frac{2f_s}{GA} \int_0^{L/2} \frac{F}{2} \frac{1}{2} dx = \\ &= \frac{FL^3}{192EI} + f_s \frac{FL}{4GA} \end{aligned} \quad (\text{A.72})$$

The same method yields for the deflection  $\delta$  at the free end of a cantilevered beam with a concentrated load  $F$  at the free end:

$$\delta = \frac{FL^3}{3EI} + f_s \frac{EI}{GA} \quad (\text{A.73})$$



# Bibliography

- [1] G. Binnig, H. Rohrer, C. Gerber and E. Weibel: *Tunneling through a Controllable Vacuum Gap*, Applied Physics Letters **40**, 178 (1982); G. Binnig and H. Rohrer: *Vacuum Tunnel Microscope*, Helvetica Physica Acta **55**, 128 (1982).
- [2] <http://www.nobel.se/physics/laureates/1986/>
- [3] G. Binnig, C. F. Quate and C. Gerber: *Atomic Force Microscope*, Physical Review Letters **56**, 930 (1986).
- [4] S. A. C. Gould, B. Drake, C. B. Prater, A. L. Weisenhorn, S. Manne, H. G. Hansma, P. K. Hansma, J. Massie, M. Longmire, V. Elings, B. D. Northern, B. Mukergee, C. M. Peterson, W. Stoeckenius, T. R. Albrecht and C. F. Quate: *From Atoms to Integrated-Circuit Chips, Blood-Cells, and Bacteria with the Atomic Force Microscope*, Journal of Vacuum Science & Technology A **8**, 369 (1990).
- [5] U. D. Schwarz, H. Hölscher and R. Wiesendanger: *Atomic Resolution in Scanning Force Microscopy: Concepts, Requirements, Contrast Mechanisms and Image Interpretation*, Physical Review B **62**, 13089 (2000).
- [6] R. Erlandsson, G. M. McClelland, C. M. Mate and S. Chiang: *Atomic Force Microscopy Using Optical Interferometry*, Journal of Vacuum Science & Technology A **6**, 266 (1988); D. Rugar, H. J. Mamin, R. Erlandsson, J. E. Stern and B. D. Terris: *Force Microscope Using a Fiber-Optic Displacement Sensor*, Review of Scientific Instruments **59**, 2337 (1988).
- [7] E. Meyer, H. Heinzelmann, P. Grutter, T. Jung, H. R. Hidber, H. Rudin and H. J. Guntherodt: *Atomic Force Microscopy for the Study of Tribology and Adhesion*, Thin Solid Films **181**, 527 (1989).
- [8] C. W. Yuan, E. Batalla, M. Zacher, A. L. Delozanne, M. D. Kirk and M. Tortonese: *Low-Temperature Magnetic Force Microscope Utilizing a Piezoresistive Cantilever*, Applied Physics Letters **65**, 1308 (1994).
- [9] J. P. Aime, Z. Elkaakour, S. Gauthier, D. Michel, T. Bouhacina and J. Curely: *Role of the Force of Friction on Curved Surfaces in Scanning Force Microscopy*, Surface Science **329**, 149 (1995).
- [10] H. K. Wickramasinghe: *Scanning Probe Microscopy - Current Status and Future Trends*, Journal of Vacuum Science & Technology A **8**, 363 (1990); F. Ohnesorge and G. Binnig: *True Atomic-Resolution by Atomic Force Microscopy through Repulsive and Attractive Forces*, Science **260**, 1451 (1993); Y. Martin, C. C. Williams and H. K. Wickramasinghe:

- Atomic Force Microscope Force Mapping and Profiling on a Sub 100-Å Scale*, Journal of Applied Physics **61**, 4723 (1987).
- [11] P. K. Hansma, J. P. Cleveland, M. Radmacher, D. A. Walters, P. E. Hillner, M. Bezanilla, M. Fritz, D. Vie, H. G. Hansma, C. B. Prater, J. Massie, L. Fukunaga, J. Gurley and V. Elings: *Tapping Mode Atomic Force Microscopy in Liquids*, Applied Physics Letters **64**, 1738 (1994).
- [12] M. Radmacher, R. W. Tillmann, M. Fritz and H. E. Gaub: *From Molecules to Cells - Imaging Soft Samples with the Atomic Force Microscope*, Science **257**, 1900 (1992).
- [13] A. Hammiche, M. Reading, H. M. Pollock, M. Song and D. J. Hourston: *Localized Thermal Analysis Using a Miniaturized Resistive Probe*, Review of Scientific Instruments **67**, 4268 (1996).
- [14] <http://www.ntmdt.ru/products/SFM%20Probes/WT>
- [15] A. T. Woolley, C. L. Cheung, J. H. Hafner and C. M. Lieber: *Structural Biology with Carbon Nanotube AFM Probes*, Chemistry & Biology **7**, R193 (2000).
- [16] J. P. Cleveland, S. Manne, D. Bocek and P. K. Hansma: *A Nondestructive Method for Determining the Spring Constant of Cantilevers for Scanning Force Microscopy*, Review of Scientific Instruments **64**, 403 (1993).
- [17] Formerly Park Scientific Instruments, Thermomicroscopes, Acquired by Veeco, <http://www.veeco.com>
- [18] G. Binnig and D. P. E. Smith: *Single-Tube 3-Dimensional Scanner for Scanning Tunneling Microscopy*, Review of Scientific Instruments **57**, 1688 (1986).
- [19] Park Scientific Instruments SPM guide.
- [20] D. B. Williams and C. B. Carter: *Transmission Electron Microscopy*, Plenum Press, New York and London (1996).
- [21] S. Iijima: *Helical Microtubules of Graphitic Carbon*, Nature **354**, 56 (1991).
- [22] S. Amelinckx, A. Lucas and P. Lambin: *Electron Diffraction and Microscopy of Nanotubes*, Reports on Progress in Physics **62**, 1471 (1999).
- [23] X. F. Zhang, X. B. Zhang, S. Amelinckx, G. Van Tendeloo and J. Van Landuyt: *The Reciprocal Space of Carbon-Tubes: A Detailed Interpretation of the Electron Diffraction Effects*, Ultramicroscopy **54**, 237 (1994).
- [24] H. W. Kroto, J. R. Heath, S. C. O'Brien, R. F. Curl and R. E. Smalley: *C-60 - Buckminsterfullerene*, Nature **318**, 162 (1985).
- [25] [http://www.ruf.rice.edu/~smalley/image\\_gallery.htm](http://www.ruf.rice.edu/~smalley/image_gallery.htm)
- [26] S. Iijima: *High-Resolution Electron-Microscopy of Some Carbonaceous Materials*, Journal of Microscopy **119**, 99 (1980).
- [27] H. W. Zhu, C. L. Xu, D. H. Wu, B. Q. Wei, R. Vajtai and P. M. Ajayan: *Direct Synthesis of Long Single-Walled Carbon Nanotube Strands*, Science **296**, 884 (2002).
- [28] C.-H. Kiang, M. Endo, P. M. Ajayan, G. Dresselhaus and M. S. Dresselhaus: *Size Effects in Carbon Nanotubes*, Physical Review Letters **81**, 1869 (1998).
- [29] A. Thess, R. Lee, P. Nikolaev, H. Dai, P. Petit, J. Robert, C. Xu, Y. H. Lee, S. G. Kim, A. G. Rinzler, Daniel T. Colbert, G. Scuseria, D. Tománek, J. E. Fischer and R. E. Smalley: *Crystalline Ropes of Metallic Carbon Nanotubes*, Science **273**, 483 (1996).

- 
- [30] W. Kratschmer, L. D. Lamb, K. Fostiropoulos and D. R. Huffman: *Solid C-60 - a New Form of Carbon*, Nature **347**, 354 (1990).
- [31] D. S. Bethune, C. H. Kiang, M. S. Devries, G. Gorman, R. Savoy, J. Vazquez and R. Beyers: *Cobalt-Catalyzed Growth of Carbon Nanotubes with Single-Atomic-Layer Walls*, Nature **363**, 605 (1993).
- [32] J. P. Lu: *Elastic Properties of Carbon Nanotubes and Nanoropes*, Physical Review Letters **79**, 1297 (1997).
- [33] W. Z. Li, S. S. Xie, L. X. Qian, B. H. Chang, B. S. Zou, W. Y. Zhou, R. A. Zhao and G. Wang: *Large-Scale Synthesis of Aligned Carbon Nanotubes*, Science **274**, 1701 (1996).
- [34] J. Kong, H. T. Soh, A. M. Cassell, C. F. Quate and H. J. Dai: *Synthesis of Individual Single-Walled Carbon Nanotubes on Patterned Silicon Wafers*, Nature **395**, 878 (1998).
- [35] S. Fan, M. G. Chapline, N. R. Franklin, T. W. Tomblor, A. M. Cassell and H. Dai: *Self-Oriented Regular Arrays of Carbon Nanotubes and Their Field Emission Properties*, Science **283**, 512 (1999).
- [36] Y. G. Zhang, A. L. Chang, J. Cao, Q. Wang, W. Kim, Y. M. Li, N. Morris, E. Yenilmez, J. Kong and H. J. Dai: *Electric-Field-Directed Growth of Aligned Single-Walled Carbon Nanotubes*, Applied Physics Letters **79**, 3155 (2001).
- [37] N. R. Franklin and H. Dai: *An Enhanced CVD Approach to Extensive Nanotube Networks with Directionality*, Advanced Materials **12**, 890 (2000).
- [38] J.-P. Salvetat, A. J. Kulik, J.-M. Bonard, G. A. D. Briggs, T. Stöckli, K. Méténier, S. Bonnamy, F. Béguin, N. A. Burnham and L. Forró: *Elastic Modulus of Ordered and Disordered Multiwalled Carbon Nanotubes*, Advanced Materials **11**, 161 (1999).
- [39] H. Hiura, T. W. Ebbesen and K. Tanigaki: *Opening and Purification of Carbon Nanotubes in High Yields*, Advanced Materials **7**, 275 (1995).
- [40] J. Liu, A. G. Rinzler, H. Dai, J. H. Hafner, R. K. Bradley, P. J. Boul, A. Lu, T. Iverson, K. Shelimov, C. B. Huffman, F. Rodriguez-Macias, Y.-S. Shon, T. R. Lee, D. T. Colbert and R. E. Smalley: *Fullerene Pipes*, Science **280**, 1253 (1998).
- [41] P. M. Ajayan and T. W. Ebbesen: *Nanometre-Size Tubes of Carbon*, Reports on Progress in Physics **60**, 1025 (1997).
- [42] L. Thien-Nga, K. Hernadi, E. Ljubovic, S. Garaj and L. Forró: *Mechanical Purification of Single-Walled Carbon Nanotube Bundles from Catalytic Particles*, Nano Letters **2**, 1349 (2002).
- [43] L. Chico, V. H. Crespi, L. X. Benedict, S. G. Louie and M. L. Cohen: *Pure Carbon Nanoscale Devices: Nanotube Heterojunctions*, Physical Review Letters **76**, 971 (1996); X. Blase, L. X. Benedict, E. L. Shirley and S. G. Louie: *Hybridization Effects and Metallicity in Small Radius Carbon Nanotubes*, Physical Review Letters **72**, 1878 (1994); J. W. Mintmire, B. I. Dunlap and C. T. White: *Are Fullerene Tubules Metallic*, Physical Review Letters **68**, 631 (1992).
- [44] R. Saito, M. Fujita, G. Dresselhaus and M. S. Dresselhaus: *Electronic-Structure of Chiral Graphene Tubules*, Applied Physics Letters **60**, 2204 (1992).
- [45] T. W. Odom, J.-L. Huang, P. Kim and C. M. Lieber: *Structure and Electronic Properties of Carbon Nanotubes*, Journal of Physical Chemistry B **104**, 2794 (2000).

- [46] J. M. Zuo, I. Vartanyants, M. Gao, R. Zhang and L. A. Nagahara: *Atomic Resolution Imaging of a Carbon Nanotube from Diffraction Intensities*, *Science* **300**, 1419 (2003).
- [47] M. Kociak, K. Suenaga, K. Hirahara, Y. Saito, T. Nakahira and S. Iijima: *Linking Chiral Indices and Transport Properties of Double-Walled Carbon Nanotubes*, *Physical Review Letters* **89**, 155501 (2002); Xiao-Feng Zhang and Z. Zhang: *Progress in Transmission Electron Microscopy*, Springer Verlag, Berlin Heidelberg New York (2001).
- [48] R. Krupke, F. Hennrich, H. V. Lohneysen and M. M. Kappes: *Separation of Metallic from Semiconducting Single-Walled Carbon Nanotubes*, *Science* **301**, 344 (2003).
- [49] M. S. Strano, C. A. Dyke, M. L. Usrey, P. W. Barone, M. J. Allen, H. Shan, C. Kittrell, R. H. Hauge, J. M. Tour and R. E. Smalley: *Electronic Structure Control of Single-Walled Carbon Nanotube Functionalization*, *Science* **301**, 1519 (2003).
- [50] S. G. Lemay, Jorg w. janssen, Michiel van den hout, Maarten mooij, Michael j. bronikowski, Peter a. willis, Richard e. smalley, Leo p. kouwenhoven and Cees dekker: *Two-Dimensional Imaging of Electronic Wavefunctions in Carbon Nanotubes*, *Nature* **412**, 617 (2001).
- [51] S. G. Louie: *Electronic Properties, Junctions, and Defects of Carbon Nanotubes*, *Topics in Applied Physics* **80**, 113 (2001); N. Hamada, S. Sawada and A. Oshiyama: *New One-Dimensional Conductors: Graphitic Microtubules*, *Physical Review Letters* **68**, 1579 (1992).
- [52] M. Ouyang, J.-L. Huang, C. L. Cheung and C. M. Lieber: *Energy Gaps in "Metallic" Single-Walled Carbon Nanotubes*, *Science* **292**, 702 (2001).
- [53] R. Saito, G. Dresselhaus and M. S. Dresselhaus: *Physical Properties of Carbon Nanotubes*, Imperial College Press, London (1998).
- [54] E. Hernandez, C. Goze, P. Bernier and A. Rubio: *Elastic Properties of C and Bxcynz Composite Nanotubes*, *Physical Review Letters* **80**, 4502 (1998).
- [55] D. Sanchez-Portal, E. Artacho, J. M. Solar, A. Rubio and P. Ordejon: *Ab Initio Structural, Elastic, and Vibrational Properties of Carbon Nanotubes*, *Physical Review B* **59**, 12678 (1999).
- [56] B. I. Yakobson, C. J. Brabec and J. Bernholc: *Nanomechanics of Carbon Tubes: Instabilities Beyond the Linear Response.*, *Physical Review Letters* **76**, 2511 (1996).
- [57] S. Iijima, C. Brabec, A. Maiti and J. Bernholc: *Structural Flexibility of Carbon Nanotubes*, *Journal of Chemical Physics* **104**, 2089 (1996).
- [58] E. W. Wong, P. E. Sheehan and C. M. Lieber: *Nanobeam Mechanics: Elasticity, Strength and Toughness of Nanorods and Nanotubes*, *Science* **277**, 1971 (1997).
- [59] A. J. Stone and D. J. Wales: *Theoretical-Studies of Icosahedral C60 and Some Related Species*, *Chemical Physics Letters* **128**, 501 (1986).
- [60] M. B. Nardelli, B. I. Yakobson and J. Bernholc: *Mechanism of Strain Release in Carbon Nanotubes*, *Physical Review B* **57**, R4277 (1998).
- [61] M. B. Nardelli, B. I. Yakobson and J. Bernholc: *Brittle and Ductile Behavior in Carbon Nanotubes*, *Physical Review Letters* **81**, 4656 (1998).
- [62] G. G. Samsonidze, G. G. Samsonidze and B. I. Yakobson: *Kinetic Theory of Symmetry-Dependent Strength in Carbon Nanotubes*, *Physical Review Letters* **88**, 065501 (2002).



- 
- [63] B. I. Yakobson, M. P. Campbell, C. J. Brabec and J. Bernholc: *High Strain Rate Fracture and C-Chain Unraveling in Carbon Nanotubes*, *Computational Materials Science* **8**, 341 (1997).
- [64] D. Appell: *Wired for Success*, *Nature* **419**, 553 (2002).
- [65] <http://www.ruf.rice.edu/~smalley/>
- [66] M. M. J. Treacy, T. W. Ebbesen and J. M. Gibson: *Exceptionally High Young's Modulus Observed for Individual Carbon Nanotubes*, *Nature* **381**, 678 (1996).
- [67] A. Krishnan, E. Dujardin, T. W. Ebbesen, P. N. Yianilos and M. M. J. Treacy: *Young's Modulus of Single-Walled Nanotubes*, *Physical Review B* **58**, 14013 (1998).
- [68] N. G. Chopra and A. Zettl: *Measurement of the Elastic Modulus of a Multi-Wall Boron Nitride Nanotube*, *Solid State Communications* **105**, 297 (1998).
- [69] P. Poncharal, Z. L. Wang, D. Ugarte and W. A. De Heer: *Electrostatic Deflections and Electromechanical Resonances of Carbon Nanotubes*, *Science* **283**, 1513 (1999).
- [70] D. A. Walters, L. M. Ericson, M. J. Casavant, J. Liu, D. T. Colbert, K. A. Smith and R. E. Smalley: *Elastic Strain of Freely Suspended Single-Wall Carbon Nanotube Ropes*, *Applied Physics Letters* **74**, 3803 (1999).
- [71] J.-P. Salvetat, J. M. Bonard, N. H. Thomson, A. J. Kulik, L. Forró, W. Benoit and L. Zuppiroli: *Mechanical Properties of Carbon Nanotubes*, *Applied Physics A* **69**, 255 (1999).
- [72] J.-P. Salvetat, G. A. D. Briggs, J.-M. Bonard, R. R. Bacsa, A. J. Kulik, T. Stöckli, N. Burnham and L. Forró: *Elastic and Shear Moduli of Single-Walled Carbon Nanotube Ropes*, *Physical Review Letters* **82**, 944 (1999).
- [73] J. M. Gere and S. P. Timoshenko: *Mechanics of Materials*, PWS-Kent, Boston (1984).
- [74] M.-F. Yu, T. Kowalewski and R. S. Ruoff: *Investigation of the Radial Deformability of Individual Carbon Nanotubes under Controlled Indentation Force*, *Physical Review Letters* **85**, 1456 (2000).
- [75] A. P. Boresi and O. M. Sidebottom: *Advanced Mechanics of Materials*, John Wiley & Sons, New York (1985).
- [76] M.-F. Yu, O. Lourie, M. J. Dyer, K. Moloni, T. F. Kelly and R. S. Ruoff: *Strength and Breaking Mechanism of Multiwalled Carbon Nanotubes under Tensile Load*, *Science* **287**, 637 (2000).
- [77] M.-F. Yu, B. S. Files, S. Arepalli and R. S. Ruoff: *Tensile Loading of Ropes of Single Wall Carbon Nanotubes and Their Mechanical Properties*, *Physical Review Letters* **84**, 5552 (2000).
- [78] T. Fujii, M. Suzuki, M. Miyashita, M. Yamaguchi, T. Onuki, H. Nakamura, T. Matsubara, H. Yamada and K. Nakayama: *Micropattern Measurement with an Atomic Force Microscope*, *Journal of Vacuum Science & Technology B* **9**, 666 (1991).
- [79] L. Margulis, G. Salitra, R. Tenne and M. Talianker: *Nested Fullerene-Like Structures*, *Nature* **365**, 113 (1993); R. Tenne, L. Margulis, M. Genut and G. Hodes: *Polyhedral and Cylindrical Structures of Tungsten Disulfide*, *Nature* **360**, 444 (1992).
- [80] N. G. Chopra, R. J. Luyken, K. Cherrey, V. H. Crespi, M. L. Cohen, S. G. Louie and A. Zettl: *Boron-Nitride Nanotubes*, *Science* **269**, 966 (1995).
- [81] R. G. Dickinson and L. Pauling: *The Crystal Structure of Mollibdenite*, *Journal of American Chemical Society* **45**, 1466 (1923).
-

- [82] L. Rapoport, Y. Bilik, Y. Feldman, M. Homyonfer, S. R. Cohen and R. Tenne: *Hollow Nanoparticles of WS<sub>2</sub> as Potential Solid-State Lubricants*, Nature **387**, 791 (1997).
- [83] M. Chhowalla and G. A. J. Amaratunga: *Thin Films of Fullerene-Like MoS<sub>2</sub> Nanoparticles with Ultra-Low Friction and Wear*, Nature **407**, 164 (2000).
- [84] M. Nath, A. Govindaraj and C. N. R. Rao: *Simple Synthesis of MoS<sub>2</sub> and WS<sub>2</sub> Nanotubes*, Advanced Materials **13**, 283 (2001).
- [85] M. Remskar, Z. Skraba, F. Cléton, R. Sanjinés and F. Lévy: *MoS<sub>2</sub> as Microtubes*, Applied Physics Letters **69**, 351 (1996).
- [86] G. Seifert, H. Terrones, M. Terrones, G. Jungnickel and T. Frauenheim: *Structure and Electronic Properties of MoS<sub>2</sub> Nanotubes*, Physical Review Letters **85**, 146 (2000).
- [87] R. Tenne, M. Homyonfer and Y. Feldman: *Nanoparticles of Layered Compounds with Hollow Cage Structures (Inorganic Fullerene-Like Structures)*, Chemistry of Materials **10**, 3225 (1998).
- [88] G. L. Frey, S. Elani, M. Homyonfer, Y. Feldman and R. Tenne: *Optical Absorption Spectra of Inorganic Fullerene-Like MS<sub>2</sub> (M=Mo, W)*, Physical Review B **57**, 6666 (1998).
- [89] M. Remskar, A. Mrzel, Z. Skraba, A. Jesih, M. Ceh, J. Demsar, P. Stadelmann, F. Levy and D. Mihailovic: *Self-Assembly of Subnanometer-Diameter Single-Wall MoS<sub>2</sub> Nanotubes*, Science **292**, 479 (2001).
- [90] A. Kis, D. Mihailovic, M. Remskar, A. Mrzel, A. Jesih, I. Piwonski, A. J. Kulik, W. Benoit and L. Forró: *Shear and Young's Moduli of MoS<sub>2</sub> Nanotube Ropes*, Advanced Materials **15**, 733 (2003).
- [91] J. Liu, H. Dai, J. H. Hafner, D. T. Colbert, R. E. Smalley, S. J. Tans and C. Dekker: *Fullerene 'Crop Circles'*, Nature **385**, 780 (1997).
- [92] H. R. Shea, R. Martel and P. Avouris: *Electrical Transport in Rings of Single-Wall Nanotubes: One-Dimensional Localization*, Physical Review Letters **84**, 4441 (2000).
- [93] T. L. Mogne, C. Donnet, J. M. Martin, A. Tonck, N. Millard-Pinard, S. Fayeulle and N. Moncoffre: *Nature of Super-Lubricating MoS<sub>2</sub> Physical Vapor Deposition Coatings*, Journal of Vacuum Science & Technology A **12**, 1998 (1994).
- [94] G. Csanyi: *Unpublished Results*, (2003).
- [95] B. Vigolo, A. Penicaud, C. Coulon, C. Sauder, R. Paillet, C. Journet, P. Bernier and P. Poulin: *Macroscopic Fibers and Ribbons of Oriented Carbon Nanotubes*, Science **290**, 1331 (2000).
- [96] L. W. Hobbs in *Quantitative Electron Microscopy, Vol. Xxv of NATO Advanced Study Institute, Series B: Physics*, edited by J. N. Chapman and A. J. Craven (Plenum, New York, 1984).
- [97] V. H. Crespi, N. G. Chopra, M. L. Cohen, A. Zettl and S. G. Louie: *Anisotropic Electron-Beam Damage and the Collapse of Carbon Nanotubes*, Physical Review B **54**, 5927 (1996).
- [98] J. C. Bourgoin and B. Massarani: *Threshold Energy for Atomic Displacement in Diamond*, Physical Review B **14**, 3690 (1976).
- [99] W. A. McKinley and H. Feschbach: *The Coulomb Scattering of Relativistic Electrons by Nuclei*, Physical Review **74**, 1759 (1948).

- 
- [100] F. Banhart: *Irradiation Effects in Carbon Nanostructures*, Reports on Progress in Physics **62**, 1181 (1999).
- [101] B. T. Kelly: *The Physics of Graphite*, Applied Science, London (1981).
- [102] F. Banhart, T. Füller, P. Redlich and P. M. Ajayan: *The Formation, Annealing and Self-Compression of Carbon Onions under Electron Irradiation*, Chemical Physics Letters **269**, 349 (1997).
- [103] K. Niwase: *Irradiation-Induced Amorphization of Graphite*, Physical Review B **52**, 15785 (1995).
- [104] R. H. Telling, C. P. Ewels, A. A. El-Barbary and M. I. Heggie: *Wigner Defects Bridge the Graphite Gap*, Nature Materials **2**, 333 (2003).
- [105] F. Banhart and P. M. Ajayan: *Carbon Onions as Nanoscopic Pressure Cells for Diamond Formation*, Nature **382**, 433 (1996).
- [106] D. Ugarte: *Curling and Closure of Graphitic Networks under Electron-Beam Irradiation*, Nature **359**, 707 (1992).
- [107] F. Banhart, M. Zwanger and H. Muhr: *The Formation of Curled Concentric-Shell Clusters in Boron-Nitride under Electron-Irradiation*, Chemical Physics Letters **231**, 98 (1994); G. Lulli, A. Parisini and G. Mattei: *Influence of Electron-Beam Parameters on the Radiation-Induced Formation of Graphitic Onions*, Ultramicroscopy **60**, 187 (1995).
- [108] M. S. Zwanger, F. Banhart and A. Seeger: *Formation and Decay of Spherical Concentric-Shell Carbon Clusters*, Journal of Crystal Growth **163**, 445 (1996).
- [109] P. Redlich, F. Banhart, Y. Lyutovich and P. M. Ajayan: *EELS Study of the Irradiation-Induced Compression of Carbon Onions and Their Transformation to Diamond*, Carbon **36**, 561 (1998).
- [110] Y. Lyutovich and F. Banhart: *Low-Pressure Transformation of Graphite to Diamond under Irradiation*, Applied Physics Letters **74**, 659 (1999).
- [111] P. M. Ajayan, C. Colliex, P. Bernier and J. M. Lambert: *Shape Transformations in Single-Layer Carbon Nanotubes*, Microscopy Microanalysis Microstructures **4**, 501 (1993).
- [112] C. H. Kiang, W. A. Goddard, R. Beyers and D. S. Bethune: *Structural Modification of Single-Layer Carbon Nanotubes with an Electron Beam*, Journal of Physical Chemistry **100**, 3749 (1996).
- [113] B. W. Smith and D. E. Luzzi: *Electron Irradiation Effects in Single Wall Carbon Nanotubes*, Journal of Applied Physics **90**, 3509 (2001).
- [114] P. M. Ajayan, V. Ravikumar and J.-C. Charlier: *Surface Reconstructions and Dimensional Changes in Single-Walled Carbon Nanotubes*, Physical Review Letters **81**, 1437 (1998).
- [115] M. Terrones, H. Terrones, F. Banhart, J.-C. Charlier and P. M. Ajayan: *Coalescence of Single-Walled Carbon Nanotubes*, Science **288**, 1226 (2000).
- [116] Y. Zhang and S. Iijima: *Microstructural Evolution of Single-Walled Carbon Nanotubes under Electron Irradiation*, Philosophical Magazine Letters **80**, 427 (2000).
- [117] M. Terrones, F. Banhart, N. Grobert, J.-C. Charlier, H. Terrones and P. M. Ajayan: *Molecular Junctions by Joining Single-Walled Carbon Nanotubes*, Physical Review Letters **89**, 075505 (2002).
- [118] V. H. Crespi, N. G. Chopra, M. L. Cohen, A. Zettl and V. Radmilovic: *Site-Selective Radiation Damage of Collapsed Carbon Nanotubes*, Applied Physics Letters **73**, 1435 (1998).
-

- [119] A. V. Krasheninnikov, K. Nordlund, J. Keinonen and F. Banhart: *Ion-Irradiation-Induced Welding of Carbon Nanotubes*, Physical Review B **66**, 245403 (2002).
- [120] H. Stahl, J. Appenzeller, R. Martel, Ph. Avouris and B. Lengeler: *Intertube Coupling in Ropes of Single-Wall Carbon Nanotubes*, Physical Review Letters **85**, 5186 (2000).
- [121] B. W. Smith, M. Monthieux and D. E. Luzzi: *Encapsulated C60 in Carbon Nanotubes*, Nature **396**, 323 (1998).
- [122] B. W. Smith, M. Monthieux and D. E. Luzzi: *Carbon Nanotube Encapsulated Fullerenes: A Unique Class of Hybrid Materials*, Chemical Physics Letters **315**, 31 (1999).
- [123] W. Mickelson, S. Aloni, W.-Q. Han, J. Cumings and A. Zettl: *Packing C60 in Boron Nitride Nanotubes*, Science **300**, 467 (2003).
- [124] A. B. Dalton, S. Collins, E. Muñoz, J. M. Razal, V. H. Ebron, J. P. Ferraris, J. N. Coleman, B. G. Kim and R. H. Baughman: *Super-Tough Carbon-Nanotube Fibres*, Nature **423**, 703 (2003).
- [125] A. Kis, G. Csanyi, J.-P. Salvetat, T.-N. Lee, E. Coureau, A. J. Kulik, W. Benoit, J. Brugger and L. Forró: *Bridging Single-Walled Carbon Nanotubes in Bundles*, submitted to Nature Materials.
- [126] E. Salonen, A. V. Krasheninnikov and K. Nordlund: *Ion-Irradiation-Induced Defects in Bundles of Carbon Nanotubes*, Nuclear Instruments and Methods in Physics Research B **193**, 603 (2002).
- [127] A. V. Krasheninnikov, K. Nordlund, M. Sirviö, E. Salonen and J. Keinonen: *Formation of Ion-Irradiation-Induced Atomic-Scale Defects on Walls of Carbon Nanotubes*, Physical Review B **63**, 245405 (2001).
- [128] B. Alberts, A. Johnson, J. Lewis, M. Raff, K. Roberts and J. D. Watson: *Molecular Biology of the Cell*, Garland Publishing, New York (2002).
- [129] B. Alberts, D. Bray, J. Lewis, M. Raff, K. Roberts and J. D. Watson: *Molecular Biology of the Cell*, Garland Publishing, New York (1994).
- [130] <http://www.ccd.com/camimages.html>
- [131] J. B. Olmsted and G. G. Borisy: *Ionic and Nucleotide Requirements for Microtubule Polymerization in Vitro*, Biochemistry **14**, 2996 (1975).
- [132] Y. H. Song and E. Mandelkow: *Recombinant Kinesin Motor Domain Binds to Beta-Tubulin and Decorates Microtubules with a B-Surface Lattice*, Proceedings of the National Academy of Sciences of the United States of America **90**, 1671 (1993).
- [133] B. A. Afzelius, P. L. Bellon and S. Lanzavecchia: *Microtubules and Their Protofilaments in the Flagellum of an Insect Spermatozoon*, Journal of Cell Science **95**, 207 (1990); U. Eichenlaubritter and J. B. Tucker: *Microtubules with More Than 13 Protofilaments in the Dividing Nuclei of Ciliates*, Nature **307**, 60 (1984).
- [134] P. R. Burton, R. E. Hinkley and G. B. Pierson: *Tannic Acid-Stained Microtubules with 12, 13, and 15 Protofilaments*, Journal of Cell Biology **65**, 227 (1975); J. B. Tucker, M. J. Milner, D. A. Currie, J. W. Muir, D. A. Forrest and M. J. Spencer: *Centrosomal Microtubule-Organizing Centers and a Switch in the Control of Protofilament Number for Cell Surface-Associated Microtubules During Drosophila Wing Morphogenesis*, European Journal of Cell Biology **41**, 279 (1986).

- 
- [135] C. Savage, M. Hamelin, J. G. Culotti, A. Coulson, D. G. Albertson and M. Chalfie: *Mec-7 Is a Beta-Tubulin Gene Required for the Production of 15- Protofilament Microtubules in Caenorhabditis-Elegans*, *Genes & Development* **3**, 870 (1989).
- [136] D. Chretien and R. H. Wade: *New Data on the Microtubule Surface Lattice*, *Biology of the Cell* **71**, 161 (1991).
- [137] R. Schultheiss and E. Mandelkow: *3-Dimensional Reconstruction of Tubulin Sheets and Reinvestigation of Microtubule Surface Lattice*, *Journal of Molecular Biology* **170**, 471 (1983).
- [138] P. Meurer-Grob, J. Kasparian and R. H. Wade: *Microtubule Structure at Improved Resolution*, *Biochemistry* **40**, 8000 (2001).
- [139] D. Chretien and S. D. Fuller: *Microtubules Switch Occasionally into Unfavorable Configurations During Elongation*, *Journal of Molecular Biology* **298**, 663 (2000).
- [140] T. Horio and H. Hotani: *Visualization of the Dynamic Instability of Individual Microtubules by Dark-Field Microscopy*, *Nature* **321**, 605 (1986).
- [141] D. K. Fygenson, E. Braun and A. Libchaber: *Phase Diagram of Microtubules*, *Physical Review E* **50**, 1579 (1994).
- [142] R. H. Wade and A. A. Hyman: *Microtubule Structure and Dynamics*, *Current Opinion in Cell Biology* **9**, 12 (1997).
- [143] P. J. Sammak and G. G. Borisy: *Direct Observation of Microtubule Dynamics in Living Cells*, *Nature* **332**, 724 (1988).
- [144] E.-M. Mandelkow, E. Mandelkow and R. A. Milligan: *Microtubule Dynamics and Microtubule Caps: A Time Resolved Cryo-Electron Study*, *Journal of Cell Biology* **114**, 977 (1991).
- [145] F. Gaskin, C. R. Cantor and M. Shelanski: *Turbidimetric Studies of in Vitro Assembly and Disassembly of Porcine Neurotubules*, *Journal of Molecular Biology* **89**, 737 (1974).
- [146] J. Howard: *Mechanics of Motor Proteins and the Cytoskeleton*, Sinauer Associates, Inc., Sunderland, MA (2001).
- [147] E. Nogales, S. G. Wolf and K. H. Downing: *Structure of the Alphabeta Tubulin Dimer by Electron Crystallography*, *Nature* **391**, 199 (1998).
- [148] J. Lowe, H. Li, K. H. Downing and E. Nogales: *Refined Structure of Alpha Beta-Tubulin at 3.5 Angstrom Resolution*, *Journal of Molecular Biology* **313**, 1045 (2001).
- [149] E. Nogales, M. Whittaker, R. Milligan and K. Downing: *High-Resolution Model of the Microtubule*, *Cell* **96**, 79 (1999).
- [150] H. Li, D. J. Derosier, W. V. Nicholson, E. Nogales and K. H. Downing: *Microtubule Structure at 8 Angstrom Resolution*, *Structure* **10**, 1317 (2002).
- [151] L. A. Amos: *Focusing-in on Microtubules*, *Current Opinion in Structural Biology* **10**, 236 (2000).
- [152] H. W. Detrich, S. K. Parker, R. C. Williams, Jr., E. Nogales and K. H. Downing: *Cold Adaptation of Microtubule Assembly and Dynamics. Structural Interpretation of Primary Sequence Changes Present in the Alpha - and Beta -Tubulins of Antarctic Fishes*, *Journal of Biological Chemistry* **275**, 37038 (2000).

- [153] J. Mizushima-Sugano, T. Maeda and T. Miki-Noumura: *Flexural Rigidity of Single Microtubules Estimated from Statistical Analysis of Their Contour Lengths and End-to-End Distances*, *Biochimica et Biophysica Acta* **755**, 257 (1983).
- [154] L. D. Landau and E. M. Lifshitz: *Statistical Physics*, Pergamon Press, New York (1969).
- [155] F. Gittes, B. Mickey, J. Nettleton and J. Howard: *Flexural Rigidity of Microtubules and Actin Filaments Measured from Thermal Fluctuations in Shape*, *Journal of Cell Biology* **120**, 923 (1993).
- [156] B. Mickey and J. Howard: *Rigidity of Microtubules Is Increased by Stabilizing Agents*, *Journal of Cell Biology* **130**, 909 (1995).
- [157] P. Venier, A. C. Maggs, M.-F. Carlier and D. Pantaloni: *Analysis of Microtubule Rigidity Using Hydrodynamic Flow and Thermal Fluctuations*, *Journal of Biological Chemistry* **269**, 13353 (1994).
- [158] A. Ashkin and J. M. Dziedzic: *Optical Trapping and Manipulation of Viruses and Bacteria*, *Science* **235**, 1517 (1987).
- [159] H. Felgner, R. Frank and M. Schliwa: *Flexural Rigidity of Microtubules Measured with the Use of Optical Tweezers*, *Journal of Cell Science* **109**, 509 (1996).
- [160] A. Vinckier, C. Dumortier, Y. Engelborghs and L. Hellemans: *Dynamical and Mechanical Study of Immobilized Microtubules with Atomic Force Microscopy*, *Journal of Vacuum Science and Technology B* **14**, 1427 (1996).
- [161] P. J. D. Pablo, I. A. T. Schaap, F. C. Mackintosh and C. F. Schmidt: *Deformation and Collapse of Microtubules on the Nanometer Scale*, *Physical Review Letters* **91**, 098101 (2003).
- [162] F. Moreno-Herrero, P. J. De Pablo, R. Fernández-Sánchez, J. Colchero, J. Gómez-Herrero and A. M. Baró: *Scanning Force Microscopy Jumping and Tapping Modes in Liquids*, *Applied Physics Letters* **81**, 2620 (2002).
- [163] R. Vale, C. Coppin, F. Malik, F. Kull and R. Milligan: *Tubulin GTP Hydrolysis Influences the Structure, Mechanical Properties and Kinesin-Driven Transport of Microtubules*, *Journal of Biological Chemistry* **269**, 23769 (1994).
- [164] A. R. Cross and R. C. Williams: *Kinky Microtubules: Bending and Breaking Induced by Fixation in Vitro with Glutaraldehyde and Formaldehyde*, *Cell Motility and the Cytoskeleton* **20**, 272 (1991).
- [165] W. Vater, W. Fritzsche, A. Schaper, K. J. Böhm, E. Unger and T. M. Jovin: *Scanning Force Microscopy of Microtubules and Polymorphic Tubulin Assemblies in Air and in Liquid*, *Journal of Cell Science* **108**, 1063 (1995).
- [166] N. A. Baker, D. Sept, M. J. Holst and J. A. Mccammon: *The Adaptive Multilevel Finite Element Solution of the Poisson–Boltzmann Equation on Massively Parallel Computers*, *IBM Journal of research and Development* **45**, 427 (2001).
- [167] Y. L. Lyubchenko, A. A. Gall, L. S. Shlyakhtenko, R. E. Harrington, B. L. Jacobs, P. I. Oden and S. M. Lindsay: *Atomic Force Microscopy Imaging of Double-Stranded DNA and RNA*, *Journal of Biomolecular Structure & Dynamics* **10**, 589 (1992).
- [168] M. Rief, V. T. Moy, E.-L. Florin, M. Ludwig and H. E. Gaub in *Procedures in Scanning Probe Microscopies* (John Wiley & Sons, Chichester, 1998), p. 497.
- [169] <http://www.cytoskeleton.com/tptier2.htm>

- 
- [170] Z. Yang, I. Mochalkin, L. Veerapandian, M. Riley and R. F. Doolittle: *Crystal Structure of Native Chicken Fibrinogen at 5.5 Angstrom Resolution*, PNAS **97**, 3907 (2000); J. R. Horton and X. Cheng: *PvuII Endonuclease Contains Two Calcium Ions in Active Sites*, Journal of Molecular Biology **300**, 1051 (2000).
- [171] D. Turner, C. Chang, K. Fang, P. Cuomo and D. Murphy: *Kinesin Movement on Glutaraldehyde-Fixed Microtubules*, Analytical Biochemistry **242**, 20 (1996).
- [172] R. H. Himes, M. A. Jordan and L. Wilson: *The Effects of Glutaraldehyde on the Bound Nucleotide Content and Morphology of Microtubules in Vitro*, Cell Biology International Reports **6**, 697 (1982).
- [173] Temperature Control Stage, Molecular Imaging, <http://www.molec.com/tempcontrol/index.html>
- [174] A. Kis, S. Kasas, B. Babic, A. J. Kulik, W. Benoît, G. A. D. Briggs, C. Schönenberger, S. Catsicas and L. Forró: *Nanomechanics of Microtubules*, Physical Review Letters **89**, 248101 (2002).
- [175] M. Grandbois, M. Beyer, M. Rief, H. Clausen-Schaumann and H. E. Gaub: *How Strong Is a Covalent Bond?*, Science **283**, 1727 (1999).
- [176] O. Keskin, S. R. Durell, I. Bahar, R. L. Jernigan and D. G. Covell: *Relating Molecular Flexibility to Function: A Case Study of Tubulin*, Biophysical Journal **83**, 663 (2002).
- [177] S. Kasas, A. Kis, B. M. Riederer, L. Forró, G. Dietler and S. Catsicas: *Mechanical Properties of Microtubules Explored Using the Finite Elements Method*, accepted for publication in ChemPhysChem (2003).
- [178] D. Mihailovic, Z. Jaglicic, D. Arcon, A. Mrzel, A. Zorko, M. Remskar, V. V. Kabanov, R. Dominko, M. Gaberscek, C. J. Gomez-Garcia, J. M. Martinez-Agudo and E. Coronado: *Unusual Magnetic State in Lithium-Doped MoS<sub>2</sub> Nanotubes*, Physical Review Letters **90**, 146401 (2003).

*Note: This manuscript can be downloaded as a pdf file from:*

*<http://library.epfl.ch/theses/>*





# *Curriculum Vitae*

NAME: KIS András

DATE OF BIRTH: 1st of November 1975 in Zagreb, Croatia  
Hungarian and Croatian citizen

## ***Education***

2000-2003 PhD student at EPFL, Faculty of basic sciences, Institute of physics of complex matter under supervision and in the group of prof. Forró

1999 Diploma thesis on the subject of the development of microcalorimetric measurements and measurements of the heat capacity of  $(\text{TaSe}_4)_2\text{I}$

1994-1999 Physics department of the University of Zagreb, Croatia, experimental and theoretical solid-state physics

1994 Baccalaureate, MIOC (Mathematical and Informational Educational Center) high school, Zagreb, Croatia

## ***Languages***

Speaking English, German, French, Hungarian and Croatian.

## ***Research interests***

Nanophysics and nanoscience – fundamental properties of nanotubes and applications in devices, molecular biophysics, Alzheimer's disease.

## ***Experimental methods***

Atomic force, transmission electron and scanning electron microscopies  
Synchrotron-source infrared microspectroscopy, UV spectrophotometry  
Thin-film evaporation, sputtering  
Microcalorimetry, electrical resistivity

### ***Teaching experience***

- 2001-2003 Teaching assistant – exercises, General Physics I (Mécanique générale), EPFL (prof. Benoit)
- 2001 Teaching assistant, Introduction to Metrology (Travaux pratiques de Metrologie), EPFL (Dr. Gremaud, Dr. Schaller)
- 2000 Teaching assistant, Physics Lab (Travaux pratiques de physique), EPFL, (Dr. Gremaud, Dr. Schaller)

### ***Achievements***

- 1997 Scholarship of the University of Zagreb
- 1997 Rector's award for the best student work in the academic year 1996/97 for the paper "Application of hierarchical models on the thermal relaxation in SDW systems"
- 1994 Participation on the 25th International Physics Olimpiad in Beijing

### ***Oral presentations***

- 2003 "Reinforcement of carbon nanotube ropes by local irradiation"  
Materials Research Society spring meeting, San Francisco, USA
- "Irradiation of carbon nanotube ropes"  
Annual meeting of the Swiss Physical society, Basel, Switzerland
- "Nanomechanics of individual tubular structures"  
International Winterschool "Electronic properties of Novel materials: Molecular Nanostructures" IWEPNM21, Kirchberg, Austria
- 2002 "Carbon nanotubes and nanomechanics"  
tutorial on the Twannberg nanoscience workshop, Switzerland
- 2001 "Binding carbon nanotubes together by irradiation"  
Seminar of the National Synchrotron Light Source, Brookhaven National Laboratory, USA
- "Mechanical properties of microtubules"  
Seminar of the European Molecular Biology Laboratory, Heidelberg, Germany

# Publications

## Articles

“Shear and Young's moduli of MoS<sub>2</sub> nanotube ropes”

A. Kis, D. Mihailovic, M. Remskar, A. Mrzel, A. Jesih, I. Piwonski, A. J. Kulik, W. Benoit, L. Forró

Advanced Materials 15, 733 (2003).

DOI: 10.1002/adma.200304549

“Nanomechanics of microtubules”

A. Kis, S. Kasas, B. Babic, A. J. Kulik, W. Benoît, G. A. D. Briggs, C. Schönenberger, S. Catsicas, L. Forró

Physical Review Letters 89, 248101 (2002).

DOI: 10.1103/PhysRevLett.89.248101

“Specific heats of the charge density wave compounds o-TaS<sub>3</sub> and (TaSe<sub>4</sub>)<sub>2</sub>I”

D. Staresinic, A. Kis, K. Biljakovic, B. Emerling, J. W. Brill, J. Souletie, H. Berger F. Levy

European Physical Journal B 29, 71-7 (2002). DOI: 10.1140/epjb/e2002-00263-1

## Book chapter

“Nanoscale Mechanical Properties Using SPM – Techniques and Applications”

A. J. Kulik, A. Kis, G. Gremaud, S. Hengsberger and L. Forró

in Handbook of Nanotechnology (in press), B. Bushan, ed. Heidelberg, Springer-Verlag (2004). ISBN: 3-540-01218-4

## Submitted and in preparation

“Mechanical properties of microtubules explored using the finite elements method”

S. Kasas, A. Kis, B.M. Riederer, L. Forró, G. Dietler, and S. Catsicas

accepted for publication in ChemPhysChem

“Connecting single-walled carbon nanotubes inside ropes”

A. Kis, G. Csanyi, J.-P. Salvetat, T.-N. Lee, E. Couteau, A.J. Kulik, W. Benoit, J. Brugger, L. Forró

in preparation



# *Acknowledgements*

During the four years that I have spent on the EPFL, many people have helped me finish the work described in this thesis.

I thank my thesis advisor, Prof. László Forró for his confidence in my abilities and for giving me the opportunity to work in his research group under excellent working conditions. This thesis is built on his creative ideas and constructive propositions which helped me find my way. Andrzej Kulik helped me by sharing a part of his technical expertise and lending me his enthusiastic support. I owe him for his patience not only in the lab, but also on the slopes where he taught me how to ski.

Prof. Benoit was always open for discussion, showing great moral and material support. His advice were always helpful. Thanks to Prof. Forró and Prof. Benoit, I was able to participate on numerous scientific conferences.

Many thanks to Dr. Sándor Kasas for his endless optimism, many insights into the biological relevance of this work and also for the finite elements modeling presented at the end of chapter 7. His legendary jokes on group meetings always made us laugh.

Thanks also to Dr. Gérard Gremaud for theoretical modelling and numerous discussions. I am also thankful to Dr. Neil Thomson who helped in the first months of this thesis by teaching me how to work with the AFM. Bakir Babić, Dr. Thomas Nussbaumer and Prof. Christian Schönenberger are gratefully acknowledged for the fruitful collaboration in the frames of the “Nanoscale Science” NCCR of the Swiss National Science Foundation. This collaboration resulted in the fabrication of the substrate necessary for measurements of the shear modulus of microtubules. Many thanks to Prof. Dragan Mihailović for initiating measurements on MoS<sub>2</sub> and help on publishing the results. Many thanks also go to him and his group for providing these unique samples. I am grateful to Prof. Jürgen Brugger for providing the perforated substrates that made the measurements on irradiated nanotubes possible. Thanks to Dr. Thien-Nga Lee for the initial TEM work on nanotube irradiation and Dr. Edina Couteau for nanotube purification.

Stimulating discussions with Prof. Jean-Pierre Aimé and Prof. Andrew Briggs brought many new insights and reminded me how one has to be careful when interpreting the experimental data, for which I am grateful to them. I am also thankful to Dr. Jean-Paul Salvetat for numerous discussions and his good sense of humor. I would also like to thank Dr. Gábor Csányi for theoretical modelling and discussions.

I thank Prof. Ueli Aebi and Prof. Harald Brune, together with Prof. Jean-Pierre Aimé for accepting to participate on the jury of this thesis.

I am indebted to Gerald Beney for his tireless polishing of the alumina substrates, Antonio Gentile and Bernard Guisolan of the mechanical workshop for the machined pieces used in this thesis (the copper fluid chamber). I also thank Alessandro Ichino for his help with electronic parts and his unique sense of humor, and Guido Milanese for help and troubleshooting of the electron microscope and the CIME for access to the electron microscopes.

Many thanks to Monique Bettinger and Sigrid Lovato, who helped me a lot as our institute secretaries, by their efficiency and smiles.

Many thanks to my friends and colleagues with whom I have passed many pleasurable moments not only on the institute, but also in the outside world (in the alphabetic order): Katharina Buss, Maren&Zornica Daraktchiev, Olivier&Edina Couteau, Titusz Fehér, Richard Gaál, Xavier Hoffer, Sylvia Jeney, Kyumin Lee, Pierre Marcoux, Csilla Mikó, Slobodan Mitrović, Mirko Milas, Tim Otterburg, Maria Seo, Robert Szoszkiewicz, Iva Tkalčec, Bertrand Vileno (also many thanks for the help with French!). Thanks to Branimir Lukić who had been working with me during six months on his diploma thesis, for teaching me the joy of teaching. Thanks also to Iva, Bert, Maria and Titusz for critical reading of the manuscript.

Great thanks also to my roommates: Emmanuel Dupas, Ireneusz Piwonski, Raphael Foschia, Brian Huey, and Marc Jobin.

Many thanks to my beloved parents Ildikó and Miklós and my sister Margita for their unconditional love and support that helped me through these last four years.

At the end, my thanks go to beloved Aleksandra, who was with me for better, for worse and shared all the joys and troubles of these four laborious years.